Multiscale Investigations of Nanoprecipitate Nucleation, Growth, and Coarsening in ODS FeCrAl Alloys: Optimizing Sink Strength for Nuclear Applications

A Dissertation Presented for the
Doctor of Philosophy
Degree
The University of Tennessee, Knoxville

Caleb Patrick Massey

December 2018

Copyright © 2018 by Caleb P. Massey
All rights reserved.

DEDICATION

To my wife,

Logan Gravitt Massey

For your steadfast encouragement,

For your patience,

For your unwavering devotion,

With Love.

ACKNOWLEDGEMENTS

Over the course of my graduate career, I have been fortunate to have many years of experience in materials development, irradiation effect, and characterization techniques constantly at my disposal. Although technology provides a limitless reservoir of knowledge through the internet, I have treasured the ability to pick the minds of experts and to establish lasting personal and professional friendships in the process.

First and foremost, I would like to thank Dr. Steven Zinkle for mentoring me throughout my graduate career at the University of Tennessee. Although my transfer to the university occurred within the middle of an academic year, Dr. Zinkle made sure that my acclimation to the university was a smooth process. I will always be grateful for the amount of time he continues to prioritize for the success of his students, and his willingness to sacrifice many hours of his own time over the course of the week so that we can make the most of ours. I would also like to extend a special thanks to Dr. Brian Wirth for continuously challenging me to become a better researcher. Not one conversation omitted an opportunity to critically evaluate aspects of my theoretical or experimental approach, which made each conversation uniquely enjoyable.

I am greatly appreciative of the support given to me by Dr. Sebastien Dryepondt, Dr. Kevin Field, Kory Linton, Tom Geer, and countless others at Oak Ridge National Laboratory. My gratitude for Phil Edmondson's patience, guidance, and expertise cannot be understated. I would like to specifically acknowledge and thank Dr. Jonathan Poplawsky for his flexibility and willingness to assist me in acquiring much of the robust data that has made this work possible. I am also thankful to have had Dr. David Hoelzer as a mentor over the course of my graduate career. I will always be grateful to Dr. Kurt Terrani for his unwavering trust and support, and for constantly encouraging me to take on new projects and challenges.

I am thankful as well for the unique opportunity to travel to Germany and study under Dr. Baptiste Gault at the Max-Planck-Institut für Eisenforschung (MPIE). Collaborating with Anoop Kini and Dr. Gault was a memorable and incredibly beneficial experience, and I cannot wait for more collaboration opportunities.

It is difficult to find the appropriate words to acknowledge the impact Dr. Gokul Vasudevamurthy has had over the course of my academic career. In-fact, without him I would have never even thought of attending graduate school. Dr. V, thank you for being a confidant, a mentor, a teacher, and a friend. Thank you for the stories, the lessons, and for believing in me, even when I was an undergraduate who had no idea what I was doing.

Finally, I would like to thank my friends and family. My mother and father have sacrificed considerably to ensure that I had the opportunity to pursue and achieve my goals, and I am forever thankful for their love and devotion. To my mother-in-law, Gay Gravitt, I extend my gratitude for her continuous support and encouragement. In addition to the long list of friends and acquaintances that have supported and encouraged me during my academic career, I would like to thank Dr. Rachel Seibert for her unconditional friendship and kindness. Lastly, but certainly not least, I would like to thank my wife, Logan Massey, for her unwavering love, support, and sacrifice over the course of my graduate career. I cannot thank you enough for accompanying me during this journey spanning two universities in two different states, for enduring the many hours of research day and night, and for always believing in the realization of this goal through times of happiness and adversity.

ABSTRACT

One of the major obstacles in the realization of advanced nuclear reactor concepts is the lack of materials that can withstand the extreme conditions associated with these environments. High-temperatures, irradiation damage, and environmental degradation all limit the viability of conventional materials and requires the development of advanced materials to overcome these challenges. Fortunately, alloys containing a high number density of dispersed second phase particles, termed oxide dispersion strengthened (ODS) alloys, have been under investigation due to their high temperature strength, their exceptional oxidation resistance in the presence of steam, and their irradiation resistance.

Although there exists substantial data on the optimization of ODS FeCr alloys in the literature, the increasing demand for improved oxidation resistance in both current and advanced nuclear reactors has resulted in renewed interest in ODS FeCrAl alloys that have competitive properties in comparison to ODS FeCr alloys while simultaneously increasing the resistance to corrosion and oxidation in nuclear environments. However, there are still substantial gaps in knowledge pertaining to the effects of alloy composition and thermomechanical treatments on the nanoprecipitate distributions in these ODS FeCrAl alloys.

In this study, ODS Fe-based alloy powders with alloying additions CrAZY (Cr-Al-Zr-Y) were fabricated using a mechanical alloying approach followed by either powder heat treatment or alloy consolidation treatments to study the nucleation and growth kinetics for nanoscale precipitation. Using a multi-scale approach combining the near-atomic scale resolution of atom probe tomography (APT) with macro-scale small-angle neutron scattering (SANS) powder experiments, it has been shown that the composition and structure match closely to the yttrium aluminum garnet (YAG) or yttrium aluminum perovskite (YAP) phase depending on thermal annealing temperature and time. It was

also determined that Zr preferentially sequesters impurity C and N elements within the alloy microstructure to form carbonitrides.

Using long-term coarsening data for annealed CrAZY powders, a power law coarsening model was developed for representative thermomechanical processing temperature ranges. Using the results of this model, an innovative two-step thermal annealing treatment for alloy consolidation is proposed that maximizes alloy irradiation resistance through an increase in sink-strength while also allowing for the optimization of alloy strength and ductility.

Keywords: oxide dispersion strengthened (ODS) alloy, precipitation, coarsening, atom probe tomography (APT), small-angle neutron scattering (SANS)

TABLE OF CONTENTS

CHAPTER 1: Introduction 1
1.1. The Need for Advanced Materials for Nuclear Reactors 1
1.2. Radiation Damage 4
1.2.1. Irradiation-Induced Defects 4
The Importance of Interfaces: A First-Principles Approach 7
1.2.2. Irradiated Nanoprecipitate Stability in Ferritic ODS Alloys 8
1.2.3. Sink-Strength Dependence for Irradiated ODS FeCr(Al) Alloys 11
CHAPTER 2: Literature Review of ODS Alloys 14
2.1. Strengthening Mechanisms in ODS Alloys 14
2.2. Precipitate Nucleation, Growth, and Coarsening 19
2.3. Grain Recovery and Recrystallization 25
2.4. Conventional Processing Route for ODS Alloys 31
2.4.1. Powder Composition Selection 32
2.4.2. Mechanical Alloying 42
2.4.3. Consolidation Methods and Thermomechanical Treatments 46
2.4.4. Summary of Research Objectives 52
CHAPTER 3: Characterization Techniques 58
3.1. Atom Probe Tomography (APT) 58
3.1.1. Fundamental Principles of the APT Technique 58
3.1.2. Artifacts, Errors, and Limitations of APT 63
3.2. Small Angle Neutron Scattering (SANS) 66
3.2.1. Macroscale Properties from Nanoscale Interactions 67
3.2.2. Limitations and Errors of the SANS Technique 73
3.3. Electron Microscopy Methods 74
CHAPTER 4: Experimental Materials and Methods 78
4.1. Process Development for Powder Experiments 78
4.1.1. Powder Composition and Mechanical Alloying 79

4.1.2. Powder Packaging/Encapsulation and Annealing 81
4.1.3. Focused Ion Beam (FIB) Specimen Preparation 85
4.2. APT Data Collection and Analysis 87
4.2.1. Sample Reconstruction Parameters 89
4.2.2. Cluster Identification 90
4.2.3. Mass-Spectrum Peak Identification 92
4.2.4. Field-Induced Trajectory Aberrations 95
4.3. SANS Data Collection 102
4.3.1. Data Fitting and Structure Identification 104
4.4. Electron Microscopy Data Collection 108
CHAPTER 5: Parametric Evaluation of Processing Parameters on Microstructure and Dispersion Characteristics 109
5.1. Extruded Rod vs. Annealed Powder 109
5.2. Effect of Mechanical Alloying Device 123
5.3. Effect of Binning Parameters and LEAP Detection Efficiency on Precipitate Compositions 125
CHAPTER 6: Multi-scale Characterization of Nanoprecipitation in ODS FeCrAl Alloy Powders and Alloys 134
6.1. Effect of Added Zr on Observed Precipitate Populations 136
6.2. Compositional Measurements using APT 146
6.3. Structure Identification using SANS 157
6.4. Comparison with Computational Thermodynamics 168
CHAPTER 7: Nanoprecipitate Nucleation, Growth, and Coarsening Kinetics 175
7.1. In-situ Observation of Precipitate Nucleation and Growth 175
7.2. Long-term Nanoprecipitate Coarsening Kinetics 179
7.3. Applied Kinetics to the Design of ODS FeCrAl with high Sink Strength and Ductility 193
CHAPTER 8: Conclusions 202
8.1. Summary of Experimental Findings 202

8.2. Contributions to the State-of-the-Art....203
8.3. Future Work....204
List of References....206
Appendix....223
Reconstructed Control Volumes....224
Lumped Capacitance Comparison of Temperature Profiles....228
Vita....231

LIST OF TABLES

Table 2.1. Nominal Composition of Popular Ferritic ODS Alloys 33
Table 2.2. Summary of elemental activities for various elements, reproduced from Alinger.....42
Table 2.3. Review of nanoprecipitate dispersions for ODS FeCr(Al) alloys in literature as a function of consolidation methodology. 55
Table 4.1. Sample matrix used for the precipitate investigations in this work.....79
Table 4.2. Theoretical A-ratios for various Y-Al-O stochiometric phases calculated from the scattering length densities of the matrix and precipitate. 107
Table 6.1. Chemical compositions of powders (at.%) and alloys provided by DIRATS. 135
Table 6.2. Corrected nanoprecipitate compositions measured by APT. Errors are reported as one standard deviation from the mean. Compositions are reported in at.%.....135
Table 6.3. Magnetic SANS fitting results through nonlinear least squares curve fitting for two distributions of precipitates in the two specified Q-ranges of interest. Also reported are the as-measured A-ratios averaged over the Q-range of interest. Reproduced from [203]. 160
Table 7.1. Calculated sink strengths for 106ZYA15C and 106ZY15C.....197
Table A.1. Visualization of Reconstructed Sample Volumes 224

LIST OF FIGURES

Figure 1.1. Nuclear reactor operating temperature and dose regimes, reproduced from [1, 2]. Shown are the current Light Water Reactor (LWR), the ITER fusion reactor, the Very High Temperature Reactor (VHTR), the Super Critical Water Reactor (SCWR), the Lead Fast Reactor (LFR), the Gas Fast Reactor (GFR), the Sodium Fast Reactor (SFR), and the Molten Salt Reactor (MSR). 2

Figure 1.2. The variation of ultimate tensile strength (UTS) as a function of temperature for stress-relieved Zircaloy-4 [7], wrought model FeCrAl alloy C35MN [8], and the CrAZY ODS FeCrAl alloy examined in this work. 3

Figure 1.3. The five irradiation-induced degradation phenomena in materials, as reported in [2] 6

Figure 1.4. Microstructure of ion irradiated 14YWT at low and high temperatures [32] 10

Figure 2.1. Visualization of the Orowan bowing mechanism. (a) a gliding edge dislocation approaches two dispersed particles in the glide plane, (b) the dislocation bows around the dispersed particles, and (c) the ends of the dislocation annihilate after bowing around the particle, leaving two dislocation loops and a resultant gliding dislocation [48].....15

Figure 2.2. Schematic diagrams used for the derivation of coarsening kinetics dominated by (a) 3D diffusion, (b) 2D diffusion along grain boundaries, and (c) 1D diffusion along dislocations. Arrows define directions by which solute atoms can diffuse to the precipitate. 23

Figure 2.3. A collection of edge dislocations in a deformed crystal along glide planes, from [82].....27

Figure 2.4. Depiction of dislocations in (a) the as-deformed state, (b) after dipole annihilation, and (c) after the polygonization process [82]. 27

Figure 2.5. Steps associated with the subgrain coalescence mechanism resulting in a new grain with uniform subgrain texture [81]. 28

Figure 2.6. (a) The SIBM mechanism describing the bulging of a grain boundary between grains of high and low dislocation density, (b) the dragging of the dislocation cell structure by the bulging grain boundary, and (c) the resulting SIBM-induced nucleus free of dislocations. Figure reproduced from [82]. 30
Figure 2.7. Schematic of the general powder metallurgical process used for the fabrication of an ODS alloy, where the consolidation method is chosen to be extrusion. 32
Figure 2.8. The Fe-Cr phase diagram from [94].....34
Figure 2.9. Fe-Cr-Al Phase Diagram (α' Cr region shown) [97] 35
Figure 2.10. Solid Solution Strengthening in BCC Fe for various elements, reproduced from [58].....36
Figure 2.11. Gibbs free energies for various binary oxides, referenced from [102] 38
Figure 2.12. Gibbs free energies for various binary carbides, referenced from [103] 39
Figure 2.13. Gibbs free energies for various binary nitrides, referenced from [104].....40
Figure 2.14. Solubility of Yttrium in BCC Fe as a function of temperature [68] 41
Figure 2.15. Orientations Used for Mechanical Property Evaluations [130] 48
Figure 2.16. Summary of microstructural changes during ODS alloy consolidation. EBSD pole figure maps after each processing stage are reproduced from literature [62, 84, 137, 141] 51
Figure 2.17. Identified phases in ODS FeCrAl alloys by various authors, color coded by study and arranged as a function of precipitate diameter [106, 110, 111, 153-159] .54
Figure 3.1. Various applications of the atom probe tomography technique for material science [172].....59
Figure 3.2. (a) a visual representation of a metal atom (grey) field-evaporated into a subsequent ion (black). (b) a graphical interpretation of the energies required to overcome with Q(F) and without Q_0 an applied electric field at the specimen apex [172]. 61
Figure 3.3. Schematic diagram of a delay-line detector commonly used for APT [172].61

Figure 3.4. (a) point density map for high purity aluminum with three identified poles, (b) a visualization of the different interatomic planes for each identified (115), (002), and (113) poles, and (c) the corresponding Hough transform for the poles [174]. ...62
Figure 3.5. Atomic density variations associated with precipitates of varying evaporation fields in comparison to the surrounding matrix, from [172] 64
Figure 3.6. Schematic of the general approach for a small angle neutron scattering experiment [183]. A neutron beam with direction (k) is scattered across angle (θ) to calculate the resultant scattering vector (q) measured in the SANS experiment.....67
Figure 3.7. Visual illustration of the scattering lengths (b) for both x-rays and neutrons for various isotopes. Hatched symbols indicate "negative" scattering lengths, while the sizes of the circles represent the magnitude for the scattering lengths [184]. The significant changes between elements of similar atomic number allows for beneficial contrast in neutron scattering expeirments. 69
Figure 3.8. SANS detector signals in the case of (a) a sample without an applied magnetic field and (b) a fully saturated magnetic field applied horizontally and perpendicular to the incident neutron beam [188].....72
Figure 3.9. The various interactions in electron microscopy that can be used for microstructural and compositional evaluations of materials [197] 75
Figure 3.10. (a) a composite Kikuchi map for a BCC material and (b) the indexed diffraction bands from the composite image [197] 76
Figure 4.1. Process diagram for precipitate nucleation and growth studies in this work.78
Figure 4.2. The as-received particle size distribution for the FeCrAlZr powder 80
Figure 4.3. The (a) CM01 and (b) CM08 high kinetic energy Zoz Simoloyer ball mills utilized for powder mechanical alloying 81
Figure 4.4. (a) encapsulated CrAZY ZY40H powders in quartz vials and (b) the box furnace utilized for ex-situ powder annealing treatments 82
Figure 4.5. The measured powder temperature profile (red) for ZY40H powder packed in a 2" extrusion can heated in a box furnace used for pre-extrusion annealing

treatments and (b) the powder temperature profile experienced by the powder in the in-situ SANS experiment. [203] 84
Figure 4.6. (a) Aluminum and (b) Molybdenum foil packets used for powder encapsulation for ex-situ and in-situ SANS experiments, respectively. 84
Figure 4.7. (a) An SEM-BSE image of a targeted FIB lift-out region for coarse and fine grain APT measurements in annealed ODS FeCrAl powder, (b) the corresponding lift-out from the same region, and (c) the landing and sectioning procedure used to prepare each APT sample from the coarse and fine grained regions. 86
Figure 4.8. Visualization of the flight paths of the (a) straight line 4000X Si and (b) reflectron model 4000X HR and 5000 XR atom probes. Also shown are example representative mass-to-charge ratio spectra for the (c) straight-line and (d) reflectron LEAP models.....88
Figure 4.9. The basic steps for tip reconstruction using a standard voltage reconstruction procedure using ODS FeCr alloy MA957 as an example. (a) a portion of the voltage curve is chosen, (b) crystallographic poles are identified using the detector event histogram, (c) based on the crystallographic pole, the interplanar distance is tuned through the tuning of the field factor and the tip radius, which results in (d) a reconstructed control volume where the interplanar distances at specified poles match the expected interplanar distances for the material.....91
Figure 4.10. Detector event histograms for (a) an ODS FeCrAl CrAZY alloy and (b) an ODS Fe-14Cr alloy, showing the same type of (110) pole. 91
Figure 4.11. The (a) nearest neighbor distribution, (b) cluster size distribution, (c) cluster count distribution, and (d) final cluster size distribution used for the optimization of the d_{max} and N_{min} parameters of the maximum separation method for statistically significant cluster identification. 93
Figure 4.12. A portion of the mass-to-charge ratio spectrum for a representative APT specimen with both (Y,Al,O) and (Zr,C,N) nanoprecipitation showing instances of peak overlaps for both the matrix and precipitates.....94

Figure 4.13. The atomic fractions of (a) Y, (b) O, and (c) AlO ions represented by 2D contour plots in a cylindrical region of interest equal to the thickness of the precipitate (3nm). In the nanoprecipitate region, (d) a relative atomic density ρr (the ratio of the atomic density in the precipitate vs the surrounding matrix) is calculated. 96

Figure 4.14. Schematic representation of a local environment of atoms in (a) the supersaturated solid solution state and (b) after a cluster has precipitated out of solution. 100

Figure 4.15. Average precipitate compositions as a function of normalized distance across 50 different precipitates in ODS FeCrAl alloy 125YF. Error bars indicate 95% confidence intervals for each position-dependent composition [100]. 100

Figure 4.16. Pictures of (a) the CG-2 beamline at the GP-SANS beamline at HFIR and (b) a simple specimen holder for scattering without an added magnet or furnace..103

Figure 5.1. The as-extruded microstructure of ODS FeCrAl alloy CrAZY_H1 extruded at 1100°C after annealing for 1h at the same temperature. Shown are the (a) grain map showing each grain as a separate color, (b) the grain size distribution of the alloy, (c) the pole figure orientation map of the microstructure in the longitudinal direction showing significant textures and (d) the color coded grain boundary map showing the variation of grain boundary misorientation angle for fine and coarse grain regions. 110

Figure 5.2. SEM-BSE images of the microstructures of the (a) as-milled ZY40H specimen, (b) the ZY10C15 specimen annealed for 15 min. in a 1000°C box furnace, and (c) the ZY10C60 specimen annealed for 60 min. in a 1000°C box furnace. Also overlaid is the approximate temperature reached by the powder in terms of the experimentally measured powder temperature profile. [203] 112

Figure 5.3. SEM-BSE images of the as-extruded microstructure of an ODS FeCrAl CrAZY alloy extruded at 1000°C after annealing for 1h (106ZY10C8). The micrograph in the (a) longitudinal direction and (b) the transverse orientation

indicate oxide-stringers along specific grain boundaries in the as-consolidated microstructure. [225] 113
Figure 5.4. Schematic describing the proposed mechanism for stringer formation in ODS FeCrAl alloys. [225] 114
Figure 5.5. Illustration of the uniformity of the nanoprecipitate dispersions in ODS FeCrAl CrAZY powder (ZY10C60) in both the fine grain and coarse grain regions through targeted APT experiments. Smaller (Y,Al,O) precipitates are illustrated using red 1.5% (Y,YO,AlO) isoconcentration surfaces and larger Zr-rich precipitates are shown as purple 10% Zr isoconcentration surfaces. [203] 115
Figure 5.6. (a)-(d) present the nanoprecipitate dissolution and re-precipitation mechanism proposed by Sallez [84], while (e) illustrates one APT control volume identified in this work providing similar nanoprecipitate features in alloy 106ZY10C8 supporting this conjectured mechanism. 118
Figure 5.7. A comparative illustration of the similarity of nanoprecipitate dispersions in both annealed powders and extruded alloys with 1000°C annealing treatments. Also shown is a qualitative increase in precipitate size with a decreasing number density for alloys consolidated via extrusion with increasing extrusion temperature. Red 1.5% (Y,YO,AlO) iso-concentration surfaces are shown for all samples with overlaid background matrix atoms. The purple feature in sample 106ZY10C1 is a Zr-rich region.....119
Figure 5.8. The experimentally measured (a) ultimate tensile strength, (b) yield strength, and (c) total elongation as a function of temperature for 106ZY10C1 and 106ZY15C as a function of temperature [113]. Also shown for comparison is a non-ODS wrought FeCrAl alloy (C35MN) [8]. In (d), room temperature yield strength values are compared with the computed yield strength using the RMS methodology.....122
Figure 5.9. SEM-BSE micrographs of alloys 106ZY10C1 and 106ZY10C8 mechanically alloyed in CM01 and CM08 ball-mills, respectively. Both alloys were subjected to a 1h heat treatment at 1000°C followed by extrusion at the same temperature. Oxide

stringers decorating grain boundaries are noted in both alloys, with sparse porosity also indicated. 124

Figure 5.10. Grain pole figure orientation maps (left) are shown for samples 106ZY10C1 and 106ZY10C8 for both (a-b) transverse (T) and (c-d) longitudinal (L) orientations. Also shown is (e) the grain size distribution for both samples (right) with average grain size values tabulated. 124

Figure 5.11. APT reconstructions for CrAZY ODS FeCrAl alloys extruded at 1000°C after annealing for 1h at the same temperature following mechanical alloying in either a CM01 (106ZY10C1) or CM08 (106ZY10C8) Zoz Simoloyer ball mill. Smaller (Y,Al,O) nanoprecipitates are shown using 1.5% (Y,YO,AlO) iso-concentration surfaces while a second population of Zr-rich precipitates are identified using 10% Zr iso-concentration surfaces. A comparison of nanoprecipitates size distributions is shown in (c). 126

Figure 5.12. APT reconstructions of sample ZY10C60 for a fine-grained region of CrAZY powder annealed for 60 min. in a 1000°C box furnace. Smaller (Y,Al,O) nanoprecipitates are shown using 1.5% (Y,YO,AlO) iso-concentration surfaces while a second population of Zr-rich precipitates are identified using 10% Zr iso-concentration surfaces. 0.1% of Fe matrix atoms are also overlaid as black dots. Dimensional axes units are in nm. 126

Figure 5.13. The effect of mass-to-charge ratio peak binning on the compositions and size distributions for identified (Y,Al,O)-rich nanoprecipitates in the ZY10C60 specimen previously shown in **Figure 5.12**. Illustrated are the Y/Al ratio, the ternary Y-Al-O diagram (point size proportional to precipitate diameter), and the particle radius distribution for cases where the mass spectra is binned with the perceived full width (user defined, red), the full-width tenth-maximum (FWTM, blue), and as the full-width half-maximum (FWTM, green). [225] 128

Figure 5.14. The dependence of composition and average precipitate size on binning parameters in the ZY10C60 specimen previously shown in **Figure 5.12**. The Y/Al ratio shows minimal change with decreasing binning width, while a more substantial

variation in precipitate size is noted as the width of the defined mass-to-charge ratio peak is decreased from the user-defined full width to the full-width half-max value. [225] 130
Figure 5.15. Mass-to-charge ratio spectra for various Cameca LEAP models studying ZY10C60 fine-grained specimens. [225] 130
Figure 5.16. The effect of atom probe, and thus detection efficiency, on the composition and nanoprecipitate distributions for CrAZY ODS FeCrAl powder (ZY10C60) annealed for 60 min. at 1000°C. For consistency, all specimens were taken from fine-grained regions of the powder. Compared are specimens analyzed using the Cameca LEAP models 4000X HR (36% detection efficiency, purple), 4000X Si (50% detection efficiency, blue), and 5000 XR (52% detection efficiency, red). [225] 132
Figure 6.1. Atom maps showing atom maps in two representative control volumes for the As-milled powder (ZY40H) and for the extruded CrAZY alloy (106ZY10C1). Atom maps for (a) Y+YO, (b) Zr, and (c) Al+AlO are shown. [225].....138
Figure 6.2. (a) A representative (Y,Al,O) nanocluster in the CrAZY ODS FeCrAl alloy is highlighted using atom maps of the constituent elements atop a matrix of black Fe matrix atoms. In (b) a 1D concentration profile through the precipitate is graphed showing increases in Y, YO, AlO, and O through the precipitate, but not Zr. 138
Figure 6.3. Stacked bar graphs illustrate the ratio of Y, Al, O, Zr, and C within each nanoprecipitate (normalized to these 5 elements) in the total population of 3644 total precipitates identified in the CrAZY APT control volumes in this work. In (a) the precipitates are arranged along the x-axis as a function of increasing measured precipitate radius. In (b), the precipitates are arranged as a function of increasing Zr content. 139
Figure 6.4. STEM+EDS results for the larger populations of precipitates in the ODS FeCrAl alloy 106ZY10C8. Multivariate statistical analysis results show two populations of precipitates (Al,Fe,N) + (Zr,C,N) and the background FeCrAl matrix. [225] 141

Figure 6.5. APT reconstruction of CrAZY alloy (106ZY15C) showing three types of precipitates within the control volume: (a) the smallest (Y,Al,O) precipitates shown using red atom maps of Y, (b) a (Zr,C,N) rich precipitate shown using the Zr, C, and N atom maps and a corresponding 1D concentration profile, and (c) a (Al,Fe)-rich nanoprecipitate highlighted using a green 25% Al iso-concentration surface and a 1D concentration profile into the precipitate. In (d), overlaid Y and YO atom maps indicate segregation to Al-rich precipitate boundaries. [225] 142

Figure 6.6. APT reconstruction of CrAZY powder (ZY10C60) showing a variety of different precipitates. The reconstructed control volume contains (a) a precipitate with composition matching ZrC, (b) a (Zr,C,N)-rich precipitate with a core/shell type structure, and (c) a (Fe,Cr,C)-rich precipitate highlighted as a brown 5% C isoconcentration surface. The smallest (Y,Al,O)-rich precipitates are respresented as red 1.5% (Y,YO,AlO) isoconcentration surfaces. [225] 144

Figure 6.7. (a) a reconstructed APT specimen for ZY10C60 showing the high-density of red (Y,Al,O) precipitates in red and the co-precipitation of an (Al,O)-rich and a (Zr,C) rich precipitate. In (b), a semi-transparent 25% Al iso-concentration surface in blue and a 10% Zr iso-concentration surface in purple are overlaid with an atom map of Y and YO, showing a Y-rich shell surrounding the Al-bearing precipitate. A 1D concentration profile through the two precipitates in (c) highlights the Y-rich shell and the corresponding increases constituent elements for the two precipitates. [225] 144

Figure 6.8. (a) the average uncorrected (as-measured APT) cluster compositions for 1141 clusters analyzed in the ZY10C60 specimens showing an abnormally large Fe+Cr content. The (b) reduced density corrected cluster compositions showing insufficient subtraction of Fe and Cr from the matrix. The application of the CCC (reduced density and shape factor) methodology has also been applied for (c) the case where FeCrAl matrix is erroneously measured in the precipitates and (d) the case where an Al-depleted, (Fe,Cr)-rich shell exists locally around the precipitates. [225] 149

Figure 6.9. Ternary diagrams for 1141 ZY10C60 clusters are illustrated for four compared conditions: (a) the uncorrected normalized Y, Al, and O contents measured in each cluster, with point diameters plotted proportional to the precipitate size, (b) the cluster compositions after density-correction, (c) the cluster compositions corrected using the CCC method assuming no Cr-rich shell surrounding the precipitates, and (d) the applied CCC method assuming that a (Fe,Cr) rich shell exists that is responsible for 80% of the trajectory abberations..150

Figure 6.10. For the ZY10C60 specimens investigated in this work, shown are (a) the frequency hit map for the Y/Al ratio as a function of precipitate size and (b) the corresponding size dependency of the ternary Y-Al-O diagram (bottom). Finally, the size dependency of the nanoprecipitates for the ternary diagram is shown in addition to the expected stochiometric (Y,Al,O) compositions as a function of omitted measured oxygen content are overlaid, showing substantial underestimations of oxygen content in all nanoprecipitates at for all sizes. [225] 152

Figure 6.11. (Y,Al,O) precipitates in a CrAZY_H1 control volume shown by (a) 1.5% (Y,YO,AlO) isoconcentration surfaces and (b) through identification through the maximum separation method. In (b), the atom maps for Y, YO, AlO, and O atoms are shown. Similarly for one representative precipitate, the Y, YO, AlO, and O atoms are illustrated in (c) while 1% atomic isoconcentration surfaces are overlaid for Y and O atoms in (d).....155

Figure 6.12. Ternary diagrams for CrAZY powders annealed at either 1000°C (red), 1050°C (orange), or 1100°C (purple), for various times. Highly consistent clustering is found for all samples, and subtle compositional trends as a function of temperature at 60 min. or as a function of time at 1050°C are noted.....156

Figure 6.13. (a) The as-measured magnetic and nuclear scattering intensities as a function of increasing scattering vector. From these two intensity curves, the (b) A-ratio as a function of scattering vector is computed. 158

Figure 6.14. Background-subtracted magnetic scattering data for the ZY10C15 sample with respective least-squares fits for both precipitate populations.....160

Figure 6.15. Results of SANS nonlinear least squares fits for CrAZY powder annealed for 15 min. (ZY10C15) and 60 min. (ZY10C60) in a 1000°C box furnace. (a) and (c) show the raw SANS data for ZY10C15 and ZY10C60 overlaid with the three functions representing the power-law background and the two populations of nanoprecipitates. For the same specimens, (b) and (d) show the comparison between the nanoprecipitate profiles identified by the APT and SANS technique, respectively. [203] 162

Figure 6.16. The variation of the theoretical atomic density of the cubic garnet $Y_3Al_xFe_{5-x}O_{12}$ phase, where x is the stochiometric composition of Al, data produced using lattice parameter data from Musa et al. [215].....165

Figure 6.17. The variation of the magnetic scattering contrast (Eq. 3.6) as a function of matrix composition in the precipitates, assuming either ideal or matrix atom densities in the precipitates [203]. 167

Figure 6.18. Simulated mole fractions of various stochiometric phases in ODS FeCrAl alloys with various inputted compositions using Thermocalc (Courtesy of Dr. Ying Yang at ORNL) [225]. The mole fractions as a function of consolidation temperature are reported for (a) the 106ZY10C8 alloy with C and N impurity elements as reported in **Table 6.1**, (b) the 106ZY10C8 alloy omitting C and N impurities, and (c) the SOC-14 (FeCrAlZrY) ODS FeCrAl alloy developed by Dou et al. [105].....170

Figure 6.19. Schematic representation of the calculation of the driving force for nucleation for various phases β and γ with respect to a reference phase α, from [234] 172

Figure 6.20. A comparison of simulated driving forces for nucleation for various noted stochiometric phases in the ODS FeCrAlZrY alloy system using Thermocalc (Courtesy of Dr. Ying Yang at ORNL). [225] 173

Figure 7.1. Temperature dependent SANS intensities as a function of annealing time and temperature for ZY40H powder investigated through in-situ SANS using a heating rate of 20°C/min. [203].....177

Figure 7.2. Total diffusion distances for Y, Al, and O atoms in BCC-Fe for increasing temperatures from 23-1000°C at a ramp rate of 20°C/min. 180
Figure 7.3. (a) the dependence of the Y/Al ratio measured in the precipitates in annealed CrAZY powders/alloys as a function of precipitate radius for 1h heat treatments at 1000°C, 1050°C, and 1100°C. (b) the dependence on the size dependent Y/Al ratio as a function of increasing annealing time for extended heat treatments at 1050°C. Error bars indicate 95% confidence intervals for each sample population. [203]...181
Figure 7.4. (a) APT reconstructions of CrAZY powders annealed at 1050°C for 10-500h. 0.1% of the matrix Fe atoms are shown in black dots while the (Y,Al,O)-rich nanoprecipitates are shown using red 1.5% (Y,YO,AlO) isoconcentration surfaces. Also shown in (b) are atom maps of respective clusters normalized to the same dimensional scale. [203].....182
Figure 7.5. (a) the comparison of power law coarsening exponents for CrAZY powders annealed for 10-500h at 1050°C, showing the best linear correlation for an exponent of n=6. The activation energy for coarsening is estimated through the slope calculated in (b) through the linear regression of the natural logarithm of the coarsening curves vs. inverse temperature. In (c) the long term n=6 coarsening model is overlaid with 95% confidence intervals for measured APT precipitate sizes as a function of annealing time at 1050°C. [203].....184
Figure 7.6. Kinetic exponent calculations using linear regressions through various sets of 1-500h annealed samples at 1050°C. The outlying nature of extruded sample 106ZY15C (1h) in comparison to annealed powder samples 10-50h is noted.....186
Figure 7.7. The simulation of precipitate size increases during pre-extrusion annealing treatments of using 1000°C, 1050°C, and 1100°C simulated time-temperature profiles scaled from the as-measured 1000°C powder temperature profile measured in **Figure 4.5**. The modeled sizes as a function of time are compared with APT data measured at the three respective temperatures. Errors for APT data are reported as 95% confidence intervals. [203].....188

Figure 7.8. A comparison of coarsening data for ODS FeCr and ODS FeCrAl alloys reported in literature [78, 79, 115, 160] with the long term coarsening behavior of the CrAZY powder annealed up to 500h at 1050°C.....190
Figure 7.9. EBSD orientation maps for a CrAZY ODS FeCrAl alloy annealed at 850°C for 1h followed by extrusion at 1050°C (106ZYA15C) in comparison to alloy annealed for 1h at 1050°C followed by extrusion at the same temperature (106ZY15C) 195
Figure 7.10. EBSD grain maps representing each grain as a unique color for a CrAZY ODS FeCrAl alloy annealed at 850°C for 1h followed by extrusion at 1050°C (106ZYA15C) in comparison to alloy annealed for 1h at 1050°C followed by extrusion at the same temperature (106ZY15C). Also shown are the respective grain size distributions measured by EBSD for both alloys. 195
Figure 7.11. APT reconstructed control volumes for 106ZYA15C (annealed 1h at 850°C) vs. 106ZY15C (annealed 1h at 1050°C) showing red (Y,Al,O) nanoprecipitates in red with black Fe matrix atoms in the background. Also illustrated is the shift in nanoprecipitate size distributions due to the difference in pre-extrusion annealing temperatures. 196
Figure 7.12. The variation of (a) ultimate tensile strength, (b) yield strength, and (c) plastic deformation for alloys 106ZY15C and 106ZYA15C as a function of increasing test temperature. Also shown are an ODS FeCrAl alloy 125YZ [99] and a non-ODS wrought FeCrAl alloy C35MN [8] for comparison. 199
Figure A.1. Visual schematic of the lumped capacitance problem 228
Figure A.2. The comparison of the LC curve fits for the extrusion can and quartz vial with the experimentally measured extrusion can temperature profile.....230

CHAPTER 1: Introduction

1.1. The Need for Advanced Materials for Nuclear Reactors

Even though nuclear power has emerged as a robust and reliable source of emissions-free energy across the globe, it has proved difficult for the nuclear industry to move forward with newer reactor designs that would improve safety margins and reliability. Many nuclear power plants are reaching the end of their licensing periods and are seeking extensions in plant life, while next generation III and IV designs remain unbuilt. The primary reason behind the difficulty in designing advanced Gen IV nuclear power plants is the lack of materials that can endure the temperatures and radiation doses that accompany these newer generation reactors. In comparison to current Light Water Reactor (LWR) operating conditions where the maximum radiation doses for reactor structural materials are tens of displacements per atom (dpa), advanced fission and fusion reactor design concepts will require materials to withstand doses up to 200 dpa at operating temperatures within the 300-1000°C temperature range [1, 2]. The temperature and irradiation dose regimes are illustrated in **Figure 1.1**.

With a capacity factor of over 90% for current reactors, and with many power plants reaching the end of their economic lifetime, the development of materials that can withstand the extreme temperatures and radiation doses is crucial to the sustainment and growth of nuclear power in the coming years [3]. Over the past few years, much research has been aimed at the prospects of producing radiation resistant materials using concepts based on high sink strengths. This concept attempts to use a high number density of interfaces (sinks) so that defects accumulated via the radiation damage events can be absorbed and erased under operating conditions. One class of material designed using this approach is the oxide dispersion strengthened (ODS) alloy, which has shown great promise in improving radiation resistance in key areas and have one of the largest temperature operating windows for structural materials aimed at withstanding higher dpa ranges [2].

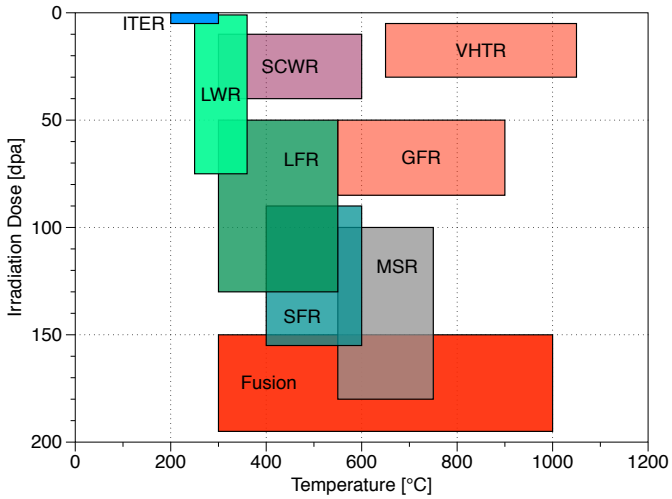


Figure 1.1. Nuclear reactor operating temperature and dose regimes, reproduced from [1, 2]. Shown are the current Light Water Reactor (LWR), the ITER fusion reactor, the Very High Temperature Reactor (VHTR), the Super Critical Water Reactor (SCWR), the Lead Fast Reactor (LFR), the Gas Fast Reactor (GFR), the Sodium Fast Reactor (SFR), and the Molten Salt Reactor (MSR).

After the Fukushima Daiichi accident in 2011, there is also a renewed interest in alloys that can increase safety margins in existing LWRs in the event of beyond design basis accident scenarios [4, 5]. These alloys must be superior to existing Zr-based alloys while also exhibiting the multiple qualities desirable in fuel cladding applications. These desirable attributes include a low parasitic neutron absorption, good mechanical strength, sufficient chemical compatibility between the cladding with both the fuel and coolant, good thermal and irradiation stability, high conductivity and melting temperature, and isotropic material properties.

New low-Cr (<12 wt%) FeCrAl alloys have shown promise in terms of oxidation resistance [6], but the use of a Fe-based alloy would negatively affect the parasitic absorption cross-section within the reactor environment; thus, to utilize these alloys as an accident tolerant fuel (ATF) cladding, the thickness of the thin-walled cladding tube would need to be reduced to allow an Fe-based alloy to serve as a drop-in replacement for existing Zr-based LWR cladding [4].

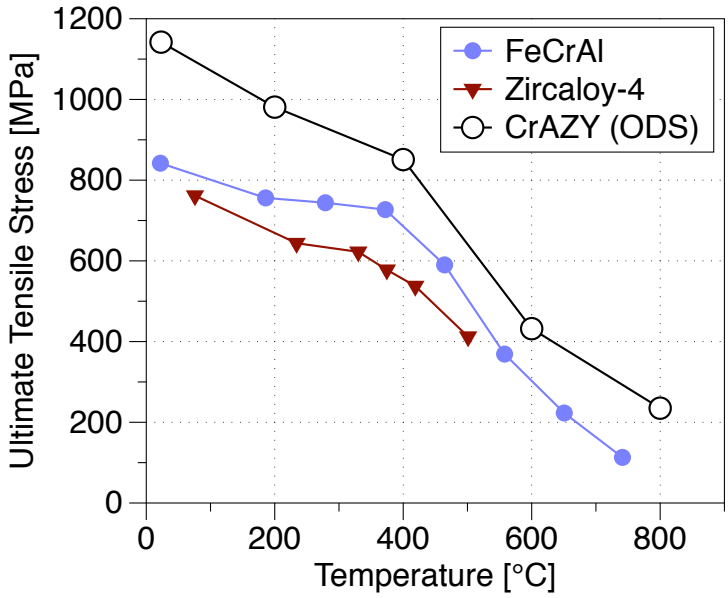


Figure 1.2. The variation of ultimate tensile strength (UTS) as a function of temperature for stress-relieved Zircaloy-4 [7], wrought model FeCrAl alloy C35MN [8], and the CrAZY ODS FeCrAl alloy examined in this work.

As **Figure 1.2** illustrates, the ultimate tensile strength of model FeCrAl alloys already surpasses the strength of Zircaloy. This is true even in comparison to the properties of stress-relieved Zircaloy-4, which is much stronger than its recrystallized version commonly used in light water reactors [7]. For these Fe-based alloys, it has been previously illustrated that under nuclear accident scenarios, the failure of cladding tubes through cladding burst is limited by the ultimate tensile strength of the material [9]. Due to the successful development of ODS FeCr alloys as structural materials for advanced fission and fusion structural materials, there is an interest to use a fine dispersion of nanoprecipitates to further strengthen FeCrAl alloys. The superior mechanical strength attributed to a fine dispersion of nanoparticles in the ODS FeCrAl alloys would potentially improve burst properties by increasing the alloy's strength while simultaneously enhancing the radiation resistance of the cladding under normal operating conditions.

Irrespective of whether the ODS FeCrAl concept is used for accident tolerance in existing light water reactors, or if these alloys are developed for advanced fission and fusion reactor concepts, careful attention must be paid to optimizing the dispersion of nanoscale precipitates within the microstructure that give dispersion strengthened alloys their beneficial material properties. In the subsequent sections, the physical basis for designing dispersion strengthened alloys with high sink strengths is presented, followed by a detailed review of the conventional approach for the production of these alloys. Finally, current gaps in understanding pertaining to the optimization of nanoprecipitate distributions in these alloys are presented with the associated objectives targeted in the studies herein.

1.2. Radiation Damage

1.2.1. Irradiation-Induced Defects

Irradiation damage, though measured at the macroscopic level through material property changes after irradiation, stems from atomistic interactions at the microscopic level. Primary knock-on atoms (PKAs) generated through the interaction between incoming particles and the material lattice are displaced from their original lattice site and travel through the material, displacing other atoms and forming pairs of displaced interstitial atoms and vacancies called Frenkel pairs. High PKA energies result in the generation of more defects through these collision cascades, and these defects can substantially change not only the mechanical properties of irradiated materials, but also the physical properties such as shape and volume.

Although the creation of Frenkel pairs grows exponentially within these collision cascades, luckily most of these Frenkel pairs naturally recombine and self-healing occurs, erasing most of the irradiation damage that was generated. This self-healing is a combination of in-cascade recombination driven by ejected interstitials recombining with previously generated vacancies as well as spontaneous recombination aided by random walk interstitial migration. The latter spontaneous recombination process will usually

occur if the existing Frenkel pair exists within a given relaxation volume, which is dependent on temperature [10]. At higher temperatures where vacancies also become mobile, comparable to temperatures that exist within existing and next generation reactors, 80-90% of Frenkel defects recombine, which substantially helps alleviate issues associated with radiation damage at the macroscopic level [11].

Surviving Frenkel defects within an irradiated material's microstructure can sometimes form very specific microscopic defects. As the thermal spike portion of the cascade event comes to an end, it is well known that along the path of the cascade there exists a depleted zone with a high concentration of vacancies, with a periphery of ejected interstitials at a high concentration [12-14]. The high concentration of Frenkel defects in close proximity gives rise to different types of defect clusters. A high number density of vacancies can create perfect or faulted planar dislocation loops, cavities, and in FCC metals stacking fault tetrahedra, while interstitials can form perfect or faulted dislocation loops themselves [13, 15]. The energetically favored type of defect is a strong function of both the material and the number of vacancies or interstitials [16].

Depending on the irradiation temperature, the creation and/or coalescence of these aforementioned defects results in different macroscopic material property changes. These irradiation effects are dependent both on temperature and dose. To more easily expand this discussion to more material systems, a homologous temperature is defined as the ratio between the irradiation temperature and the melting temperature of the alloy. At low homologous temperatures ($T/T_M < 0.4$), the development of dislocation loops and other defects causes irradiation-induced hardening of the material [2]. This occurs at even low irradiation doses and can result in a loss of uniform elongation (the plastic deformation the material is able to undergo prior to entering the plastic instability "necking" regime of the engineering tensile curve). These defects also in many cases result in an embrittlement of the alloy through a lowering of the impact energy of the material required for fracture. At higher doses and temperatures, other mechanisms such as radiation induced segregation and precipitation of solute atoms will occur, which is of specific interest for reactor pressure vessel steels [17]. In Fe-based ODS alloys with Cr

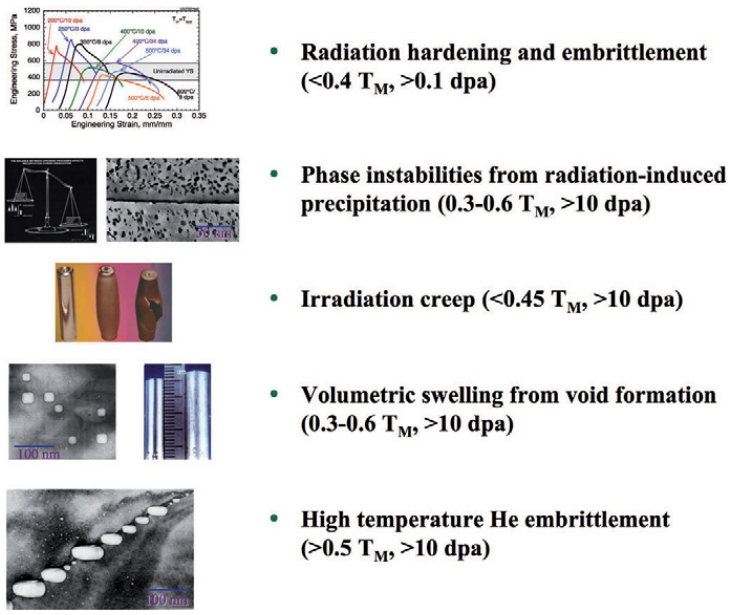


Figure 1.3. The five irradiation-induced degradation phenomena in materials, as reported in [2]

addition, thermodynamically driven segregation phenomena can be exacerbated through radiation accelerated precipitation of a deleterious Cr-rich α' phase [18-26], which is a primary reason why the Cr content in the ODS FeCrAl alloys in this study are limited to only 10 weight percent.

A significant irradiation effect that is expected in the ($0.3<T/T_M<0.6$) range is volumetric swelling. For the ODS Fe-based alloy system, this temperature range encompasses almost every advanced fission/fusion reactor concept (**Figure 1.1**). Volumetric swelling can either be due to the coalescence of vacancies into macroscopic voids within the material, or it could be exacerbated by the stabilization of these cavities by He atoms generated either by transmutation reactions in fission reactors or through He generation in the fusion reaction [1, 2]. All of these irradiation effects have been previously reviewed by Zinkle et al. and are illustrated in **Figure 1.3**.

The Importance of Interfaces: A First-Principles Approach

One methodology for designing radiation resistant materials involves the addition of interfaces within the material. These interfaces, whether they are grain boundaries, multiple nanoscale layers of different materials, or nanoscale precipitates within a lattice, serve as sinks for the defects produced during irradiation. To investigate the fundamental interactions responsible for the radiation resistance of materials with high sink strengths, authors have used techniques ranging from molecular dynamics (MD) simulations, Monte Carlo simulations, and ab initio simulations based on density functional theory (DFT).

Vattre and colleagues used kinetic Monte Carlo simulations to investigate the importance of elastic interactions on the sink strength of semicoherent interfaces in multilayered composites for radiation resistance [27]. Due to the stress-fields surrounding the interfaces and their interaction with nearby defects, recombination is accelerated substantially and thus radiation resistance is increased. In addition, Jiang et al. investigated the impact of grain boundary orientation and found that a localized maximum in grain boundary sink strength exists for low angle grain boundaries. This is because their MD simulations show that as the misorientation angle increases, the stress field around the grain boundary decreases as well as the corresponding defect stabilization area [28]. Huang et al. used the LAMMPS MD simulation code to model the radiation resistance of a copper-graphene multilayered composite. Even though the Cu-C interface effectively served as a successful sink for point-defect recombination, the simulations also indicated a ballistic-mixing induced deterioration of the graphene layer [29]. Although these studies focused on interfaces in general, the results can be readily extended to the particle and grain boundary interfaces within ODS alloys. These theoretical results indicate that maximizing the number of interfaces through a high number of precipitate and grain boundary interfaces accelerates point-defect recombination and thus decreases the available number of defects within the material. The interface dissolution through ballistic mixing illustrates, however, that careful attention must also be paid to the stability of the nanoprecipitates in the given irradiation

temperature regime to ensure that the precipitates are not suffering from dissolution due to ballistic mixing phenomena.

1.2.2. Irradiated Nanoprecipitate Stability in Ferritic ODS Alloys

Since the high number density of precipitate interfaces directly contributes to the irradiation resistance of Fe-based ODS alloys, it is first of importance to understand the resistance of the nanoprecipitates to irradiation prior to examining the resistance of these materials to macroscopic material property changes such as irradiation-induced hardening and volumetric swelling. Since most of the ODS alloy research has focused on ODS FeCr alloys, research is presented in this section on both ODS FeCr and FeCrAl alloys without a consideration yet about the nature of the smallest precipitates. Questions pertaining to the composition and structure differences between the ODS FeCr(Al) alloys will be addressed in subsequent chapters.

In short, the nanoprecipitates within Fe-based ODS alloys with and without Al additions are highly stable irrespective of whether ion, proton, or neutron irradiation is considered. It is important to note, however, that the irradiation resistance of these nanoprecipitate strengthened alloys is temperature dependent. Neutron irradiated MA957 (50 dpa at 412°C and 75 dpa at 430°C) was studied by Ribis to determine microstructural changes and the chemical evolution following irradiation. The grain size and morphology remained unchanged, but larger TiO_2 particles lost Ti and O after irradiation due to ballistic dissolution, which was confirmed by a peak of Ti in the matrix, a jump in oxygen at the grain boundaries, and the dissolution of large particle interfaces after irradiation [30]. Kishimoto et al. irradiated Fe-19Cr ODS alloys at 670°C and a dose rate of 10^{-3} dpa/s using 6.4 MeV Fe ions to minimize heavy-ion implantation effects. After irradiation, TEM investigations showed that no morphological changes occurred to the reinforcing particles [31]. In a different ion beam study, 10 MeV Pt ions were used at -100°C and 750°C by Parish et al. to irradiate 14YWT to high radiation doses at a damage dose rate of 10^{-2} dpa/s to gauge the resistance of this nanoprecipitate strengthened material to high doses of radiation. For the low temperature ion studies, any nanoclusters

or grain boundary solute segregation present in the original sample dissolved into a homogeneous matrix at doses as low as 16 dpa, with only a few larger TiN particles surviving at 160 dpa as shown in **Figure 1.4**. At the higher 750°C irradiation temperature, a significant portion of nanofeatures remained within the microstructure [32]. These results match the results of Certain et al., who performed irradiation studies on two ODS variants (14YWT and 9Cr ODS) using 2.0 MeV protons at 400°C, and both 5 MeV Ni ions and thermal neutrons over a variety of temperatures and doses. No substantial changes in morphology or number density were noted for the low dpa proton and neutron irradiations. However, during the heavy ion irradiations at low temperatures, the high dose rate coupled with the high energy of the incident heavy ion caused the (Y,Ti,O) nanoclusters to dissolve into solution at 100 dpa and -75°C due to the low diffusivity of the Y and Ti atoms within the lattice, while at higher temperatures there did not seem to be a change in cluster number density. After annealing at 850°C for 5 h, the clusters re-formed that originally dissolved during low temperature ion irradiation [33]. It is conjectured that the nanoclusters are dynamically stable through a diffusive self-healing process. During this process, Y and Ti atoms are ejected from the nanoculsters due to ballistic mixing, and then these highly insoluble atoms back-diffuse to re-form the nanoclusters at higher temperatures due to the high affinity of Y and Ti to react with free O within the matrix. This dynamic equilibrium is supported by simulations by Lazauskas et al. that show that yttria has the potential to absorb some propagated energy from a displacement cascade and potentially amorphize, followed by some recovery after longer time frames [34]. Ion irradiation studies of 12Cr ODS ferritic-martensitic alloys have shown that the coherency of nanoprecipitates with the matrix strongly influences their irradiation stability [35]. It was reported that coherent precipitates are more irradiation resistant than incoherent precipitates under irradiation due to the lower surface interfacial energy for coherent precipitates.

To date, there have been few irradiation studies on ODS FeCrAl alloys, and those that do exist have only focused on either macroscopic material property changes [36, 37] or studies pertaining to the radiation enhanced α' phase in legacy high Cr ODS FeCrAl

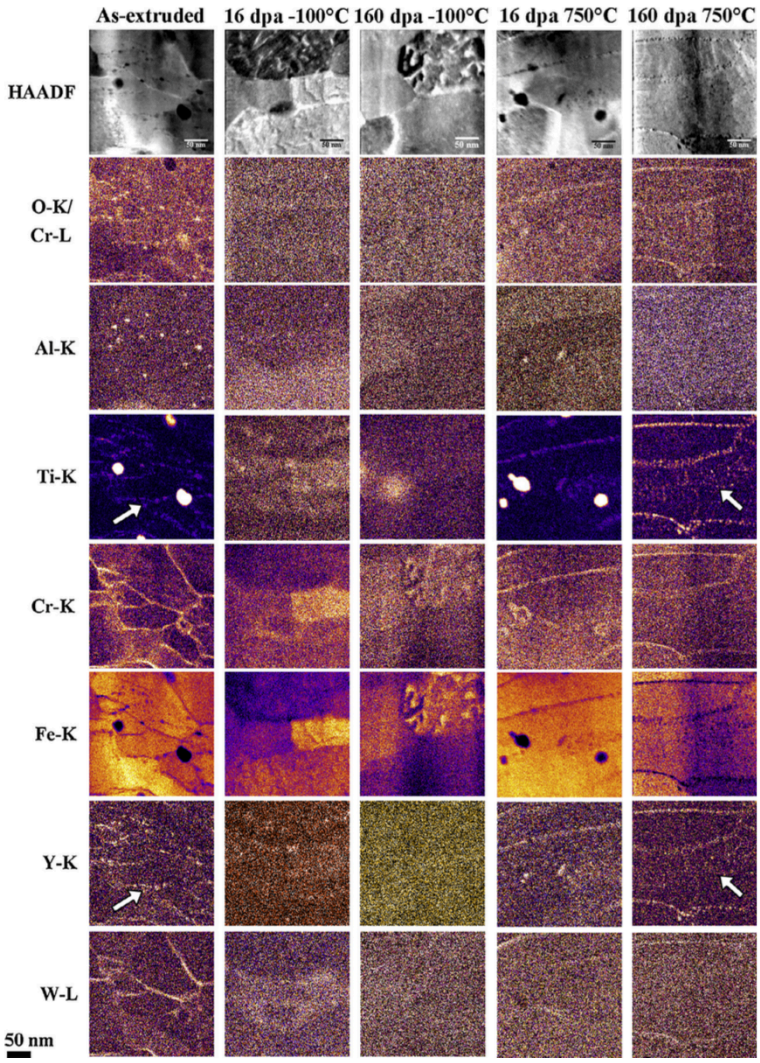


Figure 1.4. Microstructure of ion irradiated 14YWT at low and high temperatures [32]

alloys such as PM2000 [19-22]. The nanoprecipitate stability in low Cr (12 weight percent) ODS FeCrAl after neutron irradiation was studied as a part of this comprehensive work, and is presented later in this work to provide significant contributions to the state-of-the-art.

1.2.3. Sink-Strength Dependence for Irradiated ODS FeCr(Al) Alloys

The mechanical properties of nanocluster and nanoprecipitate strengthened alloys are superior to their non-strengthened counterparts, but these ODS alloys are not immune to irradiation-induced material property changes. Though some studies have attested to the hardening resistance of ODS alloys under irradiation [38], the ability of these materials to mitigate radiation damage has been shown to vary greatly with sink strength. It has been illustrated by Zinkle and Snead that above sink strengths of 10^{16} $1/m^2$, materials exhibit drastically reduced radiation hardening [1]. However, it is important to note that even though the hardening was smallest for the 14YWT alloy with the highest sink strength, the unirradiated 14YWT sample already started with a UTS of 1.56 GPa and a measured uniform elongation of only 0.8% [39, 40]. In the same study it was also shown that due to the high sink strength, 14YWT did not suffer any substantial decrease in fracture toughness after neutron irradiation to 1.5 dpa. An increase in sink strength between alloys drastically improves their resistance to irradiation hardening, but it also drastically increases UTS while reducing ductility associated with the inhibition of dislocation motion within the matrix due to a combination of Hall-Petch and Orowan strengthening mechanisms.

Though the operating temperatures within light water reactors are too low for volumetric swelling to become an issue for ODS FeCr(Al) alloys, in temperature regimes relevant for advanced fission/fusion reactors volumetric void/cavity swelling must also be considered. The morphology studies of ODS FeCr alloys indicate that at temperatures relevant to void swelling, the nanoclusters within the microstructures are stable, which has shown to aid in the suppression of irradiation induced void swelling. Chen et al. performed Fe self-ion irradiations of 12Cr ferritic-martensitic ODS alloy at 475°C to

doses up to 800 dpa. Larger (>10 nm) nanoprecipitates were reported to be ballistically dissolved, but smaller (~2-4 nm clusters) were unaffected by the high dpa irradiation [41]. Furthermore, the measured void swelling was less than 5% at doses up to 500 dpa. ODS FeCrAl samples also showed beneficial void swelling resistance up to high irradiation doses. For instance, MA956 irradiated at the Fast Flux Test Facility (FFTF) to 205 dpa showed insignificant swelling (0.21%) with a void size and density of only 26.7 nm and 1.9×10^{14} m^{-3}, respectively. MA956 even outperformed MA957 irradiated to the same irradiation dose, where MA957 experienced 3.7% swelling with a void size of 36.1 nm and a void density of 9.2×10^{14} m^{-3} [42].

Volumetric swelling has also been studied in ODS alloys where He stabilized cavity swelling is of importance. An in-situ method for He implantation was used by Yamamoto et al. to inject He into ferritic ODS variants. The technique involved layering the specimens and a NiAl substrate to utilize the $^{59}Ni(n,\alpha)$ reaction within a thermal neutron flux to generate helium [43]. ODS specimens were characterized using TEM, and it was found that entrapped helium bubbles were associated with nanofeatures after irradiation at 500°C to 9 dpa and 380 appm He. Volumetric swelling at 500°C was compared for a 16Cr–4.5Al ODS alloy and a 9Cr reduced activation ferritic (RAF) steel using dual-ion irradiation. 6.4 MeV Fe ions and 1.0 MeV He ions were used to irradiate the steels at a dose rate of 10^{-3} dpa/s [44]. It was found that the ODS steel had twice the number density of cavities at half of the size as the cavities formed in the RAF steel, and that the ODS variant developed negligible cavity swelling to 150 dpa. The authors attributed the superior void swelling resistance in the ODS steel to the entrapment of He at the nano-sized sinks within the material. In a study on a different ferritic ODS alloy (14YWT), Li et al. investigated the distribution of He bubbles and voids after implantation of 375 keV He ions at 400°C to a fluence of 6.75×10^{20} He/m^2. TEM and APT were used to map the concentration of He bubbles and their association with features within the material. 94% of implanted bubbles existed in the ferrite matrix without any association with particular features, while less than 5% of He bubbles were associated with nanoclusters within the material. However, almost half (44%) of

nanoclusters were associated with a He bubble [45]. Another recent study used dual Fe and He ion implantation (650°C, ~50 dpa, ~15 appm He/dpa) to investigate the helium trapping capability of ODS FeCrAl alloys [46]. Multivariate statistical analysis (MVSA) was used to identify nanoprecipitates using TEM combined with energy dispersive spectroscopy (EDS). Identified nanoprecipitates were compared with bright-field (BF) TEM images showing the distribution of helium bubbles within the irradiation microstructure, and it was found that 40% of helium bubbles were associated with nanoprecipitates within the ODS FeCrAl alloys.

CHAPTER 2: Literature Review of ODS Alloys

2.1. Strengthening Mechanisms in ODS Alloys

The use of second phase particles to enhance the mechanical properties of materials dates back to the early 20th century with the use of dispersed thoria particles to reinforce Tungsten [47]. However, the fundamental theory behind the interaction of dispersed particles and dislocations wasn't established until decades later, when Orowan related the strength of ODS alloys to the resistance of these particles to gliding dislocations within the matrix [48]. Since then, the theory of dispersion strengthening has expanded and second phase particles have been used to strengthen a variety of materials to enhance their mechanical strength to high temperatures [49].

The simplified Orowan bowing process is illustrated in **Figure 2.1**, where a gliding dislocation approaching two particles separated by a distance L is shown [48]. The further glide of the dislocation is inhibited by the precipitates and it begins to bow around the dispersed particles. As the dislocation continues to propagate, the edges of the dislocation continue to bow around the particle until the dislocation dipole (two oppositely oriented dislocation lines) locally annihilates at the opposite side of the precipitate, resulting in two dislocation loops and the remaining dislocation line. This is a highly simplified model because it assumes that the obstacles are incoherent and impenetrable by the dislocation. Although this model provided a strong foundation for dislocation-particle interactions, the assumption that the precipitates in ODS alloys are impenetrable is not an accurate one in many cases. In addition, the model neglects multiple aspects such as the ability of dislocations to bypass precipitates through cross-slip or through direct shearing of precipitates [49].

In the case of ODS alloy development, the individual dislocation-particle interactions require scaling to estimate macroscale properties, such as increases in the yield strength of the alloy as a function of nanoprecipitate distributions. Thus, for cases

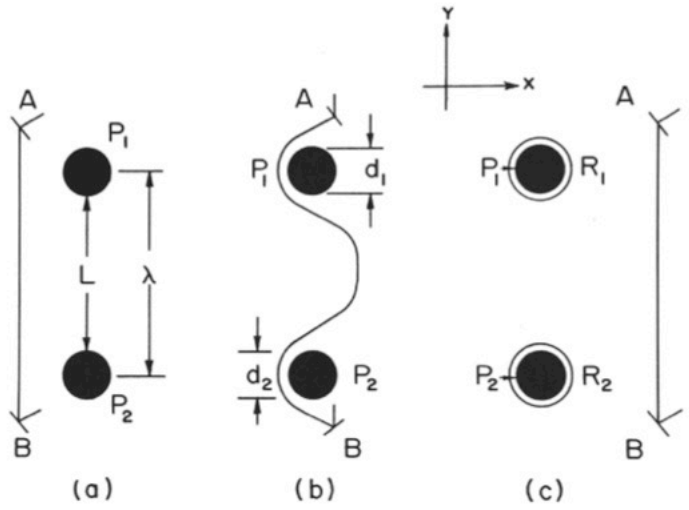


Figure 2.1. Visualization of the Orowan bowing mechanism. (a) a gliding edge dislocation approaches two dispersed particles in the glide plane, (b) the dislocation bows around the dispersed particles, and (c) the ends of the dislocation annihilate after bowing around the particle, leaving two dislocation loops and a resultant gliding dislocation [48].

where particles serve as obstacles for dislocation pinning, Seeger developed the widely used dispersed barrier hardening model to estimate the increase of alloy strength, where the effective strength of dispersed particles is incorporated through a factor α, defined as the barrier strength factor [50]:

$$\Delta\sigma_p = M\alpha\mu b\sqrt{Nd} \quad \text{.....} \quad (2.1)$$

where M is the Taylor factor for the material (M=3 for BCC Fe), μ is the shear modulus, b is the Burgers vector for the gliding dislocations, N is the particle number density, and d is the diameter of the dispersed particles. The value for α varies from 0 to 1, where unity represents completely impenetrable particles.

Friedel later extended the formulation where the strength of the weaker obstacles was accounted for by adjusting the interparticle distance to larger values, thereby reducing the amount of bowing the dislocation experiences as it attempts to bypass the weaker obstacles [51]:

$$\Delta\sigma_p = \frac{1}{8} M\mu b d N^{\frac{2}{3}} \quad \text{(2.2)}$$

The application of these models is highly dependent on the strength of the dispersed phase. It has been reported that for very weak precipitates ($0 < \alpha < 0.25$), Eq. 2.2 more accurately represents particle strengthening, while for stronger particles ($0.25 < \alpha < 1$) Eq. 2.1 is more appropriate for modeling alloy strengths [52]. For ODS FeCr alloys with dispersed 2-4 nm precipitates enriched in Y, Ti, and O, the dispersed barrier strengthening coefficient α is 0.2, which suggests that the high number density of precipitates in ODS Fe-based alloys deviate substantially from ideal impenetrable obstacles.

Although the strengthening contribution from direct particle-dislocation interactions is significant, it is only one of many strengthening components adding to the strength of ODS alloys. In-fact, the total yield strength of ODS alloys is a superposition of strengthening due to precipitates ($\Delta\sigma_p$), grain boundaries ($\Delta\sigma_{gb}$), dislocation-dislocation interactions ($\Delta\sigma_\rho$), solid-solution strengthening ($\Delta\sigma_{ss}$), and the intrinsic resistance of the matrix to slip ($\Delta\sigma_0$). Because a linear summation of these strengthening contributions erroneously overestimates the total yield strength of dispersion-strengthened alloys, Kocks [53, 54] previously developed the root mean square (RMS) methodology based off of simulations by Foreman [55] for estimating ODS alloy yield strength by considering that many of the strengthening mechanisms show dependency with one another. This RMS summation is presented in Eq. (2.3) below. This methodology has been applied with respect to both ODS alloys [56] and clustering involved with reactor pressure vessel steel embrittlement [17].

$$\sigma_{rms} = \sqrt{\sigma_\rho^2 + {\sigma_{db}}^2 + {\sigma_{GB}}^2 + {\sigma_m}^2} \quad \text{(2.3)}$$

where σ_m is the matrix hardening component incorporating both solid solution strengthening and the matrix resistance to deformation (Peierls-Nabarro stress). The matrix hardening component is defined as:

$$\sigma_m = \sigma_0 + \sigma_{ss} = \frac{2M\mu}{1-\nu}\exp\left[\frac{-2\pi a}{b(1-\nu)}\right] + \sum_i k_i X_i^n \quad \text{..... (2.4)}$$

In this equation, ν=0.3 is the Poisson's ratio and a is the lattice parameter of the unit cell. For the estimation of the solid solution strengthening component of the matrix hardening, X_i and k_i represent the atomic fraction and the strengthening constant for alloying element i used in the matrix composition. For ODS FeCrAl, solid solution strengthening is expected for the Cr and Al additions to the ferritic matrix, and the corresponding values of these strengthening components have previously been reported in the literature (k_{Al}=27.56 MPa and k_{Cr}=9.65 MPa) [57, 58].

The strengthening component due to dislocation interactions ($\Delta\sigma_\rho$) is known as dislocation forest hardening and is primarily a function of the dislocation density ρ. This is an intrinsically difficult parameter to measure because it is highly dependent on the processing path for the ODS alloy.

$$\sigma_\rho = M\alpha\mu b\sqrt{\rho} \quad \text{..... (2.5)}$$

The dislocation density is usually measured through electron microscopy methods. This method only gives a snapshot of the dislocation characteristics in specific grains and can significantly vary from grain to grain [59]. However, dislocation densities measured through electron microscopy have generally agreed relatively well with X-ray scattering experiments within an order of magnitude [59-61]. For extruded alloys, the dislocation density is on the order of 10^{14} m^{-2} [59-61] while for alloys consolidated by hot isostatic pressing (HIP) the dislocation density is an order of magnitude lower (10^{13} m^{-2}) [62].

The strengthening component due to grain boundaries is known as Hall-Petch strengthening. This component is inversely proportional to the square root of the average alloy grain size D. The proportionality constant k_{GB} is estimated through a linear regression of the yield strength and $D^{1/2}$. The total grain boundary strengthening (σ_{GB}) is thus:

$$\sigma_{GB} = \frac{k_{GB}}{\sqrt{D}} \quad \text{(2.6)}$$

Recently, alterations to this RMS methodology have been made to account for similar interaction distances between dislocation-dislocation and particle-dislocation interactions. More specifically, Kim and colleagues have asserted that the dislocation forest hardening component should be separated from the other terms due to its strain-hardening dependence [56]:

$$\sigma_{rms,1} = \sqrt{\sigma_\rho^2 + (\sigma_{db} + \sigma_{GB} + \sigma_m)^2} \quad \text{(2.7)}$$

Other authors have used a combination of linear summation and the aforementioned RMS methodology for the estimation of ODS alloy yield strength [61, 63, 64]. These studies have argued that since the interaction distances for dislocation strengthening and particle strengthening components are of similar magnitude, a separate square root dependence should be incorporated for these terms while mechanisms with larger interaction distances (grain matrix and grain boundary strengthening) should be separate from the square root term:

$$\sigma_{rms,2} = \sigma_m + \sigma_{GB} + \sqrt{\sigma_\rho^2 + {\sigma_{db}}^2} \quad \text{(2.8)}$$

As will be discussed in the following sections, there is a complex interplay between some of the aforementioned strengthening mechanisms. Although the grain matrix strengthening component is a function of the base composition and the Fe matrix, a change in the effective nanoprecipitate dispersion will strongly influence the dislocation density and the grain size. Consequently, an optimization of the alloy's grain size and dislocation density requires a careful evaluation of the nanoprecipitate evolution during the annealing stages leading up to alloy consolidation.

2.2. Precipitate Nucleation, Growth, and Coarsening

To optimize the precipitate distribution for enhanced alloy strengthening and irradiation resistance, first it is imperative to understand how the precipitates nucleate and grow within the material. Unfortunately this is an incredibly difficult task to accomplish because ODS alloys developed through the powder metallurgy approach exhibit highly complex nucleation and growth kinetics. This is due to the significant deformation associated with the mechanical alloying step of alloy fabrication. Classical nucleation theory outlines two separate mechanisms for precipitate nucleation: homogeneous and heterogeneous nucleation. Homogeneous nucleation is described as the formation of precipitate embryos without relying on the existence of pre-existing defects within the matrix [65]. This mechanism requires the change in volume free energy associated with the nucleation of the new phase to overcome the increase in interfacial free energy and lattice strains associated with the implantation of this new phase in the matrix. In the case of designing Fe-based ODS alloys, oxides with a highly negative Gibbs free energy of formation are usually added during the mechanical alloying step to ensure that the required energy barrier for nucleation is easily overcome [66, 67]. In addition, the addition of elements like yttrium with low intrinsic solubilities in the BCC Fe matrix assist in the nucleation of nanoprecipitates during the heating of mechanically alloyed powders [68].

Alternatively, heterogeneous nucleation is characterized by the preferential nucleation of nanoprecipitates coincident with pre-existing defects within the matrix.

These defects are generated through the deformation associated with the mechanical alloying step of powder production and can exist as vacancies, dislocations, and grain boundaries [65]. The increased free energy associated with these intrinsic defects allows the precipitates nucleating on these sites to more easily overcome the energy barrier for nucleation; thus, heterogeneous nucleation is expected to be the dominant mechanism for nanoprecipitate nucleation in ODS alloys fabricated using the powder metallurgy approach.

Immediately following the precipitate nucleation stage, these nuclei rapidly grow to decrease the interfacial free energy while decreasing the local supersaturation of the solute phase within the matrix. During the growth stage, the number density of precipitates remains relatively constant while the sizes grow to larger sizes. The growth of the nanoprecipitates during this stage is dominated at small sizes by the incorporation of the solute atoms into the interface of the growing precipitate [65, 69] because the matrix solute concentration has not reached equilibrium and the diffusion distances are relatively short. As the precipitates continue to increase in size and the diffusion distances increase, the further growth of the precipitates becomes limited by the rate of solute diffusion through the matrix. For the case of supersaturated solid solutions as in the ODS alloy system, the nucleation and growth regimes occur too rapidly and are difficult to quantify. As a result, the only existing study attempting to capture the nucleation and growth of nanoprecipitates in an ODS Fe-14Cr alloy (14YWT) was conducted by Zhang and colleagues on mechanically alloyed powders annealed for up to 20h at 500°C, where it was asserted that the strong binding between Y and the high density of pre-existing vacancies in the mechanically alloyed powder promoted the heterogeneous nucleation and growth of the (Y,Ti,O) nanoprecipitates within the lattice [70].

Sometime near the end of the growth regime, precipitates begin to coarsen to even larger sizes. This is because even though the solute concentration in the matrix has reached a presumed equilibrium concentration, the nucleated and grown precipitates now have an increased interfacial energy at the particle/matrix boundary. This can be illustrated by considering the same number of atoms comprised in either (a) a large

number of small precipitates or (b) a fewer number of larger precipitates. For these populations, the total surface area (and thus interfacial energy) is minimized for the lower number density of coarser precipitates. The driving force for precipitate coarsening is most commonly derived through the use of the Gibbs-Thomson relationship (also historically known as the Thomson-Freundlich equation), which describes the effect of the curvature of spherical precipitates on the equilibrium solubility at the precipitate/matrix interface [71, 72]:

$$X_m = X_e \exp\left(\frac{2\gamma\Omega}{rRT}\right) \quad \text{(2.9)}$$

where X_m is the concentration of the solute at the interface, X_e is the equilibrium concentration of the solute in the matrix, γ is the interfacial energy of the precipitate, Ω is the atomic volume of the growing precipitate, r is the precipitate radius, R is the universal gas constant, and T is the absolute temperature. If it is assumed that small supersaturations exist, as in the case for a low volume fraction of precipitates, the Gibbs-Thomson relationship can be linearized:

$$X_m = X_e \left[1 + \frac{2\gamma\Omega}{rRT}\right] \quad \text{(2.10)}$$

Considering a smaller and larger precipitate in a given matrix, it can be seen from Eqn. 2.2 that the smaller precipitate will have a higher concentration at the precipitate/matrix interface in comparison to the larger precipitate since $X_m \propto 1/r$. The result is a concentration gradient where smaller precipitates will preferentially dissolve at the expense of the larger coarsening precipitates. In general particle coarsening, which is otherwise generally called Ostwald ripening, can be kinetically modeled using power law relations that give meaningful insights into the mechanisms dominating the particular coarsening process. This power law relationship is expressed commonly as:

$$r^n - r_0^n = K_n t \quad \text{(2.11)}$$

where r is the radius at a given time t, r_0 is the initial radius at the onset of coarsening, and K_n is a constant exponentially dependent on temperature. Of specific importance is the power law exponent n, which can be used to evaluate the rate limiting mechanism for particle coarsening.

Previous authors have derived the kinetics for particle coarsening for a variety of limiting cases. For example, **Figure 2.2** lists the three most commonly discussed cases in the literature for scenarios in which Ostwald ripening is dominated by 3D solute diffusion within the matrix, 2D solute diffusion along grain boundaries, and 1D diffusion along dislocations intersecting precipitates. The most simplified approach to these derivations assumes a zero-volume fraction approximation for precipitates, the application of the linearized Gibbs-Thompson relationship for particle/matrix solute concentrations, and a conservation of mass between the growing precipitate and the incoming flux of particles.

Depending on the rate limiting mechanism, the power law exponent has been shown to vary between n=2 and n=6. For coarsening kinetics dominated by the incorporation of incoming solute atoms into the growing precipitate, the radius is proportional to the square root of time (n=2) [69, 73]. The corresponding proportionality constant is approximated as:

$$K_2 = \left(\frac{64}{81}\right)\left(\frac{C_1 X_e \Omega^2 \gamma}{RT}\right) \quad \text{(2.12)}$$

where C_1 is a constant dependent on the specific matrix/interface system. In the case of diffusion limited growth the power law exponent increases to n=3 and the matrix diffusivity of the rate limiting solute atom is incorporated into the rate constant [69, 73, 74]. Both n=2 and n=3 coarsening kinetics have been well established since 1961 as the Lifshitz-Slyozov-Wagner (LSW) theory for particle coarsening. It is through the lens of the LSW theory that most of the coarsening papers in literature focus.

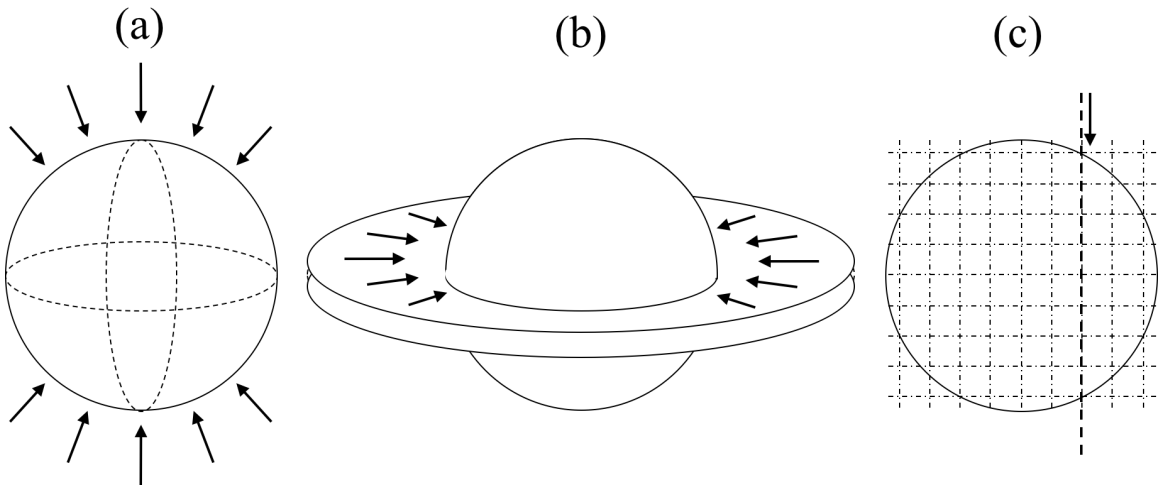


Figure 2.2. Schematic diagrams used for the derivation of coarsening kinetics dominated by (a) 3D diffusion, (b) 2D diffusion along grain boundaries, and (c) 1D diffusion along dislocations. Arrows define directions by which solute atoms can diffuse to the precipitate.

$$K_3 = \left(\frac{8}{9}\right)\left(\frac{X_e D_m \Omega^2 \gamma}{RT}\right) \quad (2.13)$$

Higher-order coarsening mechanisms have also been conjectured to play a role in particle coarsening kinetics, especially in situations such as ODS alloys where heterogeneous nucleation plays a significant part in the development of the dispersion-strengthened microstructure. Specifically of interest are the roles of dislocations and grain boundaries on the potential coarsening kinetics. As presented in **Figure 2.2**, the general scenarios for (a) 3D matrix diffusion, (b) 2D grain boundary diffusion, and (c) 1D dislocation diffusion. For grain boundary diffusion, it is assumed that a precipitate has nucleated on a grain boundary with thickness w and the rate limiting mechanism for the growth of the precipitate is the influx of solute through the shared grain boundary/precipitate interfacial area [71, 75]. Grain boundary diffusion kinetics lead to a power law exponent of n=4 and a corresponding constant [75]:

$$K_4 = \left(\frac{8}{3}\right)\left(\frac{\sin^4(\theta)}{C_2}\right)\left(\frac{w X_e D_g \Omega^2 \gamma}{RT}\right) \quad (2.14)$$

In this equation, C_2 is a constant based on the interfacial energy of the grain boundary, θ is the angle between the grain boundary and the precipitate at the interface, and D_g is the coefficient for grain boundary diffusion.

In the dislocation pipe diffusion formulation postulated by Ardell [75], it was assumed that solute atoms diffused through the lattice along dislocations in one dimension, and the growth rate was dependent on the number of dislocations (Z_0) intersecting the precipitate at any given moment in time in addition to the effective cross sectional area of the precipitate (A_d). Using the diffusion coefficient describing the movement of atoms along dislocation pipes, this n=5 rate limiting mechanism gives a constant approximated by:

$$K_5 = (1.0338)^5 \left(\frac{3}{4}\right)^4 \left(\frac{5}{6\pi}\right)\left(\frac{Z_0 A_d X_e D_d \Omega^2 \gamma}{RT}\right) \quad (2.15)$$

The applicability of the n=4 and n=5 derivations has been questioned by many authors, especially based on the highly specific assumptions used in their derivations. For example, Vengrenovich [76] has noted that in Ardell's dislocation pipe diffusion model it is assumed that the number of dislocations intersecting the precipitate is constant, while realistically it should change as the precipitates grow and the precipitates lose coherency (and their respective strengthening capability). This would result in dislocation detachment for increased precipitate sizes, adding another dependence of the constant on the precipitate radius:

$$K_6 = \left(\frac{1}{2\pi^2}\right)\left(\frac{Z_0 A_d^{\frac{3}{2}} X_e D_d \Omega^2 \gamma}{RT}\right) \quad (2.16)$$

Although higher-order reaction kinetics are conjectured to be possible, no theoretical predictions exist for these possible mechanisms where n > 6. Consequently, most ODS particle coarsening literature frame the kinetics in terms of the mechanisms

described here [77-79]. This work will expand on the current state-of-the-art on ODS precipitate coarsening while also calling attention to the weaknesses of these formulations in sufficiently explaining certain observed kinetics in dispersion strengthened alloys.

2.3. Grain Recovery and Recrystallization

As mechanical work is performed on a material, as is in the case of high-energy mechanical alloying processes or deformation associated with cold work, some energy is dispersed as heat while a fraction of the energy is transferred to the material. The mechanisms by which the deformed alloy stores this energy input is highly important in the context of ODS alloy processing because it directly influences the resulting microstructure of the alloy after subsequent heat treatments. This section details the mechanisms by which energy is stored and released during the deformation and annealing treatments associated with a particular interest in the driving forces for grain recovery, growth, and subsequent recrystallization.

A material has two main mechanisms for the storage of energy during mechanical deformation: lattice strain and the formation of defects within the microstructure [65]. Since the material's lattice can only maintain a certain level of elastic strain before becoming permanently deformed through plastic strain, most of this stored energy arises from the formation of various defects to accommodate the increased amounts of energy input associated with significant deformation. In fact, the lattice strain accommodation only accounts for ~3% of the stored energy in the deformed material [65]. Consequently, imperfections such as vacancies, dislocations, and planar defects account for most of the stored energy, with the most important of these defects being generated dislocations. A simplified dislocation can be envisioned simply as an extra half-plane of atoms inserted within the lattice, and it is the formation and propagation of these planes of atoms that results in the plastic deformation of the material [80].

In the case of powder deformation through mechanical alloying, the resultant grain size of the powder decreases from tens of microns in the as-received gas atomized

powder to only tens of nanometers in the ball-milled powder. This grain refinement is directly due to the generation of a high density of dislocations, which results in the formation of low angle and high angle grain boundaries. These boundaries are areas of high atomic disorder that separate different regions of lattice atoms oriented in the same direction (grains). It has been well established in the literature that a low-angle grain boundary (defined as a boundary with less than approximately a 10-15 degree malorientation between neighboring grains) can be represented by an array of dislocations [80]. As the dislocation density increases the misfit between neighboring grains increases and a higher number of smaller sub-grains begin to form within the deformed material. The result is a highly refined grain structure with an incredibly high dislocation density ($>10^{16}$ m^{-2}) and an unstable microstructure needing to release this increased stored energy during subsequent thermal annealing treatments.

Upon subsequent thermal annealing treatments in the deformed state, the material attempts to release this increased stored energy through a combination of recovery and grain recrystallization phenomena listed in terms of increasing required activation energies. The first of these phenomena, recovery, is generally defined as modifications to the defect structures in the material that occur before the onset of the nucleation and growth of strain-free grains through recrystallization [81]. At low temperatures, recovery comprises the recombination of point defects such as vacancies with interstitials, dislocations, and grain boundaries. As the temperature increases and dislocations become mobile, mechanisms such as dislocation dipole annihilation, polygonization, and coalescence also begin to occur [80, 81].

To better visualize these mechanisms, consider a collection of dislocations presented in **Figure 2.3**. For dislocations on the same glide plane with opposite Burgers vectors (a dislocation dipole), such as dislocations labeled A and B in the figure, an annihilation process can occur if these dislocations glide toward each other, thereby restoring the local matrix to the undeformed state. Dislocation dipole annihilation is a bit more complicated for cases where the dislocations are propagating along different glide

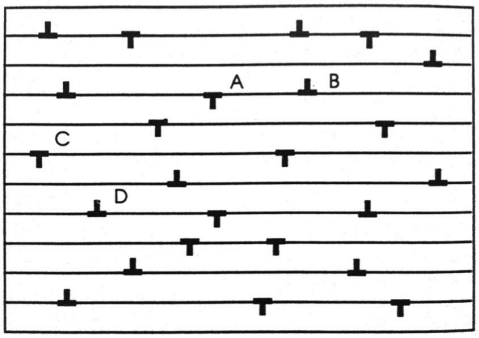


Figure 2.3. A collection of edge dislocations in a deformed crystal along glide planes, from [82]

planes, as is the case for dislocations C and D. In this case, it will require one of the dislocations to climb to the same glide plane for dipole annihilation to occur [82].

In addition to dislocation dipole annihilation, polygonization and subgrain coalescence are additional recovery mechanisms that allow the material to lower its stored energy upon annealing. Polygonization has been discussed by various authors [80-82]. This mechanism occurs due to the tendency of dislocations to reorganize and stand atop one another to form low angle (twin) grain boundaries, as illustrated in **Figure 2.4** [82]. In the case of neighboring grains with low-angle grain boundaries with minimal misorientations, the collective movement of dislocations allows for reorientation of the subgrain cell walls so that uniform cells can be formed [81]. An illustration of this mechanism is represented below in **Figure 2.5**.

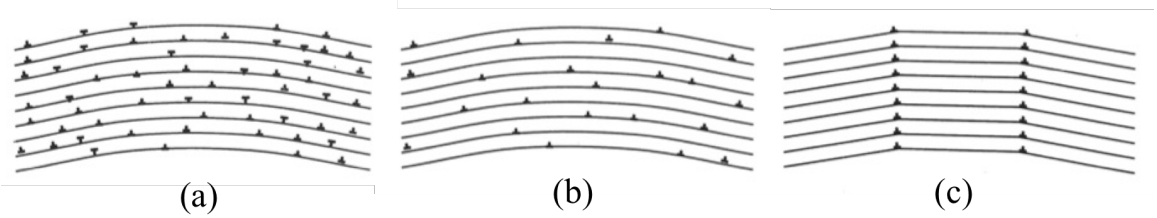


Figure 2.4. Depiction of dislocations in (a) the as-deformed state, (b) after dipole annihilation, and (c) after the polygonization process [82].

In all of these mechanisms, a fraction of the stored energy is expended through the activation of the defects within the deformed material. The remaining stored energy serves as the driving force for the nucleation and growth of new strain-free grains in a process called recrystallization. In ODS alloys, the recrystallization process is quite complex and can be separated into either primary or secondary recrystallization stages. In primary recrystallization, grains nucleate and grow homogeneously while in secondary recrystallization, certain grains grow rapidly at the expense of neighboring grains within the microstructure resulting in a highly bi-modal grain structure. For this reason, secondary recrystallization is often termed “abnormal grain growth”.

For recrystallization to occur, new grains must first nucleate within the deformed microstructure. Classical nucleation theory describes the nucleation of these new grains as random thermal fluctuations of the atoms that create small crystallites that subsequently grow within the material due to the high interfacial energy of the small crystallite size [83]. In many materials, however, a different mechanism for the formation of recrystallization nuclei has been observed that extends to the ODS alloy systems

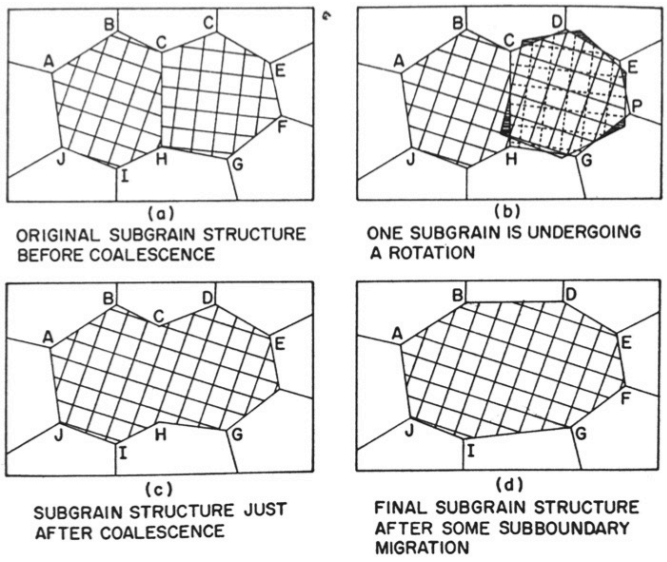


Figure 2.5. Steps associated with the subgrain coalescence mechanism resulting in a new grain with uniform subgrain texture [81].

studied in literature [82, 84]. This mechanism, titled strain-induced grain boundary migration (SIBM), results from the heterogeneity of dislocation densities across two neighboring grains [85]. Consider the case where two neighboring grains have dislocation densities ρ_1 and ρ_2 as shown schematically in **Figure 2.6**. Bailey and Hirsh established that to accommodate the interfacial energy of the protruding grain boundary, the energy difference across the boundary must be balanced by the stored energy difference across the boundary due to the difference in dislocation densities between grains 1 and 2. Consequently, for the growth of the hemispherical protruding boundary with equivalent radius R, it was found that [85]:

$$R > \frac{2\gamma_{gb}}{\Delta E_d} \quad \text{(2.17)}$$

where the energy stored by dislocations is a function of the dislocation density [82]:

$$E_d = \frac{1}{2}\mu b^2 \rho_d \quad \text{(2.18)}$$

Thus the minimum bulge radius required for the boundary to grow into the grain of higher dislocation density is inversely proportional to the dislocation density difference across the boundary (Eq. 2.17). For the case of ODS alloys with an abnormally high dislocation density, it follows that a high number of very small recrystallization nuclei can form due to the minimization of the critical bulge radii.

$$R > \frac{4\gamma_{gb}}{\mu b^2(\rho_1 - \rho_2)} \quad \text{(2.17)}$$

For ODS alloy powders annealed following mechanical alloying, differentiating between primary and secondary recrystallization processes is quite difficult, specifically due to the nucleation of recrystallization sites through the SIBM phenomenon. Sallez has extensively studied the abnormal grain growth of ball milled and annealed ODS FeCr

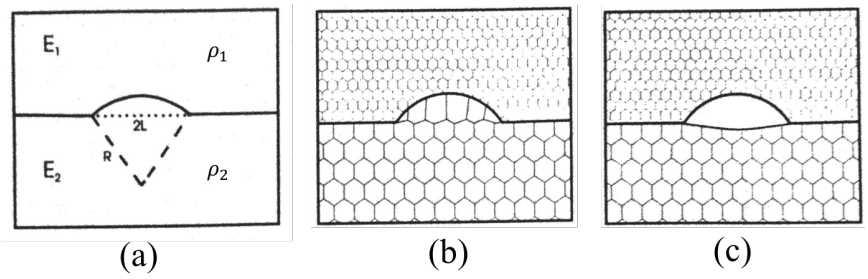


Figure 2.6. (a) The SIBM mechanism describing the bulging of a grain boundary between grains of high and low dislocation density, (b) the dragging of the dislocation cell structure by the bulging grain boundary, and (c) the resulting SIBM- induced nucleus free of dislocations. Figure reproduced from [82].

powders and has found that abnormal grain growth occurs incredibly rapidly at temperatures as low as 800°C, corresponding with an order of magnitude drop in dislocation density which was directly attributed to the increased mobility of grain boundaries conceptualized through the SIBM mechanism [84].

It is important to consider the effect of precipitation on the grain growth behavior of ODS alloys, especially in the context of annealed mechanically alloyed powders. In the ODS literature, it is commonly asserted that due to the presence of a high density of precipitates within the microstructure, the recrystallization temperature of popular ODS alloys such as PM2000 and MA957 is on the order of $0.9T_M$ [86-88], where T_M is the melting temperature of the alloy. However, it was just noted for mechanically alloyed ODS powders that this temperature has decreased to only ~$0.5T_M$. To better understand this discrepancy, it is important to consider the driving forces behind the migration of a migrating grain boundary recrystallization front. As the grain boundary attempts to propagate through the material, a force balance must be considered between the grain boundary interfacial pressure (E_{gb}), the stored energy of defects/dislocations (E_d), and the pinning pressure by the nanoprecipitates within the lattice (E_z) [84, 89-91]:

$$\Delta P = E_{gb} + E_d - E_z = \frac{2\gamma_{gb}}{R_{gb}} + \frac{1}{2}\mu b^2 \Delta\rho_d - \frac{3\gamma_{gb} f_p}{2r_p} \quad \ldots\ldots\ldots\ldots\ldots\ldots\ldots\ldots \quad (2.18)$$

For the highly deformed microstructure of a representative ball milled ODS alloy, the average grain size is R_{gb} = 25 nm [84] and γ_{gb} = 0.2 J/m^2 for the ultra-fine grained material [91], which results in a grain boundary pressure of E_{gb} = 16 MPa. With a Burgers vector of b = 0.248 nm for the ferritic alloy [57], μ = 81.07 GPa for a nanostructured ODS alloy 14YWT [92], and a representative dislocation density of $\Delta\rho_d$ = 7x10^{15} m^{-2} in recovered but non-recrystallized mechanically alloyed powder [84], the stored energy contribution is calculated to be E_d = 17.5 MPa. For a representative ODS nanoprecipitate particle size distribution, the average radius is r_p = 2 nm with a volume fraction of only f_p = 0.01, resulting in a Zener pinning pressure [93] of only 1.5 MPa. Thus, for the mechanically alloyed powder undergoing a thermal annealing treatment, the driving pressures for grain growth are an order of magnitude larger than the pinning force by the nanoprecipitates. Consequently, in the pre-consolidation annealing stage comprising ODS alloy consolidation, significant grain growth through secondary recrystallization processes is expected and the high temperature stability is only realized after subsequent thermomechanical treatments that decrease the dislocation density and increase the final grain size.

Although the underlying mechanisms for grain nucleation, recrystallization and abnormal grain growth are important in this context, the reader is referred elsewhere for a more comprehensive discussion on the subject [65, 81, 82, 84]. As will be extensively discussed in this work, however, this abnormal grain growth has significant implications on the as-consolidated microstructures of the ODS alloy, which is irrespective of the consolidation methodology.

2.4. Conventional Processing Route for ODS Alloys

ODS alloys have been historically manufactured using a mechanical alloying approach followed by consolidation at high temperatures. Mechanical alloying has been preferred as the mechanism for oxide dispersion due to its high degree of reproducibility. There are many different types of consolidation methods, such as hot-extrusion (HE), hot-isostatic pressing (HIP), and spark plasma sintering (SPS), but hot-extrusion has

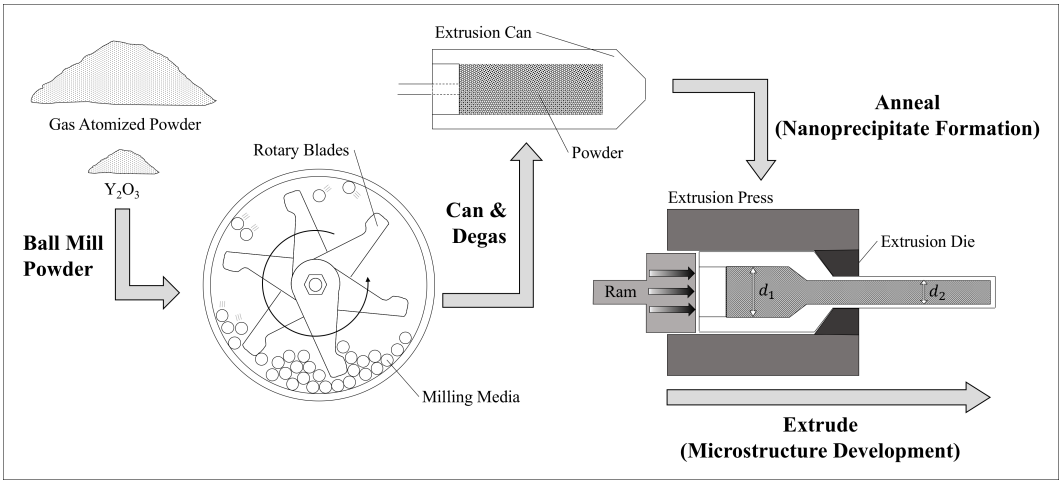


Figure 2.7. Schematic of the general powder metallurgical process used for the fabrication of an ODS alloy, where the consolidation method is chosen to be extrusion.

historically proven to be the most successful in comparison to other methodologies and will be used to perform all of the proposed research in this work. **Figure 2.7** illustrates the steps in the processing route for ODS alloys. This section reviews each processing step and how it affects the subsequent alloy properties.

2.4.1. Powder Composition Selection

Even before the ODS alloy has been fabricated through the extensive process described in **Figure 2.7**, the base material must be specified in terms of the desired elements for both the gas atomized powder composition and the type of oxide used in the mechanical alloying process. In this context, this work focuses solely on Fe-based alloys with additions of Cr, Al and other added elements to attain a desired microstructure. In the development of steels, it is well known that the additions of elements can shift the temperature dependent phase of the base metal. Pure iron undergoes a phase transition at 912°C from the BCC phase to the face-centered cubic (FCC) structure, and by controlling the cooling rate this FCC phase can transform into the martensitic phase (either a BCC or body centered tetragonal (BCT) structure), which allows for the tuning of the mechanical properties for required applications. It is this phase transformation capability that has made ferritic/martensitic (F/M) alloys popular both in ODS and non-ODS variants.

Although some F/M steels may be cited in this literature review for the purpose of better understanding the irradiation resistance or thermomechanical response of these alloys, this work focuses primarily on fully ferritic (BCC-Fe) ODS alloys. Consequently, much discussion will focus on popular ODS FeCr alloy 14YWT, and legacy ODS FeCr (MA957) and FeCrAl (MA956 & PM2000) alloys. The compositions of these alloys are listed below in **Table 2.1**. Due to the fully ferritic nature of these materials and the desire to prevent the precipitation of coarse embrittling carbide phases, these materials have consistently low C contents (<0.01 wt%) and thus are terms alloys in this work and not steels.

Figure 2.8 shows that as the Cr content increases beyond 12 wt.%, the high temperature FCC-Fe phase (also known as γ-Fe or austenite) disappears and the BCC-Fe phase (termed α-Fe or ferrite) remains stable up until the point of melting [94]. Chromium is not the only element that can alter the phase stability of Fe. In-fact, elements such as Cr, Si, Mo, V, Al, Nb, Ti, W, Zr, and others are all ferrite stabilizing alloying additions while Ni, Co, Mn, Cu, N, and C conversely stabilize the austenite region (expanding the γ-Fe loop) [95]. The ferrite stabilization capabilities of these elements can be estimated through a chromium equivalent formula, which can be visually illustrated through Schaeffler diagrams [96]. The equivalent chromium is calculated as:

$$Cr_{eq}\ (wt.\%) = (Cr)+2(Si)+1.5(Mo)+5(V)+5.5(Al)+1.75(Nb)+1.5(Ti)+ 0.75(W)+0.5(Ta) \quad (2.19)$$

Table 2.1. Nominal Composition of Popular Ferritic ODS Alloys

Alloy	Fe	Cr	Ti	Mo	W	Al	Y_2O_3
14YWT	Bal	14	0.4	0	3	0	0.3
MA957	Bal	14	1.0	0.3	0	0	0.3
PM2000	Bal	20	0.5	0	0	5.5	0.5
MA956	Bal	20	0.5	0	0	4.5	0.5

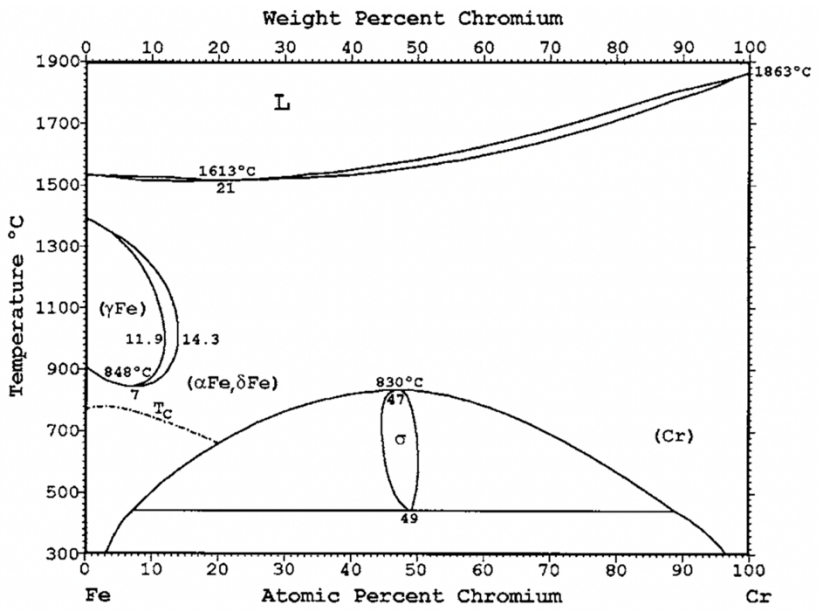


Figure 2.8. The Fe-Cr phase diagram from [94]

From this equation, it is possible to use a lower amount of Cr to guarantee the formation of a fully ferritic structure if strong ferrite stabilizing elements such as Al are added to the alloy. This becomes important due to the well-known Cr-rich α' phase that forms under both thermal aging and under irradiation at temperatures below 450°C [18-26]. The Fe-Cr phase diagram shows this $\alpha - \alpha'$ phase instability region at low temperatures. Luckily, previous authors have already optimized the Fe-Cr-Al matrix composition to minimize $\alpha - \alpha'$ phase separation phenomena while simultaneously preserving the ferritic structure and the resistance of FeCrAl alloys in both hydrothermal corrosion and high temperature steam oxidation [97]. The Fe-Cr-Al ternary diagram with overlaid microhardness measurements is presented in **Figure 2.9**. From this diagram, ODS FeCrAl alloys have been developed with nominal compositions in the Fe-(10-12)Cr-(5-6)Al range that exhibit beneficial high temperature steam oxidation resistance and mechanical properties [98, 99] while simultaneously inhibiting the formation of the deleterious Cr-rich α' phase [100].

Another reason that alloying elements are added to the alloy's base microstructure is that the addition of substitutional elements with different atomic radii than the base

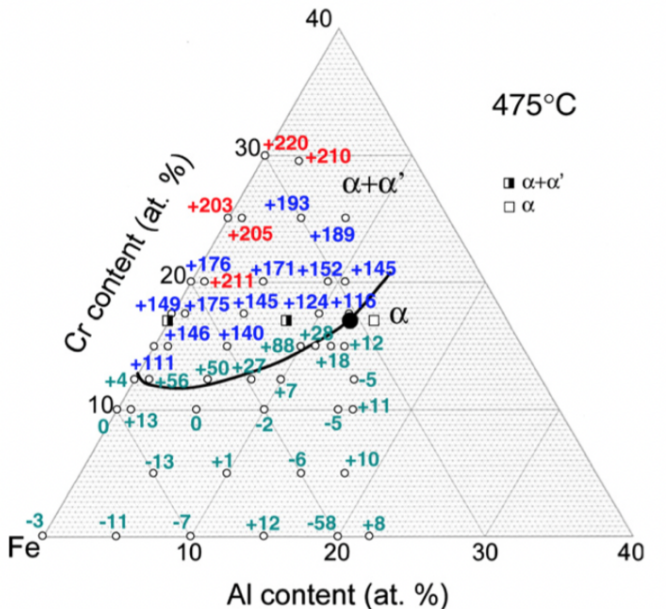


Figure 2.9. Fe-Cr-Al Phase Diagram (α' Cr region shown) [97]

element causes local strains in the surrounding atomic structure. The solid solution strengthening for various elements has been measured in BCC-Fe, and the results are summarized in **Figure 2.10** [58]. These substitutional atoms strengthen the matrix through this solid solution strengthening process, where dislocation motion becomes affected by the local strains introduced by these lattice imperfections. In stainless steel metallurgy, Mo has been added to steels to increase the high temperature strength of AISI Type 316 stainless steel [95]. In ODS alloy manufacturing, Mo has been previously used for solid solution strengthening in the MA957 alloy developed by the INCO Nickel Co. in 1978 [101].

In addition to the control of the phases within the microstructure, certain elements are added specifically to sequester impurity elements within the microstructure through the formation of oxides, nitrides, and carbides within the matrix. Some of these carbides, like those formed through the interaction of Fe and Cr with C, are quite large and can serve as crack-propagation sites, thereby embrittling the as-fabricated alloy [58, 59]. However, some elements such as Zr, Nb, V, Mo, and W can form finer carbides, nitrides, and oxides within the material that can more efficiently strengthen the matrix without

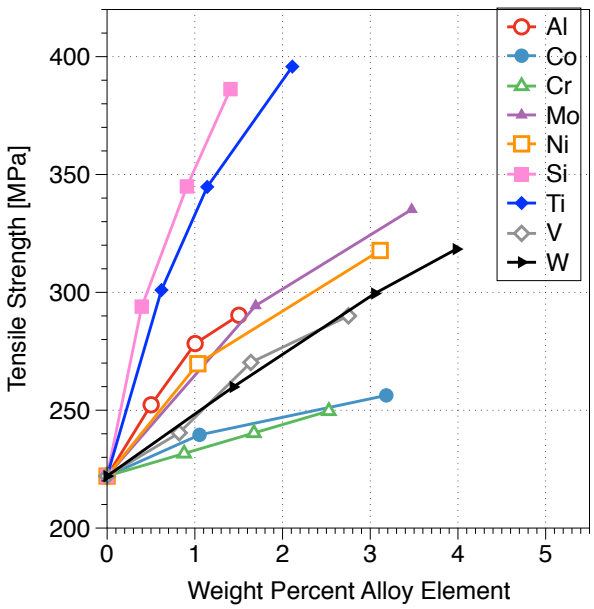


Figure 2.10. Solid Solution Strengthening in BCC Fe for various elements, reproduced from [58]

accelerating the propagation of cracks though the microstructure. Elements such as Nb and V are commonly added to stainless steels to promote the formation of MX type carbonitrides, which are specifically of interest in F/M steels due to the ability for secondary precipitation of a high number density of carbides during the austenite-ferrite phase transformation. Zr and Hf both have a strong affinity for all three types of interstitial impurity elements.

The tendency for elements to react with oxygen, carbon, and nitrogen within the alloy is commonly discussed thermodynamically through the calculation of Ellingham diagrams, where the standard reference states of each element are reacted with oxygen gas, nitrogen gas, or graphite (the most common allotrope of carbon). Since the Gibbs free energies of formation for elements in their reference states is zero, the formation energy of the resulting oxide, carbide, or nitride phases can be compared to determine which alloying elements form the most stable compounds and thus have the highest affinity for the impurity element of interest. Ellingham diagrams for common oxides, carbides, and nitrides referenced from literature are shown below in **Figure 2.11**, **Figure**

2.12, and **Figure 2.13** respectively [102-104]. Referencing the oxide Ellingham diagram in **Figure 2.11**, the beneficial presence of Al in the ODS Fe-Cr matrix can be readily seen. Due to the higher negativity of the free energy for Al in comparison to Cr, having Al in the matrix allows this highly reactive element to react preferentially in steam atmospheres, creating a stable and highly adherent alumina layer, which is the primary reason that ODS FeCrAl alloys have found applications in fossil applications in the past. The presence of Al also shifts the types of nanoprecipitates that nucleate in ODS FeCrAl alloys in comparison to their ODS FeCr counterparts, which is discussed in the later sections. Also of importance in the current work is Zr. In all three Ellingham diagrams, Zr is a highly reactive element that will react with O, C, or N in the matrix, which has resulted in differences in identified nanoprecipitate populations in ODS FeCrAl alloys with Zr addition in the literature [105, 106].

Though not shown, yttria is the most stable of the binary oxides shown, and for this reason this oxide is the most commonly used oxide in the fabrication of ODS Fe-based alloys. The stability of this phase in Fe alloys is also aided by the incredibly low solubility of Y in the BCC-Fe matrix (**Figure 2.14**), which allows Y to easily precipitate out of solution after the mechanical alloying step [68]. The final nanoprecipitate composition within the ODS alloy is commonly not the same as the initially added oxide, and predicting the resulting phase is much more complex than a consideration only of the Ellingham diagram at the temperature of interest.

Ti solute additions to the base ODS FeCr matrix promote the formation of smaller ~3 nm Y-Ti-O nanoclusters within the alloy when yttria is mechanically alloyed with the base metal powders, shifting the average crystallite sizes down from 10 nm Y_2O_3 [107]. The addition of Ti to ODS FeCr alloys reduces the particle size and changes the chemistry of the nanoprecipitates, shifting from cubic and monoclinic yttria to orthorhombic Y_2TiO_5 and pyrochlore $Y_2Ti_2O_7$. The addition of Cr is not shown to change the chemistry of these particles, although some authors have shared evidence of a Cr shell surrounding nano-oxide precipitates [108-111] in ODS alloys. Zirconium and hafnium are also being used in ODS FeCrAl alloys due to their ability to refine particle sizes in a

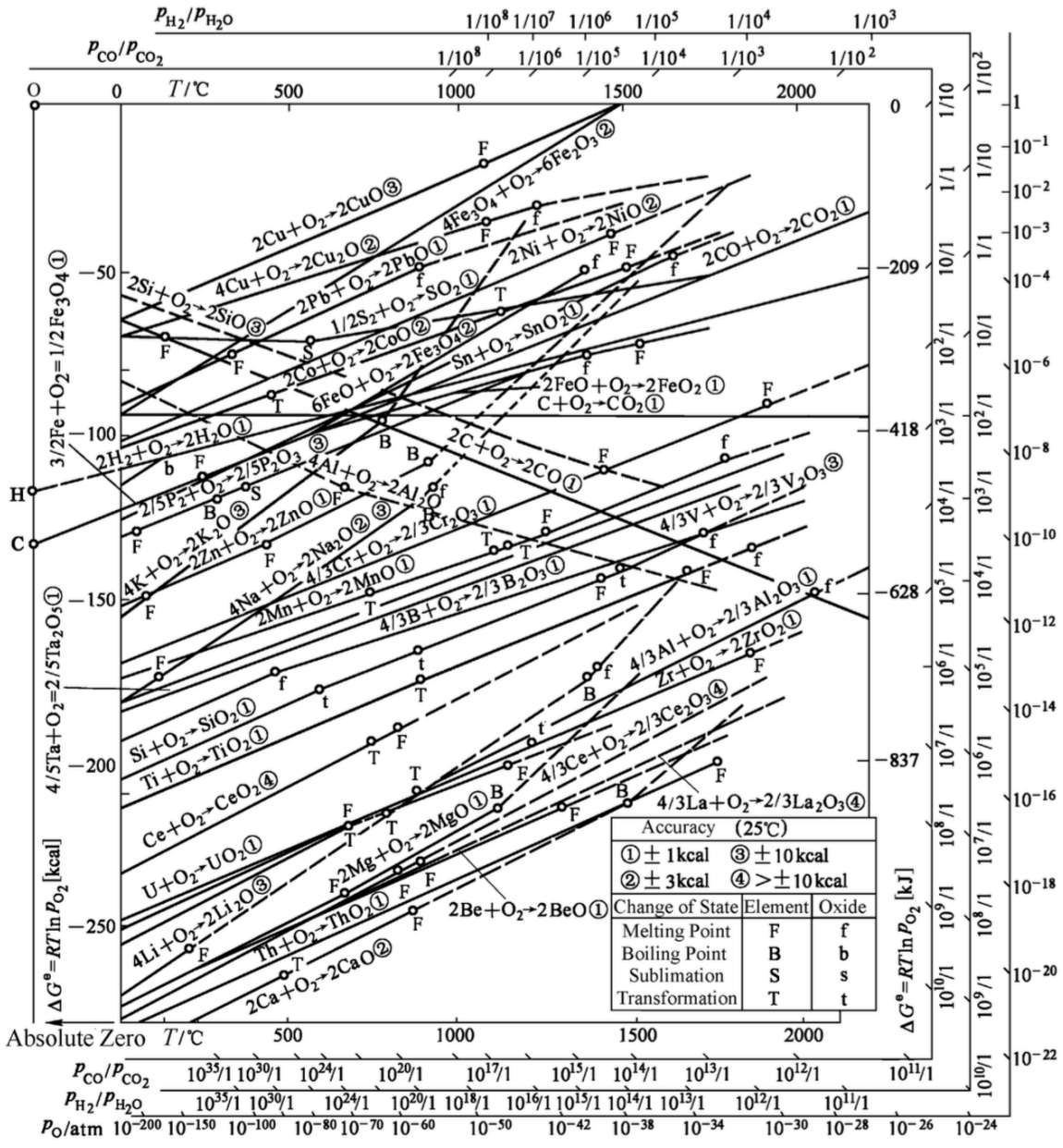


Figure 2.11. Gibbs free energies for various binary oxides, referenced from [102]

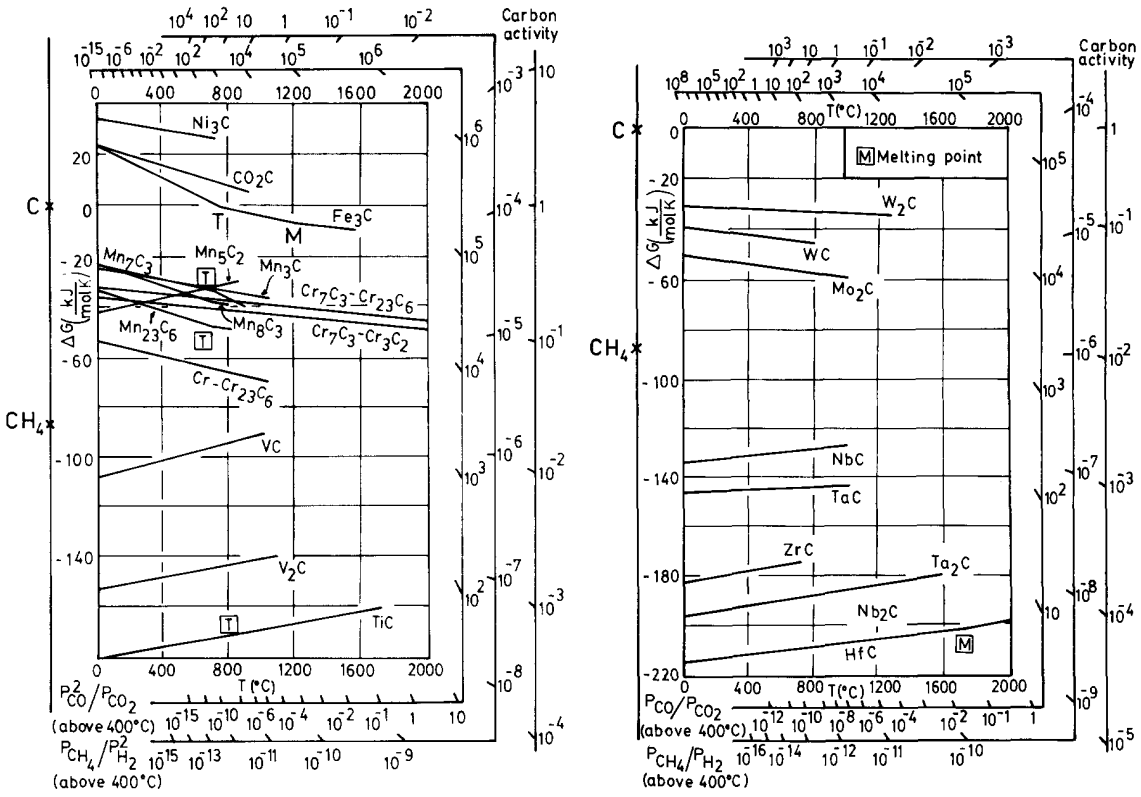


Figure 2.12. Gibbs free energies for various binary carbides, referenced from [103]

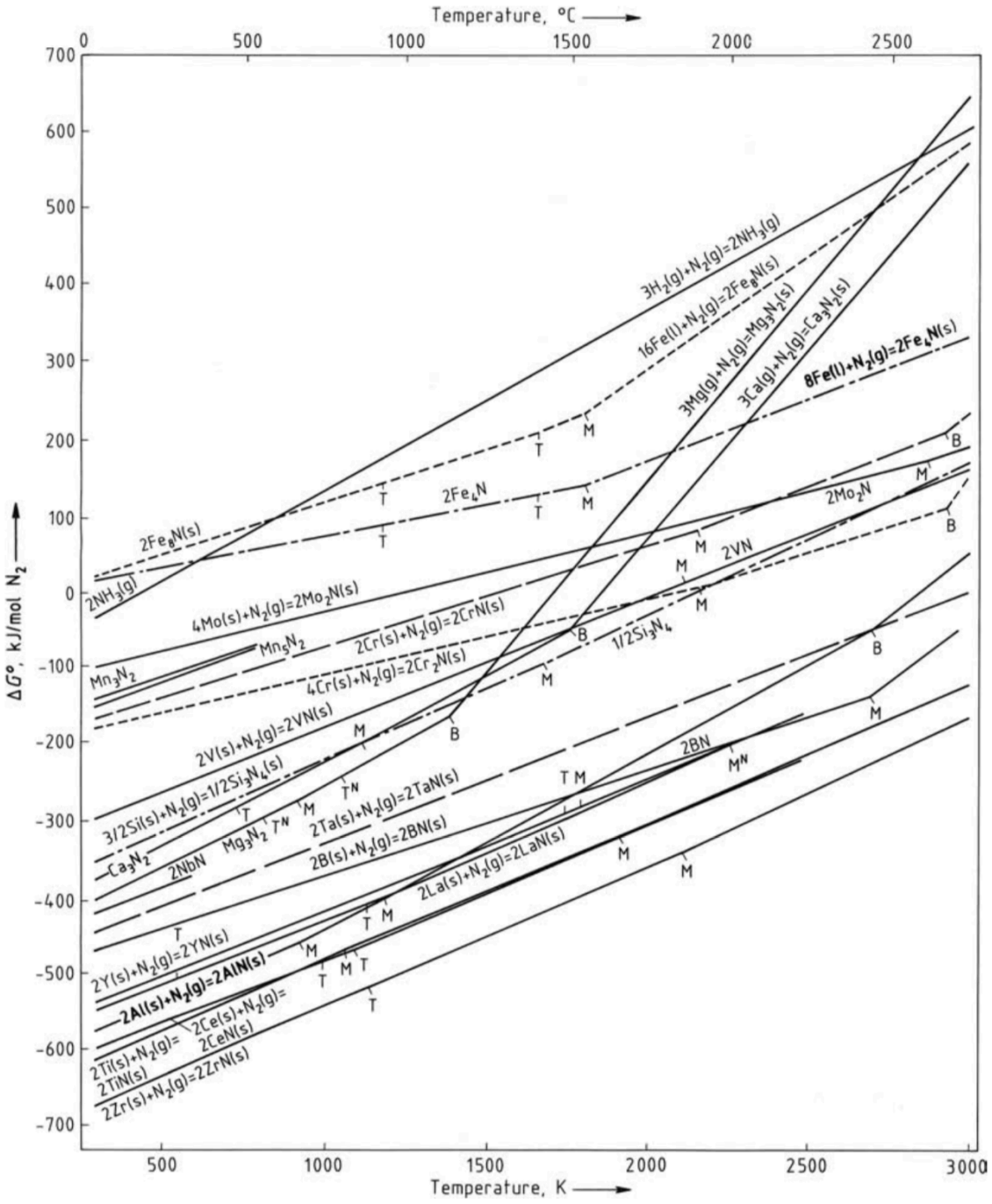


Figure 2.13. Gibbs free energies for various binary nitrides, referenced from [104]

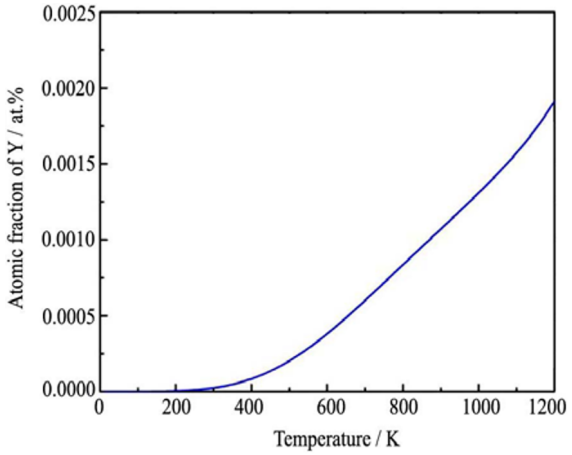


Figure 2.14. Solubility of Yttrium in BCC Fe as a function of temperature [68]

similar fashion to Ti in ODS FeCr alloys [105, 107, 112]. Zr also has the capability of reacting with excess C and N in solution to form carbides and nitrides, potentially alleviating the grain boundary segregation of these impurities [106, 113].

From a radiation resistance perspective, the choice of alloying elements is quite limited if the resulting ODS ferritic alloy is required to exhibit minimal neutronic activation in advanced fission and fusion reactor environments. Sublet and Butterworth have evaluated the specific activities of a variety of alloying element additions in comparison to Fe as a base material to aid in the design of reduced activation structural materials for high fluence reactor conditions, and have categorized the alloying elements as a function of their activities [114]. Alinger has conveniently categorized these elements as a function of their activity, presented in **Table 2.2** [115]. From this summary, it can be seen that elements such as Mo undergo greater activation (and transmutation) in fusion environments. Instead of Mo, the element W exhibits lower levels of activation and for this reason Mo has been substituted for W in popular ODS ferritic alloys such as 14YWT. For the present investigation into ODS FeCrAl alloys for nuclear applications, Al is an integral element for oxidation resistance but is a high activation element. For this reason, ODS FeCrAl alloys may not be suitable for use as first-wall components in fusion

Table 2.2. Summary of elemental activities for various elements, reproduced from Alinger

Activation Category	Elements
Very Low Activation (< 2 week decay time)	Li, Be, B, C, O, Mg, Si, P, S
Low Activation (1 month – 5 year decay time)	Ti, V, Cr, Zr, W, Pb, Y
Moderate Activation (10-30 year decay time)	Mn, Fe, Zn, Hf
High Activation (>100 year decay time)	Al, Ni, Cu, Nb, Mo, Sn

reactor environments but are still viable for use as other fusion reactor components, as accident tolerant fuel cladding candidates in light water reactors, and as structural materials in advanced fission reactors.

2.4.2. Mechanical Alloying

The many steps involved in the processing of ODS alloys was presented previously in **Figure 2.7**. Gas atomized powders are mixed with added oxide additions prior to being mechanically alloyed (MA) in one of many types of ball mills. The alloyed powder is then canned and degassed under high vacuum prior to being consolidated at high temperatures to provide the final product. Thermo-mechanical treatments (TMTs) such as hot rolling and annealing usually follow hot extrusion to carefully fine-tune the microstructure for commercial uses. Of the many processing steps listed above, by far the most important is the mechanical alloying step. The importance of this initial step is crucial to the homogeneous dispersion of oxides within the microstructure and will consequently determine the irradiation resistance and the mechanical properties. Gas atomized powder or elemental powders are mixed with an oxide powder (conventionally yttria) within a ball mill of some type (attrition, planetary, spex) and are rapidly deformed and fractured due to collisions with small spherical milling media. As particles deform, the added oxide powder is slowly incorporated into the microstructure of the gas-atomized particles, creating the final alloy powder. With regards to mill types, attrition milling is specifically beneficial because it has been shown to be an order of magnitude more efficient in terms of milling time than planetary ball milling. Furthermore, attrition

ball milling allows for powder batches on a semi-industrial (0.5 kg) to industrial scale (100 kg) [116].

Mechanical alloying is not solely applicable to the ODS alloy system, even though the process was first commercialized for Ni-based ODS alloys [117]. Instead, many different composite and alloy systems have been investigated, providing best practices for the ball milling of many different materials [118]. Many of the different factors ultimately affecting the quality of the final alloyed powder are: the starting powder size, powder handling, atmosphere, milling media size and composition, ball to powder (BTP) ratio, milling speed/intensity, milling time, and other impurities (chamber contamination). To decrease contamination, low carbon steel milling media has historically been used for the development of Fe-based ODS alloys. Increasing the ball-to-powder ratio has been shown to more quickly refine particle sizes, but since limits exist on milling efficiency versus the space occupied by the milling media this variable is not feasible to change substantially [116].

Many authors have compared different milling atmospheres specifically during ODS FeCr processing. Iwata et al. investigated differences in ODS alloy (Fe-15.5Cr-2W-4Al-1Zr-0.35Y_2O_3) mechanical and microstructural properties when mechanically alloyed in either argon or hydrogen atmospheres. The H_2 atmosphere provided a smaller particle size in comparison to Ar, but resulted in lower impact properties. This was attributed to higher nitrogen contamination as seen in the formation of carbonitrides within the as extruded sample [119]. This formation of nitrides, however, was most likely due to nitrogen glove box contamination and not due to the hydrogen milling since other studies have shown superior impact properties for hydrogen milling instead of argon milling with no nitride formation [120]. Milling in hydrogen atmosphere also led to a lower micro-hardness for alloys consolidation through HIP [121]. Noh and colleagues found that milling in Ar atmosphere resulted in smaller particle diameters; also, the Ar and Ar-H_2 MA samples showed homogeneous, fine grain distributions while the sample milled in He atmosphere was bimodal in grain size distribution [122]. Cryomilling has

shown to be the most efficient at refining the particle size and creating microstructures with a high number density of nanoprecipitates [123].

Some authors have attempted to describe the microstructural evolution and deformation processes during the mechanical alloying of ODS FeCr powders. Iwata et al. tabulated the particle sizes of mechanically alloyed powders milled for up to 50h in a planetary ball mill, but only used one milling intensity [124]. Furthermore, in a particle morphology study of 14YWT, scanning electron microscopy (SEM), energy dispersive spectroscopy (EDS), and X-ray diffraction (XRD) were used to study the incorporation of solute atoms Cr, W, and Ti into the microstructure of 14YWT [125]. Mechanical alloying was performed in a high purity Ar atmosphere for 5, 20, 35, 50 and 80h with rotation speed of 250 rpm and the ball-to-powder weight ratio of 10:1 using a planetary ball mill. Five stages of milling were identified for the mechanical alloying process: 1) solute atoms coat the iron particles, forming a core-rim structure, 2) particles begin to aggregate to form loosely bound clusters, 3) particles deform and begin to fracture into equiaxed particles, 4) a lamellar interlayered structure forms within each particle, and 5) fracture and re-welding of these final particles occurs, forming homogenized equiaxed particles. This work only used one milling speed, assuming that this 5-step deformation process is applicable to all milling intensities when it could be different based on how quickly particles work-harden and fracture. This work also only considered elemental powders and did not investigate the oxide incorporation into the microstructure, which is more important when considering the homogeneous nucleation of nanoclusters after heat treatment. Milling intensity was investigated by Rahmanifard et al. to quantify particle size versus time distributions for different milling media sizes and milling intensities. The authors found that decreasing the milling media size allows for more refinement of the extracted powder size. The authors also found that increasing the milling intensity did not affect the final particle size, but the particle size began to approach the equilibrium value at a faster rate [126]. Massey and coworkers on ODS FeCrAl alloys found bi-modal microstructures for milling times less than 20h and a more homogeneous microstructure

for samples milled for 40h, which suggests that homogeneous incorporation of yttria into the powders was not attained at milling times less than 40h [113].

Hilger et al. attempted to describe this oxide incorporation by using both XRD and atom-probe tomography (APT) on both pure Y_2O_3 and additions of Y_2O_3 to atomized FeCr powder milled in a high energy mill. XRD on as-milled pure Y_2O_3 indicated partial amorphization of the cubic phase with no change in the monoclinic phase fraction, giving quantitative support to the conjecture that Y_2O_3 is not dissolving into the FeCr matrix and that Y and O dissolution is not occurring; instead, the milling intensity causes severe crystallite refinement, leading to a partial amorphization of Y_2O_3 within the microstructure [127]. Decreasing the initial particle size of added Y_2O_3 milled to create nanostructured ODS alloys results in a finer grain distribution, a smaller nanoprecipitate size, and improved creep properties due to the refinement of the already nanoscale Y_2O_3 additions [128].

From the extensive literature on the mechanical alloying of powders for the creation of various optimized ODS microstructures, the following best-practices were summarized for the production of the ODS FeCrAl powders in this work:

- Initial oxide crystallite/powder size – the reduction of the initial powder particle size of Y_2O_3 results in a finer grain distribution; nanocrystalline yttria powder is used in this work with 25-50 nm crystallite sizes.
- Powder handling – although some authors have found higher N contents in powders handled in N_2 glove boxes, most authors using Ar atmosphere did not see issues in atmosphere contamination even if controlled atmospheres were not used. Powder will be handled in air atmosphere before and after the ball milling process to allow for more simplified commercial scaling if applied.
- Milling atmosphere – Ar consistently resulted in a finer powder size and more homogeneous microstructural and mechanical properties. Thus, Ar atmosphere will be used for all mechanical alloying.

- Milling media – a finer milling media results in a finer particle size. The milling media will be kept as small as possible (5 mm diameter steel milling media) and the ball-to-powder ratio will be kept at 10:1.
- Milling intensity – the use of higher milling intensities more quickly refines the particle size due to a quicker work-hardening and fracture of the particles. During milling, the intensity will be varied between lower rpm (350-400 rpm) and high intensity (600-900 rpm) so that the particle size can be reduced while simultaneously allowing for more efficient incorporation of Y and O into the lattice. This two-step process will also help prevent "dead-zones" within the ball mill where some powder falls in pockets without sufficient deformation.
- Milling time – to ensure homogeneous incorporation of Y and O in the matrix, mechanical alloying will be performed for 40h.

2.4.3. Consolidation Methods and Thermomechanical Treatments

Transforming the mechanically alloyed powder into a functional material requires some type of consolidation methodology, which involves some combination of high temperature and pressure to aid in the sintering of the alloyed powder into a final part. The three most popular methodologies for conventional consolidation are hot-extrusion, hot-isostatic pressing (HIP), and spark plasma sintering (SPS).

Extrusion is the most common consolidation process, and comprises two main steps: 1) a pre-heating of the alloyed powder in a sealed can and 2) the forcing of this extrusion can through a die of smaller orifice size to reduce the cross sectional area and accelerate particle sintering/cohesion in the process. The severe deformation that defines this technique means that minimal porosity can be achieved and large aspect ratio components a such as tubes, rods, and bars can be easily manufactured. This significant deformation also creates significant preferred orientations (or textures) for grains comprising the as-extruded microstructure, which leads to anisotropic material properties for extruded components. Previous heats of 14YWT have shown anisotropic mechanical properties along the transverse and longitudinal (extrusion) axes due to elongated grains

with significant associated texture. Aydogan et al. investigated different processing methods, including both hot extrusion and isostatic extrusion. The authors determined that compared to standard hot extrusion and cross-rolling that develops strong alpha-fiber (001)[110] and weak gamma-fiber (111) [112] components, hydrostatic extrusion develops only weak alpha and gamma fiber components of (001)[110] and (111)[110], respectively. Although less texture exists for the hydrostatically extruded samples, there exists a higher number density of low angle grain boundaries for the hydrostatically extruded sample [92]. Similar alpha-fiber textures in the rolling direction after extrusion have also been identified in ODS FeCr and FeCrAl alloys MA957 and MA956, respectively [129]. Strong texture and grain elongation is associated with grain boundary decohesion at higher temperatures, resulting in deteriorated high temperature fracture toughness [130, 131]. Luckily, thermo-mechanical treatments (TMTs) of 9Cr ODS alloys have been shown to enhance diffusion at grain boundaries, helping alleviate issues associated with grain boundary decohesion previously associated with the lower fracture toughness of 14WYT [132]. Using these hot rolling treatments, high temperature fracture toughness of select 9Cr-ODS alloys was able to increase to over 200 MPa $m^{1/2}$, which is competitive with non-ODS alloys such as HT9.

Many studies have compared the anisotropy of different orientations in extruded ODS alloys. **Figure 2.15** shows the different types of grain orientations used for various mechanical property measurements. 14YWT alloy FCRD NFA-1 (Fe-14Cr-3W-0.4Ti-0.2Y+0.125FeO) was milled in a Zoz CM100b attritor ball mill under argon atmosphere, extruded, and cross-rolled at ORNL for mechanical property evaluation at different orientations. The grain structure consisted of a bimodal distribution of small (60% area fraction) submicron grains and larger (40% area fraction) 1-10 micron grains. The existence of microcracks parallel to the rolling and extrusion directions resulted in cleavage fracture along low-angle grain boundaries, causing a notable difference in tensile properties at different temperatures depending on orientation [133]. Alinger et al. performed tensile and 3-point bend tests on extruded MA957 to study the origins of previously observed brittle behavior. The LT orientation provided the highest values for

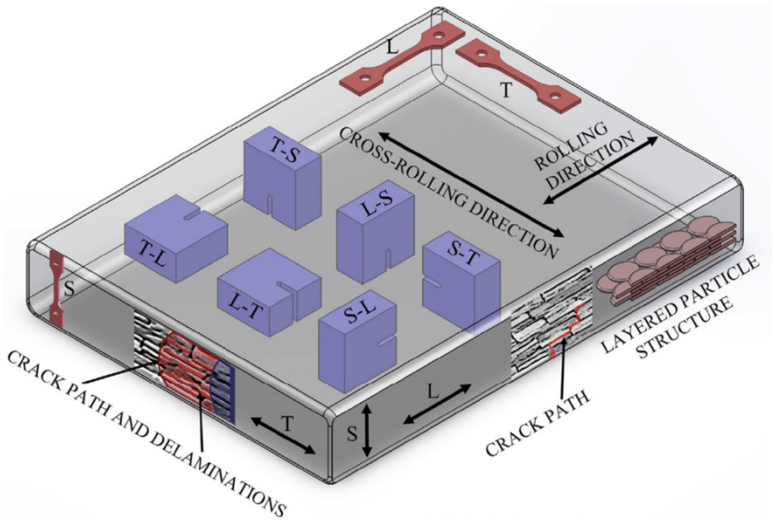


Figure 2.15. Orientations Used for Mechanical Property Evaluations [130]

ductility and fracture toughness, while the TS and LS orientations had low toughness but high ultimate tensile stress values. The existence of alumina stringers (lines of precipitates decorating grain boundaries) existing in the fracture planes of the TS and LS orientations indicated that the existence of these intergranular particles within the MA957 microstructure are deleterious to the fracture characteristics of the alloy, accelerating micro-void coalescence and cleavage [134]. This same anisotropy is noted in ODS FeCrAl alloys fabricated via hot extrusion. Chao and Capdevila analyzed the mechanical behavior of ODS Fe-20Cr-5Al using both hardness measurements, tensile tests, and impact testing. Hardness was a minimum for planes parallel to the LT orientation, coupled with cracks propagating in this plane along the notch plane during impact testing; furthermore, for the LS and TS orientations the hardness was comparable and cracks form normal to the notch plane. Samples failed by crack propagation enhanced by the strong <110> texture and the presence of impurities and oxides along delaminated grain boundaries [135, 136].

In comparison to extrusion, HIP and SPS do not create significant textures during component consolidation. In the HIP process, the sample is sealed in a can and degassed under vacuum to prevent contamination and to desorb gas atoms from the particles. In

this respect HIP is similar to extrusion. However, the HIP can is thinner than the extrusion can, allowing for the can to buckle under applied pressure. This can is then hydrostatically compressed to hundreds of MPa in pressure through the injection of an inert gas into the chamber. Then, the furnace heats the sample for an extended period of time to allow the high temperatures and pressures to sinter the prior particle boundaries together to form a fully dense part [115]. In the SPS process, the powder is placed in a die and is compressed in 1 dimension through the die orifice. After vacuum is pulled in the SPS chamber, electric current is supplied through the die, resulting in rapid resistive heating of the sample. The hold-times for SPS are only a few minutes in comparison to HIP, which holds for multiple hours.

Hilger et al. performed a comprehensive comparison between these three processes to characterize 14Cr steels milled in attritor mills, planetary mills, and commercial mills [137]. It was found that samples consolidated via HIP and SPS had much lower impact energies than samples formed using hot extrusion techniques; also, HIP'd specimens exhibited a bimodal grain size, which was attributed to differences in stored energy in the powder during the consolidation step. Similar results were obtained for HIP'd samples by Hoelzer et al., where extruded and cross-rolled 14YWT-SM11 (4 in. can, 850°C) was compared with 14YWT-OW4 fabricated via HIP (1150°C and 200 MPa). The authors found a large area fraction of coarser grains for 14YWT-OW4 compared to a more unimodal equiaxed distribution of nanometer scale grains with some texture for extruded 14YWT-SM11. Extrusion led to higher strength and fracture toughness than HIP with less ductility [138]. Thermomechanical treatments such as hot pressing and hot rolling were successful in refining microstructures of ODS specimens consolidated via HIP while also improving Charpy impact properties [139]. A similar study illustrated that hot rolling and high-speed hydrostatic extrusion were both successful in improving the mechanical properties of 14Cr-ODS specimens consolidated via HIP, but hydrostatic extrusion outperformed hot rolled specimens both in tensile strength and ductility [140].

Although it is quite difficult to attempt to draw conclusions about the relative proficiencies of these processing methodologies from a few comparative studies, it is possible to better understand the microstructural evolution of the powder during these consolidation and post-consolidation TMT's by considering **Figure 2.16**. As was discussed previously in Section 2.3, as the powder is mechanically alloyed significant amounts of defects are generated that accommodate the increased amounts of stored energy within the microstructure. This increased stored energy reduces the necessary thermal activation required to initiate recrystallization and grain growth phenomena. In all three consolidation processes, the temperature is increased to high temperatures to allow for powder sintering. During this thermal annealing step immediately prior to consolidation, the powder experiences recovery and both primary and secondary recrystallization phenomena resulting in the formation of a highly bi-modal grain microstructure in the powder [84, 90]. This is a very important result, since many authors erroneously attribute a bi-modal grain size to the lack of sufficient nanoprecipitate dispersions within the alloy's matrix. In many cases, the powder that is being sintered and deformed into the final alloy microstructure already has a highly bimodal microstructure due to secondary recrystallization. From this bi-modal powder microstructure, the subsequent consolidation by extrusion, HIP, or SPS results in a similar microstructure for the alloy (**Figure 2.16**). This is the reason why most extruded alloys show "larger" grained regions with significant sub-grain texture, since the pre-existing nanoprecipitates pin newly formed dislocations within the large grains during the significant deformations associated with the high aspect ratio dimensional changes in the extrusion process. After subsequent rolling treatments, the microstructure deforms and creates a preferred texture in the rolling direction; furthermore, this subsequent deformation has been shown to cause nanoprecipitate dissolution [141]. Post-rolling thermal anneals then produce preferred recrystallization orientations in the alloy.

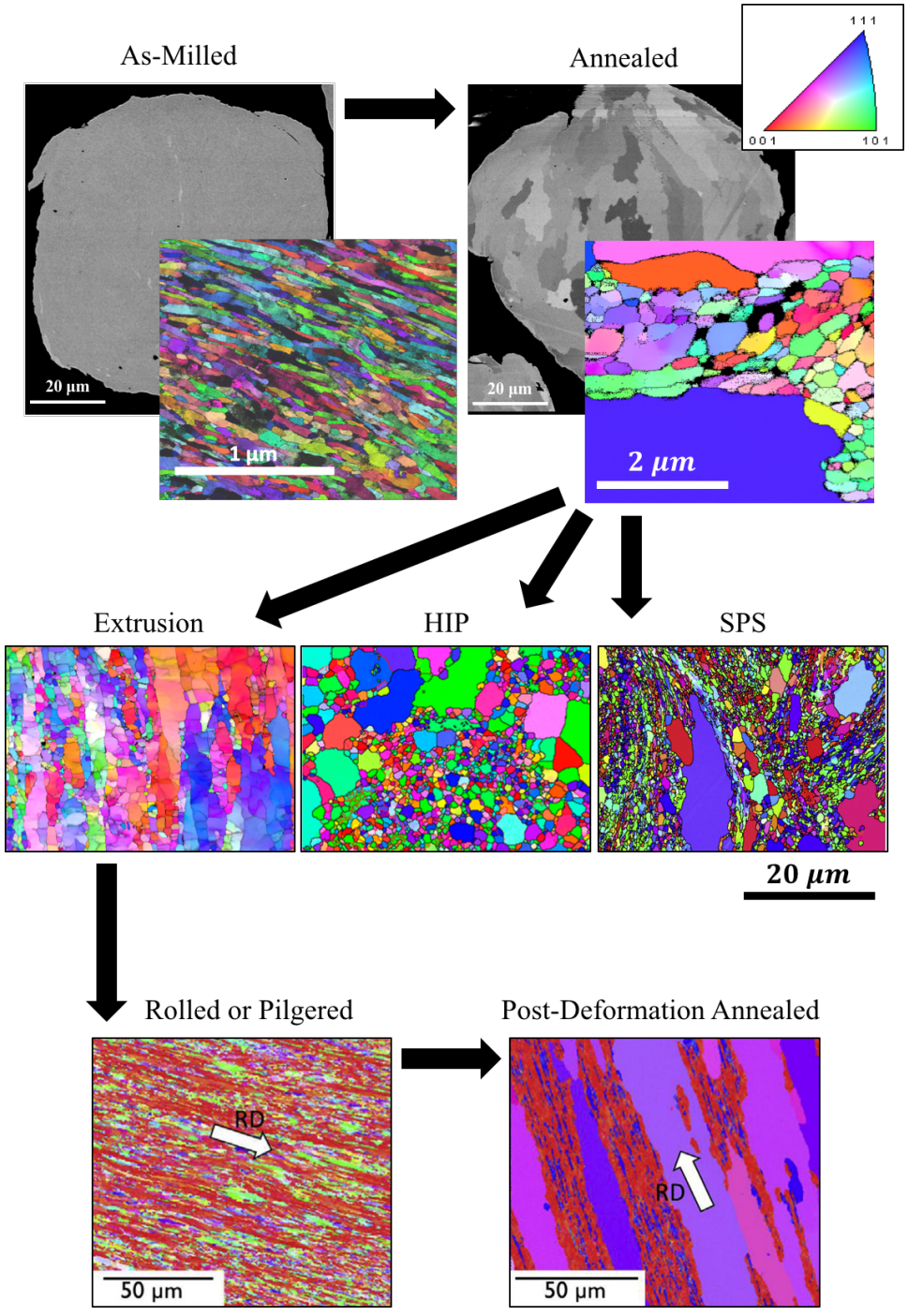


Figure 2.16. Summary of microstructural changes during ODS alloy consolidation. EBSD pole figure maps after each processing stage are reproduced from literature [62, 84, 137, 141]

2.4.4. Summary of Research Objectives

To optimize the sink strength of ODS alloys, one must know (a) the types of precipitates being formed and (b) how the sizes of these precipitates change as a function of the thermomechanical history of the component in question. The answer to (b) has been extensively reviewed through an investigation of the consolidation and thermomechanical treatments commonly seen in the conventional ODS process diagram. These factors will determine the extent to which precipitated dispersions either dissolve under significant deformation or coarsen due to significant exposure times to high temperature environments. However, the accurate determination of the types of precipitates being formed is a much more complicated question because the thermodynamics are a function of the homogeneity of the solid solution and the temperature at which precipitates are nucleating and growing. In the case of mechanically alloyed ODS materials, it is commonly assumed that all of the elements are in solid solution after the ball-milling step; however, it cannot be expected that 100% dissolution of the added oxide has occurred and it must be noted that the stored energy held by defects within the matrix vary widely across the microstructure. With these factors in mind, it is important to at least try and understand the types of precipitates so that the properties of the resultant ODS component can be understood after subsequent thermomechanical treatments.

Though authors have been investigating ODS Fe-based alloys for decades, only recently has there been investigations into the morphological and structural identity of these nanoscale precipitates. Much of the literature on the characterization of nanoprecipitates has focused on Ti-bearing ODS FeCr alloys like 14YWT. The smallest 2-4 nm nanoclusters have been claimed to have defective cubic [142, 143], orthorhombic Y_2TiO_5 [144], pyrochlore $Y_2Ti_2O_7$ [144-146], or defective/amorphous [147-149] structures, with precipitates many times deviating from expected stochiometric compositions. All of the authors have noted that nanoclusters and nanoprecipitates found within the microstructure are enriched in Y, Ti, and O, which is consistent with DFT modeling results [150, 151]. Larger oxide particles have been noted by some authors, and

it has been conjectured that the oxygen availability in the lattice strongly influences the types and morphologies of nanoprecipitates that nucleate during consolidation [151, 152]. In Al-bearing ODS alloys, precipitation becomes much more complicated, and there is wide disagreement between the types of precipitates that may exist within the matrix. A schematic representation of the types of precipitates commonly found in ODS FeCrAl literature is illustrated in **Figure 2.17** [106, 110, 111, 153-159]. This is not intended to be an exhaustive list of the phases noted in all ODS FeCrAl alloys. On the contrary, some studies such as those adding Zr or Hf to shift the types of precipitates from (Y,Al,O) to (Y,Zr,O) or (Y,Hf,O) are not illustrated in the current figure [105, 112]. This figure only covers ODS FeCrAl alloys in the compositional range of Fe-(12-20Cr)-(4.5-6)Al+(0.3-0.5)Y_2O_3 and the significant differences in experimental findings between these alloys. A variety of (Y,Al,O) phases have been identified for the fine-scale precipitates within the ODS FeCrAl microstructure. These compositions and structures include yttrium aluminum tetragonal (YAT, $Y_3Al_5O_{12}$) [159, 160], cubic yttrium aluminum garnet (YAG, $Y_3Al_5O_{12}$) [106, 161], yttrium aluminum perovskite (YAP ,$YAlO_3$) [154, 156, 158, 160, 161], yttrium aluminum hexagonal (YAH, $YAlO_3$) [158], and yttrium aluminum monoclinic (YAM, $Y_4Al_2O_9$) [110, 111]. It is surely possible that a variety of these compositions exist in the ODS FeCrAl alloys, but the significant disagreement in the current literature requires an in-depth characterization of these precipitates for the alloys investigated in this work.

It is also of crucial importance to understand differences in nanoprecipitate dispersions as a function of processing route. **Table 2.3** lists the dispersion characteristics for a variety of ODS alloys fabricated through the use of extrusion, HIP, and SPS at increasing consolidation temperature while the corresponding number density decreases. This trend is characteristic of nanoprecipitate coarsening through an Ostwald ripening mechanism. The increase in nanoprecipitate diameter as a function of extrusion temperature is well documented in literature [162]. However, authors have largely failed to quantify how nanoprecipitate nucleation, growth, and coarsening kinetics affect the as-consolidated nanoprecipitate compositions and dispersions.

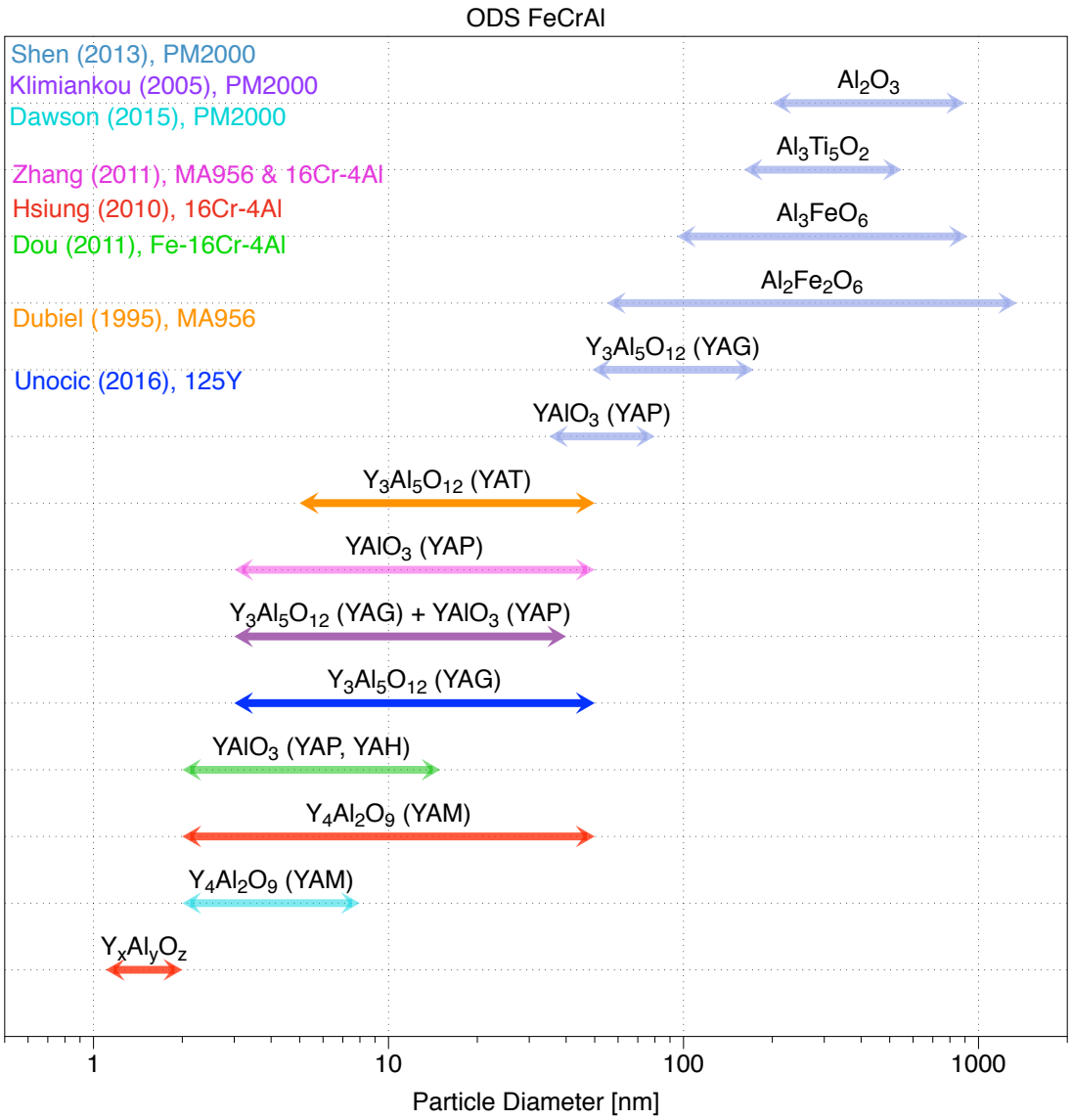


Figure 2.17. Identified phases in ODS FeCrAl alloys by various authors, color coded by study and arranged as a function of precipitate diameter [106, 110, 111, 153-159]

Table 2.3. Review of nanoprecipitate dispersions for ODS FeCr(Al) alloys in literature as a function of consolidation methodology.

Alloy Compositions		Consolidation Parameters				Precipitates		Reference
Alloy	**Designation**	**Type**	**T [C]**	**t [h]**	**P [Mpa]**	**d [nm]**	**N [x10^{23} m^{-3}]**	
FeCr	12YWT	Ext	850	1	n/a	60.0	n/a	[163]
			1150	1	n/a	3.4	4	[115]
	14YWT	Ext	850	1	n/a	2.0-2.8	1-6.9	[92, 133, 164, 165]
			1000	1	n/a	2.5	1.3	[165]
			1150	1	n/a	3.2-3.6	0.8	[165]
			1175	1	n/a	10.0	n/a	[166]
		HIP	850	3	200	1.8-2.6	10-26	[115, 164]
			1000	3	200	3.2	8	[115]
			1150	3	200	2.1-3.4	3-7	[115, 152, 164, 167]
	CEA1	HIP	1160	3	100	3.2	n/a	[137]
	CEA7	SPS	1150	0.08	76	2.8	n/a	[137]
	MA957	Ext	1150	1	n/a	2.6	7-12.6	[115, 168]
FeCrAl	PM2000	Ext	1150	1	n/a	16-28	0.005	[88, 115, 169]
	MA956	Ext	1000	1	n/a	8.9-10	0.05	[156, 159]
	ODS01	Ext	1100	1	n/a	3.2	n/a	[170]
	ODS02	HIP	1050	4	140	2.8	n/a	[170]
	K3	Ext	1150	1	n/a	5.9	0.13	[157]
	SOC-9	Ext	1150	1	n/a	6-6.7	0.17-0.3	[156, 162]
	SOC-9-ET-1	Ext	1050	1	n/a	3.2	0.92	[162]
	16Cr3Al	HIP	1150	3	200	9.8	2.1	[171]
	16Cr3Al-0.5Zr	HIP	1150	3	200	8.0	3.2	[171]
	SOC-14 (+Zr)	Ext	1150	1	n/a	4.8	0.72	[105]
	SOC-16 (+Hf)	Ext	1150	1	n/a	4.3	0.58	[112]
	125Y	Ext	950	1	n/a	~3	1.4	[99, 106]
	125YZ	Ext	950	1	n/a	2.9	2.5	[99, 106]
	125YH	Ext	950	1	n/a	3.2	2.3	[99, 106]

various temperatures. For both ODS alloys with and without Al additions, general accepted trends are noted. The average nanoprecipitate diameter increases with In the context of conventional ODS alloy processing, this extensive review of literature presented in these sections has illustrated that significant advancements in the development of ODS alloys have been made, specifically with respect to understanding (a) the role of mechanical alloying in the sufficient dispersion of elements for the homogeneous nucleation of nanoprecipitates, (b) how consolidation methodologies affect the microstructure and mechanical properties of these alloys, and (c) how subsequent thermomechanical treatments can at least partially alleviate anisotropic material properties as a function of processing path. However, there is a fundamental gap in knowledge pertaining to a theoretical understanding of how these nanoprecipitates nucleate, grow, and coarsen in these ODS alloys.

Although there appears to be a growing consensus as to the types of precipitates that form in ODS FeCr alloys with Ti additions, there is a surprising lack of understanding as to the types of precipitates that are expected in ODS FeCrAl alloys and how these precipitates coarsen during consolidation and subsequent thermomechanical processing treatments. Because legacy ODS FeCrAl alloys PM2000 and MA957 have undergone high temperature recrystallization treatments, most of the literature on these ODS FeCrAl alloys has identified much larger particles with much lower number densities. Consequently, many authors overgeneralize the distributions of precipitates in ODS FeCrAl alloys as “coarser” than those seen in ODS FeCr alloys without properly assessing the processing history of these FeCrAl alloys.

The objectives of this comprehensive parametric study have thus been specifically targeted to achieve the following outcomes:

- To assess the nanoprecipitate compositions and phases in annealed ODS FeCrAl alloy powders and consolidated alloys.
- To quantify the effect of alloying element (Zr) and impurity element (C & N) additions on the nanoprecipitate characteristics in ODS FeCrAl alloys.

- To quantify the nucleation, growth, and coarsening kinetics of the smallest nanoprecipitates in these alloys, specifically in the temperature regimes of interest for alloy consolidation and thermomechanical treatments.

The successful application of these objectives is then applied to the current ODS FeCrAl system to design a high-sink strength alloy for use in radiation environments. A combination of atom probe tomography, small angle neutron scattering, and electron microscopy are used for a multi-scale approach to address these challenges.

CHAPTER 3: Characterization Techniques

3.1. Atom Probe Tomography (APT)

Atom probe tomography (APT) is a powerful near-atomic scale resolution tool for the probing of nanoscale structures in materials. Gault has conveniently summarized the many uses of this microscopy tool, as shown in **Figure 3.1** [172]. Due to the ability of this technique to map elemental variations across a 3D control volume, it is possible to probe the compositions of nanoscale structures and elemental segregations at interfaces. In addition, due to the ability of this technique to resolve the interatomic distances between atoms, in some cases it is possible to resolve grain orientations as would be expected in high resolution electron microscopy methods. The most important aspect to APT in the study of ODS alloys, however, is the ability of this technique to study nanoscale clustering and precipitation phenomena with quantitative accuracy. In comparison to techniques such as energy dispersive X-ray spectroscopy (EDS), APT is able to accurately resolve even the lightest elements such as H, C, N, and O with quantitative accuracy.

Due to the powerful nature of this technique, APT is the only microscopy technique at a scientist's disposal for the accurate elemental investigation of precipitates in dispersion strengthened alloys. For this reason, APT has been heavily utilized in this work to analyze the precipitation of nanoscale precipitates in this work. In this section, the fundamental principle of the APT technique is presented with the respective challenges associated with accurately quantifying the identities of nanoscale precipitates in these alloys.

3.1.1. Fundamental Principles of the APT Technique

To ionize and remove an atom from a material's surface, a sufficient amount of energy must be transferred to a given atom to 1) overcome the bonding energy (Λ) between the atom of interest and the material surface, and 2) to subsequently ionize the atom so that it can interact with an applied electric field and escape the material's surface.

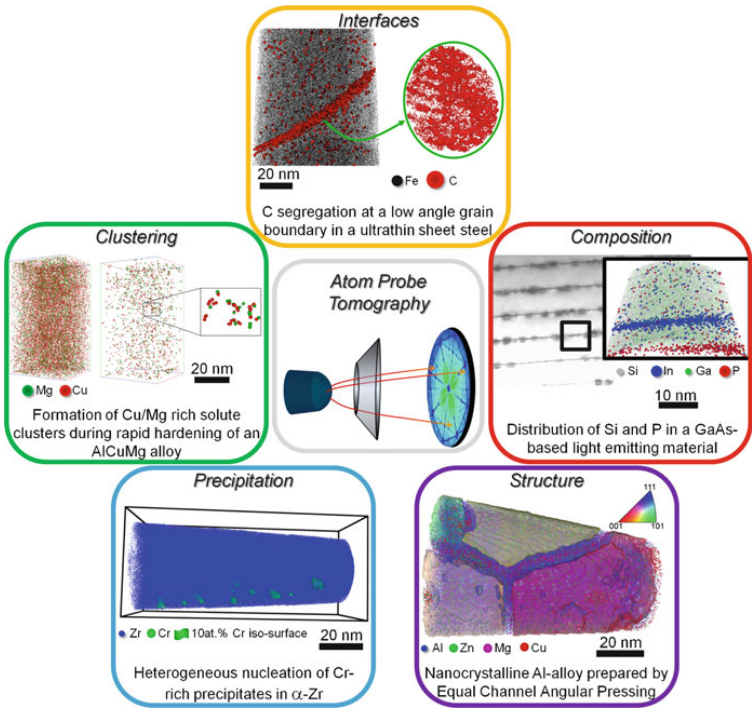


Figure 3.1. Various applications of the atom probe tomography technique for material science [172]

If the energy required to ionize the atom to an n_{th} ionization state is I_n minus the work function ($n\phi_e$) associated with the transfer of the lost electrons to the materials surface, the total energy barrier required to overcome is defined as [172]:

$$Q_0 = \Lambda + \sum_i^n I_n - n\phi_e \quad \text{.....} \quad (3.1)$$

when the material surface is subjected to a static electric field of magnitude F in a vacuum, the required energy barrier to overcome is lowered:

$$Q(F) = \mathrm{Q}_0 - \sqrt{\frac{n^3 e^3}{4\pi\varepsilon_0} F} \quad \text{.....} \quad (3.2)$$

where ε_0 is the dielectric permittivity in the vacuum and e is the fundamental charge of an electron. When this energy barrier is overcome by a supplemental pulsed electric field or laser pulse, it is possible for individual atoms to become ionized and escape the material's surface which is termed field-evaporation. It is at this point that the newly field-evaporated ion travels through the induced electric field to a position-sensitive detector. A schematic of the field-evaporation process is illustrated in **Figure 3.2**. After the ion is field-evaporated from the material surface, it travels through an electric field to a position-sensitive delay-line detector. This detector allows for the calculation of two parameters: 1) the time of flight of the ion from the instance of field-evaporation to the point where the ion impacts the detector, and 2) the X and Y coordinates on the detector where the particle collides. The position is extracted through the use of a multi-channel plate (MCP). The interaction of the ion with the MCP induces a cascade of secondary electrons that are detected by a grid of wires arranged in a X,Y coordinate grid (**Figure 3.3**). This interaction gives the position of each ion as a function of time, and thus allows for the subsequent reconstruction of each atom in the three-dimensional volume as a function of time.

The final parameter required for the determination of the identity of the field-evaporated ion is the mass-to-charge ratio. It is the mass-to-charge ratio (M) spectrum that (analyzed in a similar manner to a mass spectrum) that allows for the accurate elemental identification of various ions in the sample. To calculate M, it is assumed that all of the potential energy of the atom at the specimen apex is converted to kinetic energy as it travels through the electric field, which results in a mass-to-charge ratio that is a function of the specimen voltage (V), time of flight (t_{flight}) and the detector distance (L):

$$M = \frac{m}{n} = 2eV\left(\frac{t_{flight}}{L}\right)^2 \quad \text{(3.3)}$$

The evaporation field required to induce field-evaporation is approximated by the field at a hemispherical specimen apex with radius R. This field is a function of the

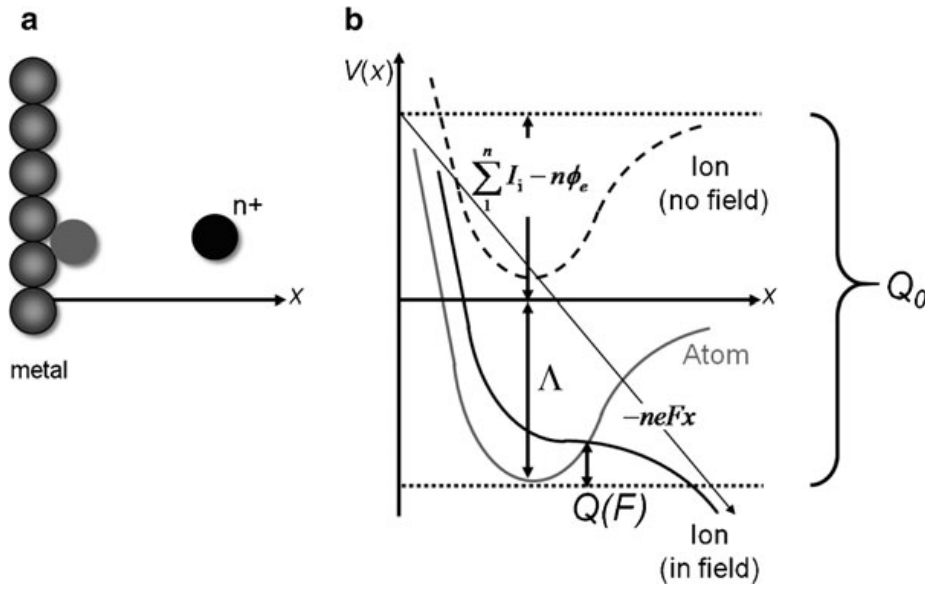


Figure 3.2. (a) a visual representation of a metal atom (grey) field-evaporated into a subsequent ion (black). (b) a graphical interpretation of the energies required to overcome with Q(F) and without Q_0 an applied electric field at the specimen apex [172].

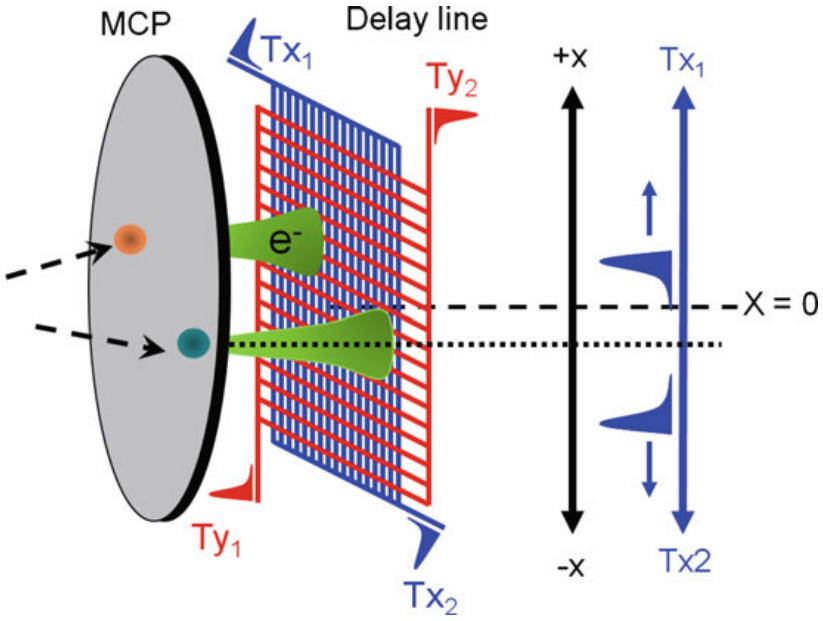


Figure 3.3. Schematic diagram of a delay-line detector commonly used for APT [172]

applied voltage and a "field factor" k_f, which is a function of the specimen shape and electrostatic environment [172, 173]:

$$F = \frac{V}{k_f R} \quad \text{..... (3.4)}$$

Although the evaporation field will theoretically vary from element to element, when reconstructing APT data the field is assumed constant. This way, the applied voltage at the specimen apex (which is directly measured over the course of data collection) can be directly related to the specimen radius as a function of time, which is how the digital control volume is reconstructed. In a similar manner to the analysis of electron diffraction patterns, the preferred field-evaporation of ions at facets within the crystal structure results in the formation of "poles" in detector hit maps. Since the interatomic distances are known and tabulated for various crystal structures, the interplanar spacing can be used to determine the field factor, and thus the specimen radius as a function of specimen voltage (and thus time). For example, consider the point density map generated for high purity aluminum by Araullo-Peters et al. in **Figure 3.4**

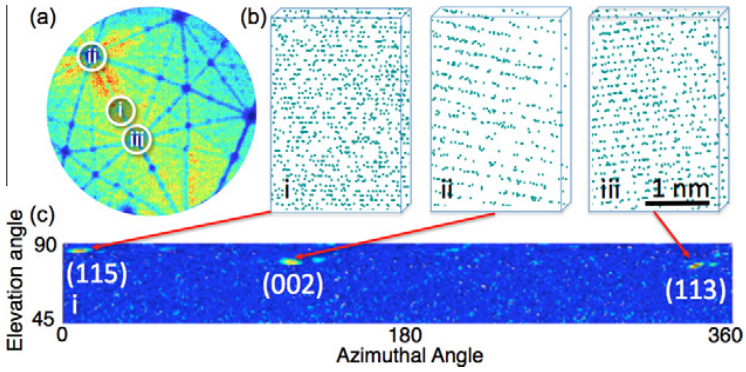


Figure 3.4. (a) point density map for high purity aluminum with three identified poles, (b) a visualization of the different interatomic planes for each identified (115), (002), and (113) poles, and (c) the corresponding Hough transform for the poles [174].

[174]. Since the voltage and evaporation field are known for aluminum, the radius can be determined by tuning the field-factor so that the interatomic distances seen in the figure match those tabulated for each pole in the FCC aluminum matrix. Once the field-factor is known, the specimen shape (R) can be accurately determined, which provides an accurate geometric specimen shape for APT reconstruction.

3.1.2. Artifacts, Errors, and Limitations of APT

Although the primary advantage of the APT technique is the ability for near-atomic scale quantitative analysis, differences in the evaporation fields of elements within nanoscale precipitates makes accurate compositional measurements quite difficult. The difficulties in analysis originate from trajectory aberrations associated with two phenomena: (1) local magnification effects for precipitates with elements of differing evaporation fields and (2) resultant spatial overlaps between the precipitate of interest and the surrounding matrix due to tip geometry induced changes in ion trajectories at the precipitate/matrix interface. To better illustrate this challenge, consider the schematic of a low-field precipitate in a high-field matrix compared with a high-field precipitate in a low-field matrix as presented in **Figure 3.5**. For the case of a low-field precipitate in a high-field matrix, when exposed to the same electric field the precipitate will field-evaporate more quickly than the surrounding matrix which results in a higher density of precipitate atoms than would be expected. As the precipitate loses atoms, the interface between the precipitate and the matrix slightly protrudes outward and the geometry of the tip changes so that a local radial curvature at the interface increases the field felt by the matrix atoms at the interface, resulting in "inward" trajectories of matrix atoms that overlap with the precipitate on the detector. For the case where a high-field precipitate exists in a low-field matrix, the precipitate evaporates at a slower rate, causing a protrusion of the precipitate locally at the specimen apex. The trajectories in this case result in outward trajectories for both the precipitate and the matrix and causes a local demagnification of the precipitate (a lower density precipitate region). In both of these

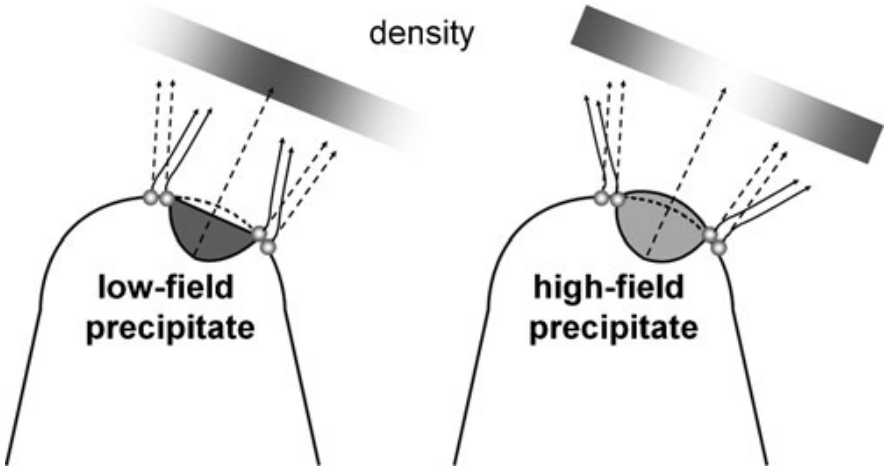


Figure 3.5. Atomic density variations associated with precipitates of varying evaporation fields in comparison to the surrounding matrix, from [172]

cases, there will be at least some overlap between the precipitate and the matrix regions on the detector and erroneous compositions measured within the precipitates [175].

Low-field precipitates (**Figure 3.5**) frequently exhibit an elongated particle morphology in the evaporation "z" direction, with compression in the perpendicular "x,y" plane due to the nature of the evaporation process. Similarly, high-field precipitates usually have a compressed "z" dimension in the evaporation direction. However, although nanoprecipitates in ODS alloys are categorized as low-field precipitates, they have been shown to exhibit a transition in particle morphology as a function of size, which has been attributed to the di-electric nature of the precipitates [176, 177].

Important consequences result from these trajectory aberrations that directly affect the validity of compositional measurements and the assumptions used for any attempted compositional corrections. For ODS FeCr alloys, there have been extensive studies on these smallest nanoprecipitates studied by APT [108, 178, 179]. The first APT studies on ODS FeCr alloys showed that the smallest (Y,Ti,O) nanoprecipitates exhibited high levels of Fe and Cr, which was directly attributed to these artifacts [180, 181]. The first model for accounting for these spatial overlaps was proposed by Blavette [175]. In this study, a reduced density was defined as the ratio between the observed atomic

density in the nanoprecipitate and the surrounding matrix. Based on this reduced atomic density ($\rho_r = \rho_{NP}/\rho_{Mat}$), the amount of matrix atoms erroneously measured in the precipitate could be determined and subtracted from the precipitate to result in corrected compositions. However, this assumption assumes that the atomic density remains constant across the precipitate in comparison to the surrounding matrix. For the pyrochlore $Y_2Ti_2O_7$ phase, this was shown to be a sufficiently good assumption [177].

Williams [178] used a different methodology to correct for erroneous Fe and Cr within precipitates in an ODS F/M steel. In his approach, the Fe and Cr contents in precipitates of increasing size were measured, and it was found that as the precipitate size increased, the Fe and Cr contents decreased and became negligible at higher particle sizes. With this information, he then asserted that because the Fe and Cr were known to be artifacts, the Fe content was subtracted fully from the precipitates and the corresponding number of Cr and other matrix elements were subtracted with the appropriate matrix fractions with respect to the number of Fe atoms removed from the precipitate. Although this technique was not based on an analytical model, it resulted in accurate Y, Ti, and O compositions relative to expected stochiometric phases [178].

Recently, Hatzoglou [177] developed a methodology for compositional correction for nanoprecipitates in ODS FeCr alloys that takes into consideration both changes in the shape of precipitates due to local magnification effects and spatial overlaps associated with the trajectory aberrations. This technique calculates the shape factor of assumed spherical or cubic precipitates (which is a function of the differing evaporation field between the precipitate and the matrix) and the reduced density of the precipitate. The composition of individual elements is then corrected with known values of the surrounding matrix composition.

For ODS FeCrAl alloys, the correction of APT compositions due to trajectory aberrations is unfortunately a more difficult task. The dual presence of Al in both the ODS FeCrAl matrix and as a primary reacting element in the nanoprecipitates means that simply subtracting the matrix from the precipitates is not a suitable approach for the removal of Fe and Cr matrix atoms from the precipitates, because doing so will also

result in the removal of Al atoms that may be statistically significant in the nanoprecipitates as well. This means that simply removing matrix atoms in proportion to the surrounding matrix composition to remove all of the erroneous Fe and Cr may not be a suitable option for ODS FeCrAl alloys like those investigated in this work.

3.2. Small Angle Neutron Scattering (SANS)

The neutron is a quite versatile subatomic particle, having the capability to both investigate the fine-scale atomic structure of materials while simultaneously providing a plethora of information about macroscale material properties. Though quantum mechanics govern neutron-nucleus interactions at the subatomic scale, in many cases the dimensions of interest are much larger than the atomistic length scale. In the case where features of interest lie in the range of 1 to 100 nm, the scattering of neutrons at small diffraction angles can be utilized to probe these larger dimensions [182]. This technique, aptly named Small Angle Neutron Scattering (SANS), measures the transmission of neutrons through a sample to determine material characteristics. The experimental setup for SANS is best illustrated in **Figure 3.6**, with the axis scales perpendicular to the beam (z-direction) exaggerated for visualization purposes [183]. As the incident neutron beam k interacts with aggregates of atoms in the specimen, the transfer of momentum between the neutron and the atomic nuclei scatter the neutron away from the incident path into a new scattering direction k_s. The difference between the incident and scattered neutron paths is known as the scattering vector $q = k - k_s$. Relating the scattering vector to the incident neutron beam allows for the quantification of q as a function of θ, as also shown in the image. Since scattering can occur in any direction, not all scattering events will be captured; instead, the transmission of scattered neutrons will be collected within a certain detector angle range ($d\Omega$) corresponding with a given surface area perpendicular to the scattering direction (dS).

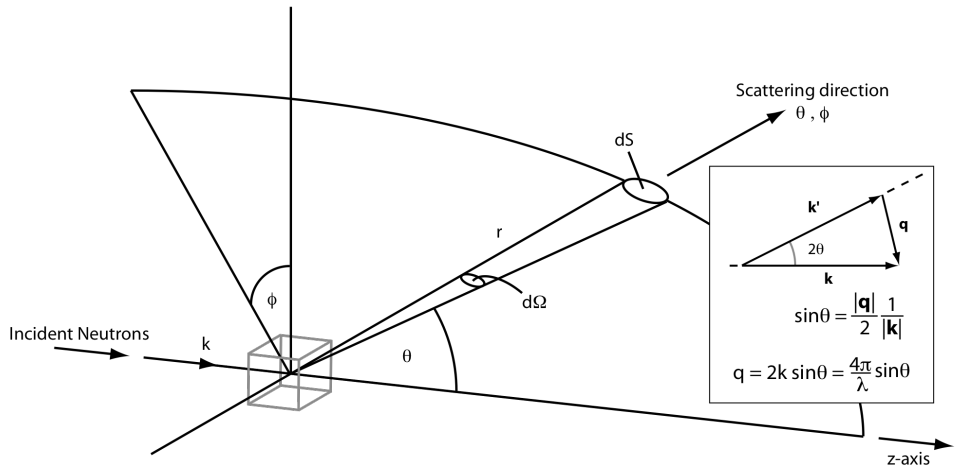


Figure 3.6. Schematic of the general approach for a small angle neutron scattering experiment [183]. A neutron beam with direction (k) is scattered across angle (θ) to calculate the resultant scattering vector (q) measured in the SANS experiment.

3.2.1. Macroscale Properties from Nanoscale Interactions

One of the major benefits of the SANS technique is that material-averaged properties can be obtained for macroscopic specimens. To put simply, in comparison to APT, which investigates control volumes on the order of several hundred nanometers, the SANS technique can provide averaged nanoprecipitate populations for samples several millimeters in thickness. Thus, the SANS technique is highly complementary to the APT technique for ODS alloy characterization.

The interaction between the incident neutron beam and the sample material is determined by the probability of neutrons to interact with the atomic nuclei as they pass through the specimen. This probability is known as a cross section, and can either describe coherent scattering, incoherent scattering, or absorption interactions. Coherent scattering is what SANS attempts to target, since it is this type of scattering that provides meaningful information about the material's structure. Incoherent scattering contributes to noise in the experiment, and absorbed neutrons are removed altogether from the beam and decrease the transmitted flux to the detector. For the purposes of the neutron

scattering experiment, the total scattering cross section (the sum of incoherent and coherent scattering) is given as:

$$\sigma_s = 4\pi < b^2 > \quad \text{(3.5)}$$

where b is the scattering length of a neutron for a particular elemental isotope. In comparison to the scattering lengths of various elemental atoms by X-rays, which is proportional to the atomic number (corresponding to larger electron clouds), the scattering length of neutrons varies widely not only between elements, but also between various isotopes of the same element. To illustrate this difference, consider the visual representation of scattering lengths for X-rays and neutrons in **Figure 3.7** [184]. Using this distinct feature, neutrons can sometimes provide better scattering contrast than X-rays for elements of similar atomic number on the periodic table [185].

Because the SANS technique is probing size ranges on the nm scale, the scattering from individual atoms is not as important as the cumulative scattering from a collection of atoms in a given control volume; consequently, the description of neutron interactions within a given control volume is expanded to include what is known as the scattering length density, ρ. The scattering length density is defined as the ratio of the scattering lengths for various atoms (b) divided by the total control volume in which the atoms comprise (Ω) [183]. Of equal importance to the scattering length density is the scattering contrast factor, denoted $\Delta\rho^2$, which is the squared difference in scattering length densities between the surrounding matrix and the scattering objects in question, assuming a two-phase system. The contrast factor is important in the fitting of SANS data as it is proportional to the scattering intensity. To put this another way, the scattering contrast is analogous to the contrast one sees in electron microscopy images: if the scattering contrast is too small, differences between the matrix and the nanoprecipitates cannot be effectively resolved and it becomes impossible to fit the data to determine the characteristics of the nanoprecipitate population [183]. The general case below can be extended easily to the matrix-nanoprecipitate system where the subscript A denotes the

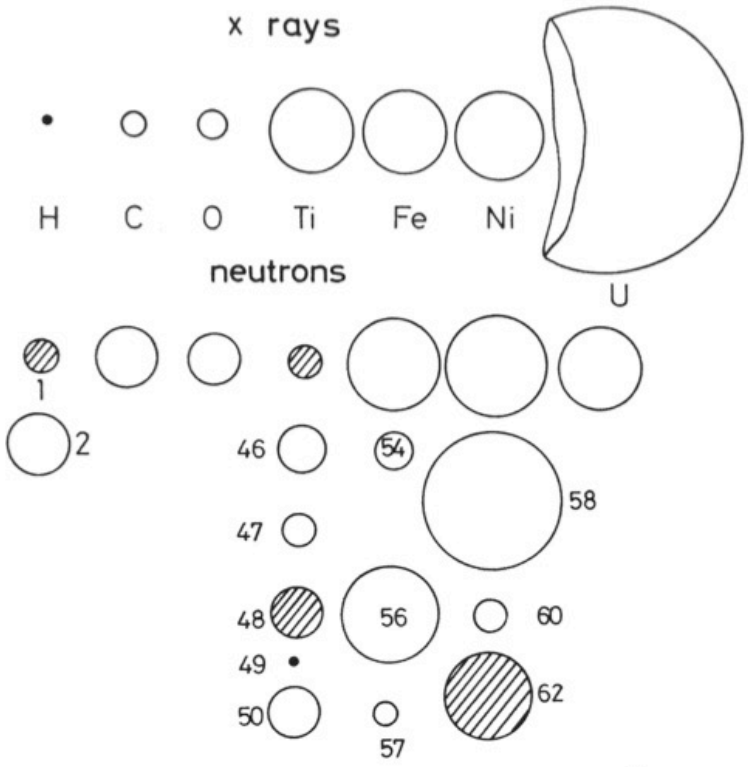


Figure 3.7. Visual illustration of the scattering lengths (b) for both x-rays and neutrons for various isotopes. Hatched symbols indicate “negative” scattering lengths, while the sizes of the circles represent the magnitude for the scattering lengths [184]. The significant changes between elements of similar atomic number allows for beneficial contrast in neutron scattering expeirments.

structural material matrix while the B subscript denotes the nanoprecipitate population. The scattering contrast can be either due to the nuclear (n) scattering of neutrons or due to the magnetic (m) scattering of neutrons with the atoms.

$$\Delta\rho^2 = [\rho_A - \rho_B]^2 = \left[\frac{b_A}{\Omega_A} - \frac{b_B}{\Omega_B}\right]^2 \quad \text{..... (3.6)}$$

The scattering intensity measured by the detector can be described by the general expression for small-angle neutron scattering [182]:

$$\left[\frac{d\Sigma}{d\Omega}(q)\right]_{m,n} = \int_0^\infty \Delta\rho_{m,n}^2 N(R)\Phi(q,R)^2 S(q, R_{HS}, \gamma_{HS})\, dR \quad \text{..... (3.7)}$$

In this formulation, $\Delta\rho_{m,n}^2$ refers to the magnetic or nuclear scattering contrast as a function of scattering length and atomic density (inverse of molar volume in Eq. 3.6). N(R) is the nanoprecipitate distribution as a function of particle size, $\Phi(q,R)^2$ is a geometry dependent form-factor for the scattering object, and $S(q, R_{HS}, \gamma_{HS})$ is known as the structure factor for the scattering object population.

The form factor, $\Phi(q,R)^2$, has been tabulated for a variety of shapes but for nanoprecipitates it is usually assumed that the scattering objects are spherical in nature [186-188]:

$$\Phi(q,R)^2 = \left\{3V\left[\frac{\sin(qR) - qR\cos(qR)}{(qR)^3}\right]\right\}^2 \quad \text{..... (3.8)}$$

Conveniently, this spherical form factor is a function only of the radius of the scattering object (R), and the scattering vector (q). The term V corresponds to the equivalent spherical volume of the precipitate ($V = \frac{4}{3}\pi R^3$).

Though routinely omitted from the analysis of nanoprecipitates in ODS alloys, the structure factor (S) is sometimes included in the SANS equation to take into

consideration multiple scattering events as a function of the distribution of scattering objects within the material. The structure factor implemented in this work comes from Pedersen's local monodispersed spheres approximation described in [189]. In this study, the structure factor was related to an equivalent hard sphere interaction radius proportional to the radius of the nanoprecipitates of interest ($R_{HS} = CR$) and a hard sphere volume fraction (η_{HS}) that is similarly related to the volume fraction of precipitates in the material (f) by [190]:

$$f = {\eta_{HS}}\Big/{\left(\frac{R_{HS}}{R}\right)^3} \quad \ldots\ldots\ldots\ldots\ldots\ldots\ldots\ldots\ldots\ldots\ldots\ldots\ldots\ldots\ldots\ldots\ldots\ldots \quad (3.9)$$

The resulting general expression for small-angle neutron scattering results in a multivariable expression with 5 unknowns for simultaneous non-linear least squares fitting. SANS results are directly compared with measured APT results to provide confidence in the APT results and to delve into the structural characteristics of the nanoprecipitates. Referencing Eq. 3.6 above, it can be seen that the scattering contrast obtained through the use of the generalized SANS formula is a function of both composition (scattering length) and structure (atomic density). Thus, it is possible to compare the magnetic and nuclear scattering contrasts to delve into the possible structures of the nanoprecipitates. This structural analysis is performed through the calculation of the A-ratio [191] (sometimes designated R-ratio by some authors) [192].

If a magnetic field is applied perpendicular to the incident neutron beam during the neutron scattering experiment sufficient enough to fully saturate the material's magnetic moment, scattering events will be generated by both the nuclear and magnetic scattering components from atoms. The generated magnetic field will result in a difference in magnetic and nuclear scattering components on the detector plane as a function of azimuthal angle (ϕ) [192], as presented in Eq. 3.10. The deconvolution of nuclear and magnetic components of scattering intensity is a maximum as the magnetic field is applied perpendicular to the incident neutron beam, resulting in a total scattering

component in the vertical direction equal to the sum of the magnetic and nuclear scattering components while the horizontal component only comprises nuclear scattering (**Figure 3.8**) [188].

$$\left[\frac{d\Sigma}{d\Omega}(q)\right]_{tot} = \left[\frac{d\Sigma}{d\Omega}(q)\right]_{n} + \left[\frac{d\Sigma}{d\Omega}(q)\right]_{m} \sin^2\phi \quad \text{.....} \quad (3.10)$$

The previously described A-ratio is then defined as the ratio between the total (magnetic + nuclear) scattering intensity and the nuclear scattering intensity (Eq. 3.11). This equation simplifies simply to unity plus the ratio of the magnetic and nuclear scattering contrasts, which are simply a function of nanoprecipitate elemental composition and atomic structure.

$$A(q) = \frac{\left[\frac{d\Sigma}{d\Omega}(q)\right]_{n} + \left[\frac{d\Sigma}{d\Omega}(q)\right]_{m}}{\left[\frac{d\Sigma}{d\Omega}(q)\right]_{n}} = 1 + {\Delta\rho_m^2}/{\Delta\rho_n^2} \quad \text{.....} \quad (3.11)$$

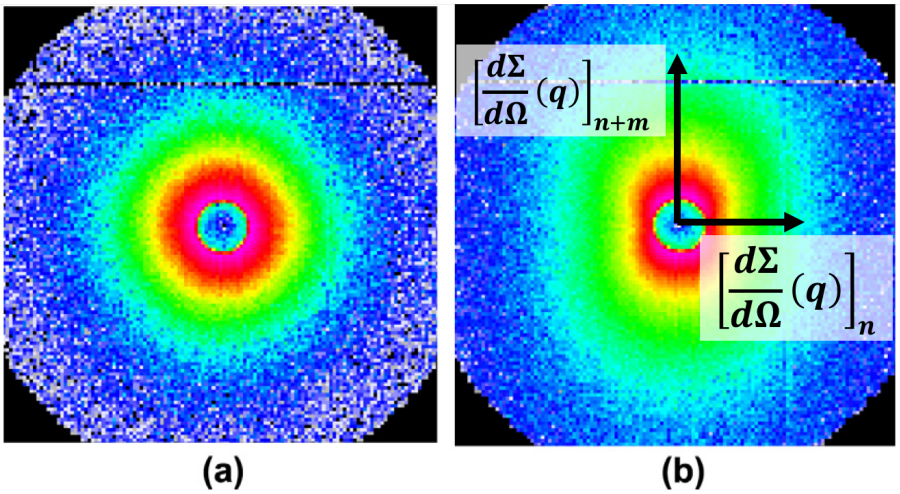


Figure 3.8. SANS detector signals in the case of (a) a sample without an applied magnetic field and (b) a fully saturated magnetic field applied horizontally and perpendicular to the incident neutron beam [188]

Using these relationships, the compositional data obtained through a detailed APT analysis can be supplemented and compared to fitted SANS distributions for the ODS FeCrAl system.

3.2.2. Limitations and Errors of the SANS Technique

The primary errors associated with the SANS technique result from the assumptions made during the fitting of the generalized SANS expression and in the interpretation of the A-ratio. Though not a substantial source of error, the accurate normalization of the incident neutron beam intensity and the subtraction of the background scattering from the sample holder and incoherent scattering contributions may alter the absolute intensity of the scattering intensity curve.

The larger source of error associated with the SANS technique is the validity of the non-magnetic precipitate assumption for the determination of contrast factors. For the study of ODS FeCr and FeCrAl alloys, nanoprecipitates are usually visualized as non-magnetic "holes" in a magnetic matrix, which allows for a simplification of the previously defined A-ratio for the accurate estimation of nanoprecipitate compositions and structures within the scattering medium [191]. Shu and colleagues have recently developed a temperature dependent SANS methodology for the study of Cu-rich precipitates in a magnetic ferritic matrix, and it was shown that this method is very efficient at estimating the magnetic nature of precipitates and the resulting validity of the non-magnetic assumptions used in the study of nanoprecipitates in Fe-based alloys [193]. Unfortunately, no temperature-dependent SANS studies to date have been performed to verify the non-magnetic nature of precipitates in ODS FeCr or FeCrAl alloys. Instead, many studies have simply used room-temperature SANS studies to calculate the A-ratios for various ODS FeCr alloys using the magnetic holes assumption [115, 170, 186, 194-196].

3.3. Electron Microscopy Methods

The electron microscope is a robust instrument that allows for the analysis of both physical and chemical properties of a material by taking advantage of the wide variety of interactions electrons make with material specimens. Due to the wide use of electron microscopy for the general characterization of materials, some electron microscopy tools have been utilized to supplement the results obtained by the APT and SANS characterization methods previously described.

The many types of interactions that can be used for microstructural evaluation using electrons are depicted in **Figure 3.9** [197]. For thin specimens transparent enough for electrons to travel through the material, the transmitted and elastically scattered electrons can be used for imaging using transmission electron microscopy (TEM). Incoherently scattered electrons can be used in TEM for the measurement of electron energy loss through the inelastic interactions, providing compositional information. The use of scanning coils to raster the electron beam across the specimen to generate an image is known as scanning transmission electron microscopy (STEM), which allows for position-sensitive compositional measurements using energy dispersive X-ray spectroscopy. Scanning electron microscopy (SEM) methods are also quite effective in microstructural evaluations of surfaces at magnifications much higher than achievable using optical microscopy. Images are formed in the SEM technique either using backscattered or secondary electrons [198, 199]. Backscattered electrons (BSE) are electrons from the incident electron beam that have made subsequent scattering interactions within the material and are able to escape the specimen through the surface, while secondary electrons (SE) are generated through the interaction of the incident electrons with the orbital electrons of the material's host atoms. When the energy transferred to an orbital electron through the inelastic scattering event between the incident electron and the orbital electron, the latter is ejected as a secondary electron. Due to the higher number of electrons with increasing atomic number, the probability of scattering also increases for a beam of incident electrons attempting to penetrate the material. Consequently, BSE imaging can provide compositional information about the

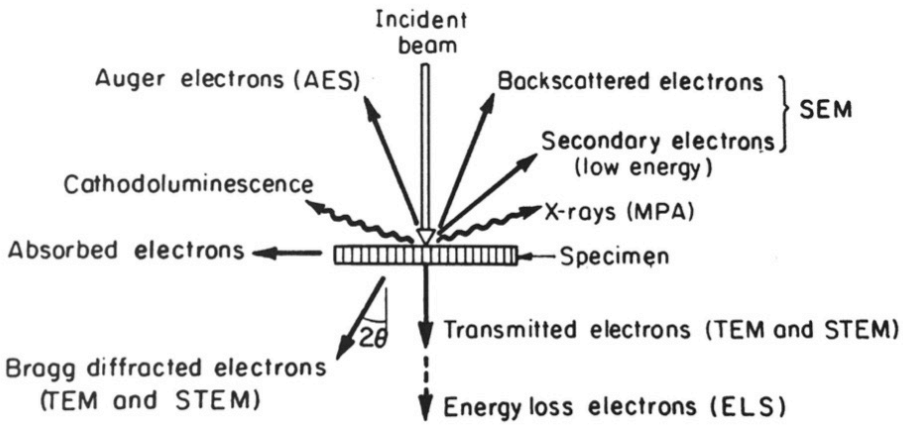


Figure 3.9. The various interactions in electron microscopy that can be used for microstructural and compositional evaluations of materials [197]

microstructure through contrast variations across the specimen. In comparison, the low energy of the secondary electrons near the surface results in a smaller surface exit depth for these electrons, meaning that any local changes in topography could result in an interaction that prevents these electrons from being read by the SE detector. An important consequence of this surface dependence is that SE imaging can be readily used for the investigation of surface topography (roughness, etched grain boundaries, etc.) for various materials.

The dual particle-wave nature of electrons also provides diffraction capabilities which allow for the identification of crystal structures using either transmitted or backscattered diffraction techniques. For scanning electron microscopy, the use of electron backscatter diffraction (EBSD) is used for crystallite sizes larger than ~50 nm to map grain orientations and to study texture [200, 201]. Orientations and crystal structure relies on comparing the observed diffraction pattern of Kikuchi bands with the orientation of poles for a specific crystal structure. To visualize this, a composite Kikuchi map for a BCC crystal is compared with the indexed diffraction bands in **Figure 3.10** [197]. The width of the Kikuchi band is related to the Bragg angle of diffraction, which can be related to the interplanar spacing of the Kikuchi band through Bragg's Law:

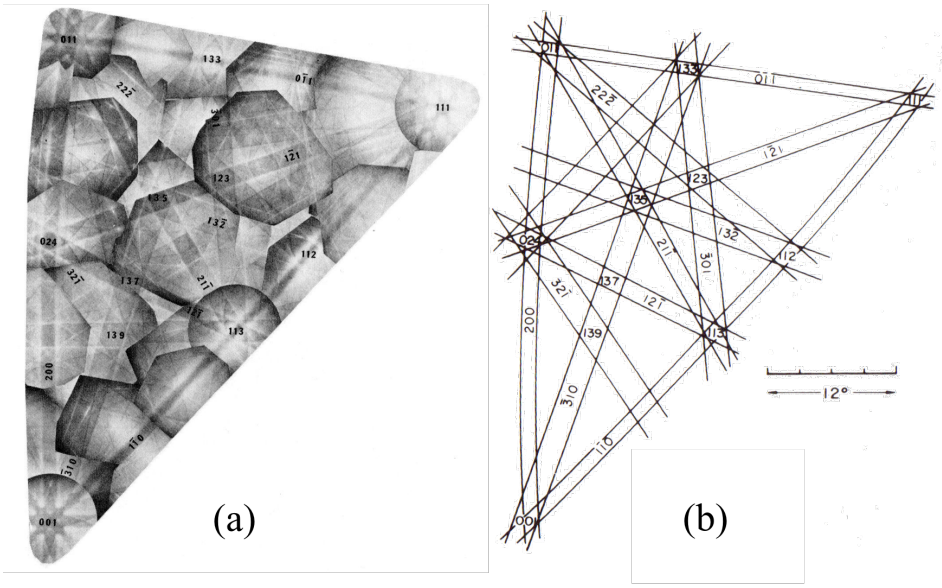


Figure 3.10. (a) a composite Kikuchi map for a BCC material and (b) the indexed diffraction bands from the composite image [197]

$$\lambda = 2d_{hkl}\sin(\theta) \quad \text{.....} \quad (3.12)$$

where λ is the wavelength of the incident electron, d_{hkl} is the interplanar spacing of the reflecting plane, and θ is the angle as a function of band width. The composite map in **Figure 3.10** also conveniently is presented in the same manner as the output inverse pole figure in EBSD outputs, showing the three major cubic poles at the vertices of the respective triangular geometry.

In addition to the generation of diffraction patterns, the interaction of the incident electron beam with orbital electrons also results in the excitation of the orbital electrons in various orbital shells. The subsequent release of energy associated with the re-filling of lower shell electrons through the jumping of electrons from higher order orbital shells results in the generation of characteristic X-rays specific to orbitals. The detection of

these X-rays and the correlation of the generated X-ray mass-spectra with various elements on the periodic table is known as energy dispersive X-ray spectroscopy (EDS).

The use of both SEM and STEM have been implemented in this work with coupled EBSD and EDS to provide supplementary microstructural analyses for both the powders and the extruded ODS FeCrAl alloys investigated in this work. For a more comprehensive description of electron microscopy methods, including TEM, STEM, EBSD, and EDS described here, the reader is referred to the many texts specializing in these techniques [197-202].

CHAPTER 4: Experimental Materials and Methods

4.1. Process Development for Powder Experiments

A comprehensive research plan was implemented to study the nucleation, growth, and coarsening of nanoprecipitates in ODS FeCrAl powders and consolidated alloys. The process diagram is presented below in **Figure 4.1**. Gas atomized FeCrAl(Zr) powders were mixed with nanocrystalline yttria (Y_2O_3) powder and mechanically alloyed to produce a supersaturated solid solution of FeCrAlZrY. The powders were then subjected to one of three thermomechanical treatments for the development of the nanoprecipitate populations. First, powder was encapsulated in quartz vials and annealed ex-situ in a box furnace for various temperatures and times. Then, either APT or room-temperature magnetic SANS experiments were performed to investigate the compositions and dispersions of nanoprecipitates in the powder. To complement this approach, the second methodology was to use in-situ SANS in a high temperature vacuum furnace to capture the initial nucleation and growth of the precipitates as a function of annealing

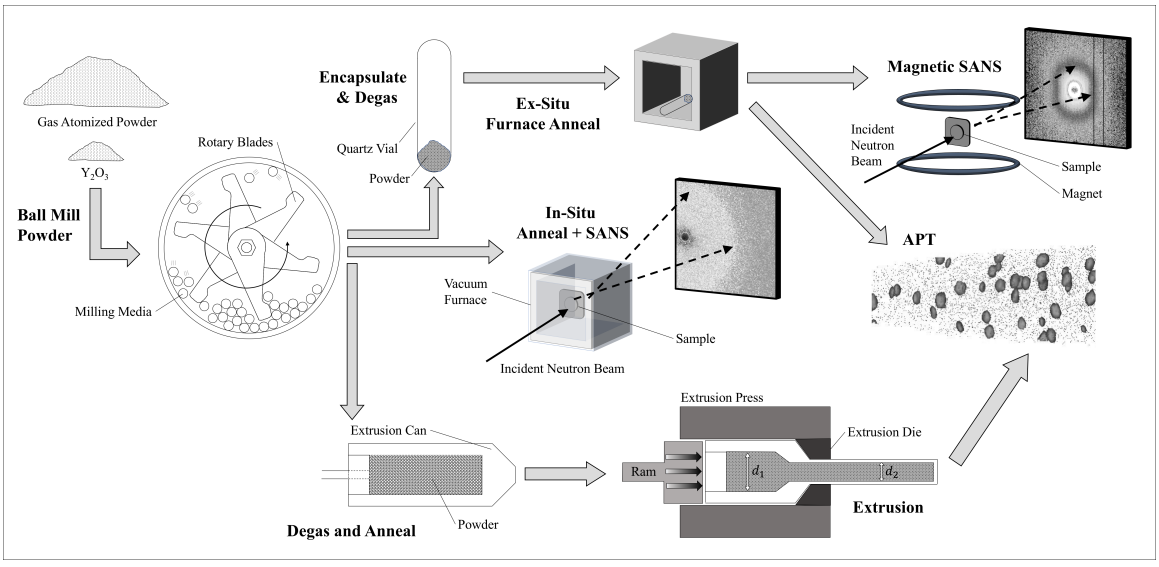


Figure 4.1. Process diagram for precipitate nucleation and growth studies in this work

temperature and time. Finally, the dispersions of the annealed powders were compared with conventional consolidated alloys through the extrusion of the remaining ball-milled powder into rods, which were also investigated using the APT technique to assess the validity of extrapolating the powder studies in this work with the wide variety of consolidated ODS alloys existing in literature to supplement the current state-of-the-art. A summary of the specimens investigated in this work are presented in **Table 4.1**.

4.1.1. Powder Composition and Mechanical Alloying

The precursor gas-atomized FeCrAlZr powder used in the entirety of this study was acquired from ATI Powder Metals and had the nominal composition of Fe-10Cr-6.1Al-0.3Zr by weight. The powder had a listed particle size distribution of 45-150μm but also contained many smaller particles as well in the as-received state (**Figure 4.2**). The gas-atomized FeCrAlZr powder composition is reported later in this work in Chapter 6 (**Table 6.1**), and was highly pure with only 0.06 at%O, 0.02 at% C, and 0.01 at% N. 99.7% of this powder was mixed with 0.3% of nanocrystalline yttria powder by weight (crystallite size: 25-50nm) which was procured from Alfa Aesar.

Table 4.1. Sample matrix used for the precipitate investigations in this work

Sample	Material	Ball Mill	Target Furnace Temp [°C]	Time [h]	SANS	APT
ZY40H	Powder	CM08	n/a	n/a		✓
ZY10C15	Powder	CM08	1000	0.25	✓	✓
ZY10C30	Powder	CM08	1000	0.5	✓	
ZY10C60	Powder	CM08	1000	1	✓	✓
106ZY10C1	Extruded	CM01	1000	1		✓
106ZY10C8	Extruded	CM08	1000	1		✓
ZY10C120	Powder	CM08	1000	2	✓	
106ZY15C	Extruded	CM01	1050	1		✓
ZY15C10h	Powder	CM08	1050	10		✓
ZY15C50h	Powder	CM08	1050	50		✓
ZY15C500h	Powder	CM08	1050	500		✓
CrAZY-H1	Extruded	CM08	1100	1		✓

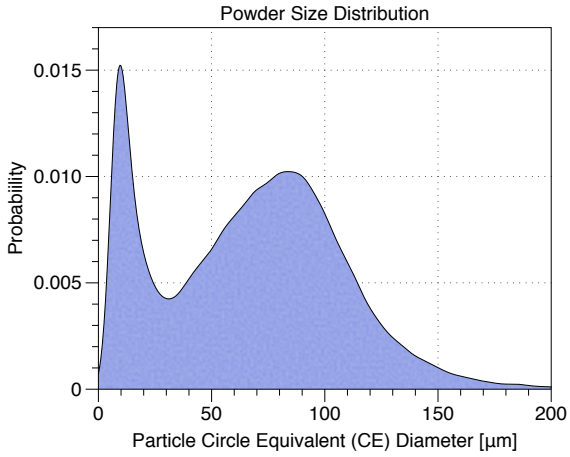


Figure 4.2. The as-received particle size distribution for the FeCrAlZr powder

The well-mixed powder was either mechanically alloyed in a high kinetic energy Zoz Simoloyer attrition type ball mill for 40h under inert Ar atmosphere using steel milling media with a ball-to-powder ratio of 10:1. Over the course of the experiments presented in this study, two different Zoz Simoloyer horizontal attritor mills were used: (1) a smaller CM01 unit with a 200g powder capacity and (2) a larger CM08 unit with a 1kg powder capacity. The two ball-mills used are housed at Oak Ridge National Laboratory (ORNL) and are illustrated in **Figure 4.3**. Milling in the CM01 ball-mill was conducted using rotational speeds alternating between 400/900rpm during the 40h mechanical alloying cycle, while milling in the CM08 ball-mill was performed at rotational speeds varying between 350/600rpm. The use of two milling speeds helped guarantee the minimization of "dead-zones" where pockets of powder may have experienced a lack of sufficient alloying. Furthermore, the use of higher rotational speeds for the smaller unit was intentional and implemented in an attempt to narrow the differences in milling media kinetic energy at the rotating attritor blade tip so that similar energy deposition existed in powders milled in the two different units. Although all of the annealed powder studies were performed on the exact same heat of milled powder performed using the CM08 milling unit (all powders with a "ZY" prefix in **Table 4.1**), two extruded alloys were created using milled powder from the smaller CM01 unit.

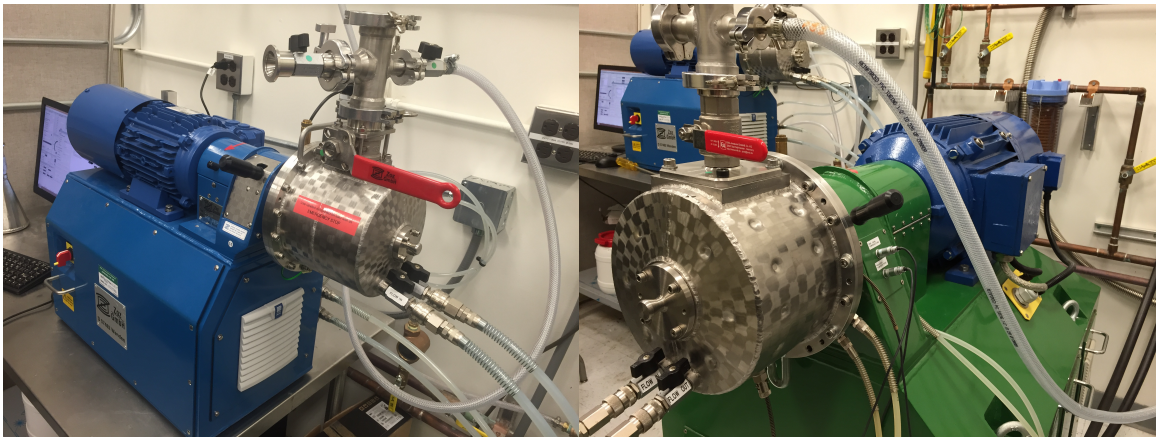


Figure 4.3. The (a) CM01 and (b) CM08 high kinetic energy Zoz Simoloyer ball mills utilized for powder mechanical alloying

Although two different mechanical alloying devices were used in these comparative studies, a detailed analysis of similarities and differences between microstructures and precipitate distributions is presented in the following section. This analysis shows that a direct comparison can be made between alloys fabricated using both mechanical alloying units without significant experimental errors.

4.1.2. Powder Packaging/Encapsulation and Annealing

The mechanically alloyed FeCrAlZrY (CrAZY) powder (sample name ZY40H indicating 40h of milling time) was prepared for subsequent thermal annealing treatments by either encapsulation in quartz vials, SANS powder packets, or in an extrusion can for consolidation.

For powders prepared for ex-situ annealing treatments, 20g powder samples were placed in quartz vials, evacuated to pressures below 10^{-4} Torr using a mechanical pump, and sealed. The size of the quartz vial was purposefully designed to exceed the height required to hold the powder volume so that the applied heat flux at the orifice of the vial using a propane torch would not induce premature nucleation of nanoprecipitates in the powder. The encapsulated quartz vials were then heated in either a box furnace (for 1000°C annealing treatments) or in a tube furnace (for 1050°C annealing treatments).

Both furnaces were calibrated to ensure that heat treatment was being performed at the target temperature. The quartz vials were placed in the furnace already at the target temperature, left for the duration of the annealing time, and then quickly removed and quenched in a room temperature water bath. Images of both the quartz vials and the box furnace used for the annealing treatments are presented below in **Figure 4.4**.

One potential source of error in isothermal annealing treatments is the erroneous assumption that the powder remains at the target temperature for the duration of the annealing experiment. This is a highly erroneous assumption for shorter annealing times due to the time required for the powder to heat to the target temperature. For alloys extruded at ORNL, the extrusion can holding the powder charge was placed in an identical manner in a furnace held at the target temperature. Thus, to give a better estimation of the heating profile of both the quartz-encapsulated powders and alloys heated for short annealing times (~1h for extrusions), 400g of the ZY40H CrAZY powder was placed in a 2" (5cm) outer diameter (OD) extrusion can with a thermocouple placed in the center of the compacted powder volume. The extrusion can was then placed in the same furnace used for pre-extrusion annealing treatments at ORNL, with the furnace held at a target temperature of 1000°C. The temperature profile was then recorded as a

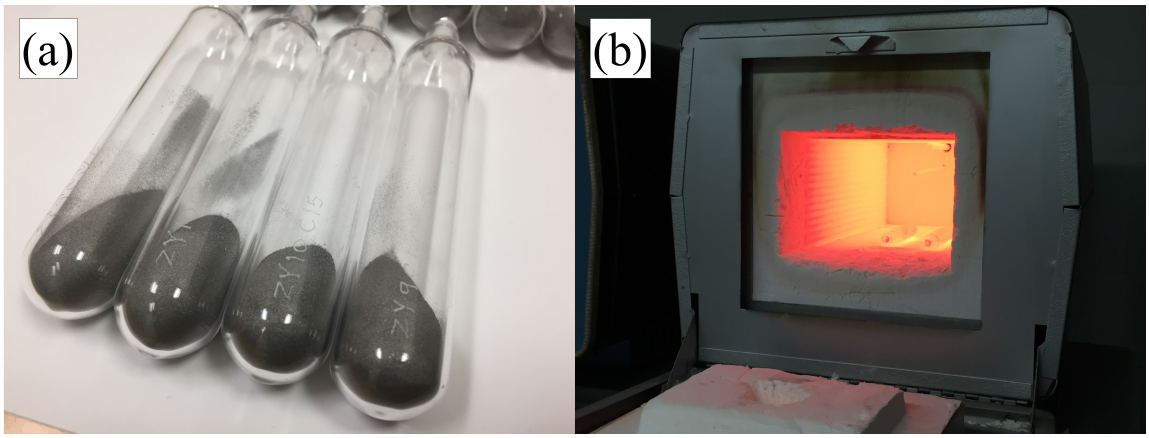


Figure 4.4. (a) encapsulated CrAZY ZY40H powders in quartz vials and (b) the box furnace utilized for ex-situ powder annealing treatments

function of heating time to establish a more accurate powder temperature history (**Figure 4.5**). As can be seen from the figure, over a third of the annealing time is characterized by powder temperatures less than the target temperature. The same thermocouple measurement was not feasible for powder encapsulated in the quartz vials due to the evacuated nature of the sample, and a thermocouple adhered to the outside of the sample would provide an over-estimated heating rate for the powder. An assumption is thus made for the current experiments that the heating profile of the ex-situ annealed powder samples matches that of the powder packed in the extrusion can. Because of the smaller sample charges in the quartz vials, the heating rate is expected to be slightly higher than for the larger powder charge measured in the extrusion can, which is described in detail using the lumped capacitance approximation for sample heating in the Appendix. However, as will be discussed later in this work, the increase in heating rate does not affect the subsequent discussion or the resulting conclusions presented in this work. Nevertheless, the use of this time-dependent heating profile is a much better approach than a simplified isothermal assumption.

Sample preparation for the ex-situ and in-situ SANS experiments required the compaction of powder into small powder-packets (**Figure 4.6**) made of either aluminum or molybdenum foil. For the ex-situ SANS experiments conducted at room temperature, simple aluminum foil was used due to the affordability and ease of workability of the foil. However, for the in-situ heating of ZY40H powder to 1000°C, the melting point of the aluminum foil disqualified this packing material from being used; consequently, molybdenum foil was used to create the powder packets. Both powder packets were prepared using a spherical die to form a 1cm diameter indentation in the foil measuring 1mm in thickness. The cross sectional area of the circular 1cm OD packet was designed so that the entirety of the powder was exposed to the neutron beam, since the applied magnetic field may have shifted the ferromagnetic powder within the control volume being analyzed.

Finally, to compare the ex-situ annealed powders to the vast ODS alloy literature investigating nanoprecipitate dispersions and compositions, extruded alloys were

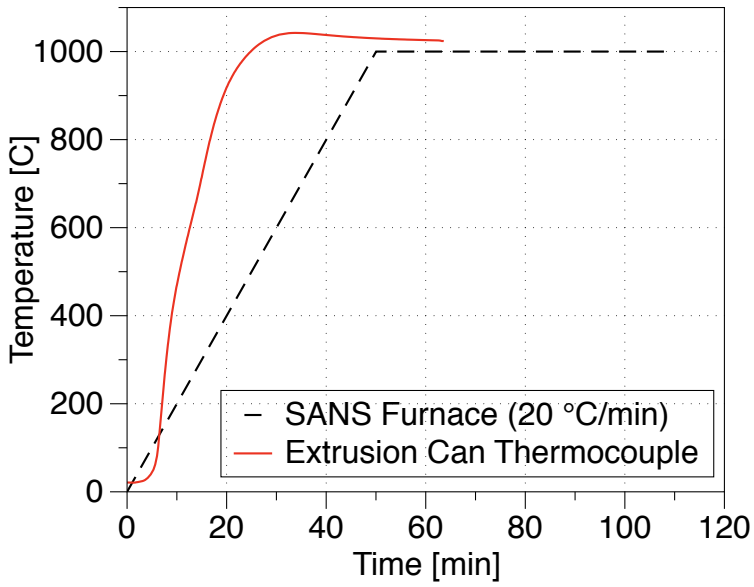


Figure 4.5. The measured powder temperature profile (red) for ZY40H powder packed in a 2" extrusion can heated in a box furnace used for pre-extrusion annealing treatments and (b) the powder temperature profile experienced by the powder in the in-situ SANS experiment. [203]

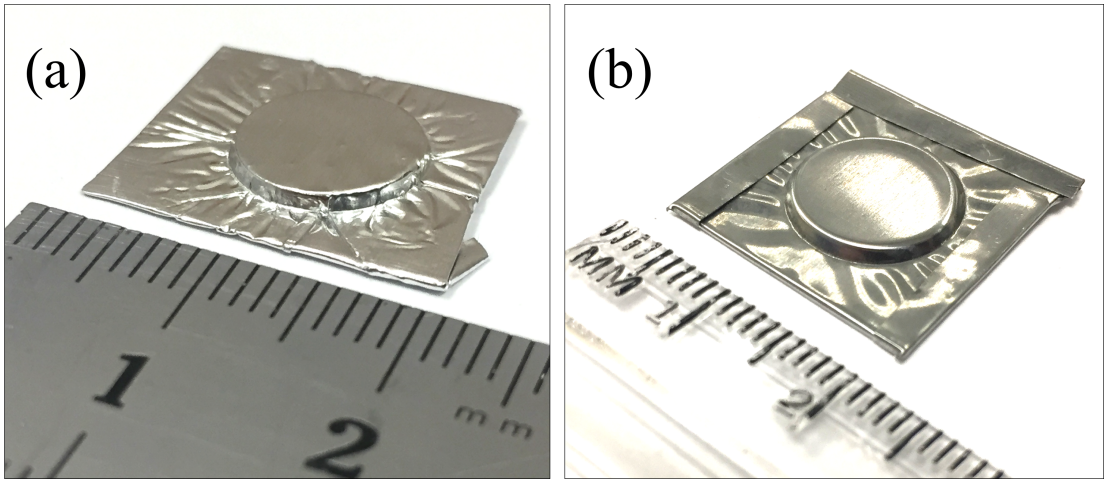


Figure 4.6. (a) Aluminum and (b) Molybdenum foil packets used for powder encapsulation for ex-situ and in-situ SANS experiments, respectively.

prepared for a select samples. Mechanically alloyed CrAZY powder was packed into either 2” (5cm) OD extrusion cans (for 1000°C or 1050°C consolidation temperatures) or into 3.9” (9.9cm) OD extrusion cans (for consolidation at 1100°C). The latter larger extrusion can was used to create a master rod for thin-walled tube production efforts on large-batch ODS FeCrAl alloys, which is the primary reason for the change in powder size [204]. It is also important to note that for the different extruded alloys, different heats of ball-milled CrAZY powder were used, which influenced slightly the levels of C and N in the resultant extruded alloys. For direct comparison with the ex-situ powder annealing treatments (all milled in the CM08 Simoloyer unit), the exact same powder was used for the extrusion of the 106ZY10C8 alloy extruded at 1000°C. The CrAZY_H1 alloy extruded at 1100°C was also milled in the CM08, but was milled at a later time and exhibited a lower N content. Alloys 106ZY10C1 and 106ZY11C extruded at 1000°C and 1050°C, respectively, were both milled in the CM01 Simoloyer unit. The chemical compositions of the ball-milled ZY40H powder and the compositions of the extruded alloys were all sent for chemical analysis by the company DIRATS, and a summary of the chemical compositions are provided in Chapter 6 (**Table 6.1**).

4.1.3. Focused Ion Beam (FIB) Specimen Preparation

A dual beam FEI Quanta focused ion beam (FIB) at the low activation material development and analysis (LAMBDA) laboratory at ORNL was utilized for all atom probe atom probe tomography specimen lift-outs in this work [205]. The APT specimens were prepared using a lift-out procedure previously developed by Miller [206], where high energy Ga ions (20kV) are used to mill away material and allow for the removal of a specific region of material that is subsequently “landed” on a grid of silicon micropillars for further sharpening to the needle-shaped tips characteristic of APT specimens. The FIB liftout procedure used to remove and land APT specimens in targeted fine-grain and coarse-grain regions in sample ZY10C60 is illustrated in **Figure 4.7**. Subsequent annular milling stages are used to mill away material in a concentric pattern with decreasing inner diameters with increasing milling time. A final lower-energy (5kV) Ga ion

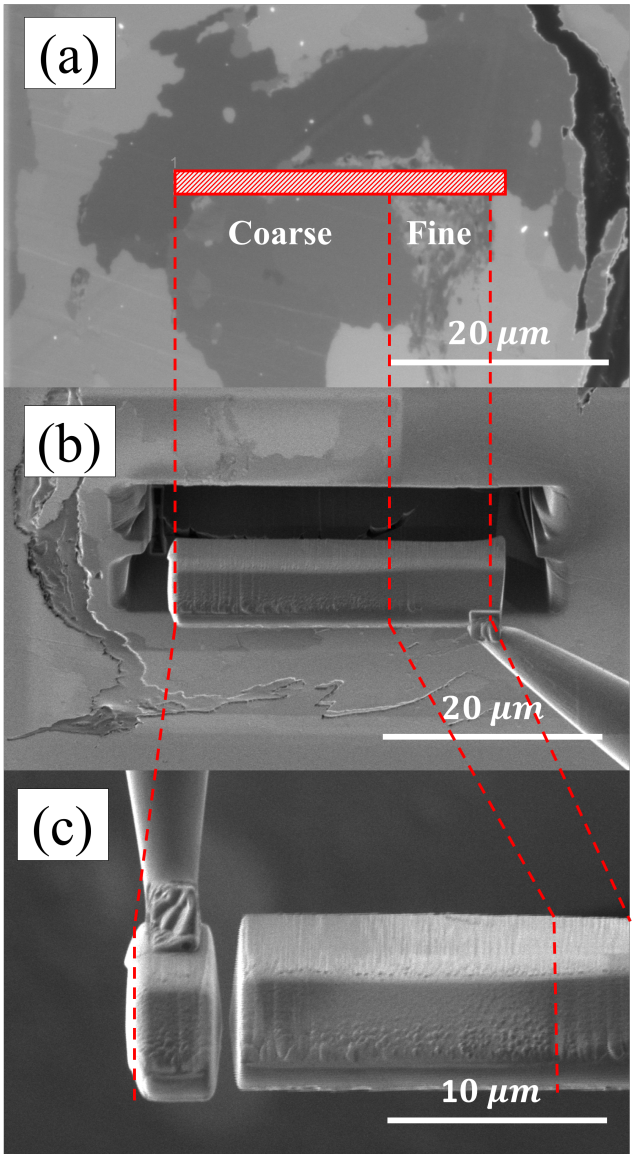


Figure 4.7. (a) An SEM-BSE image of a targeted FIB lift-out region for coarse and fine grain APT measurements in annealed ODS FeCrAl powder, (b) the corresponding lift-out from the same region, and (c) the landing and sectioning procedure used to prepare each APT sample from the coarse and fine grained regions.

cleaning/polishing step was used to minimize Ga implantation in the APT specimen, since Ga is strongly attracted to grain boundaries of Al-containing materials during sample preparation [172]. The final tip sharpening was either performed on the previously mentioned FEI Quanta at ORNL or using a FEI Helios 600 FIB housed at the Max-Planck-Institut für Eisenforschung (MPIE) in Düsseldorf, Germany. All FIB preparation for both APT and TEM samples (described in subsequent sections) were performed at room temperature.

4.2. APT Data Collection and Analysis

Following the lift-out and sharpening procedures previously outlined, the APT specimens were transferred immediately to a high-vacuum environment (10^{-8} Torr) to minimize sample oxidation and degradation in air atmosphere. For APT data collection, one of three different Cameca local electron atom probe (LEAP) models were utilized. The 4000X HR is a reflectron-type flight path atom probe with a detection efficiency of 36%, and is housed at the Center for Nanophase Materials Science at ORNL. The model 5000 XR is also a reflectron-style LEAP but has a 52% ion detection efficiency. The 5000XR LEAP used for much of the APT work in this work was performed at MPIE in Germany. Finally, a straight-line flight path model 4000X Si LEAP (50% detection efficiency) was also utilized at Northwestern University.

The primary differences between the two types of atom probes are characterized by the flight paths of ions as they traverse through the induced electric field to the detector. The straight-line flight path detector allows for a wider field of view and a more efficient collection of ions by the detector. In comparison, the reflectron model LEAP allows for a longer time of flight and thus a better resolution in the mass-to-charge ratio spectrum at the expense of a lower detection efficiency and a smaller field of view [172, 207]. A visual comparison of these aspects is presented in **Figure 4.8**.

Of particular interest is the effect of the varying detection efficiencies on the compositional measurements of the nanoprecipitates in the ODS FeCrAl alloys investigated in this work. For these ODS alloys, there are many peaks associated with the

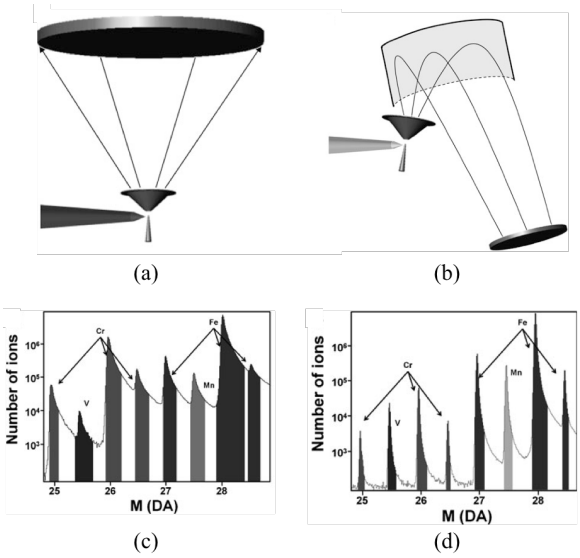


Figure 4.8. Visualization of the flight paths of the (a) straight line 4000X Si and (b) reflectron model 4000X HR and 5000 XR atom probes. Also shown are example representative mass-to-charge ratio spectra for the (c) straight-line and (d) reflectron LEAP models.

various elements and molecular ions field evaporated from the tip, so the mass-resolution must be sufficient for the identification of important peaks for accurate elemental identifications. The detection efficiency is a direct measure of the number of ions measured by the detector in comparison to the total number of field-evaporated ions. This means that a detection efficiency of 36% results in the loss of 63% of all of the atoms in the sample. Although sample reconstruction procedures and compositional analysis procedures account for the detection efficiency deficit, compositional measurements can be affected if certain elements are preferentially lost in a disproportionate manner in comparison to the rest of the atoms in the control volume. Thus, multiple fine-grained samples of the same ZY10C60 sample were measured using all three different LEAP models previously mentioned.

All APT data collection was performed in laser-pulsing mode using a 32pJ laser pulsed at a rate of 200 kHz. Laser mode involves applying the laser pulse atop the static applied electric field, which is one of two methodologies to apply the pulsed energy necessary to field-evaporate ions at the tip of the APT specimen. The other methodology is known as high-voltage pulsing mode, which involves the high-speed fluctuation of the

electric field at the tip to achieve the same result. For ODS materials and other materials that are prone to premature tip fracture in high-voltage pulsing mode, the laser-pulsing mode allows for longer run times and larger control volumes for analysis; however, the laser pulse must be carefully chosen so that the mass-spectrum is not affected by "thermal tails" associated with the ability of the tip to dissipate the heat applied to the sample by the pulsed laser [172]. The APT specimens were kept at a temperature of 50K for the collection of all data, and the target detection efficiency (the number of atoms field-evaporated per pulse) was fixed at 5 ions per 1000 laser pulses to maximize the number of single-ion hits on the detector. For all specimens, a minimum of 10 million collected ions were detected to ensure accurate sample statistics. A complete list of APT specimens that will be discussed in this work are presented in the Appendix in **Table A.1**.

4.2.1. Sample Reconstruction Parameters

After the initial data collection, an accurate 3D representation of the control volume must be reconstructed so that an accurate representation of the cluster dispersion and geometries can be assessed. This data reconstruction and analysis was performed using Cameca's Integrated Visualization & Analysis Software (IVAS) package (version 3.6.8) [208-211]. The technique used for sample reconstruction in IVAS utilizes the voltage curve as a function of collected atoms (and thus time) to estimate the APT tip radius as a function of depth in the evaporation direction. From Eq. 3.4, it was shown that the tip radius is proportional to the applied voltage at the tip apex, assuming that the field-factor and the evaporation field remains constant. Thus, by knowing the field factor for the primary constituent element in the material being investigated (F = 33 V/nm for Fe) one can determine the radius of the assumed hemispherical tip apex as a function of specimen depth.

An example voltage curve for a ODS FeCr alloy MA957 is illustrated in **Figure 4.9(a)**. From this voltage curve, a small region can be chosen to view the detector events of ions that have been field evaporated in the chosen area. As shown in in **Figure 4.9(b)**, the detector event histogram in many cases shows the crystallographic poles for the host

material due to the preferential field evaporation of atoms at the kinks associated with the crystallographic structure. At these locations, the field factor (k_f) can be tuned for the reconstructed sample since the evaporation depth is proportional to the field factor and two constants (the material's evaporation field and the image compression factor, which are 33 V/nm and 1.65 for the standard reconstruction parameters of an Fe matrix in IVAS). After the interplanar spacing has been used to calibrate the field factor, the tip radius is known as a function of voltage and the sample can be reliably reconstructed into the final APT control volume to be further analyzed by the software. in **Figure 4.9(a)** illustrates a small control volume in the reconstructed MA957 sample showing black Fe atoms as the background matrix atoms (with (110) atomic planes highlighted). Also shown in this figure is a nanoprecipitate enriched in Y, Ti, and O.

Unfortunately, the identification of poles can be quite difficult for ODS FeCrAl alloys, since the addition of Al results in a deterioration of the resolution of the detector histogram. For example, in **Figure 4.10** two detector histograms are presented for a CrAZY powder (ZY10C60) and a Fe-14Cr alloy (OFRAC). For the ODS FeCr alloy, a clear (110) pole is noted with corresponding lines of crystal plane symmetry, while the lines are almost invisible for an APT specimen with a highly similar orientation. Luckily, poles were identified for all of the ODS FeCrAl alloy powders and extruded rods investigated in this work which allowed for accurate reconstructed tip geometries for all specimens.

4.2.2. Cluster Identification

The identification of nanoprecipitates within the reconstructed control volumes was performed using the maximum separation method built into the IVAS software package [208, 210, 211]. This method uses two parameters to identify statistically significant clusters within the volume: (a) d_{max}, the maximum separation distance between atoms considered to be in a given cluster, and (b) N_{min}, the minimum number of atoms in a given cluster to be considered a statistically significant precipitate.

The first step in the maximum separation method is to determine which ions are

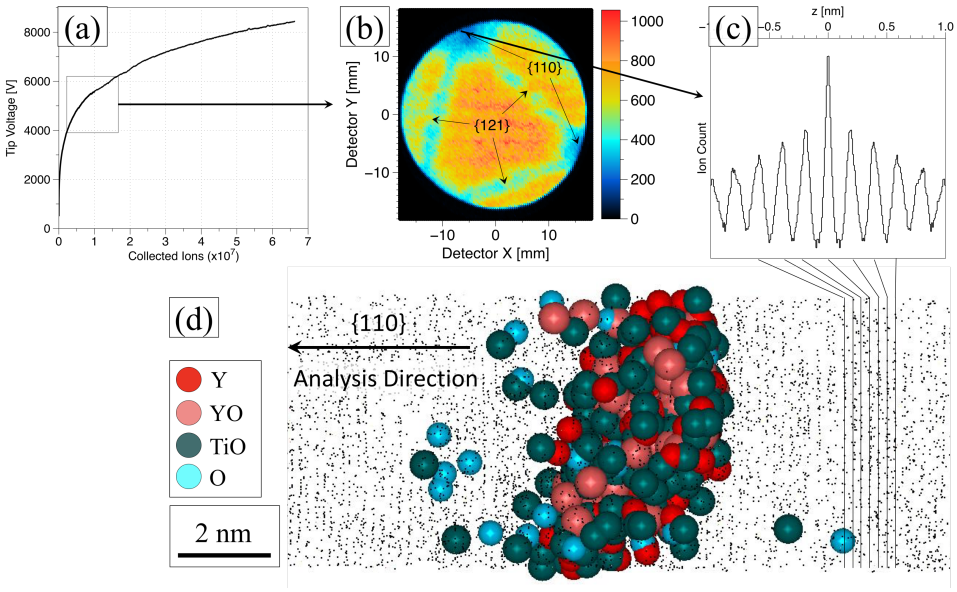


Figure 4.9. The basic steps for tip reconstruction using a standard voltage reconstruction procedure using ODS FeCr alloy MA957 as an example. (a) a portion of the voltage curve is chosen, (b) crystallographic poles are identified using the detector event histogram, (c) based on the crystallographic pole, the interplanar distance is tuned through the tuning of the field factor and the tip radius, which results in (d) a reconstructed control volume where the interplanar distances at specified poles match the expected interplanar distances for the material.

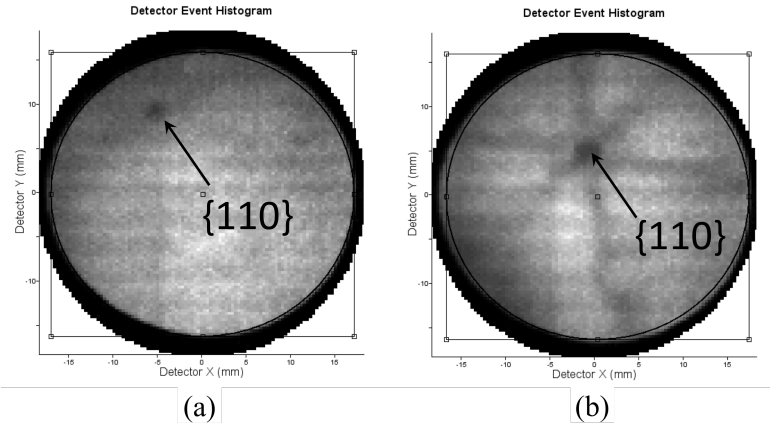


Figure 4.10. Detector event histograms for (a) an ODS FeCrAl CrAZY alloy and (b) an ODS Fe-14Cr alloy, showing the same type of (110) pole.

actually clustering together to form the precipitates. Luckily for the ODS FeCrAl alloys in this work, the ions that appear to qualitatively cluster together are Y, YO, and AlO. Thus, the collection of these ions together were used in the maximum separation algorithm for the remainder of the steps required for cluster identification. Next, a nearest neighbor distribution is computed that compares the average distances between these ions in comparison to a randomized distribution of these atoms in solution. In practice, the intersection of these two curves is used to determine the initial value of d_{max}. Choosing a value less than this will omit larger clusters later in the algorithm, but choosing a greater d_{max} will instead result in the erroneous inclusion of more diffuse clusters that may not in-fact be statistically significant since the population will tend toward the randomized distribution. Next, a cluster size distribution is calculated using the initial d_{max} value as an input. This provides a comparison of the number of identified clusters of the given size in comparison to the randomized distribution. The number of clusters exceeding the number calculated in the randomized distribution provides an initial estimation of the N_{min} value. Using the d_{max} and N_{min} values determined from steps 1 (**Figure 4.11(a)**) and 2 (**Figure 4.11(b)**), the number of clusters is calculated again in comparison to the randomized distribution of atoms, providing a new value of d_{max} (**Figure 4.11(c)**). Finally, a second iteration of the cluster size distribution with the new maximum separation distance is used to establish the final value of N_{min} (**Figure 4.11(d)**).

4.2.3. Mass-Spectrum Peak Identification

After the specimen has been accurately reconstructed and the clusters have been identified, accurate compositional measurements must be made for the entire (global) control volume, the matrix (without precipitates), and the clusters themselves. The accurate compositional estimation of these parameters requires an accurate binning of the mass-to-charge ratio spectrum. Although the APT technique is a powerful tool for elemental quantification due to its ability to detect even the lightest elements, there are multiple elemental isotopes with various charge states that exhibit the same peak locations on the mass spectrum. This results in peak-overlaps in the mass spectrum that

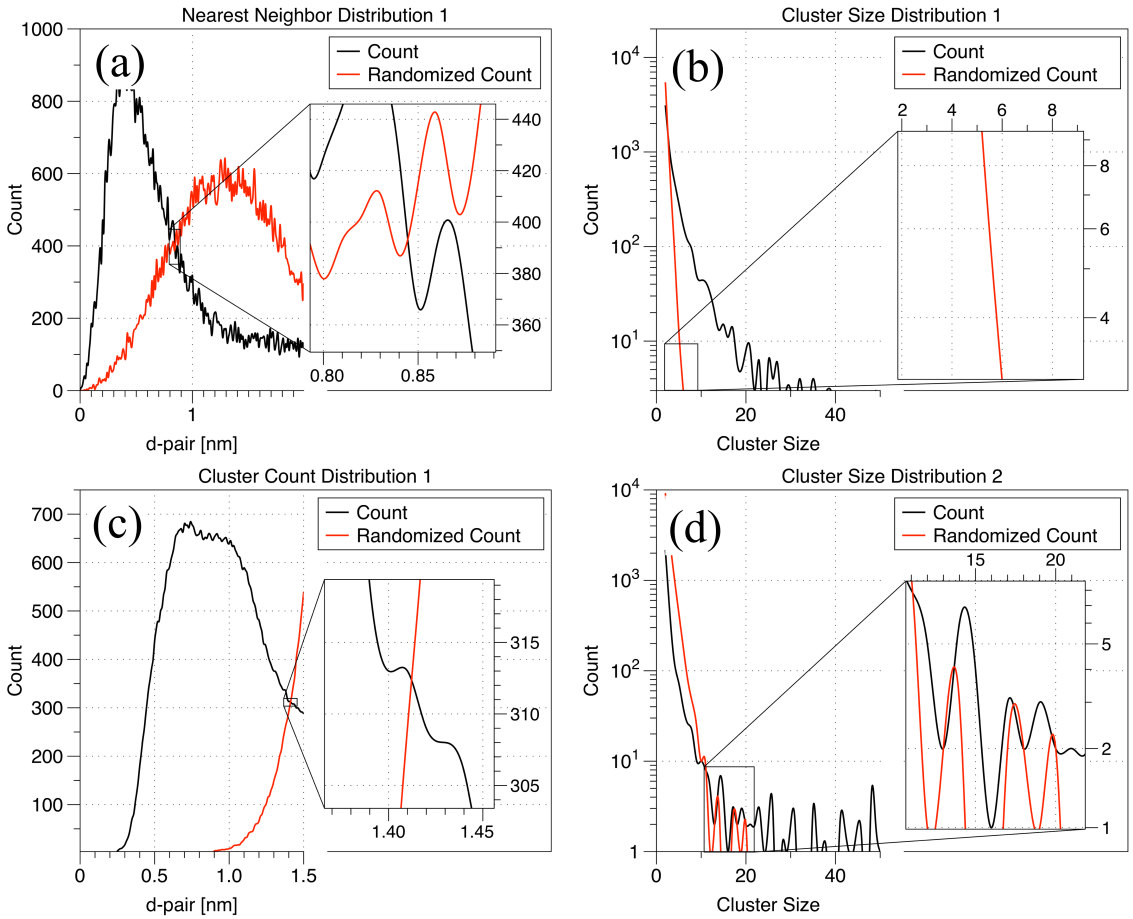


Figure 4.11. The (a) nearest neighbor distribution, (b) cluster size distribution, (c) cluster count distribution, and (d) final cluster size distribution used for the optimization of the d_{max} and N_{min} parameters of the maximum separation method for statistically significant cluster identification.

can lead to erroneous compositional measurements. A portion of the mass spectrum for a ZY10C60 specimen containing both (Y,Al,O) precipitates and Zr-rich precipitates is shown in **Figure 4.12**. In this figure, many peaks associated with individual and some molecular ions are shown, with vertically listed elements indicating peaks associated with possible peak overlaps. In the IVAS software, it is not possible to assign multiple ions with one peak, so the user must choose one of these elements to represent all of the atoms represented by the area under the peak curve. Luckily, the IVAS software also has a built-in peak deconvolution algorithm that assumes natural isotopic abundances of isotopes for each element to provide accurate bulk compositional measurements [172, 207]. However, this deconvolution algorithm is not applied when outputting 1D concentration profiles, precipitate proxigrams, and other position-dependent compositional measurements because it is unclear which ions in the peak area are distributed as a function of position across the control volume. Some authors have developed post-processing routines in MATLAB that provide more accurate peak-deconvolution algorithms for these situations [212].

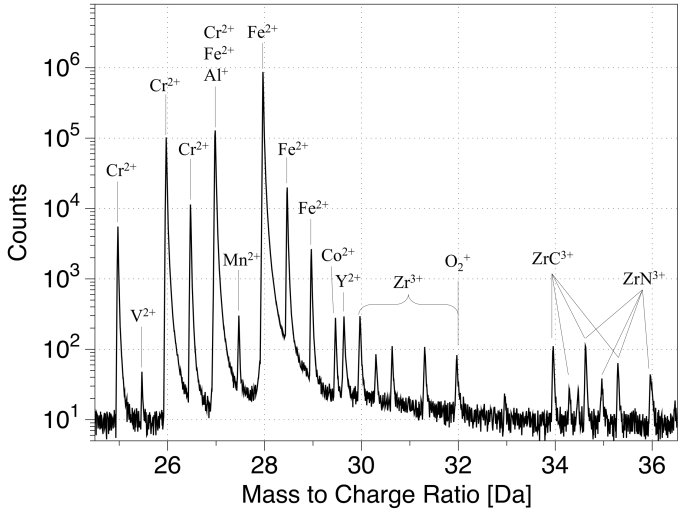


Figure 4.12. A portion of the mass-to-charge ratio spectrum for a representative APT specimen with both (Y,Al,O) and (Zr,C,N) nanoprecipitation showing instances of peak overlaps for both the matrix and precipitates.

For the present system, there are peak overlaps for mass-to-charge ratios of 27 Da ($^{27}Al^{+1}$, $^{54}Cr^{+2}$, $^{54}Fe^{+2}$), 54 Da ($^{54}Fe^{+1}$,$^{54}Cr^{+1}$), 32 Da ($^{16}O_2{}^{+1}$, $^{96}Zr^{+3}$), and 14 Da ($^{14}N^{+1}$, $^{28}Si^{+2}$). In all of these cases, the first element listed was assigned the respective peak since these elements have the highest isotopic abundances and are expected to dominate the distribution of ions for the respective peak. For general compositional measurements for the global, matrix, and cluster volumes, the peak deconvolution algorithm was utilized for correction; however, for general 1D concentration profiles presented in this work, no peak deconvolution was performed. When applicable, errors associated with this approach are discussed in the following chapters.

Similarly for the case of concentration profiles, the outputted individual cluster compositions from the maximum separation method output are also not corrected for peak overlaps. This is a significant possible source of error due to the Al and Fe peak overlap at 27 Da, since the amount of Al in the nanoprecipitates will directly affect discussions pertaining to the stochiometric composition and structure. Edmondson [23] has developed a routine for the individual correction of cluster compositions for Cr-rich α' precipitates in FeCrAl. Edmondson's approach uses the fact that a non-corrected matrix composition is also outputted by the cluster file generated from the maximum separation method. The corrected bulk matrix composition estimated from the deconvolution algorithm in IVAS is compared to the uncorrected matrix composition in the cluster file and a correction ratio is applied to each individual cluster composition. This method was shown to provide comparable results between the average deconvoluted cluster composition in IVAS to the average of the cluster compositions corrected individually in the MATLAB algorithm [23]. Thus, this method has been used for the correction of (Y,Al,O) nanoprecipitates in the CrAZY alloys studied in the subsequent chapters.

4.2.4. Field-Induced Trajectory Aberrations

There are many artifacts associated with the APT technique that can lead to erroneous compositional measurements of precipitates. The preferential evaporation of

elements, the migration of atoms on the tip surface, the dissociation of molecular ions after field-evaporation, and other issues can result in either erroneous position measurements of ions on the detector or loss of ions altogether [172, 213]. By far one of the most substantial artifacts in the study of precipitates in ODS alloys are field-induced trajectory aberrations associated with local-magnification effects and spatial overlaps between the matrix and the precipitate.

Consider a cylindrical control volume (25nm OD) with a depth equal to a 3nm slicing a nanoprecipitate in a representative CrAZY ODS FeCrAl alloy presented in **Figure 4.13**. In this figure it can be clearly seen that in the precipitate volume, an abnormally high reduced density (the relative atomic density in the precipitate divided by the surrounding matrix atomic density) is observed that approaches 2x the surrounding matrix atomic density. This increased atomic density is a direct result of the trajectory aberrations associated with the behavior of the precipitate/matrix interface at the specimen apex.

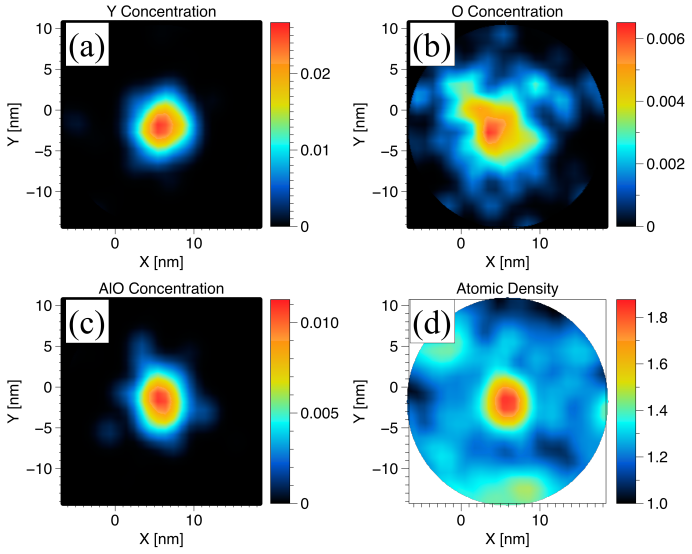


Figure 4.13. The atomic fractions of (a) Y, (b) O, and (c) AlO ions represented by 2D contour plots in a cylindrical region of interest equal to the thickness of the precipitate (3nm). In the nanoprecipitate region, (d) a relative atomic density ρ_r (the ratio of the atomic density in the precipitate vs the surrounding matrix) is calculated.

As was previously mentioned previously in Chapter 3, Williams [178] established that the high Fe and Cr contents measured in ODS FeCr alloys were attributed to trajectory aberrations, and he subtracted out the Fe (and Cr in proportion to the matrix composition) to provide more realistic aberration-corrected precipitate compositions. Hatzoglou [177] has developed a different methodology towards the correction of APT compositions due to trajectory aberrations that involves considering the precipitate shape and the reduced atomic density variations across the precipitates. In his formulation, the corrected composition (X_R^i) of constituent element "i" is:

$$X_R^i = \frac{\rho_r S}{\gamma}\left(X_M^i\right) - \frac{\rho_r S}{\gamma}\left(X_{Mat}^i\right) + \left(X_{Mat}^i\right) * \left(1 - p_{NQ}\right) + p_{NQ}^i \quad \text{..... (4.1)}$$

In this formulation, X_M^i is the initial measured composition to be corrected and X_{Mat}^i is the matrix composition surrounding the precipitate. ρ_r is the reduced density of the precipitate and S is the shape factor of the spherical or cubic precipitate, where $S = (XY/Z^2)$, the product of the horizontal precipitate dimensions divided by the square of the vertical depth dimension squared. γ is defined as the ratio between the expected atomic density of the precipitate and the surrounding matrix. The terms p_{NQ} and p_{NQ}^i represent the quantity of atoms of the precipitate and the element of interest lost preferentially during the field evaporation process not related to trajectory aberrations. It was shown for the ODS FeCr precipitates that a failure to consider the p_{NQ} term could result in a 0-18% difference in corrected precipitate compositions [177], but because an experimental evaluation of this value for the current system was not possible, this term is neglected. The resulting equation for each element becomes:

$$X_R^i = \frac{\rho_r S}{\gamma}\left(X_M^i\right) + \left(X_{Mat}^i\right) * \left(1 - \frac{\rho_r S}{\gamma}\right) \quad \text{..... (4.2)}$$

The consequences of this equation are very important for the evaluation of the ODS FeCrAl system due to the unknown partitioning of Al between the (Y,Al,O)

precipitates and the surrounding matrix (where Al content is between 11-12 at.%). The $\frac{\rho_r S}{\gamma}$ term is simply a scaling value, so this equation simply is a subtraction of the matrix composition from the precipitate composition as a function of increased atomic density across the precipitate and the variation of shape factor with precipitate size. For FeCr alloys containing precipitates only enriched in Y, Ti, and O, the forced removal of Fe and Cr ions has no substantial effect on the statistically significant atomic constituents within the precipitates. For ODS FeCrAl alloys, this is not the case. As will be shown in the later chapters of this work, Al is a critical component in the nanoprecipitates seen in these alloys. If the above procedure is implemented, it results in the removal of almost all Al from the (Y,Al,O) nanoprecipitates and drives the nanoprecipitate compositions to a composition approaching Y_2O_3. This is a highly problematic consequence of this compositional correction, and is not representative of the substantial literature on the observed precipitates in ODS FeCrAl alloys.

The potential over-correction of the Al content in the (Y,Al,O) precipitates may be possibly alleviated by assuming that a Cr-rich shell surrounds the nanoprecipitates. For ODS FeCr alloys, multiple authors have used a combination of techniques ranging from electron energy-loss spectroscopy (EELS) to APT to show that a Cr-rich shell exists around the nanoprecipitates [109-111, 178, 179, 214]. The atomic composition in the surrounding shell has been estimated to be 80% Fe and 20% Cr [179]. In addition, it has been previously estimated that 80% of the spatial overlaps of Fe and Cr in measured APT compositions of the (Y,Ti,O) precipitates in FeCr alloys comes from the shell while 20% comes from the rest of the matrix [176, 177]. In ODS FeCrAl alloys, high resolution transmission electron microscopy techniques have shown that for many precipitates, an amorphous shell exists at the periphery of the nanoscale precipitates within the matrix [110, 111]. However, there have not yet been sufficient studies to determine whether this shell is consistent over all ODS FeCrAl alloy precipitate compositions or if the shell is depleted of Al.

One possibility is that during nucleation, since the Al in the matrix is an active participant in the nucleation and growth of the precipitates, a Fe and Cr rich shell may

form locally around the newly nucleated cluster of atoms. Consider the simple schematic in **Figure 4.14**. Assuming that a sufficient stored energy in this local environment has allowed nucleation to initiate, if the favored composition of the precipitate is one enriched in Y, Al, and O then a nucleus will form and grow as atoms diffuse and incorporate into the cluster. Assuming that atoms are incorporated into the precipitate faster than the rate at which the Fe, Cr, and Al atoms are able to redistribute themselves in the host matrix due to the activation energies of diffusion for each of these elements in BCC Fe, then the local removal of Al from the immediate area surrounding the precipitates will result in a Al-depleted shell enriched in Fe and Cr (**Figure 4.14(b)**).

Recent APT results on (Y,Al,O) precipitates in a Fe-12Cr-6.1Al ODS FeCrAl alloy (125YF) by Massey et al. have not given conclusive evidence for this Al-depleted shell [100]. 1D concentration profiles through the z-axis depth dimension of 50 (Y,Al,O)-rich precipitates in the 125YF alloy in **Figure 4.15** clearly show a statistically significant increase in the Y, Al, and O atoms across the precipitates, but there does not seem to be a local increase in Cr-concentration at the periphery of the precipitates. However, as will be discussed later in this manuscript, the ratio of Cr/Fe in the matrix is slightly lower than the Cr/Fe ratio of the non-corrected APT cluster compositions, which suggests that the increased Cr may in-fact be coming from a Cr-rich shell locally around the precipitates.

The assumption of whether or not a Cr-enriched shell surrounds the FeCrAl precipitates has significant implications on the corrected cluster compositions that will be discussed in the subsequent chapters of this comprehensive work. Thus, for the purposes of the experiments conducted herein, the following assumptions are made. First, a Cr-rich shell is was not assumed to surround the precipitates. The second assumption relates to the estimation of the reduced atomic density across the precipitate. There are three ways that the reduced atomic density can be calculated for precipitates: (1) the total number of solute, ranged, or total atoms in the cluster as outputted from the maximum separation method csv file can be divided by the radius of gyration of the particle and then divided by the detection efficiency-corrected matrix atomic density, (2) the total atomic density across a precipitate can be measured by 1D concentration profiles across various

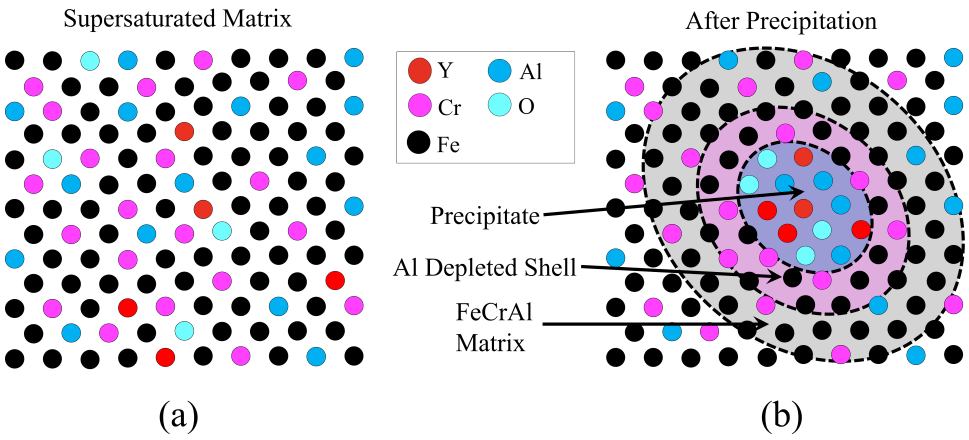


Figure 4.14. Schematic representation of a local environment of atoms in (a) the supersaturated solid solution state and (b) after a cluster has precipitated out of solution.

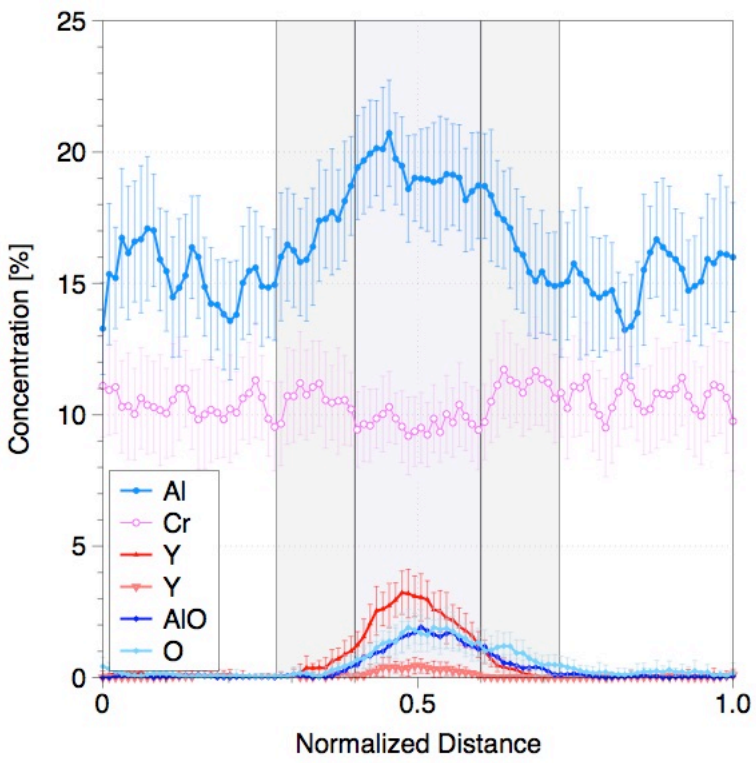


Figure 4.15. Average precipitate compositions as a function of normalized distance across 50 different precipitates in ODS FeCrAl alloy 125YF. Error bars indicate 95% confidence intervals for each position-dependent composition [100].

precipitates and then divided by the detection efficiency-corrected matrix atomic density, or (3) the total atomic density across the precipitates measured by 1D concentration profiles is divided by the measured atomic density in an elemental volume outside of the precipitate. In both (1) and (2), the matrix atomic density is calculated by multiplying the detection efficiency (Q) by the theoretical matrix density of BCC Fe (83 atoms/nm^3). In method (3) the matrix atomic density is measured directly from the raw APT data. For the estimation of the atomic density in the precipitates, method (1) provides the highest estimation since the estimation of spherical precipitate volume using the radius-of-gyration method results in smaller precipitate sizes than the atomic count method described later in this work. A more commonly used method is to estimate the area under the curve of the total atom count across precipitates measured by 1D concentration profiles, and then dividing the total number of atoms by the volume of the region of interest [176].

In this work, the corrected atom probe tomography compositions of the smallest (Y,Al,O) precipitates is performed by calculating the reduced density across the precipitates and subtracting the equivalent elemental contribution of the matrix from the precipitate assuming that the atomic density within the precipitate should be equal to the matrix atomic density. The assumption that the atomic density should be the same between the precipitate and the matrix may be erroneous since the ideal atomic density of the YAG phase is (94 atoms/nm^3) exceeds the ideal atomic density for BCC Fe (83 atoms/nm^3). However, the significant atomic strains associated with maintaining coherency between these precipitates and the matrix has resulted in authors showing that less than 2% differences in lattice spacings between the matrix and the precipitate [111]. This could decrease the atomic density of the precipitate to levels approaching the matrix. In addition, due to the increase in lattice parameter for increasing Fe incorporated into the YAG phase, the atomic density of the YAG phase decreases from 94 to 82 atoms/nm^3 as the Al is replaced by Fe and the phase changes from yttrium aluminum garnet (YAG) to yttrium iron garnet (YIG) [215]. Finally, the consequences of this assumption will only result in a 1% variation of Al compositional measurements (13% underestimation in

matrix composition → 7% change in subtracted matrix in the precipitates → 0.77% change in Al content subtracted from the precipitates). Thus, for the qualitative comparisons of Y, Al, and O contents in the nanoprecipitates in this work, this assumption is not an unreasonable one, especially since the same assumption is made for the $Y_2Ti_2O_7$ and Y_2TiO_5 in ODS FeCr alloys although this deviates from BCC Fe as well. The shape factor did not significantly vary as a function of particle size, so the variation of the local magnification effect as a function of particle size was not made part of this investigation. Instead, for the correction of cluster compositions, the precipitates were assumed spherical in shape (S=1). Thus, the equation for the general correction for precipitate compositions is reduced to the following equation, where the average reduced density for each APT control volume precipitate distribution was calculated and applied to each precipitate:

$$X_R^i = X_M^i \rho_r + X_{Mat}^i (1 - \rho_r) \quad \text{..... (4.3)}$$

Due to the underlying assumptions associated with the calculation of the cluster compositions, it will be shown that a significant amount of Fe and Cr still remain in the nanoprecipitates to preserve the Al without an assumption of an Al-depleted shell surrounding the precipitates. Consequently, the discussion on the precipitate compositions will primarily consider the Al, Y, and O fractions normalized to these three elements for ternary diagram creation. The possible existence of Fe in the clusters is discussed using the SANS results that supplement the significant APT data in this work.

4.3. SANS Data Collection

Small angle neutron scattering data was collected at the high-flux isotope reactor (HFIR) at ORNL at the general purpose (GP-SANS) beamline [216]. An image of the neutron scattering guide hall is presented in **Figure 4.16**. For neutron scattering measurements, either ex-situ scattering at room temperature or in-situ scattering in a vacuum furnace was implemented. For the ex-situ measurements, samples of pre-

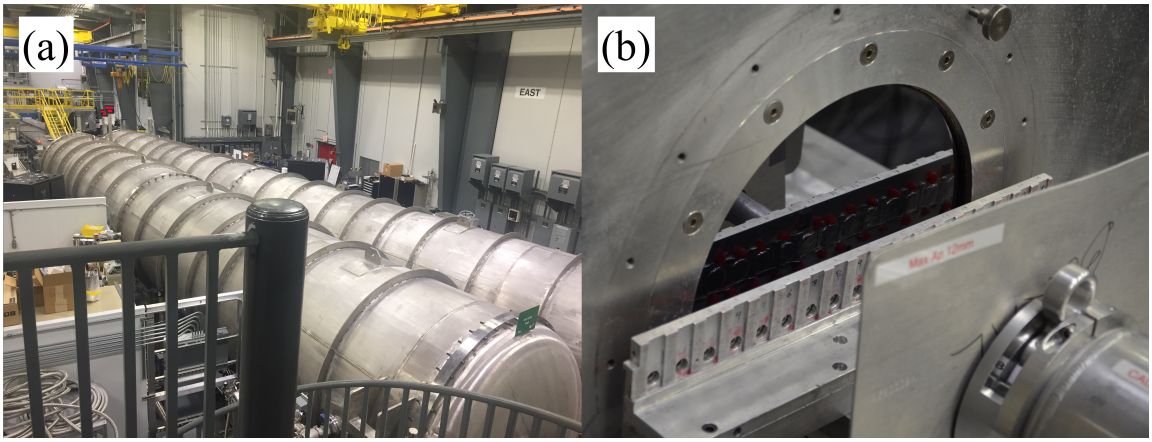


Figure 4.16. Pictures of (a) the CG-2 beamline at the GP-SANS beamline at HFIR and (b) a simple specimen holder for scattering without an added magnet or furnace.

annealed CrAZY powder annealed for 15-120 min. at 1000°C were packed in aluminum foil packets and placed in an open bore superconducting magnet (MagH) and a 2T magnetic field was applied perpendicular to the incident neutron beam to fully saturate the magnetic moments of the ferromagnetic atoms in the powder. Due to the size of the magnet, the accessible scattering range available was limited, but scattering curves were measured at two detector distances of 10m and 2m, respectively. The two detector distances allowed for the probing of scattering lengths in the range of $0.005 < Q < 0.2$ Å^{-1}. The neutrons for all scattering experiments had a neutron wavelength of 4.75 Å. The as-collected scattering data was corrected using an empty foil packet and for background, and the resulting curves were scaled to account for the packing density of the powders. The resulting scattering intensities were then normalized to the intensity of the attenuated direct beam and reduced to output the differential macroscopic scattering cross-section.

The in-situ SANS experiment was conducted using a vacuum furnace available at the CG-2 beamline that could reach a vacuum of ~10^{-5} Torr, which was maintained for the duration of the temperature ramp. As previously mentioned in the previous sections, instead of aluminum foil, molybdenum foil packets were used to encapsulate the powders due to the higher melting point of the molybdenum foil. The ZY40H as-milled powder was heated from room temperature to 1000°C at a ramp rate of 20°C/min. The heating

profile for the SANS experiment is plotted alongside the experimentally measured extrusion furnace heating profile in **Figure 4.5**. The SANS heating rate is approximately half of the profile expected during the pre-consolidation annealing treatment of the extruded powder, but this was done purposefully to allow for greater accuracy in the comparison of scattering data as a function of time. Scattering data was collected every minute during the temperature ramp, which provides an error in temperature that equals the ramp rate. With a 20°C/min ramp rate, the corresponding nucleation and growth could be tracked with an only 20°C error for each scattering curve. The slower ramp rate also allowed for more control over possible temperature overshoot based on the furnace's feedback system for temperature control. Data was collected at two detector distances (1.5m and 5m), which required two separate in-situ tests with two identical powder packets. The resultant scattering range covered was $0.01 < Q < 0.6$ Å^{-1}. The shorter detector distance data was scaled to match the 5m data in the overlapping Q range covered by both detector distances. Due to the size of the vacuum furnace, it was not possible to also use a magnetic field to deconvolute the magnetic and nuclear scattering components, which prevented a detailed quantitative analysis of the data in a similar fashion to the ex-situ data, but the in-situ data provided very beneficial qualitative visualizations of the nucleation and growth processes that occurred during powder heating.

4.3.1. Data Fitting and Structure Identification

As was previously presented in Eq. 3.7 and 3.8, the general scattering expression for the fitting of neutron scattering data is given by the master equation:

$$\left[\frac{d\Sigma}{d\Omega}(q)\right]_{m,n} = \int_0^\infty \Delta\rho_{m,n}^2 N(R)\left\{3V\left[\frac{\sin(qR)-qR\cos(qR)}{(qR)^3}\right]\right\}^2 S(q, R_{HS}, \gamma_{HS})\, dR \quad \ldots\ldots\ldots (4.4)$$

The structure factor used for the scattering analysis is the same one developed by Pedersen [189, 190]:

$$S(q, R_{HS}) = \left[\frac{1+24\eta_{HS}G(qR_{HS})}{qR_{HS}}\right]^{-1} \quad \text{(4.5)}$$

Where $G(qR_{HS})$ is a function of three variables:

$$G(qR) = G(A)_{A=qR_{HS}} = \alpha\left[\frac{\sin(A)-A\cos(A)}{A^2}\right] + \beta\left[\frac{2A\sin(A)-(2-A^2)\cos(A)-2}{A^3}\right] + \gamma\left\{\frac{-A^4\cos(A)+4[(3A^2-6)\cos(A)+(A^3-6A)\sin(A)+6]}{A^5}\right\} \quad \text{(4.6)}$$

$$\alpha = \frac{(1+2\eta_{HS})^2}{(1-\eta_{HS})^4} \quad \text{(4.7)}$$

$$\beta = \frac{-6\eta_{HS}\left(\frac{1+\eta_{HS}}{2}\right)^2}{(1-\eta_{HS})^2} \quad \text{(4.8)}$$

$$\gamma = \frac{\eta_{HS}\alpha}{2} \quad \text{(4.9)}$$

Although the structure factor seems a complicated function, it is in-fact only a function of the hard-sphere radius (R_{HS}), the hard-sphere volume fraction (η_{HS}), and the scattering vector (q). Thus, the general scattering equation is a multivariable function dependent on 5 different input parameters: (1) the product of the precipitate number density and scattering contrast ($N\Delta\rho^2$), the terms associated with the precipitate distribution (2) μ and (3) σ, and the terms associated with the hard sphere model (4) C and (5) η_{HS}, where C is a constant relating the hard-sphere interaction radius to the actual spherical precipitate radius (R).

One important aspect of the fitting procedure is to decide on the type of distribution that will be fit to the population of precipitates in the material. Weibull [190] and lognormal [186] distributions have been previously used in SANS analyses of precipitate distributions by different authors. In addition, the use of linear or cubic splines have also become popular due to their continuity and versatility for a variety of

distribution shapes [189, 217]. The precipitate distribution has been assumed to follow a lognormal distribution for the current work since this distribution more closely matches the APT data for (Y,Al,O)-rich precipitates in the CrAZY alloys.

The scattering equation presented in Eq. 4.4 has been fit using nonlinear least squares fitting procedures implemented in MATLAB. Since there are five unknowns, one major difficulty in the fitting of the scattering data is that there are multiple solutions to the equation and that erroneous initial conditions can lead to highly disparate results. For this reason, careful attention was paid to the fitting of highly coupled parameters such as the number density and the scattering contrast. Due to the highly coupled inverse relationship between the number density and the scattering contrast, the first term ($N\Delta\rho^2$) was fit as one parameter as discussed by Pedersen [189].

The fitting procedure was implemented by first subtracting a power-law background that was fit to the low-Q portion of the scattering curve. Two different scattering curve maxima were identified, signaling two different scattering populations of precipitates, which were fit individually. The three functions were then summed to provide the total fit for comparison to the raw neutron scattering data. After the precipitate population parameters were calculated, the number density (Eq. 4.10) and the precipitate volume fraction (Eq. 4.11) were then calculated using the relationship between the hard sphere and the actual precipitate radii and volume fraction reported in [190]:

$$N_p = \frac{\eta}{{}^4/_3\pi R^3} \quad \text{(4.10)}$$

$$f = {}^{\eta_{HS}}\Big/_{\left(\frac{R_{HS}}{R}\right)^3} \quad \text{(4.11)}$$

In addition to the fitting of the magnetic scattering data for precipitate dispersion calculations, the potential structure of the smallest precipitates was investigated by comparing the A-ratios of standard stochiometric phases to the experimentally measured

A-ratios over the scattering range comprising the precipitate population of interest. Recalling the definition of the A-ratio previously defined in Eq. (3.11), which is a function of the scattering contrast (Eq. (3.6)), this factor is a function of four parameters: the scattering lengths and atomic volumes of both the matrix and the precipitate. The nuclear scattering length densities (the ratio of the above parameters) was calculated using the weighted compositions of the matrix and precipitates, respectively. All of these nuclear scattering length density calculations were performed using the scattering contrast calculator developed by the NIST Center for Neutron Research [218]. Using the as-measured mass density of the FeCrAl matrix (equaling ~7.2 g/cm^3 using the Archimedes principle), the resulting scattering length density for the FeCrAl matrix is 6.82x10^{-6} A^{-2}. The magnetic scattering scattering contrast for the FeCrAl matrix was estimated to be 1.26x10^{-11} A^{-4} using the FeCrAl composition of the CrAZY powder as an input into the relations outlined in [219]. The magnetic scattering length density for each stochiometric phase of interest was initially assumed to be zero since it is initially assumed that no Fe content is present in the precipitates. The tabulated A-ratios for various (Y,Al,O) nanoprecipitate compositions are provided below in **Table 4.2**.

In the subsequent chapter, it will be shown that the measured A-ratios from the ratio of total (magnetic + nuclear) to the nuclear scattering contrast deviates significantly from what is expected for the current precipitates, irrespective of the assumed stochiometric composition. A careful consideration of the SANS and APT results are then discussed to access reasons for the deviation in A-ratio.

Table 4.2. Theoretical A-ratios for various Y-Al-O stochiometric phases calculated from the scattering length densities of the matrix and precipitate.

	FeCrAl Matrix		Precipitate		
Phase	ρ_n^{mat} (x10^{-6} A^{-2})	ρ_m^{mat} (x10^{-6} A^{-2})	ρ_n^{prec} (x10^{-6} A^{-2})	ρ_m^{prec} (x10^{-6} A^{-2})	A-Ratio
Y_2O_3	6.817	3.542	4.398	0	3.14
$Y_3Al_5O_{12}$ (YAG)	6.817	3.542	5.096	0	5.24
$YAlO_3$ (YAP)	6.817	3.542	5.604	0	9.53
$Y_4Al_2O_9$ (YAM)	6.817	3.542	4.472	0	3.28

4.4. Electron Microscopy Data Collection

Although this work relies heavily on the APT and SANS results described previously, both SEM and S/TEM techniques were also selectively used to provide microstructure and precipitate information to guide APT and SANS efforts. SEM-BSE data collection was performed using a Hitachi S4800 field emission (FE) scanning electron microscope operated using a 15kV accelerating voltage. In addition, EBSD data was collected on a JEOL 6500 high resolution FE-SEM using an accelerating voltage of 20kV with a 4nA beam current. For EBSD mapping, a 50nm step size was consistently used to resolve both the coarse and fine-grained regions. For all SEM and EBSD imaging and data collection, the sample surface was polished first using standard metallographic techniques to a colloidal silica finish. Post processing of ESBD data was performed using OIM software. A grain tolerance angle of 5 degrees was applied for all grain visualization and misorientation mapping after filtering out regions with a confidence interval less than 0.1.

TEM specimens were lifted out from extruded ODS alloys oriented in the longitudinal direction using the same FIB lift-out methodology described for APT specimens. After thinning the TEM lamella to electron transparency, the TEM specimens were subjected to a final polishing step using 900eV Ar ions in a Fischione Nanomill 1040 system prior to being plasma cleaned and transferred to the S/TEM for analysis. A FEI Talos F200X scanning/transmission electron microscope (S/TEM) [220] equipped with an X-ray energy dispersive spectroscopy (EDS) system was used to perform elemental mapping and nanoscale examination of the sample microstructures [221]. The EDS data was then analyzed using multivariate statistical analysis (MVSA) to identify potential nanoscale precipitates in the fabricated alloys [222, 223].

CHAPTER 5: Parametric Evaluation of Processing Parameters on Microstructure and Dispersion Characteristics

Prior to a detailed investigation of nanoprecipitate compositions for the current CrAZY system, it is first important to understand how the elements in the experimental matrix change the microstructural features and precipitate dispersions in the nanoprecipitate populations of interest. Thus, to provide an argument for parity between the different samples investigated, this chapter focuses on the differences and similarities between nanoprecipitate populations as a function of both processing route and analysis route. Of particular interest are the difference between the annealed powder and extruded microstructure, the use of different mechanical alloying devices, and the parameters involved in the collection and binning of nanoprecipitate mass spectra using various LEAP models.

5.1. Extruded Rod vs. Annealed Powder

The microstructures of the annealed CrAZY powders and the annealed and extruded CrAZY rods are of particular interest because of the effects of recrystallization and grain development on nanoprecipitate distributions. A representative EBSD map of extruded CrAZY_H1 annealed and extruded at 1100°C is provided in **Figure 5.1**. The figure clearly shows a bi-modal distribution of grain sizes within the microstructure. The fine-grained region is comprised of a high number density of smaller grains with high misorientation angles between the grains. In comparison, the coarser grained regions are comprised of significant subgrain texture associated with a high density of dislocations within the microstructure that form low-angle grain boundaries within the grains, as discussed in detail in Chapter 2. The development of the significant networks of dislocations within the microstructure is aided by the pinning of the generated dislocations by precipitates as the material is consolidated via extrusion. The grain size

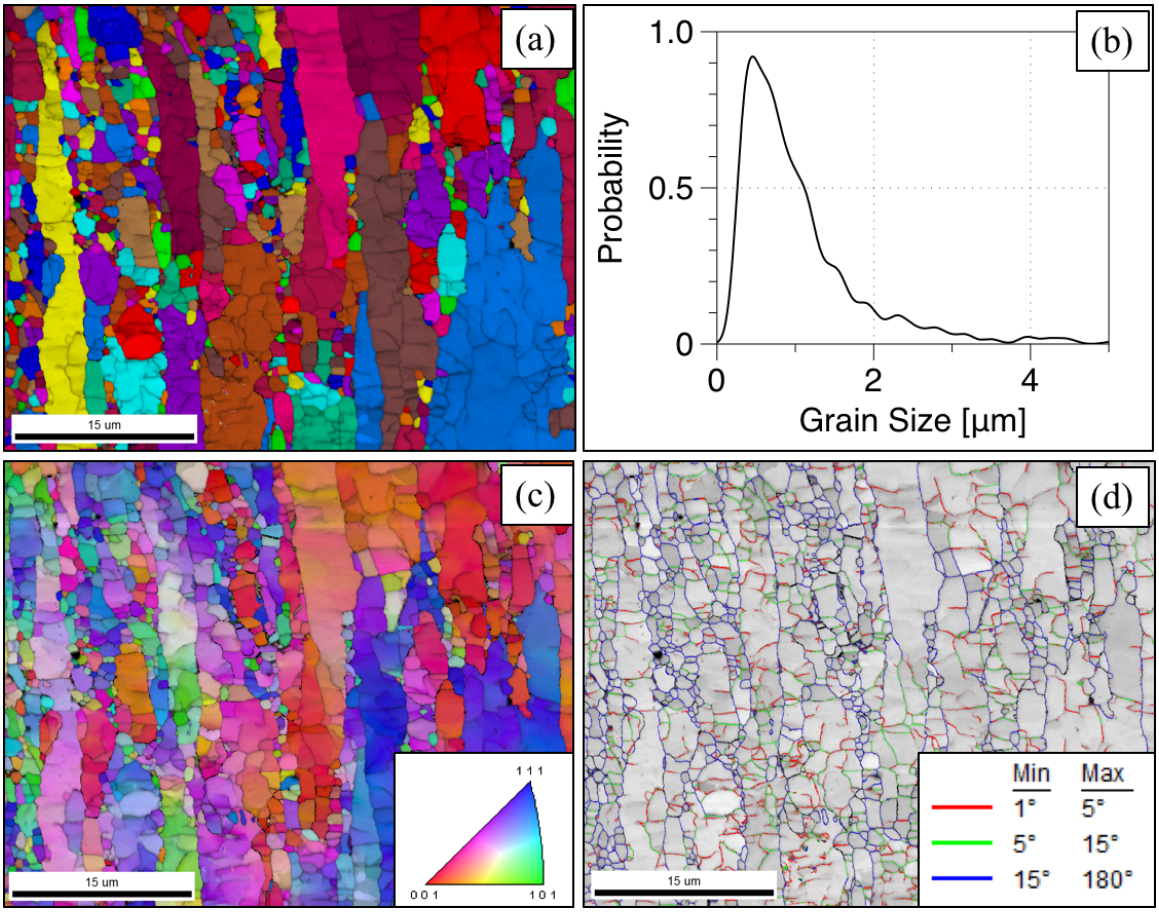


Figure 5.1. The as-extruded microstructure of ODS FeCrAl alloy CrAZY_H1 extruded at 1100°C after annealing for 1h at the same temperature. Shown are the (a) grain map showing each grain as a separate color, (b) the grain size distribution of the alloy, (c) the pole figure orientation map of the microstructure in the longitudinal direction showing significant textures and (d) the color coded grain boundary map showing the variation of grain boundary misorientation angle for fine and coarse grain regions.

distribution in **Figure 5.1(b)** fails to capture the larger grains due to the smaller number of them in this frequency distribution.

In comparison to the as-extruded microstructure, the development of the same type of bi-modal microstructure in the annealed CrAZY powder after annealing for 15 min. and 60 min. at 1000°C. However, the grains of the recrystallized powder do not show the strong texture associated with the extruded microstructure since no significant deformation was associated with the annealing process. Due to the significant stored energy variations across the microstructure, the microstructure has undergone significant abnormal grain growth at even short annealing times (**Figure 5.2**). An important point to note is that based on the powder annealing profile of the powder recorded via thermocouple, the equivalent temperature reached by the powder annealed for only 15 min. in the 1000°C box furnace is only approximately 715°C. This means that this relatively low temperature with respect to consolidation temperatures has already resulted in the recrystallization of the as-annealed powder. This also suggests that every single extruded rod also had a powder microstructure similar to that of ZY10C15 prior to the development of the extruded microstructure during consolidation.

One major point of discussion that deserves future investigation is the development of oxide stringers in the as-extruded microstructure that is not present in the microstructure of the as-annealed powder. **Figure 5.3** shows the as-extruded microstructure of alloy 106ZY10C8 that was extruded at 1000°C after annealing for 60 min. at the same temperature. Shown are both the longitudinal “L” orientation (defined as the axis parallel to the extrusion direction) and the transverse “T” orientation (conversely defined perpendicular to the extrusion direction). The oxide stringers observed in the microstructure are aligned along specific grain boundaries oriented parallel to the L orientation, while the stringers in the T orientation seem to decorate grain boundaries in a circular manner encapsulating multiple grains. These oxide stringers have been identified in previously produced ODS FeCrAl alloys [99] and in other ODS FeCr alloys with Al impurities [134, 224].

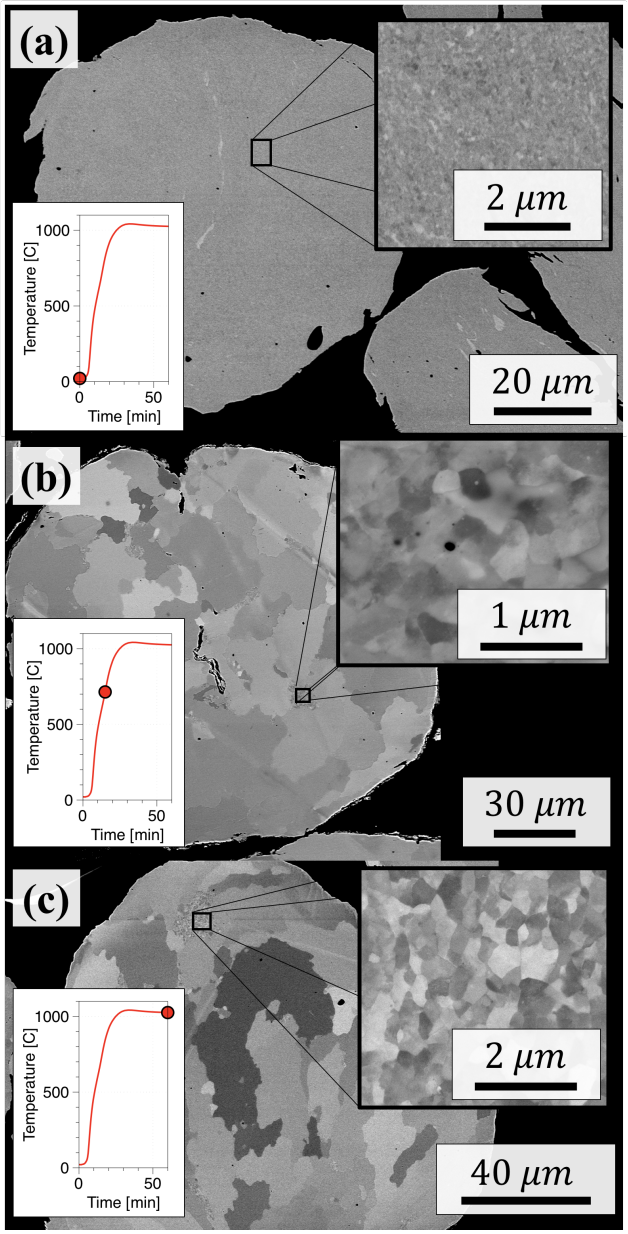


Figure 5.2. SEM-BSE images of the microstructures of the (a) as-milled ZY40H specimen, (b) the ZY10C15 specimen annealed for 15 min. in a 1000°C box furnace, and (c) the ZY10C60 specimen annealed for 60 min. in a 1000°C box furnace. Also overlaid is the approximate temperature reached by the powder in terms of the experimentally measured powder temperature profile. [203]

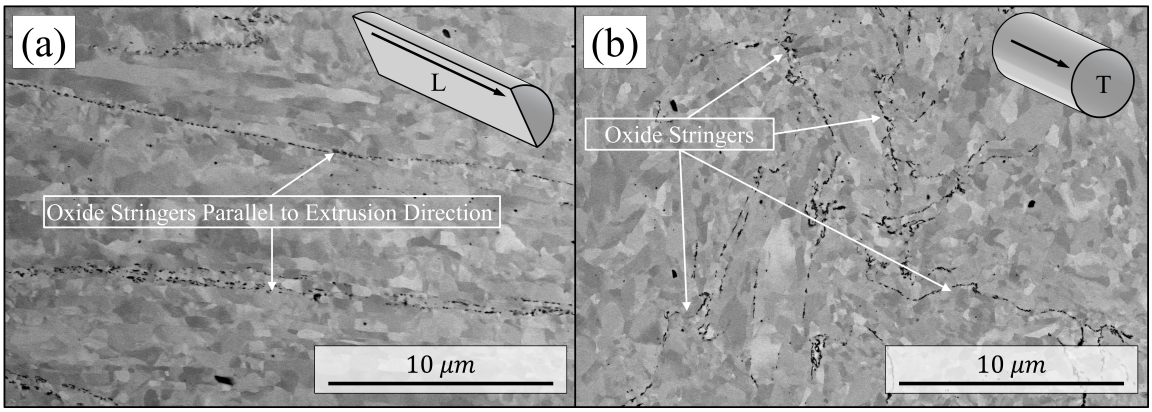


Figure 5.3. SEM-BSE images of the as-extruded microstructure of an ODS FeCrAl CrAZY alloy extruded at 1000°C after annealing for 1h (106ZY10C8). The micrograph in the (a) longitudinal direction and (b) the transverse orientation indicate oxide-stringers along specific grain boundaries in the as-consolidated microstructure. [225]

Based on the lack of observed stringers in the annealed powder, but acknowledging that the extrusion of the same annealed powder has resulted in the preferential encapsulation of collections of grains in the as-extruded alloy, attention must be called to the powder surface during consolidation. One possible mechanism for stringer formation lies in the same reason Al is added to the ODS FeCrAl microstructure: its ability to readily oxidize and form a thin oxide layer on the material's surface. **Figure 5.4** shows a visual schematic of the proposed mechanism for stringer formation in the as-extruded alloy. The presence of Al in the FeCrAl powder results in a thin film of alumina on the surface of the powder. During mechanical alloying, the alumina layer is dissociated and re-incorporated into solid solution in the same manner that yttria is during the mechanical alloying process; however, after mechanical alloying the powder has the opportunity to re-form the oxide scale if the powder is handled in air atmosphere or during the heating/degassing stage prior to thermomechanical consolidation. During consolidation, the formation of the recrystallized grain structure within each powder particle occurs, but at the same time the added pressure applied to sinter the powder particles together results in the fragmentation of the oxide layer to form oxide stringers along prior powder surface interfaces within the microstructure. Due to the low fracture

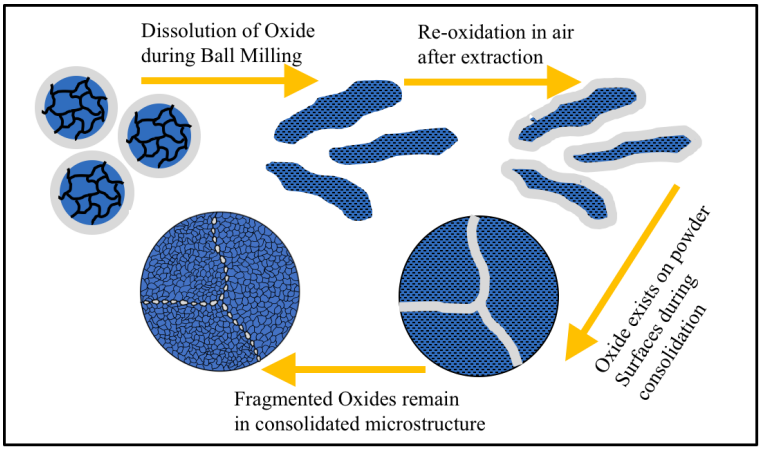


Figure 5.4. Schematic describing the proposed mechanism for stringer formation in ODS FeCrAl alloys. [225]

toughness of ODS alloys and the possible role in crack propagation that these oxide stringers play in the fracture mechanics of these alloys, future work should be aimed at finding ways to either remove the oxide layer prior to powder consolidation or through the use of inert atmospheres throughout the powder handling process.

Because of the highly bi-modal microstructure associated with the as-annealed powder, it is of crucial importance to understand how the nanoprecipitate dispersion is affected by the abnormal recrystallization process associated with secondary recrystallization. Since a majority of the experimental works in this study are focused on specimens prepared from the as-annealed powder, the dispersion characteristics of both the fine and coarse grains in the as-annealed powder were investigated. Using the targeted FIB lift-out procedure presented in Chapter 3, site-specific lift-outs were obtained for annealed CrAZY powder annealed for 60 min. at 1000°C. The resulting nanoprecipitate dispersions for the fine and coarse grained regions are shown qualitatively in **Figure 5.5**. The dispersions are highly consistent between the two regions, with a high number density of smaller (Y,Al,O)-rich precipitates and a lower number density of coarser Zr-rich precipitates.

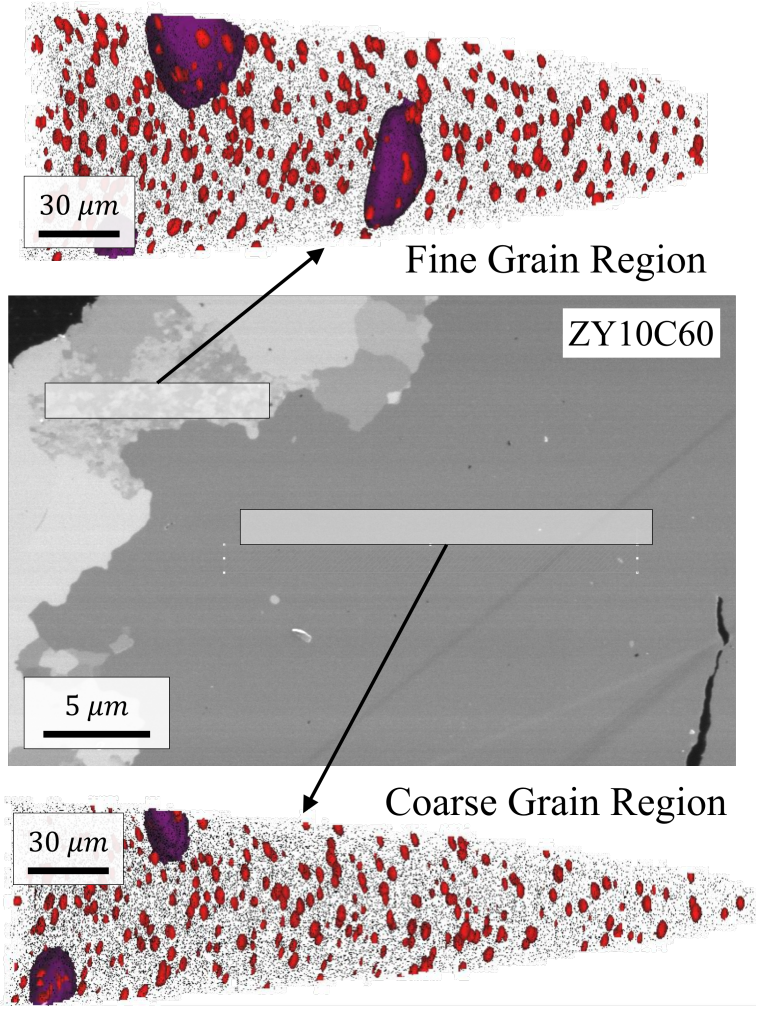


Figure 5.5. Illustration of the uniformity of the nanoprecipitate dispersions in ODS FeCrAl CrAZY powder (ZY10C60) in both the fine grain and coarse grain regions through targeted APT experiments. Smaller (Y,Al,O) precipitates are illustrated using red 1.5% (Y,YO,AlO) isoconcentration surfaces and larger Zr-rich precipitates are shown as purple 10% Zr isoconcentration surfaces. [203]

The similarity of nanoprecipitate distributions between the fine and coarse grained regions is an important result, especially since recent investigations of recrystallized ODS FeCr alloys has shown a lower number density of coarser precipitates in the coarse-grained regions [141]. The disparity between the results presented in this work and the work presented on recrystallized 14YWT can be reconciled through two major points. First, the results presented by Aydogan et al. were conducted on recrystallized 14YWT in already consolidated form. It is important to understand the presence of Al in the ODS FeCrAl powder here does not affect the recrystallization kinetics of the powder substantially. During the annealing of the ODS FeCr 14YWT powder prior to powder consolidation, it also would have had the same bi-modal microstructure with a homogeneous distribution of precipitates across the microstructure (otherwise the pre-recrystallized as-extruded form of the 14YWT alloy that the authors investigated would have already exhibited two distributions of fine and coarse precipitates prior to their recrystallization studies on the as-extruded alloy). Thus, there seems to be a difference between the recrystallization steps seen here for the annealed mechanically alloyed powder and the recrystallization steps seen for the as-extruded ODS FeCr alloy.

The second important point in support of the current result is that 90% of the powder microstructure is comprised of abnormally grown grains measuring tens of microns in diameter, as shown in **Figure 5.2**. If the distribution of nanoprecipitates in the 90% of coarse grains in the recrystallized powder would be coarser than in the fine grains, then it follows that the same coarser distribution of nanoprecipitates would expect to be seen in the as-extruded microstructure, which is not the case for both ODS FeCr alloys widely studied in literature or for the CrAZY alloys investigated in this work. The only case where precipitate distributions would be different in the as-extruded alloy is if there was insufficient dispersion of Y and O throughout the microstructure during the mechanical alloying step, which was shown by West on initial heats of 14YWT that exhibited large grains absent of nanoprecipitates due to the lack of sufficient Y content in these regions [166]. Thus, for the purposes of this work it is assumed that comparisons of fine and coarse grained regions of annealed CrAZY powder can be readily compared

without doubts as to the homogeneity of nanoprecipitate dispersions across the powder microstructure after annealing.

Although the nanoprecipitate dispersions are comparatively similar between the coarse and fine grains, there was one APT control volume that exhibited a 50 nm region that was surprisingly void of nanoprecipitates (**Figure 5.6(e)**). Although there was no evidence of a grain boundary near this precipitate free zone, there was a line of coarser nanoprecipitates in the control volume as well. This particular APT specimen (in the as-extruded state) gives support to the mechanism of nanoprecipitate dissolution and re-precipitation in recrystallized ODS powders conjectured by Sallez [84]. During the abnormal grain growth associated with secondary recrystallization in the as-annealed powder, Sallez proposed a multi-step process whereby a migrating grain boundary would cause heterogeneities in the precipitate distribution during its propagation through the microstructure. The process is presented in **Figure 5.6(a-d)**: due to the higher solubility of solute elements at the grain boundary, precipitates in front of the grain boundary recrystallization front will dissolve ahead of the grain boundary resulting in a precipitate free zone behind the grain boundary. As the solute concentration in the grain boundary exceeds the excess solubility of the boundary, it will no longer be able to cause precipitate dissolution and will either be pinned by Zener pinning or will drag precipitates as it propagates. As precipitates coarsen along the boundary due to accelerated diffusion paths due to grain boundary diffusion, the pinning force decreases and the boundary is able to break free and continue propagating; however, because the solubility of solutes in a stationary grain boundary exceeds that in a migrating boundary it will eject solute atoms in all direction and allow for the re-precipitation of precipitates on both sides of the boundary. The experimental results in this work are overlaid with the process schematic showing almost identical features. This result means that although the precipitate distributions as a general rule will be identical between coarse and fine grained regions, there will be local cases where precipitate free zones exist within both the annealed powder and the as-extruded alloy microstructure.

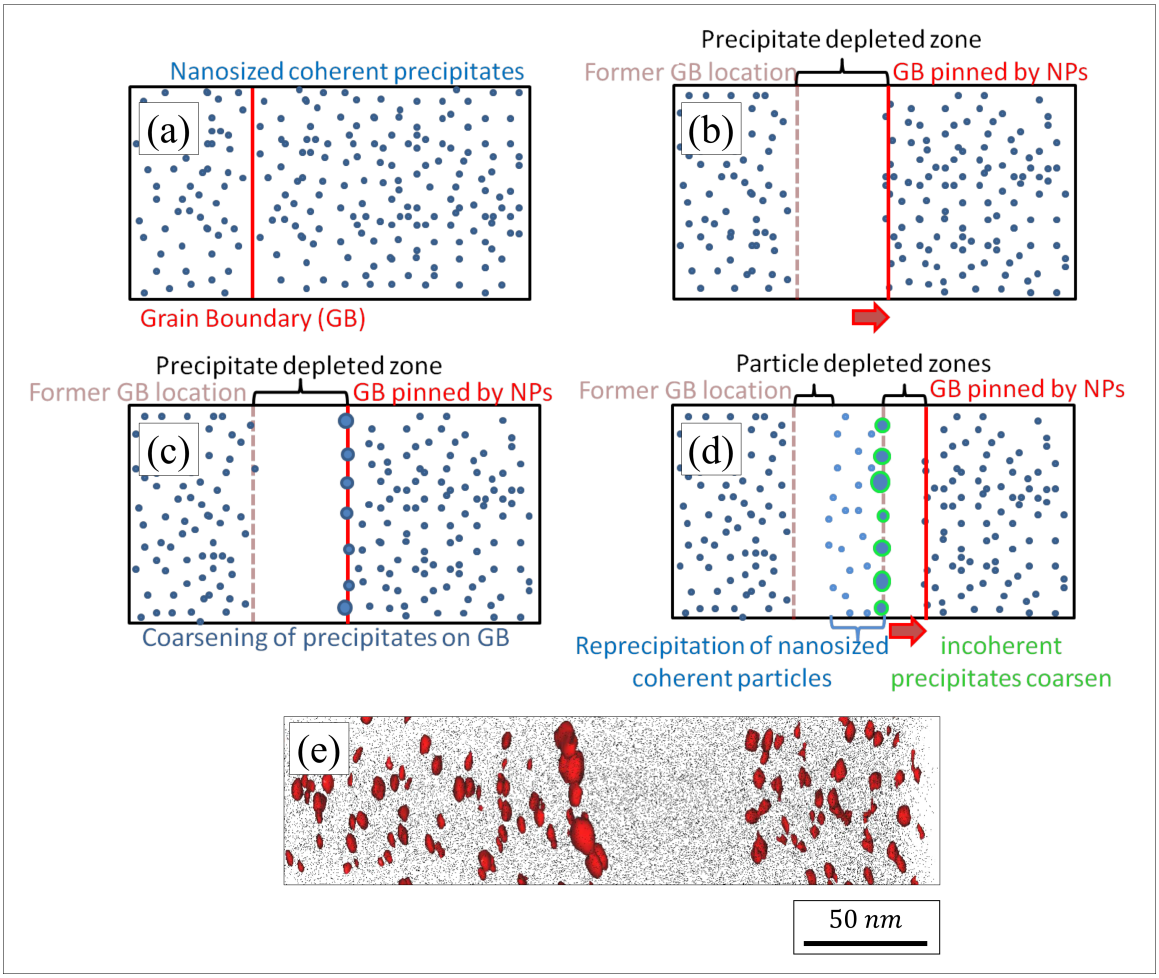


Figure 5.6. (a)-(d) present the nanoprecipitate dissolution and re-precipitation mechanism proposed by Sallez [84], while (e) illustrates one APT control volume identified in this work providing similar nanoprecipitate features in alloy 106ZY10C8 supporting this conjectured mechanism.

Since the precipitate distribution in the as-annealed powder has already been established by the time the powder has been sintered through the consolidation process, it is unsurprising that the nanoprecipitate distributions are equivalent in both the powder microstructure and in the as-consolidated alloy. To show this parity between distributions qualitatively, consider the array of APT control volumes for annealed powders and extruded alloys shown in **Figure 5.7**. Two important points are made from this comparison. First, the nanoprecipitate distributions between the powder annealed for 15 min. and 60 min. at 1000°C are identical. This is an impactful result if one considers the heating profile of the annealed powder as a function of time. Just as the powder microstructure has undergone recrystallization by 15 min. at an equivalent temperature of 715°C, this result also shows that the nanoprecipitates have already nucleated and grown to stable sizes within the first 15 min. of annealing as well.

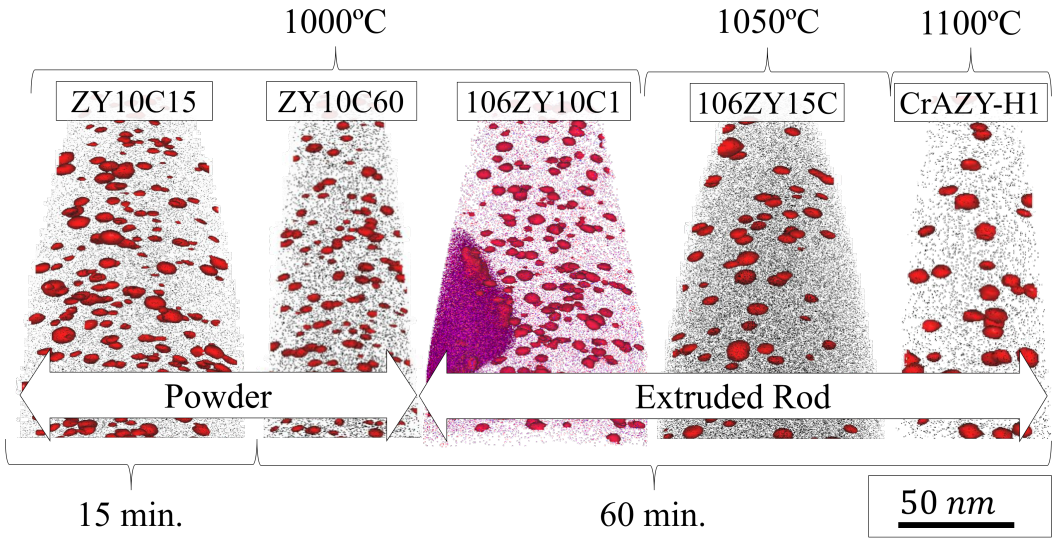


Figure 5.7. A comparative illustration of the similarity of nanoprecipitate dispersions in both annealed powders and extruded alloys with 1000°C annealing treatments. Also shown is a qualitative increase in precipitate size with a decreasing number density for alloys consolidated via extrusion with increasing extrusion temperature. Red 1.5% (Y,YO,AlO) iso-concentration surfaces are shown for all samples with overlaid background matrix atoms. The purple feature in sample 106ZY10C1 is a Zr-rich region.

This image also provides a second result that supports previous research on ODS alloys, whereby precipitate sizes increase while the corresponding number density decreases with increasing extrusion temperature [162]. Since the nanoprecipitates would have already nucleated and grown to stable sizes during the pre-consolidation annealing step at short annealing times, this result suggests a transition from nucleation and growth to precipitate coarsening at higher extrusion temperatures, even for samples annealed for only 1h prior to extrusion. This is a significant result since this change in nanoprecipitate size affects the as-consolidated microstructure and consequently the mechanical properties of the material. The number density and average radius of precipitates in sample 106ZY10C1 (extruded after annealing 60 min. at 1000°C) are 1.80×10^{23} m^{-3} and 1.95 nm, respectively [113]. Conversely, the sample annealed for 60 min. at the higher temperature of 1050°C had an average precipitate radius of 2.08 nm with a number density of 1.11×10^{23} m^{-3}.

Recalling the various strengthening mechanisms described in Chapter 2, it is possible to compare the yield strengths of these two alloys to estimated yield strengths using the RMS methodology in Eq. (2.3). Using the reported grain sizes of the 106ZY10C1 and 106ZY15C alloys, which are 947 and 1155 nm respectively, and a Hall-Petch constant of 401 MPa/$\mu m^{1/2}$, the grain boundary strengthening components of these alloys were calculated to be 412 MPa and 373 MPa [113]. Using a Burgers vector of 0.248nm [57] and a lattice parameter of 0.287nm for the ODS FeCrAl alloys investigated here, the grain matrix hardening was estimated to be 234 MPa for both alloys. The dispersed barrier hardening contribution calculated using the number densities and radii for both alloys resulted in a precipitate strengthening component of 328 MPa for 106ZY10C1 while the lower number density and larger precipitate size for 106ZY15C translated to a lower dispersed barrier hardening component of 278 MPa. Although the dislocation density was not able to be measured for these alloys, based on the consolidation methodology and temperature of extrusion, the dislocation density was assumed to be 10^{14} m^{-2} for both alloys, which is of the same order of magnitude as those reported for ODS alloys produced in similar fashion [60].

A hydraulic MTS tensile machine was utilized for mechanical testing using a strain rate of 10^{-3} s^{-1} in air atmosphere. For accurate temperature measurement, a thermocouple was adhered to the sample holder, and the specimen temperature was held at the target temperature for at least 10 min. prior to performing the tensile test. As shown in **Figure 5.8**, the strength of the sample extruded at 1000°C (106ZY10C1) exceeds that of the sample extruded at 1050°C (106ZY15C) at temperatures less than 600°C. This is because nanoprecipitates and grain boundaries become less effective as obstacles to dislocation motion at elevated temperatures [56]. Both samples show significant increases in strength in comparison with an arc-melted wrought FeCrAl alloy with Mo and Nb addition (C35MN) but exhibit lower ductility. The increase in relative strength of 106ZY10C1 in comparison to 106ZY15C directly relates to the finer precipitate distribution that has also refined the grain size. Comparing the differences between the measured room temperature yield strength values for these two alloys, there exists only a small error of ~7 MPa between the experimentally measured and modeled yield strength for the 106ZY10C1, while the error increases to ~20 MPa for the sample extruded at slightly higher temperature. This signifies that although the assumed dislocation density used for dislocation strengthening calculations was a good approximation, the increase in error for the higher extrusion temperature suggests that this sample also has a slightly reduced dislocation density in comparison to the 106ZY10C1 sample, which is expected since fewer pinning sites exist in this alloy.

Although a detailed discussion concerning the deformation modes and strengthening contributions is not the primary focus of this work, this analysis reinforces the need to develop optimized annealing treatments so that higher consolidation temperatures can be used for ductility enhancement without significantly deteriorating the precipitate dispersions in these alloys. This discussion is the primary focus of Chapter 7 of this study.

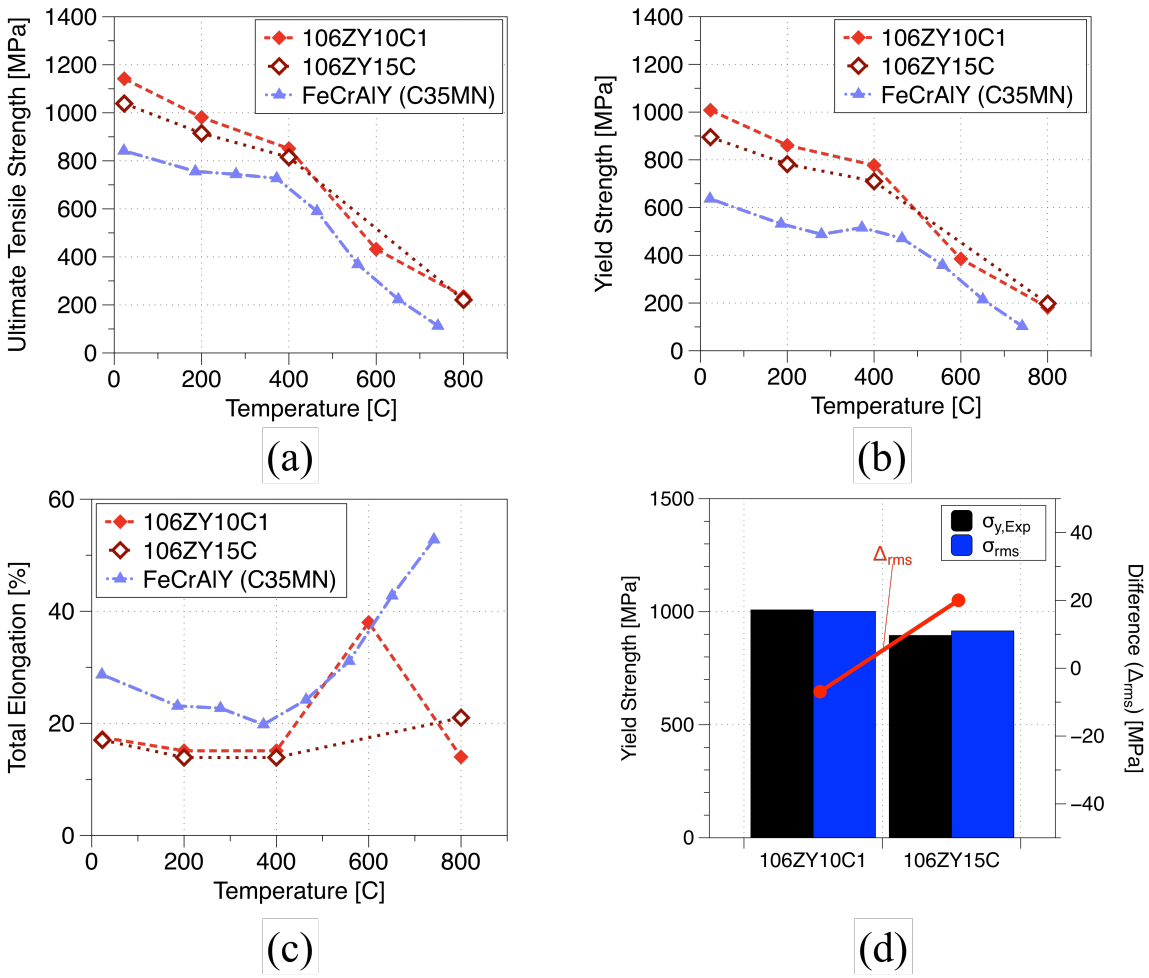


Figure 5.8. The experimentally measured (a) ultimate tensile strength, (b) yield strength, and (c) total elongation as a function of temperature for 106ZY10C1 and 106ZY15C as a function of temperature [113]. Also shown for comparison is a non-ODS wrought FeCrAl alloy (C35MN) [8]. In (d), room temperature yield strength values are compared with the computed yield strength using the RMS methodology.

5.2. Effect of Mechanical Alloying Device

The CM01 and CM08 Zoz Simoloyer ball-milling units have both been widely used for the production of ODS FeCrAl and ODS FeCr alloys in the past decade for the development of alloys such as 14YWT. In the current investigation, it is of interest to determine if the use of these different mechanical alloying devices results in similar microstructures and nanoprecipitate distributions since both of these devices has been used over the course of this study. With a larger attrition-type ball milling device, the spherical milling media have higher velocities in comparison to a smaller ball mill operating at the same rotational speed (ω) because the velocity at the tip of the attritor blade (v) is proportional to the radial blade length (r) through the relationship $v = \omega r$. With a blade length of the CM08 unit measured as 8.3cm, the average velocity of the milling media at rotational speeds 350/600 rpm are 3.0/5.2 m/s respectively. For the CM01 (blade length 5.1cm), the velocities are 2.1/4.8 m/s for 400/900 rpm rotational speeds. This means that the deposited energies may differ and the homogeneous incorporation of yttrium and oxygen in the lattice may be affected. In this section, the general microstructures and nanoprecipitate distributions between two identically annealed and extruded alloys are compared.

Figure 5.9 presents SEM-BSE images of the transverse orientations of CrAZY alloys annealed for 60 min. at 1000°C prior to extrusion at the same temperature. As mentioned previously in the previous chapter, alloy 106ZY10C1 was milled in the CM01 unit (200g powder capacity) at rotational speeds alternating between 400 and 900 rpm for 40h, while the 106ZY10C8 specimen was milled in the CM08 unit (1kg powder capacity) at rotational speeds of 350 and 600 rpm for the same duration. Both images show a fine-grained microstructure with the existence of oxide stringers and occasional porosity. The microstructures also show identical textures and grain size distributions through an investigation of the alloy microstructures in both the L and T orientations using EBSD. As referenced in **Figure 5.10**, the extruded microstructure shows a strong texture where grains in the extrusion direction are aligned in the [110] direction. This is expected since the dominant slip plane is (110) for BCC materials. Consequently, strong (001) and (111)

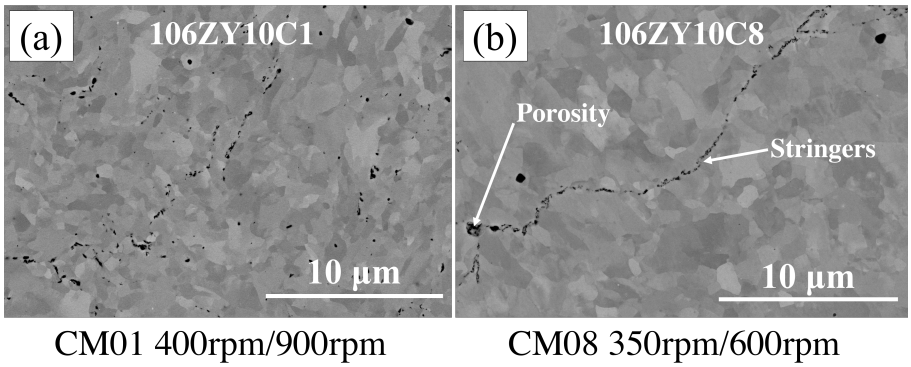


Figure 5.9. SEM-BSE micrographs of alloys 106ZY10C1 and 106ZY10C8 mechanically alloyed in CM01 and CM08 ball-mills, respectively. Both alloys were subjected to a 1h heat treatment at 1000°C followed by extrusion at the same temperature. Oxide stringers decorating grain boundaries are noted in both alloys, with sparse porosity also indicated.

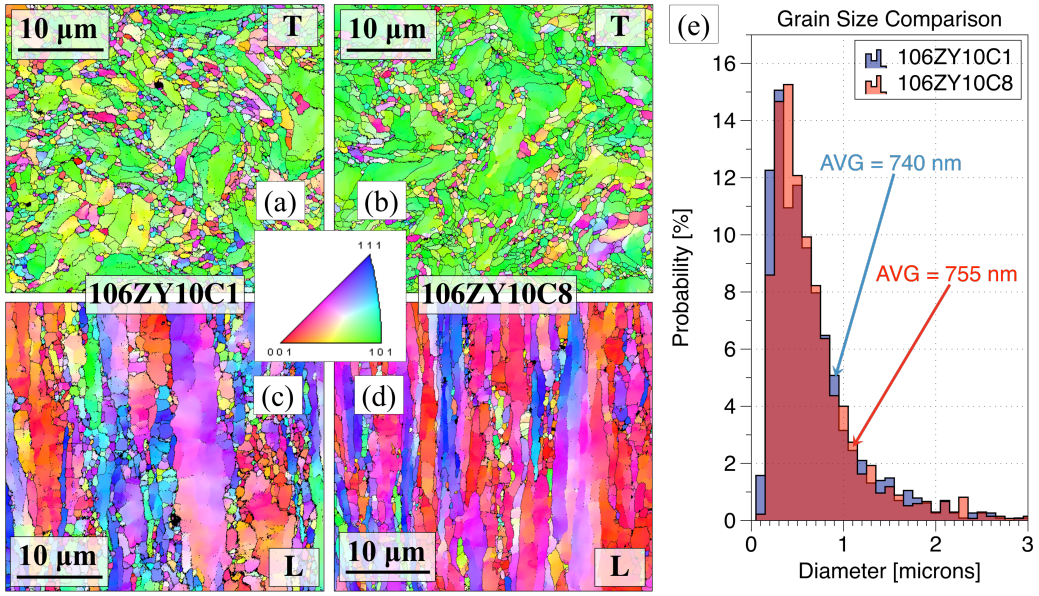


Figure 5.10. Grain pole figure orientation maps (left) are shown for samples 106ZY10C1 and 106ZY10C8 for both (a-b) transverse (T) and (c-d) longitudinal (L) orientations. Also shown is (e) the grain size distribution for both samples (right) with average grain size values tabulated.

orientations exist in the L orientation that are perpendicular to the (110) slip plane. The average grain sizes for the 106ZY10C1 and 106ZY10C8 specimens are 740±53 and 755±44 nm as measured in the L orientation, which are with all respects identical considering the 95% confidence intervals for each distribution.

Just as the microstructures are identical between the alloys milled in both Simoloyer units, the nanoprecipitate distributions also show highly similar dispersions. **Figure 5.11** compares two APT control volumes for 106ZY10C1 and 106ZY10C8. In this figure, it can be seen qualitatively that the dispersions are highly similar, both with respect to the distribution of smaller precipitates and the existence of larger Zr-rich precipitates within the control volumes. In these specific APT specimens, the 106ZY10C1 sample has an average precipitate radius of 1.8 nm while the 106ZY10C8 specimen has a slightly lower average radius of 1.55 nm. However, for the CM01 and CM08 specimens the corresponding number densities are highly similar and are reported as 1.8×10^{23} and 2.1×10^{23} atoms/m^3, respectively. It is unclear if the small difference in average precipitate size is due to slight variations in annealing times during the pre-extrusion step or if slightly different dispersions of Y and O in the lattice have attributed to the slight change in precipitate size.

5.3. Effect of Binning Parameters and LEAP Detection Efficiency on Precipitate Compositions

To this point, the focus has been aimed at the effect of different processing parameters on the dispersion of nanoprecipitates within the microstructure. Arguably more important in the comparison of this collection of APT data is to what extent this data can be compared between different control volumes as a function of how this data has been systematically studied. In this section, attention is paid to one specific CrAZY specimen type, ZY10C60, which is a powder mechanically alloyed and annealed for 60 min. at 1000°C. The smallest (Y,Al,O) nanoprecipitates in one specific control volume, analyzed on a Cameca LEAP 5000 XR model atom probe (**Figure 5.12**), are analyzed in three different binning conditions. The mass-spectrum has been binned either by the user

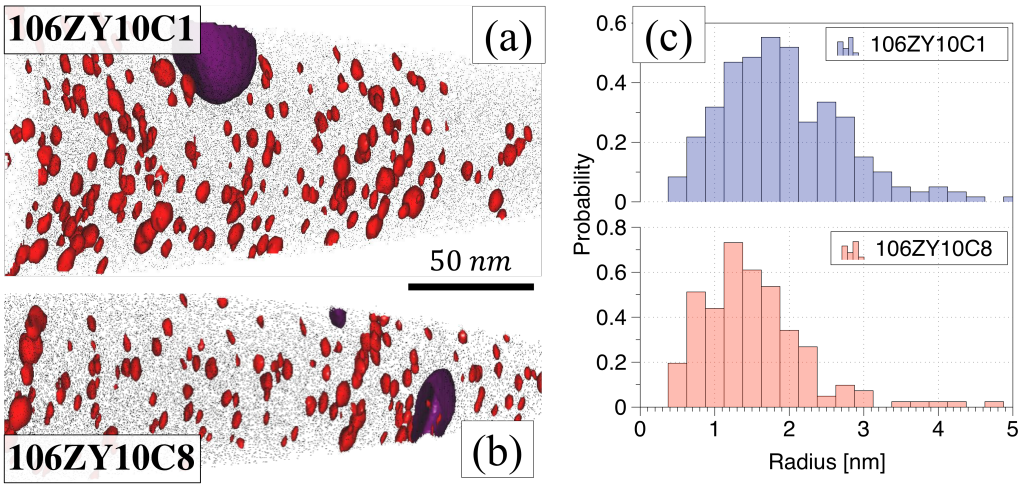


Figure 5.11. APT reconstructions for CrAZY ODS FeCrAl alloys extruded at 1000°C after annealing for 1h at the same temperature following mechanical alloying in either a CM01 (106ZY10C1) or CM08 (106ZY10C8) Zoz Simoloyer ball mill. Smaller (Y,Al,O) nanoprecipitates are shown using 1.5% (Y,YO,AlO) iso-concentration surfaces while a second population of Zr-rich precipitates are identified using 10% Zr iso-concentration surfaces. A comparison of nanoprecipitates size distributions is shown in (c).

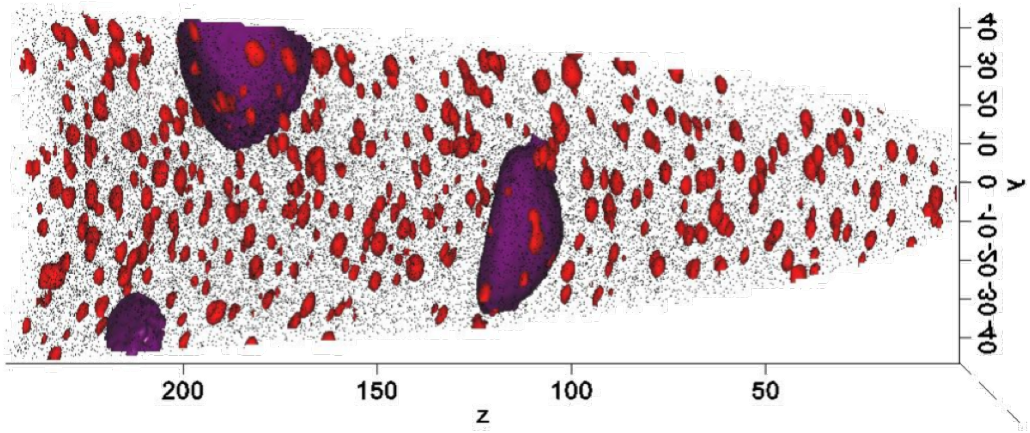


Figure 5.12. APT reconstructions of sample ZY10C60 for a fine-grained region of CrAZY powder annealed for 60 min. in a 1000°C box furnace. Smaller (Y,Al,O) nanoprecipitates are shown using 1.5% (Y,YO,AlO) iso-concentration surfaces while a second population of Zr-rich precipitates are identified using 10% Zr iso-concentration surfaces. 0.1% of Fe matrix atoms are also overlaid as black dots. Dimensional axes units are in nm.

to encompass the observed full width of each peak, and compositional results are compared with the cases where MATLAB has systematically binned each peak to either full-width tenth-maximum (FWTM) or full-width half-maximum (FWHM) conditions.

Figure 5.12 illustrates the reconstructed control volume of ZY10C60 showing a high number density of (Y,Al,O) nanoprecipitates in red with a lower number density of Zr-rich precipitates in purple. Since the effect of Zr on nanoprecipitation is the focus of the next chapter, a full discussion on these larger precipitates will not be addressed here. Instead, the results of the outputted compositions of the smaller (Y,Al,O)-rich precipitates are presented after correcting for a portion of the spatial overlaps due to the matrix using the aforementioned aberration correction procedures implemented in this work. In **Figure 5.13**, three different types of graphs are presented. First, the ratio of Y atoms to Al atoms in each precipitate are compared as a function of precipitate size. Second, the study of oxygen content is incorporated into the discussion through the construction of Y-Al-O ternary diagrams for each condition. Lastly, the nanoprecipitate size distributions for each binning condition are analyzed.

Several important results can be ascertained from **Figure 5.13**. As will be more fully investigated in Chapter 6, the ratio of Y to Al atoms decreases as a function of precipitate size. This means that as precipitates increase in size, more Al is measured in each precipitate, while for very small precipitates measuring less than 1 nm in radius Al is depleted from the nanoprecipitates. This is likely an artifact from the application of the maximum separation method in cluster identification. The cluster size distribution clearly shows that only a small number of precipitates exist in this size range. As the precipitate approaches and exceeds 1 nm, the Y/Al ratio levels out to a level slightly lower than is expected for the YAG phase.

When oxygen is considered, it is clearly seen that the oxygen content is severely underestimated in the nanoprecipitates even when binning the user-defined full width of each peak of the mass-to-charge ratio spectrum. The linear trend in the ternary diagram is another representation of the size dependence of the Y/Al ratio with increasing precipitate size. Though not clearly shown in this particular comparison, the size of each point on the

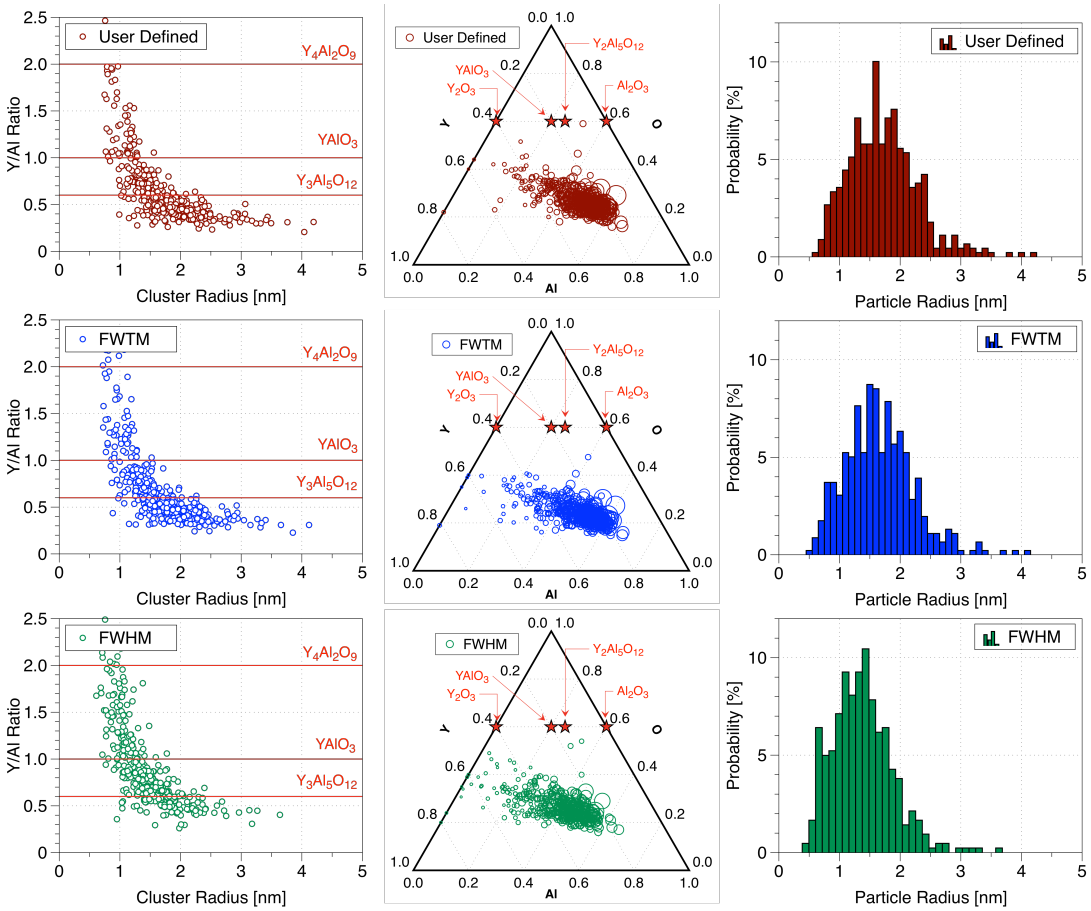


Figure 5.13. The effect of mass-to-charge ratio peak binning on the compositions and size distributions for identified (Y,Al,O)-rich nanoprecipitates in the ZY10C60 specimen previously shown in **Figure 5.12**. Illustrated are the Y/Al ratio, the ternary Y-Al-O diagram (point size proportional to precipitate diameter), and the particle radius distribution for cases where the mass spectra is binned with the perceived full width (user defined, red), the full-width tenth-maximum (FWTM, blue), and as the full-width half-maximum (FWTM, green). [225]

ternary diagram is proportional to the precipitate size, so many smaller points are shown in the tail end of the linear trend.

To more effectively summarize the data presented, **Figure 5.14** shows the variation in Y/Al ratio and nanoprecipitate size as a function of decreasing binning size. A slight variation of the Y/Al ratio is seen as the binning area decreases from the full-width to the FWHM value. All of these ratios are within 10% of the 0.6 value consistent with the YAG phase. However, a more substantial variation of nanoprecipitate radius is noted as the binning procedure changes. For the user-defined full width value, the average nanoprecipitate diameter is over 3.2 nm, while for the FWHM binning procedure this value decreases to less than 2.8 nm. This variation of nanoprecipitate size would severely affect the accurate quantification of the nanoprecipitate size as a function of processing parameters if consistency was not adhered to in the binning procedure. Consequently, all APT results reported in these chapters have been binned using the full-width tenth-maximum (FWTM) binning parameters. This procedure was chosen specifically to allow for consistency in precipitate size measurements and to ensure that as many ions can be captured and analyzed in each control volume.

Multiple LEAP models have been used for the analysis of the substantial APT data quantified over the course of this study. This has provided a unique opportunity to study the variation of nanoprecipitate quantification results as a function of the type of LEAP model used. More specifically, three Cameca LEAP models were used: a 4000X HR atom probe with a detection efficiency of 36% at ORNL, a 4000X Si atom probe with a detection efficiency of 50% at Northwestern University, and a 5000 XR atom probe at MPIE. For consistency, all units were operated in laser mode with specific parameters listed in Chapter 4. The same powder specimen ZY10C60 was studied on all three LEAP models, with specific lift-outs of fine-grain regions.

Mass-to-charge spectra for each LEAP model are compared side-by-side in **Figure 5.15** for the same region of the spectra including the major Fe, Cr, Al peaks and also smaller peaks associated with V, Mn, Co, and Y. The small amounts of V, Mn, and Co are common impurity elements in steels and either existed originally in the gas-atomized

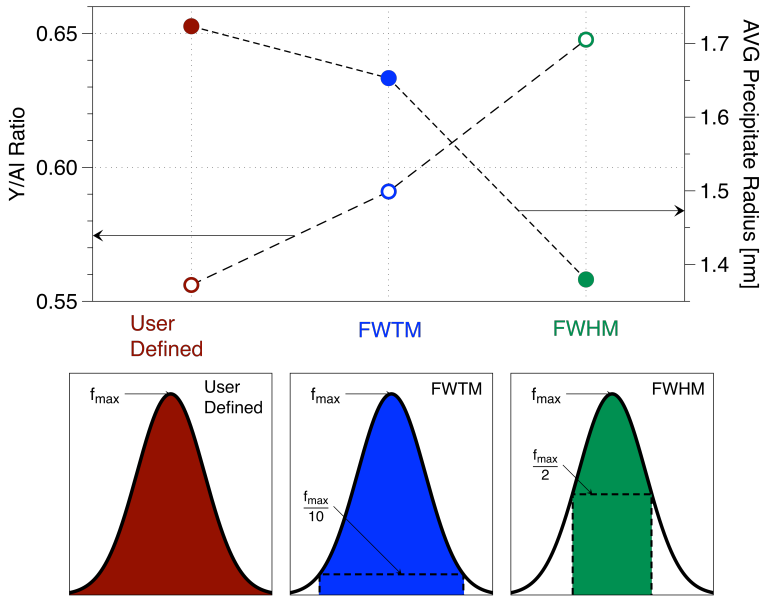


Figure 5.14. The dependence of composition and average precipitate size on binning parameters in the ZY10C60 specimen previously shown in **Figure 5.12**. The Y/Al ratio shows minimal change with decreasing binning width, while a more substantial variation in precipitate size is noted as the width of the defined mass-to-charge ratio peak is decreased from the user-defined full width to the full-width half-max value. [225]

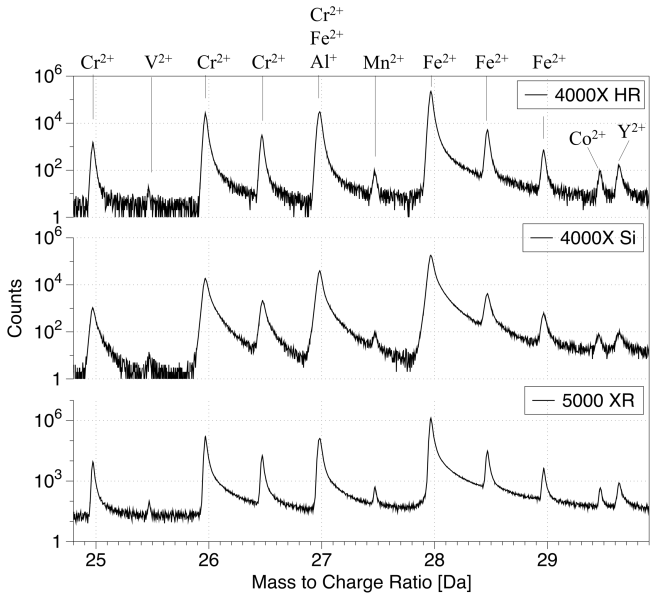


Figure 5.15. Mass-to-charge ratio spectra for various Cameca LEAP models studying ZY10C60 fine-grained specimens. [225]

powder or were transferred to the alloy by the milling media used during mechanical alloying. Regardless, all three spectra show similarities, although some minor differences exist. In all modes, the peaks have tails on the right-hand side of the distribution. This is an artifact associated with the use of laser-mode for data acquisition. After energy is deposited to the tip by the laser pulse to field-evaporate atoms, the tip increases in temperature. As the tip cools between pulses, it is possible for that thermal activation to be enough for additional field-evaporation events; furthermore, the added thermal energy shifts the energy of the field-evaporated ion, which broadens the spectrum in this "thermal tail" region. Since all three LEAP models were used in laser mode, thermal tails are noted on the major peaks. However, a clear increase in the peak resolution of the reflectron (4000X HR and 5000 XR) models is noted in comparison to the 4000X Si that uses a straight-line ion path to the detector. Specific focus is on the Y peak on the far right of the spectrum at 29.6 Da, where the reflectron models provide a better signal to noise ratio.

Since all three specimens were binned using the FWTM procedure, the precipitates within each can be readily compared as a function of composition and size. A summary of the results is presented for the three control volumes in **Figure 5.16**. Illustrated are the control volumes analyzed showing red (Y,Al,O) precipitates atop the black matrix atoms, the ternary diagrams for each LEAP model (4000X HR in purple, 4000X Si in blue, and 5000 XR in red), and the corresponding particle radius distributions for each control volume using a bin size of 0.1 nm. The model 4000X HR model has the lowest detection efficiency of 36%, while in comparison the straight-line flight path version of the same unit (the 4000X Si model) has a detection efficiency of 50%. For the newer model 5000 XR, the detection efficiency increases to 52%. The radii have been estimated using the atomic count method, which is explained in more detail in the next section but uses the detection efficiency, the expected atomic density of the precipitate, and the number of ranged ions in each precipitate control volume to determine the radius of each precipitate identified by the cluster search algorithm. Surprisingly, no significant changes in composition were noted for all three LEAP

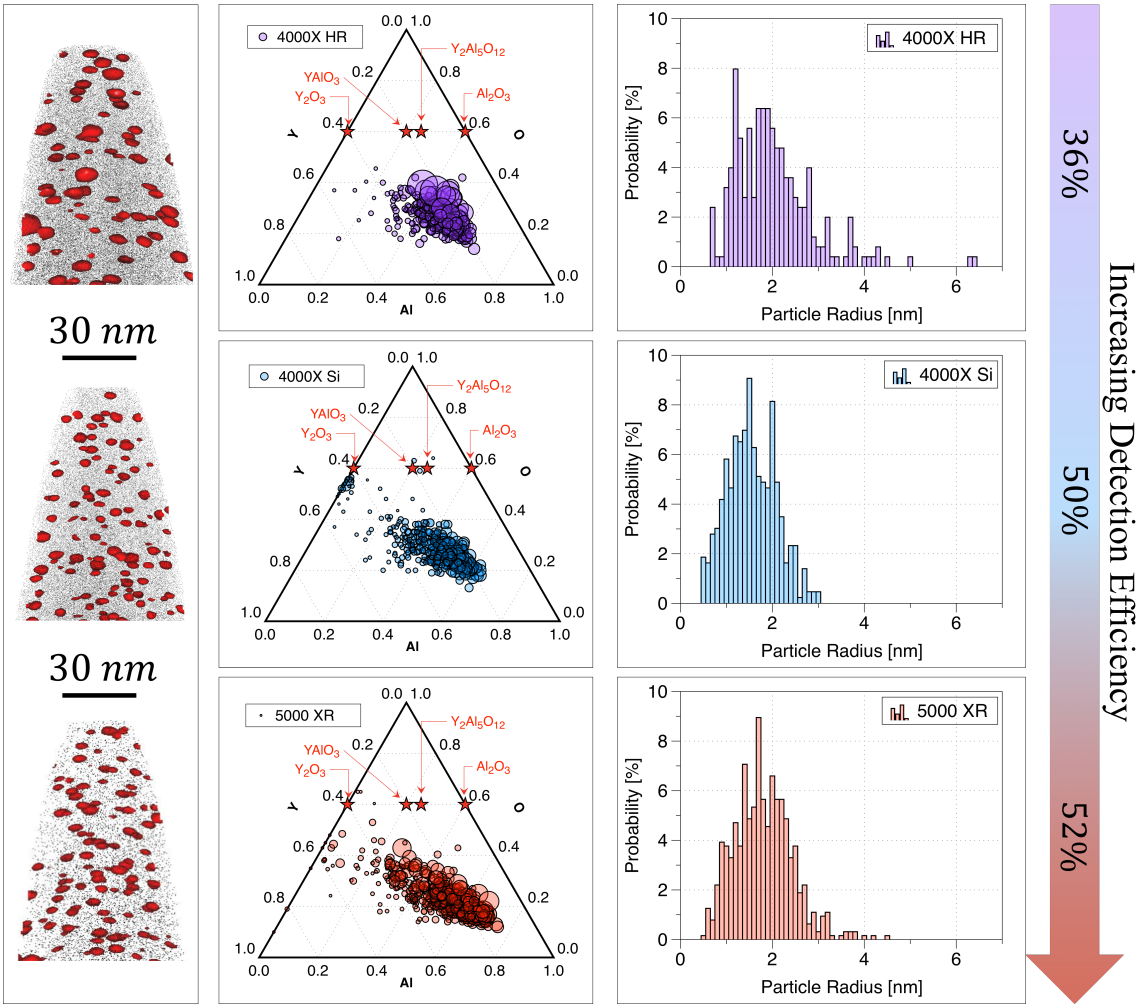


Figure 5.16. The effect of atom probe, and thus detection efficiency, on the composition and nanoprecipitate distributions for CrAZY ODS FeCrAl powder (ZY10C60) annealed for 60 min. at 1000°C. For consistency, all specimens were taken from fine-grained regions of the powder. Compared are specimens analyzed using the Cameca LEAP models 4000X HR (36% detection efficiency, purple), 4000X Si (50% detection efficiency, blue), and 5000 XR (52% detection efficiency, red). [225]

models. All three units show the same size dependency previously shown for Y and Al, shown the distribution tail in the ternary diagram. The slight decrease in the size of the tail in the 4000X HR model LEAP is because this control volume was smaller, which meant that less clusters were identified to be compared. The average radii for the 4000X HR, 4000X Si, and the 5000 XR models are 2.03±0.87 nm, 1.55±0.53 nm, and 1.80±0.63 nm with errors reported as one standard deviation from the mean.

It does not seem that the detection efficiency has a proportional impact on the precipitate size based on the control volumes analyzed. If the efficiency was biasing the results, and one element was preferentially lost in comparison to others, then the average precipitate size would have decreased with decreasing detection efficiency. However, since this linear trend was not noted, and since the ratios of the primary elements of interest (Y,Al,O) showed no significant change as a function of detection efficiency, it can be assumed that the precipitates in all samples, analyzed on all three LEAP models, can be analyzed together as one population for the same processing conditions after appropriate FWTM binning.

CHAPTER 6: Multi-scale Characterization of Nanoprecipitation in ODS FeCrAl Alloy Powders and Alloys

In the previous section, parity has been established between specimens analyzed using different APT models and for cases where powders have been either mechanical alloyed in different milling units or consolidated into bars. A detailed characterization was thus undertaken on the nanoprecipitate populations within each sample. For this analysis, individual control volumes in **Table A.1** were referenced to highlight pertinent features in certain samples. For the overall comparison of nanoprecipitate populations between samples annealed or extruded at different temperatures and times, all precipitates in all control volumes for the respective processing condition were analyzed together as one population to provide a more accurate representation of cluster compositions and sizes.

Prior to the APT and SANS analyses provided in this chapter, it is first important to understand how compositional variations within each sample will potentially affect the observed nanoprecipitate populations. **Table 6.1** presents the global compositions of the various samples investigated in this work. All samples beginning with "ZY" in **Table 4.1** represent ZY40H powder milled in the CM08 unit that were then annealed for various times and temperatures ex-situ. Each of their global compositions should thus average to be the same as that listed in **Table 6.1** for ZY40H-CM08. In addition, the aforementioned 106ZY10C1 and 106ZY10C8 specimens are the extruded alloy forms of the ZY40H-CM01 and ZY40H-CM08 milled powders, which is why the compositions between these specimens are highly similar. Of importance for all samples is the non-trivial C (0.08-0.3 at.%) and N (0.04-0.25 at.%), which will be shown in this chapter to fundamentally shift the precipitate populations seen within these alloys.

Table 6.1. Chemical compositions of powders (at.%) and alloys provided by DIRATS.

Sample	Form	Fe	Cr	Al	Zr	Y	O	C	N
Gas Atomized Powder	Powder	77.40	10.00	12.34	0.17	0.00	0.06	0.02	0.01
Milling Media	n/a	93.40	1.62	0.02	0.00	0.00	0.00	4.17	0.01
ZY40H-CM01	Powder	77.32	9.91	11.56	0.16	0.12	0.49	0.10	0.23
ZY40H-CM08	Powder	77.42	9.73	11.78	0.15	0.13	0.43	0.25	0.04
106ZY10C1	Extruded	77.55	9.73	11.58	0.16	0.13	0.42	0.08	0.21
106ZY10C8	Extruded	78.00	9.55	11.33	0.15	0.12	0.38	0.26	0.12
106ZY15C	Extruded	77.80	9.58	11.33	0.15	0.12	0.61	0.07	0.25
CrAZY_H1	Extruded	77.66	9.70	11.61	0.15	0.13	0.37	0.30	0.06

Table 6.2. Corrected nanoprecipitate compositions measured by APT. Errors are reported as one standard deviation from the mean. Compositions are reported in at.%.

Sample	R [nm]	N_p x10^{23} [m^{-3}]	$\boldsymbol{f}$ [%]	Fe	Cr	Al	Y	O	C	N
ZY10C15	1.56±0.64	4.77±1.47	1.14±0.01	57.90	6.62	11.76	11.62	11.43	0.10	0.02
ZY10C60	1.58±0.61	4.19±1.21	1.12±0.22	55.58	7.54	11.55	11.70	12.92	0.13	0.01
Y10C60	1.64±0.75	3.55±1.26	0.79±0.11	59.53	7.78	11.19	10.04	10.80	0.05	0.01
106ZY15C	2.08±0.75	1.11±0.18	0.86±0.21	57.01	8.41	11.73	9.59	12.51	0.18	0.01
ZY15C10h	2.16±0.65	1.79±0.01	0.95±0.05	58.53	8.87	11.41	10.60	9.35	0.29	0.04
ZY15C50h	2.82±1.16	0.58±0.01	0.83±0.02	51.24	7.77	11.07	13.43	15.38	0.25	0.02
ZY15C500h	4.07±1.21	0.12±0.03	0.47±0.04	60.89	7.11	8.39	9.40	11.88	0.18	0.01
CRAZY-H1	2.58±0.85	0.79±0.05	0.71±0.12	54.63	7.84	11.16	12.92	12.48	0.17	0.01

Throughout this chapter, the nanoprecipitate populations are compared, as are the compositions of the smallest nanoprecipitates within the microstructure. Thus, **Table 6.2** is referenced here at the beginning of the chapter summarizing the populations of each collection of APT specimens for each processing condition. Presented in this chapter is a comprehensive examination of the compositions and possible structures of these precipitates, while the thermal stability of these clusters is the focus of discussion in Chapter 7.

6.1. Effect of Added Zr on Observed Precipitate Populations

Due to the low number density and larger size distributions for precipitates in legacy recrystallized ODS FeCrAl alloys MA956 and PM2000 [88, 115, 156, 159, 169], much of the focus was turned away from these ODS FeCrAl alloys for nuclear applications and instead concentrated on the development of the ODS FeCr alloys that had a much finer dispersion of nanoclusters within the matrix. In-fact, some authors coined the term nanostructured ferritic alloys (NFAs) to distinguish the "superior" ODS FeCr alloys from the simply dispersion strengthened FeCrAl variants. It was not until enhanced oxidation resistance demands were sought for LWR accident tolerance or for compatibility with advanced reactor coolants that the ODS FeCrAl concept was reinvestigated. Dou and colleagues were able to refine the particle size of a Fe-16Cr-4Al ODS alloy of 6-7 nm diameter particles to 3.2 nm diameter particles simply by lowering the extrusion temperature from 1150°C to 1050°C [162]. However, the authors also found that by adding other elements with a strong affinity for O into the lattice like Zr or Hf, the particle size similarly shifted down to 4.8 nm and 4.3 nm diameter particles, respectively [105, 112]. However, for Fe-12Cr-6Al alloys developed at ORNL with similarly added Zr and Hf, the authors found that the nanoprecipitates appeared to be absent of Zr and enriched only in (Y,Al,O) with particle sizes comparable to those found for the Zr and Hf bearing alloys by Dou [99, 106]. Thus, for the ODS Fe-10Cr-6Al alloys developed in this study it is of interest to answer (1) what are the compositions of the smallest nanoprecipitates and (2) what is the role of Zr in these alloys.

In the as-milled ZY40H powder, all elements are uniformly distributed within the matrix. After the powder has been annealed, nanoprecipitates nucleate in both homogeneous and heterogeneous fashion accelerated by the high affinity of the constituent elements Cr, Al, Y, and Zr for impurity elements such as O, C, and N within the material. **Figure 6.1** clearly shows that the elements Y, Zr, and Al are all uniformly distributed within the matrix prior to annealing, as shown by the atom maps of these elements showing no significant clustering in the as-milled state. However, afterwards there is significant clustering, which is spatially correlated for the elements Y, Al, and the YO/AlO molecular ions associated with proximity to O during the field-evaporation process. Also shown in this figure is a coarser precipitate that has nucleated that is enriched in Zr, although the Zr is not associated with the fine clusters.

A closer look at a representative cluster in an annealed CrAZY alloy is presented in **Figure 6.2**, showing both the atom locations for each respective molecular species and a 1D concentration profile through a cylindrical region of interest (ROI) spanning the width of the cluster. The stacked bar graph in **Figure 6.2(b)** shows that the primary constituent elements within the cluster are Y, Al and O. Although there are a few Zr atoms in the surrounding control volume, these atoms appear to be dispersed uniformly throughout the region and are not statistically significant with respect to the clustering behavior shown for the other elements of interest.

To provide more evidence for the lack of Zr present in the fine-scale nanoprecipitate distributions measured for the numerous APT control volumes listed in CrAZY alloys and powders presented in **Table A.1**, a total of 3644 nanoprecipitates were simultaneously analyzed with specific interest in the reactive elements Y, Al, and Zr with impurity elements O and C.

Figure 6.3 presents this summarized data organized in two different graphs with atom percentages of Y, Al, Zr, O, and C normalized to the sum of these five atomic species. The first graph is organized as a function of nanoprecipitate radius. This image clearly shows that for these 5 elements only Y, Al, and O are the dominant clustering elements within the cumulative population of nanoprecipitates. To identify possible Zr

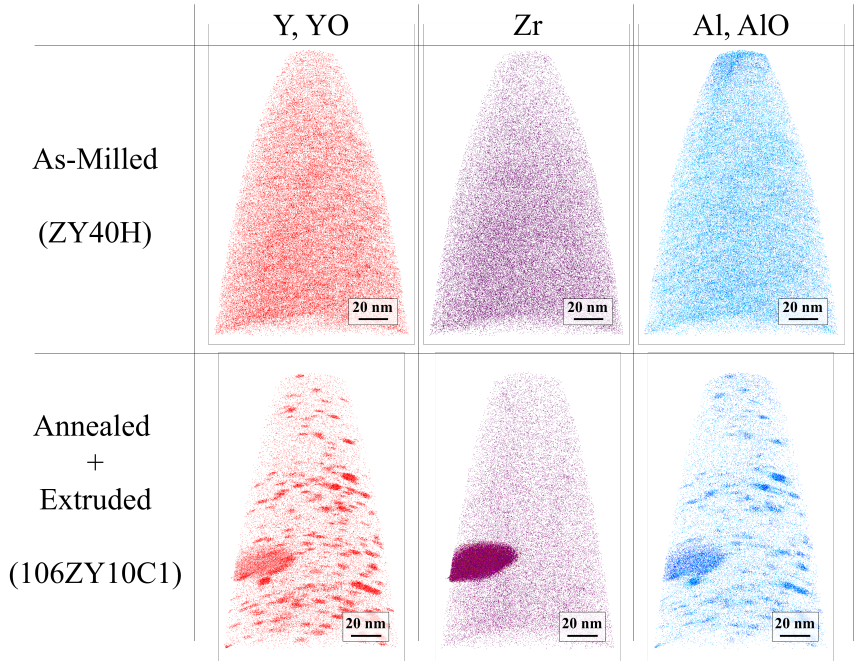


Figure 6.1. Atom maps showing atom maps in two representative control volumes for the As-milled powder (ZY40H) and for the extruded CrAZY alloy (106ZY10C1). Atom maps for (a) Y+YO, (b) Zr, and (c) Al+AlO are shown. [225]

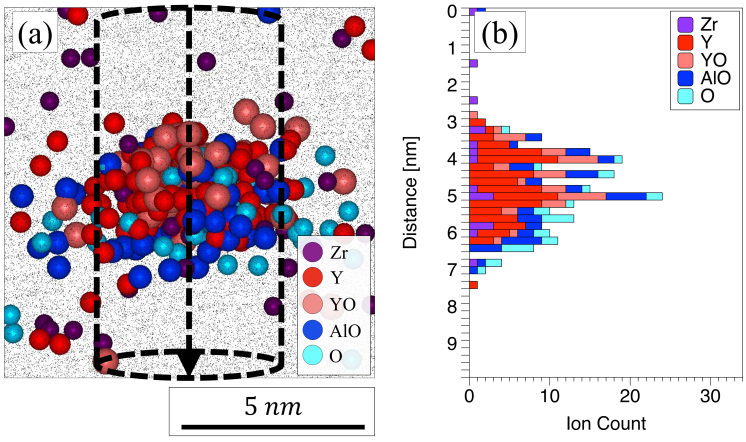


Figure 6.2. (a) A representative (Y,Al,O) nanocluster in the CrAZY ODS FeCrAl alloy is highlighted using atom maps of the constituent elements atop a matrix of black Fe matrix atoms. In (b) a 1D concentration profile through the precipitate is graphed showing increases in Y, YO, AlO, and O through the precipitate, but not Zr.

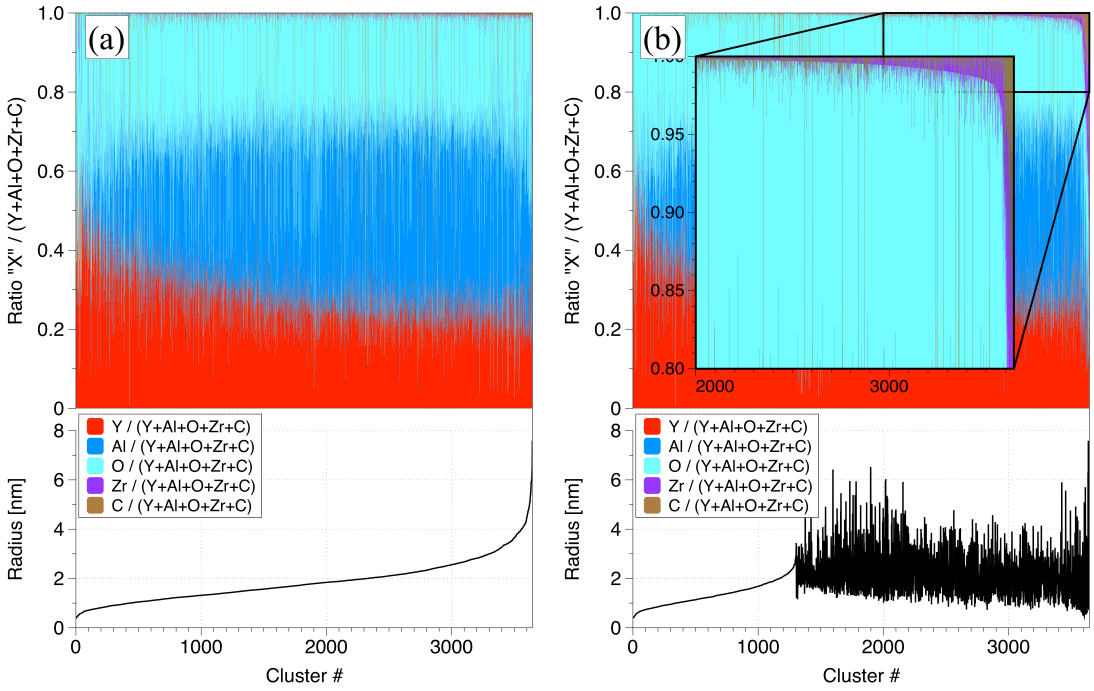


Figure 6.3. Stacked bar graphs illustrate the ratio of Y, Al, O, Zr, and C within each nanoprecipitate (normalized to these 5 elements) in the total population of 3644 total precipitates identified in the CrAZY APT control volumes in this work. In (a) the precipitates are arranged along the x-axis as a function of increasing measured precipitate radius. In (b), the precipitates are arranged as a function of increasing Zr content.

enrichments in these precipitates, these 3644 precipitates were then sorted by the Zr-enrichment within each cluster. The first ~1000 precipitates contained no Zr atoms, which is the reason why the cluster radius plot is smooth for the first third of the cluster population. For cases where Zr appears to have a non-zero enrichment, a magnified portion of the stacked bar plot shows that in cases where Zr appears to exist within the precipitates, C also shows an increasing enrichment trend. As is shown in the subsequent images, this Zr and C enrichment for these smallest precipitates is an artifact associated with the co-precipitation of smaller (Y,Al,O) clusters with larger Zr and C-rich precipitates within the reconstructed APT samples.

Although APT provides a mechanism for the detailed investigation of smaller control volumes, electron microscopy methods allow for a broader visual inspection of coarser nanoprecipitate populations in these CrAZY alloys. STEM+EDS was thus coupled with the APT data collected in this work to provide compositional information for larger fields-of-view for comparison. The high angle angular dark field (HAADF) STEM image of a region of sample 106ZY10C8 along with EDS maps of elements Al, N, Zr, and C are illustrated in **Figure 6.4(a-e)**. Two populations of coarser precipitates are identified this is region: Al-rich precipitates (darker precipitates in the HAADF-STEM image) and lighter precipitates enriched primarily in Zr. A MVSA analysis allows for the discretization of the elemental maps as a function of position, which is possible for STEM due to the ability of the electron beam to raster across the specimen surface. Three different discretized regions were identified by the MVSA algorithm: (1) the background FeCrAl matrix illustrated in black, (2) the Al-rich precipitate population depicted in green, and the Zr-rich precipitates shown in red. The deconvoluted EDS spectra for these three regions and the overlaid EDS maps are shown in **Figure 6.4(f-g)**. From the EDS spectra results, the Zr-rich precipitates appear to be enriched in either N, C, or both, with possibly some Cr also being higher in enrichment in comparison to the surrounding matrix. For the Al-rich precipitates, C does not appear to be a constituent in the precipitates; instead, Al seems to also be associated with Fe and N. The fact that there exists a significant Fe peak in the Al-precipitates but not in the Zr precipitates provides

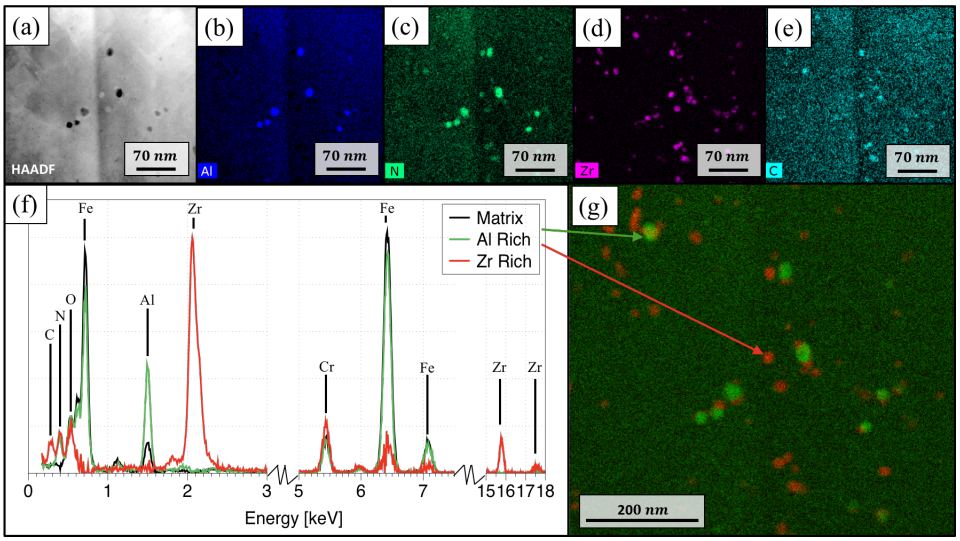


Figure 6.4. STEM+EDS results for the larger populations of precipitates in the ODS FeCrAl alloy 106ZY10C8. Multivariate statistical analysis results show two populations of precipitates (Al,Fe,N) + (Zr,C,N) and the background FeCrAl matrix. [225]

credence to the possible enrichment of the Al precipitates with Fe in addition to the observed increase in N.

The precipitation of these multiple populations of Al-rich and Zr-rich precipitates has been verified in an APT control volume for sample 106ZY15C. Although the extrusion temperature for this sample is 50°C higher than for the sample investigated by STEM+EDS, the types of nanoprecipitates are not expected to be affected by the small relative change in extrusion temperature. In addition to the fine-scale nanoprecipitates shown by Y and YO atom maps in the Fe matrix (**Figure 6.5(a)**), there exist larger precipitates in this control volume that have been highlighted by Zr and Al isoconcentration surfaces. A 1D concentration profile through the Zr-rich (purple) precipitate showed simultaneous enrichments in both C and N in equal proportions.

The ratio of Zr to the sum of the C and N contents indicate that this precipitate is of a composition equivalent to the Zr(C,N) phase. The concentration profile through the Al-rich precipitate shows an unexpected result. The ratio of Al to Fe is 3:1 within the Al-rich region, which is consistent with the $Al_{13}Fe_4$ iron aluminide phase. Although there appears to be a slight enrichment of N, it is unclear if this increase is due to the peak

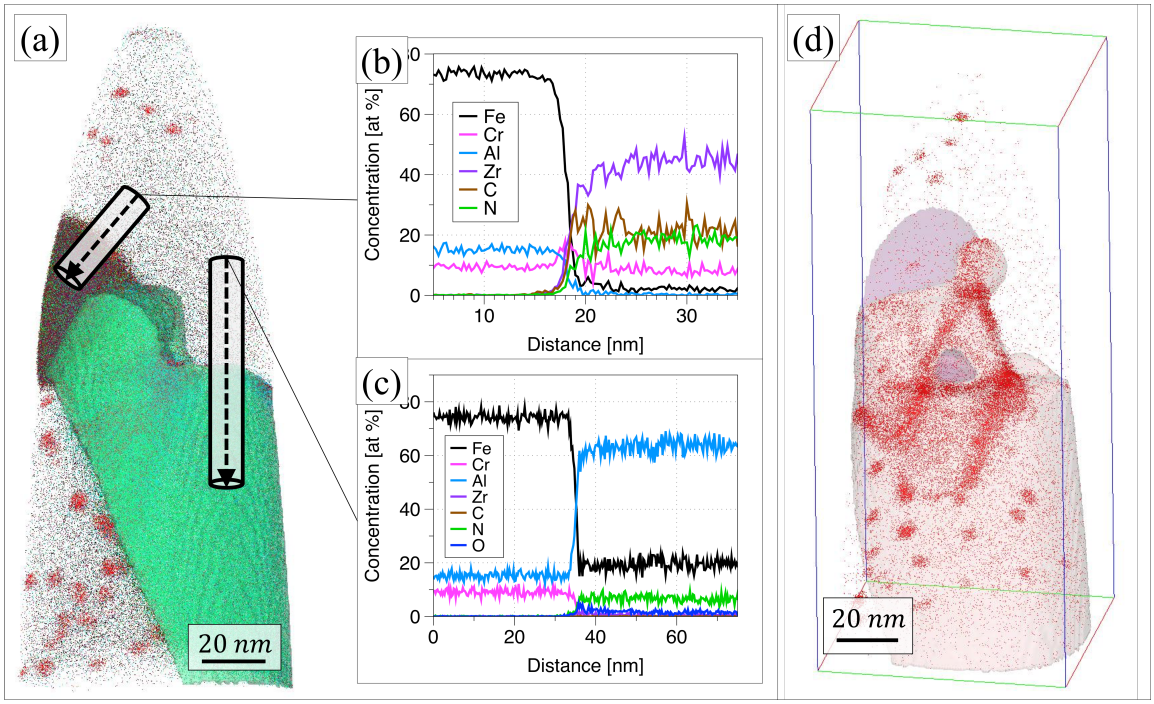


Figure 6.5. APT reconstruction of CrAZY alloy (106ZY15C) showing three types of precipitates within the control volume: (a) the smallest (Y,Al,O) precipitates shown using red atom maps of Y, (b) a (Zr,C,N) rich precipitate shown using the Zr, C, and N atom maps and a corresponding 1D concentration profile, and (c) a (Al,Fe)-rich nanoprecipitate highlighted using a green 25% Al iso-concentration surface and a 1D concentration profile into the precipitate. In (d), overlaid Y and YO atom maps indicate segregation to Al-rich precipitate boundaries. [225]

overlaps of Si and Al for the 14 Da peak in the mass-spectrum or if there is a N enrichment in the peak consistent with the STEM+EDS results. The precipitation of this $Al_{13}Fe_4$ phase is unexpected since the Fe and Al would have been uniformly dispersed throughout the matrix even in the gas atomized powder prior to mechanical alloying in a ratio of 1:7 for Al:Fe. Thus, the nucleation of this iron aluminide phase would have been the least likely with respect to the Al-Fe binary phase diagram. The enrichment of Fe in these Al-precipitates is consistent with the STEM+EDS results.

The initial dispersion of the alloying elements and the impurity elements in the as-mechanically alloyed powder also strongly affects the local precipitation in each control volume. Consider the APT control volume for sample 106ZY10C8 highlighted in **Figure 6.6**. In this reconstructed specimen, the Zr-rich precipitates are again identified, but there also appear to be Cr-rich precipitates also enriched in C. Thus, it appears that while Zr appears to be competing with Al for N within the matrix, Zr is also competing with Cr for the formation of C-rich precipitates within the matrix. One precipitate enriched in Zr shows enrichment in only C with an equal stochiometric ratio, suggesting that the ZrC phase as formed (**Figure 6.6(a)**); however, for the other Zr-rich precipitate noted in this control volume, there appears to be a core/shell structure (**Figure 6.6(b)**). The core is enriched in C and N in equal ratios, while the shell of the Zr-rich precipitate is only enriched in C. It thus appears that Zr(C,N) initially nucleated due to the local concentration of C and N in proximity to the Zr atoms within the matrix, but as the N atoms were ultimately sequestered, the remaining C atoms continued to react with available Zr within the lattice, forming a ZrC shell on the outside of the Zr(C,N) precipitate. Finally, there appear to be two Cr-rich precipitates also enriched in C. Due to the higher affinity of Zr for C in comparison to Cr [103], this suggests that the local Zr concentration was fully consumed and the remaining C atoms reacted with the matrix Cr and Fe atoms. The ratio of the Fe and Cr concentration to the C content in this precipitate matches what would be expected for an $M_{23}C_6$ type carbide (**Figure 6.6(c)**).

One interesting phenomenon in the precipitation of the coarser Al-rich nanoprecipitates is highlighted both in **Figure 6.5** and also in **Figure 6.7**. Though arguably less important

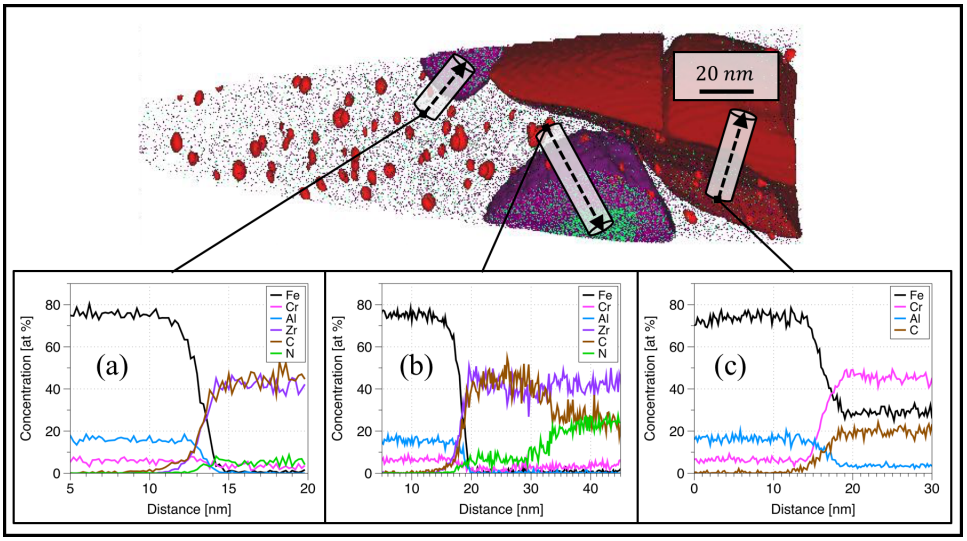


Figure 6.6. APT reconstruction of CrAZY powder (ZY10C60) showing a variety of different precipitates. The reconstructed control volume contains (a) a precipitate with composition matching ZrC, (b) a (Zr,C,N)-rich precipitate with a core/shell type structure, and (c) a (Fe,Cr,C)-rich precipitate highlighted as a brown 5% C isoconcentration surface. The smallest (Y,Al,O)-rich precipitates are respresented as red 1.5% (Y,YO,AlO) isoconcentration surfaces. [225]

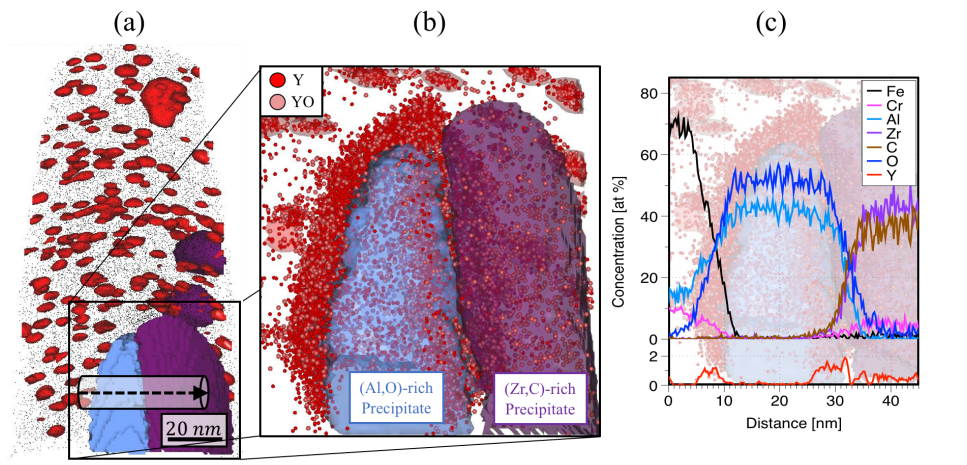


Figure 6.7. (a) a reconstructed APT specimen for ZY10C60 showing the high-density of red (Y,Al,O) precipitates in red and the co-precipitation of an (Al,O)-rich and a (Zr,C) rich precipitate. In (b), a semi-transparent 25% Al iso-concentration surface in blue and a 10% Zr iso-concentration surface in purple are overlaid with an atom map of Y and YO, showing a Y-rich shell surrounding the Al-bearing precipitate. A 1D concentration profile through the two precipitates in (c) highlights the Y-rich shell and the corresponding increases constituent elements for the two precipitates. [225]

from a processing perspective, there appears to be a strong attraction between Y atoms and coarser Al-rich precipitates noted in the APT control volumes. Consider the (Al,O)-rich precipitate that has co-precipitated alongside a precipitate enriched in (Zr,C) visualized using blue Al and purple Zr isoconcentration surfaces in **Figure 6.7**. Overlaying the Y and YO atom maps and the two isoconcentration surfaces in **Figure 6.7(b)** appears to show a Y and O-rich shell surrounding the Al-rich precipitate. The 1D concentration profiles in **Figure 6.7(c)** indicate that these two precipitates are in-fact Al_2O_3 and ZrC. The atom map and the concentration profile indicate increases in Y concentration at the periphery of the alumina precipitate in the form of an Y-rich shell. In addition, the previously identified $Al_{13}Fe_4$ precipitate in **Figure 6.5(d)** also shows the same Y and YO-rich shell surrounding the Al-rich phase. It appears that in **Figure 6.5**, there at least four co-precipitated iron aluminide precipitates, with precipitate boundaries highlighted by this Y-rich shell. This nucleation of the Y-rich shell suggests that the high affinity of Y for reaction with Al and O in the matrix for the formation of the smallest (Y,Al,O) precipitates has resulted in the local attraction of Y and O atoms to the surface of coarser Al-rich precipitates within the matrix as well.

The role of Zr in precipitation in these alloys is summarized as follows: when C and N are present within the microstructure, Zr will preferentially sequester impurity C and N within the microstructure for the formation of MX type carbides, where M = Zr and X = C, N, or both. When impurity elements are removed from the microstructure, Zr may compete with Al and preferentially react with Y and O instead of Al to form the fluorite (Zr-Y-O) phase previously identified by Dou et al. [105]. This is an important result, because the addition of Zr can be tuned based on the impurity compositions expected based on the mechanical alloying and processing route. It has been previously shown that the presence of coarse $M_{23}C_6$ type particles in the ODS matrix can deteriorate the mechanical properties of the alloy, specifically with regards to fracture toughness [226]. As for the competition between Al and Zr for oxide nanoprecipitation in the absence of C and N in solution, although adding Zr has been shown to refine the oxide-distribution, it has also been shown that the (Y,Zr,O)-rich oxides exhibit faster coarsening kinetics at

high temperature in comparison to (Y,Al,O)-rich precipitates [79]. Since nano-oxide dispersions have been proven for CrAZY alloys in this work that rival and arguably surpass the number densities reported for the previously reported (Y,Zr,O) oxides, it appears that a careful control of the temperature dependent consolidation methodologies used for the production of these ODS FeCrAl alloys is a more important factor for the development of high sink-strength alloys for nuclear applications than alloying additions for the purpose of changing nanoprecipitate dispersions.

6.2. Compositional Measurements using APT

To this point, the compositional variation of the smallest nanoprecipitates has been presented in a qualitative manner for general comparisons between different APT reconstructions. In this section, a more detailed compositional investigation of the smallest nanoprecipitates is undertaken for the purposes of identifying the phase of these fine-scale dispersions. Since Zr has been shown not to play a role in the formation of the smallest nanoprecipitates only the ratios of Y, Al, and O will be considered in the current discussion.

The measured Y, Al, and O contents in the smallest nanoprecipitates is a strong function of the methodology used to correct for possible spatial overlaps and local magnification effects associated with the APT technique. As discussed previously in Chapter 4, the correction of nanoprecipitate compositions in ODS FeCr alloys is a bit simpler since the matrix constituents (Fe and Cr) are different than the elements comprising the nanoscale precipitates (Y, Ti, and O). However, in the case of these ODS FeCrAl alloys without Zr interaction with O, Al is in both the matrix and in the precipitates. The current literature on nanoscale precipitation has not yet tackled the challenge of attempting to describe the Al partitioning between the matrix and the precipitates. Depending on the differences in clustering kinetics in comparison to the kinetics of Al diffusion through the Fe matrix, there is a chance that the local depletion of Al from the surrounding matrix during nucleation and growth of the (Y,Al,O)-rich clusters results in a Al-depleted, (Fe,Cr)-rich shell surrounding the precipitates. However,

the averaging of 50 1D concentration profiles through the analysis "z" direction for these precipitates (**Figure 4.15**) did not show a clear Cr peak at the matrix/precipitate interface in comparison to the work London et al. performed on ODS FeCr alloy 14YWT [179].

Since the Al-partitioning between the nanoscale precipitates and the matrix is unknown for the ODS FeCrAl precipitates, four different cluster composition corrections were implemented to decide on a method to apply to all nanoprecipitates in this study. All of these methods were applied using the output file for the clusters identified using the maximum separation method. The first correction is the simplest and most erroneous, and involves only correcting for peak overlaps through the comparison of the peak-deconvolution bulk composition in IVAS with the matrix composition provided by the cluster output file. Of course, this results in almost 80% of the cluster atoms being represented by Fe and Cr atoms, which is not representative of reality for clusters in ODS alloys. The cluster compositions associated with this method are considered the "Original Compositions" in the subsequent comparison of methodologies. The second composition correction method accounts only for the increases in reduced atomic point density across the nanoprecipitate in Chapter 4. This method assumes that the decrease in point density across the precipitates is minimal due to local magnification effects and that the compositions can be corrected by simply removing the predicted number of matrix atoms due to spatial overlaps from the clusters in proportion to the matrix. The compositions of the nanoprecipitates measured using this method are referred to as "density corrected" compositions.

The last two methods for cluster correction implemented are based on the chemical composition correction (CCC) model proposed by Hatzoglou, where the compositions are corrected for the reduced density, the cluster's geometric shape factor (due to local magnification effects), and due to differences between the ideal atomic density of the precipitates and the ideal atomic density of the matrix [177]. In the implementation of this state-of-the-art model for cluster composition correction, two scenarios were assumed: (1) there exists no-shell surrounding the (Y,Al,O) precipitates, and the compositions were corrected simply from equivalent matrix compositions and (2)

there exists a (80% Fe, 20%Cr)-rich shell surrounding the nanoprecipitates that contributes to 80% of the spatial overlaps associated with the APT trajectory aberrations in comparison to 20% for the FeCrAl matrix. The assumption that the shell contributes for 80% of the spatial overlaps was made to provide consistency between these results on ODS FeCrAl alloys and the procedure used by Hatzoglou for the analysis of ODS FeCr alloys [177], and the assumption that this shell is 20% enriched in Cr relies on the compositional results obtained by London [179].

Figure 6.8 provides stacked bar graph comparisons for the elements Fe, Cr, Al, Y, and O measured within each precipitate based on each of the four methods for analyzing the cluster data. The original cluster compositions show the substantial Fe and Cr contents measured in most precipitates, suggesting the need for additional correction. The density corrected cluster compositions in **Figure 6.8(b)** shows slight decreases in Fe and Cr, but the significant remaining matrix atoms illustrates that this method is not a perfect method to target the physical cluster compositions. The use of the CCC method provides cluster compositions that have erased essentially all of the Fe and Cr within the precipitates, but the constituent Y, Al, and O contents vary substantially as a function of the assumption used about the surrounding local environment of matrix atoms. For the case where a shell is not assumed, the subtraction of the equivalent matrix FeCrAl composition results in the subtraction of almost all of the Al within the clusters. For the case where a (Fe,Cr)-rich shell is assumed to contribute to 80% of the spatial overlaps, the cluster compositions show a more realistic distribution of Y-Al-O percentages.

Comparing these cluster compositions with expected stochiometric compositions, each cluster for each of these methods is plotted on a ternary diagram in **Figure 6.9** with the diameter proportional to the nanoprecipitate size. Furthermore, only the Y-Al-O contributions for each cluster is considered. The reduced density approach narrows the spread of the cluster composition distribution slightly in comparison to the original cluster compositions. What is more interesting is the distribution of precipitate compositions when the CCC method is applied with the shell or no-shell assumption. Because the Al contents in the no-shell approach were largely subtracted from the

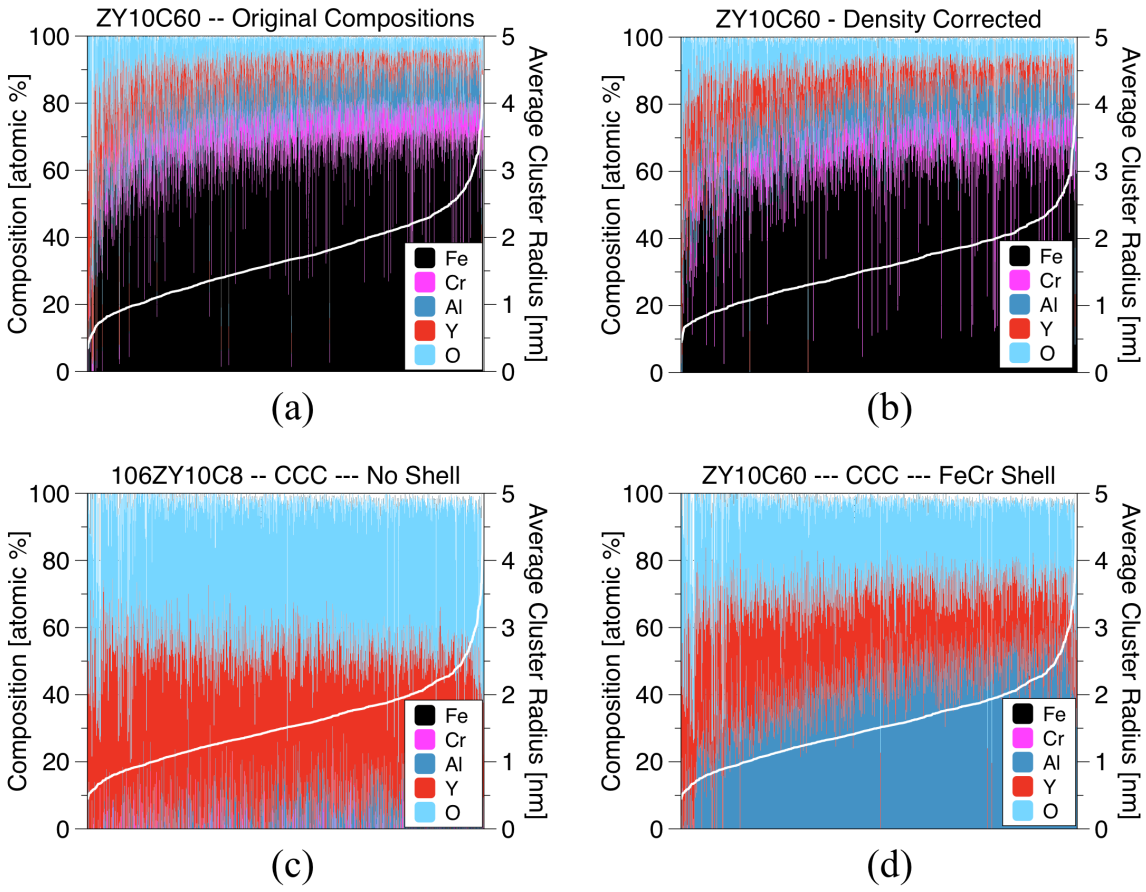


Figure 6.8. (a) the average uncorrected (as-measured APT) cluster compositions for 1141 clusters analyzed in the ZY10C60 specimens showing an abnormally large Fe+Cr content. The (b) reduced density corrected cluster compositions showing insufficient subtraction of Fe and Cr from the matrix. The application of the CCC (reduced density and shape factor) methodology has also been applied for (c) the case where FeCrAl matrix is erroneously measured in the precipitates and (d) the case where an Al-depleted, (Fe,Cr)-rich shell exists locally around the precipitates. [225]

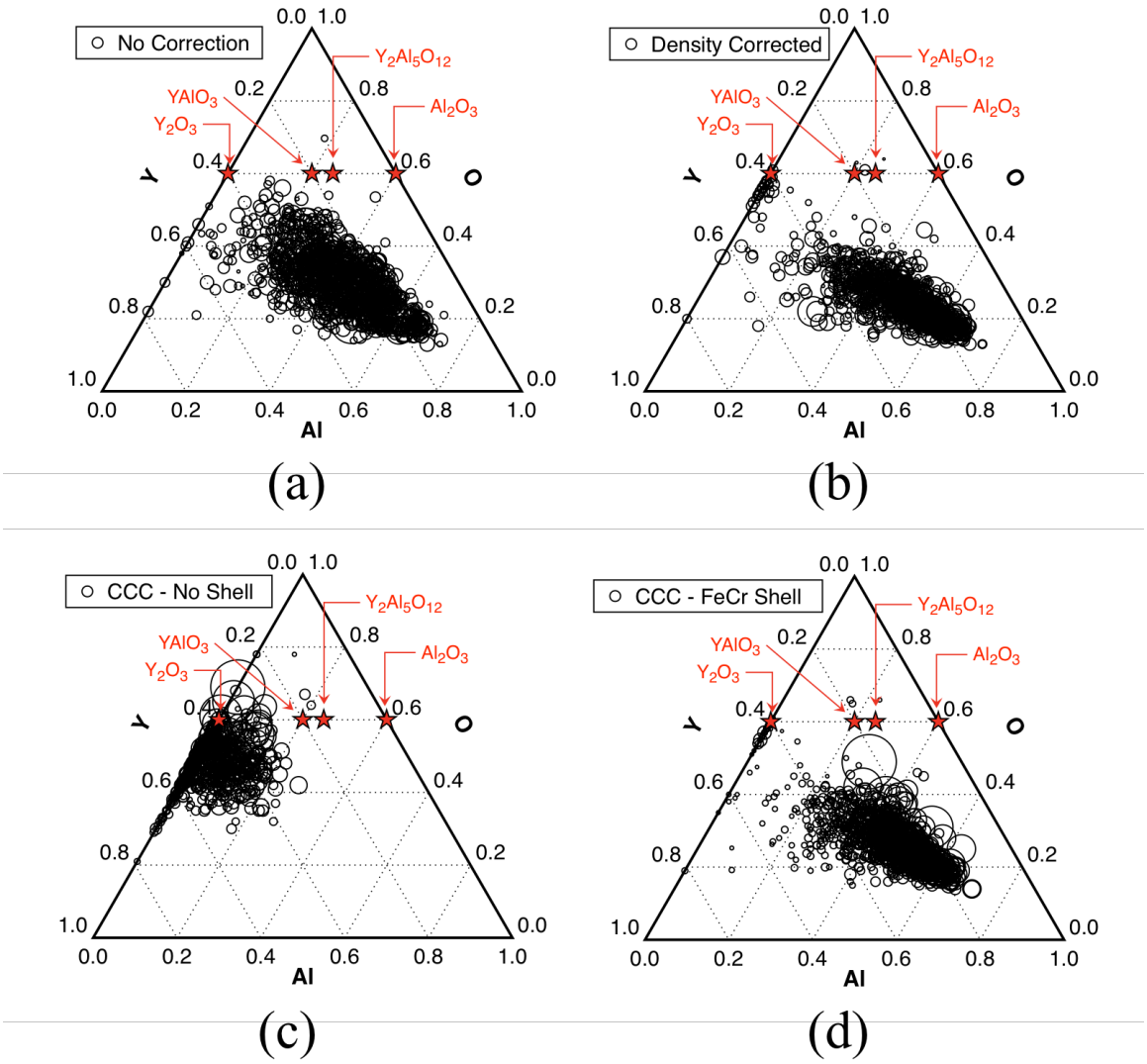


Figure 6.9. Ternary diagrams for 1141 ZY10C60 clusters are illustrated for four compared conditions: (a) the uncorrected normalized Y, Al, and O contents measured in each cluster, with point diameters plotted proportional to the precipitate size, (b) the cluster compositions after density-correction, (c) the cluster compositions corrected using the CCC method assuming no Cr-rich shell surrounding the precipitates, and (d) the applied CCC method assuming that a (Fe,Cr) rich shell exists that is responsible for 80% of the trajectory abberations.

precipitates using this CCC model, the nanoprecipitates shift to a stochiometric phase that would be consistent with Y_2O_3. This is a non-physical result since it is clearly shown in the APT atom maps (**Figure 6.1**) and concentration profiles (**Figure 4.15**) that Al concentration increases across the nanoprecipitates. For this reason, the no-shell CCC approach, and the approach presented previously by Williams [178] for ODS FeCr nanoprecipitate compositional corrections, is invalid for the current system with Al addition. In the case where an Al-depleted shell is assumed, the density corrected cluster compositions match well to those measured using the CCC model with the shell applied. It is important to note that this agreement between the density corrected model and the CCC-shell model does not give validity to either of the approaches. Instead, the agreement between these two approaches only comes from the preferential subtraction of the Fe and Cr measured through the density correction model.

To preserve the Al-content within the nanoprecipitates, and because the presence of an Al-depleted shell has not been proven for these precipitates, for the corrected precipitate compositions reported in **Table 6.2** the reduced density approach has been used for all specimens measured in this work. This results in a high Fe and Cr level measured in all precipitates, but does not result in erroneous Y, Al, and O ratios, which are the more important factors in the estimation of the potential stochiometric phases for these precipitates. Irrespective of the cluster composition correction algorithm used, the large spread in precipitate compositions shows that none of the correction methods yield compositions equal to stoichiometric line compounds.

Now that a methodology has been chosen to systematically compare the cluster compositions of each APT sample, the next step in the compositional comparison is to determine the relative Y-Al-O composition as a function of cluster size. **Figure 6.10** presents three different plots that provide a substantial amount of compositional information for 1141 nanoprecipitates measured in multiple APT specimens for CrAZY powder annealed for 60 min. at 1000°C (ZY10C60). This sample was chosen due to the high number of samples analyzed for this particular set of experimental conditions, although a similar distribution of results has been noted for different annealing times and

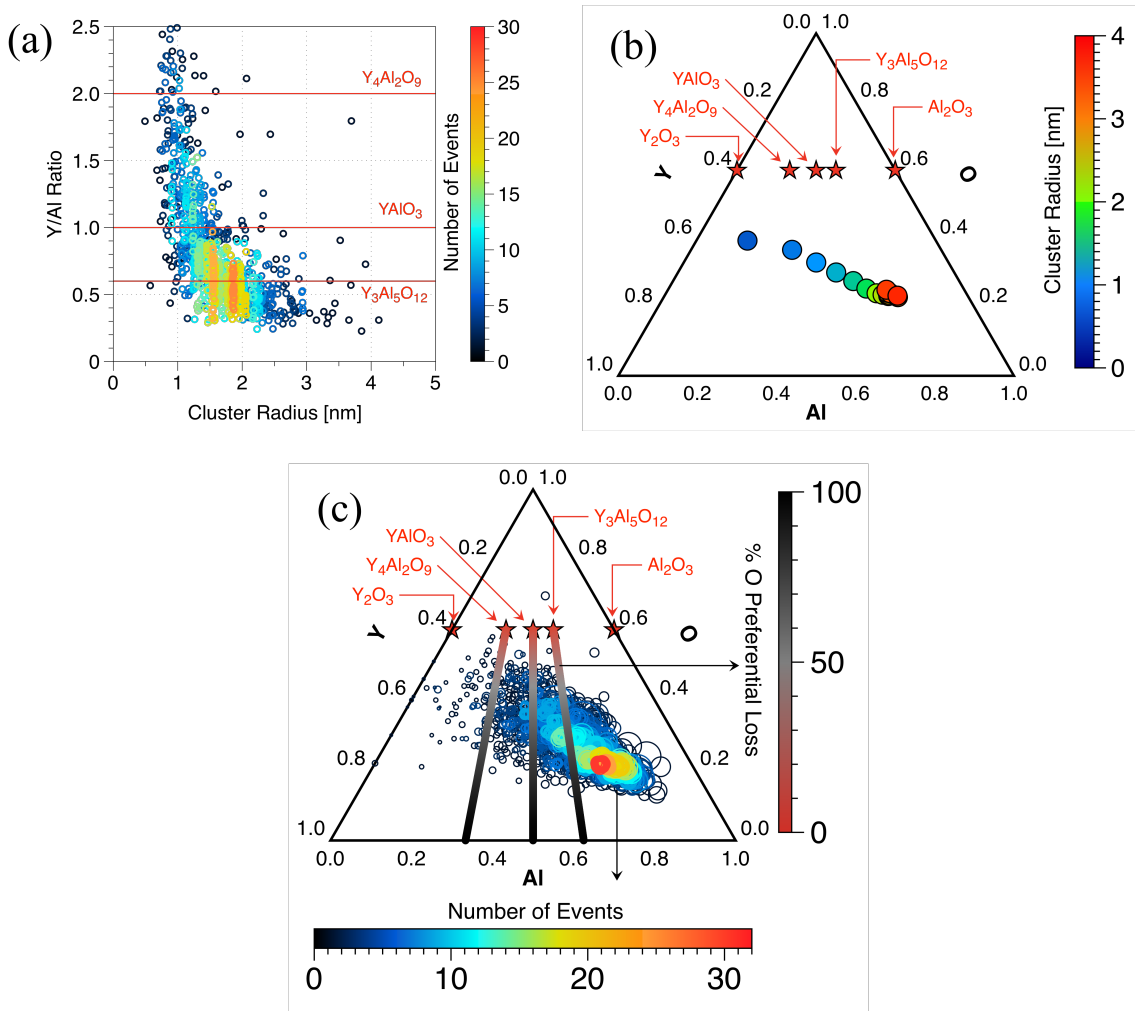


Figure 6.10. For the ZY10C60 specimens investigated in this work, shown are (a) the frequency hit map for the Y/Al ratio as a function of precipitate size and (b) the corresponding size dependency of the ternary Y-Al-O diagram (bottom). Finally, the size dependency of the nanoprecipitates for the ternary diagram is shown in addition to the expected stochiometric (Y,Al,O) compositions as a function of omitted measured oxygen content are overlaid, showing substantial underestimations of oxygen content in all nanoprecipitates at for all sizes. [225]

extrusion temperatures (although some possible variations exist as a function of these processing variables, which are discussed later in this work). First, the relative ratios of Y to Al were analyzed as a function of nanoprecipitate size, which is presented in **Figure 6.10(a)**. There appears to be a strong dependence on the Y/Al ratio as a function of increasing precipitate size at small cluster radii. For precipitates with an average radius measuring lower than 1 nm, the amount of Y measured in each precipitate is much greater than the measured Al content. This is most likely an APT artifact associated with the envelope applied to the cluster in the maximum separation method due to the small sizes of these precipitates. This region of precipitates in the size distribution only accounts for 12.8% of the total cluster population, and is not representative of the average cluster. To illustrate this, a frequency hit map is presented in the same image, with the number of overlapping instances illustrated in the color bar on the right of the image. The highest hit frequency corresponds to a Y/Al ratio around 0.6, which is consistent with the $Y_3Al_5O_{12}$ (YAG) phase.

If O is added to the discussion, the same trend is noticed on the ternary Y-Al-O diagram. To better illustrate the trend, **Figure 6.10(b)** shows the average measured and density corrected cluster composition for cluster radii ranging from 0.5-4 nm in size. Again, as the size increases, shown in the corresponding color bar, the composition moves linearly through the ternary diagram, but minimal shifts in the measured composition are noted as the precipitate size increases beyond 2 nm in radius. In comparison to the stochiometric cluster compositions shown in the figure, the oxygen content is severely underestimated for these (Y,Al,O) precipitates. **Figure 6.10(c)** adds this last layer of complexity to the ternary plot. In this image, not only is each cluster shown and color coded as a function of hit frequency, but tie-lines are drawn from the expected stochiometric compositions as a decreasing function of O content. It is readily shown that these precipitates are underestimating the O content by over 60%, which is well above the loss of oxygen commonly seen using the APT technique for ODS FeCr alloys. One possible reason for this abnormally low O content in the clusters is due to more diffuse detector hits of O atoms in comparison to the Y or Al atoms [178]. This

larger geometric spread in O atoms is shown for a variety of clusters in **Figure 6.11**. In addition to the visualization of the cluster distribution in **Figure 6.11(a)**, in **Figure 6.11(b)** illustrates the distribution of atoms for Y, YO, AlO, and O ions, respectively. In comparison to the localized hits of the other atoms in the clusters, the O atoms are quite diffuse. It has previously been shown in Al-alloys that for small precipitates <10 nm, the local variations in evaporation fields between precipitates and the surrounding matrix can create chromatic aberrations that affect the lateral positions of cluster ions [227]. Thus, in addition to the possible molecular ion dissociation of the O_2^+ molecular ion near the field-emitter [213] and other local magnification effects, it also appears that chromatic aberrations may be affecting the lateral locations of O atoms in the vicinity of the precipitates. Thus, with the current envelopes identifying clusters using the Y, YO, and AlO ions, a substantial amount of O appears to be selectively omitted from the nanoprecipitate compositions **Figure 6.10(c)**.

The variation of nanoprecipitate compositions with varying annealing/extrusion temperatures and increasing annealing times are reported for each sample in **Table 6.2** using the previously described density correction methodology. Relatively consistent compositional results are noted for all specimens, but there does appear to be a transition in nanoprecipitate compositions at very long annealing times. To visually show the variation of nanoprecipitate distributions as a function of temperature and annealing time, consider **Figure 6.10**, which compares ternary diagrams for each collection of APT specimens as a function of temperature (in color) at each annealing time. **Figure 6.12** shows that in all samples, a significant deviation from expected stochiometric oxides exist due to the underestimation of O content due to aberrations previously described; however, trends can still be noticed as a function of temperature and time. For specimens annealed for 60 min. at increasing temperature, the composition appears to shift toward greater Y/Al contents, which suggests that there may be an attempted transition from the $Y_3Al_5O_{12}$ (YAG) to $YAlO_3$ (YAP) with increasing powder annealing temperature. Furthermore, with increasing annealing time at 1050°C, a similar shift in nanoprecipitate hit maps on the ternary diagram shows the same transition from YAG to YAP. This will

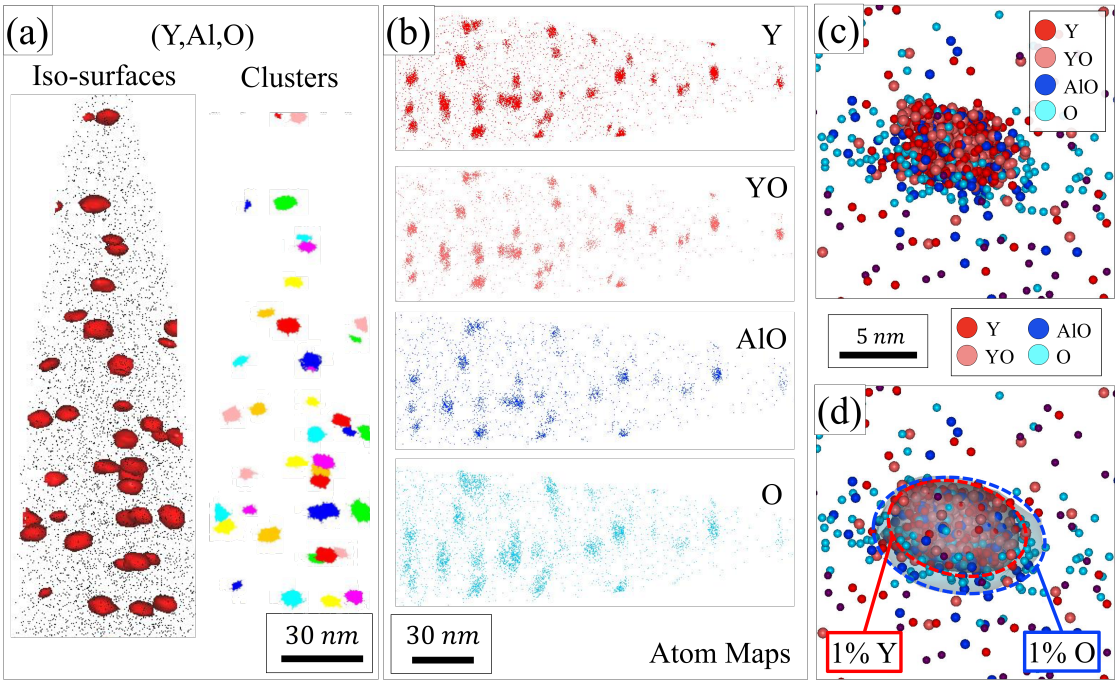


Figure 6.11. (Y,Al,O) precipitates in a CrAZY_H1 control volume shown by (a) 1.5% (Y,YO,AlO) isoconcentration surfaces and (b) through identification through the maximum separation method. In (b), the atom maps for Y, YO, AlO, and O atoms are shown. Similarly for one representative precipitate, the Y, YO, AlO, and O atoms are illustrated in (c) while 1% atomic isoconcentration surfaces are overlaid for Y and O atoms in (d).

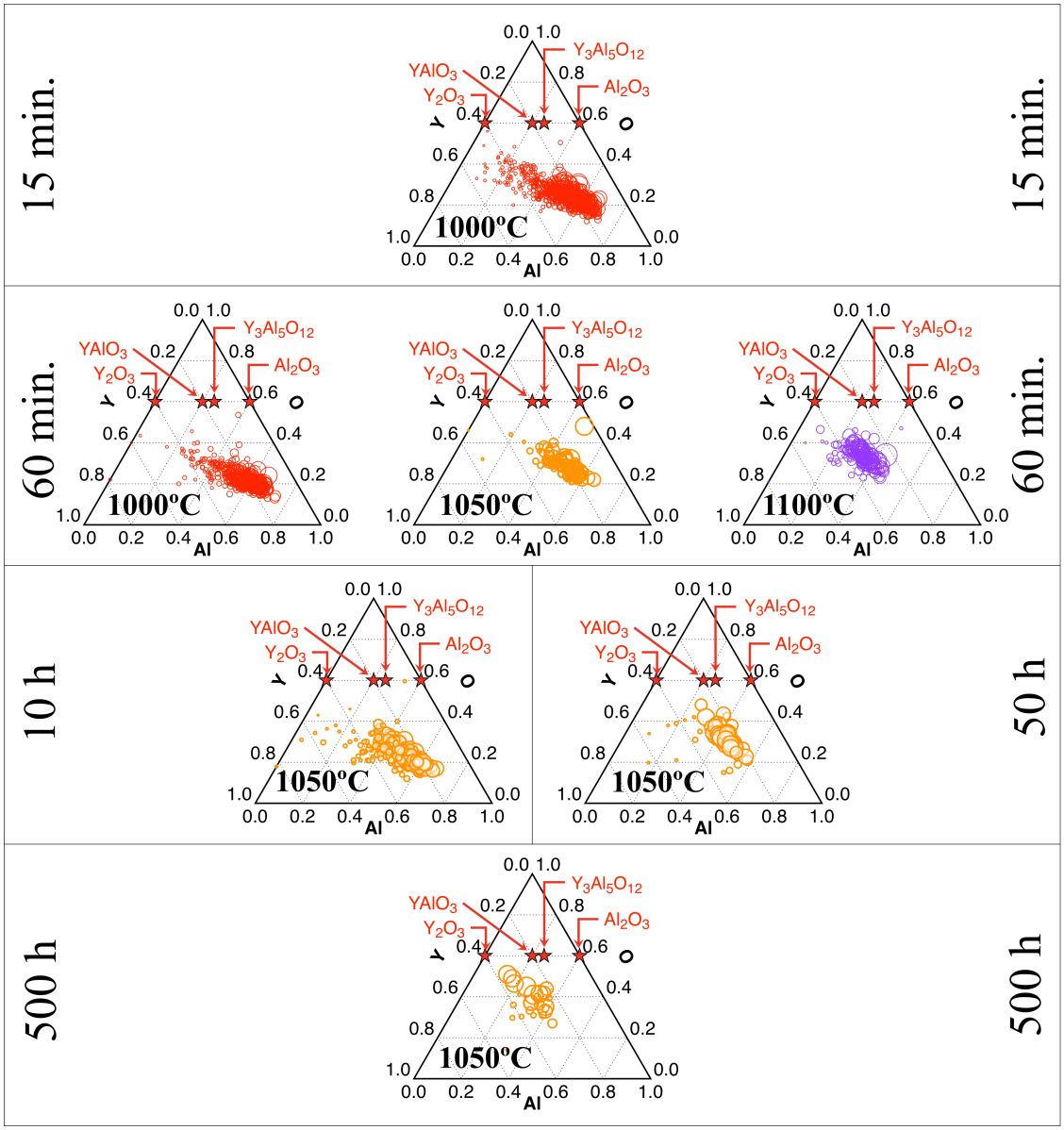


Figure 6.12. Ternary diagrams for CrAZY powders annealed at either 1000°C (red), 1050°C (orange), or 1100°C (purple), for various times. Highly consistent clustering is found for all samples, and subtle compositional trends as a function of temperature at 60 min. or as a function of time at 1050°C are noted.

be later discussed in Chapter 7 when quantifying the nanoprecipitate coarsening kinetics for these clusters.

6.3. Structure Identification using SANS

Due to the significant artifacts associated with the APT investigation of the smallest (Y,Al,O) nanoprecipitates identified in these CrAZY alloys, a magnetic SANS measurements were made on as-milled CrAZY (ZY40H-CM08) powder annealed for 15-120 min. in a box furnace. Prior to the magnetic SANS measurements, non-magnetic ex-situ SANS measurements were performed as a proof-of-concept to ensure that the nanoprecipitate dispersions within these ODS FeCrAl alloys could be resolved using the SANS technique. This was performed because Alinger was previously unable to resolve the nanoprecipitates in ODS FeCrAl alloy PM2000 in his neutron scattering studies [115, 186]. After the successful non-magnetic ex-situ experiment, the magnetic SANS measurements were taken on the five powder samples, including the as-milled powder and the four powder samples annealed ex-situ for 15-120 min. 1000°C. The magnetic component of the SANS intensities for the samples are provided in **Figure 6.13**. In this image, it can be clearly seen that the magnetic scattering intensities have increased in comparison to the as-milled powder due to the nucleation of precipitates during the high temperature heat treatment at 1000°C. The intensities of all four annealed powders are qualitatively identical with respect to both magnetic and nuclear scattering, which suggests that at this annealing temperature, the nanoprecipitates have nucleated and grown to stable sizes with negligible coarsening in the time frames studied at the heat treatment temperature of 1000°C. This result is in agreement with the APT results previously presented for the same samples (ZY10C15 and ZY10C60). In contrast to the APT results, the SANS curves show two distinct humps in scattering vector regions $0.02 < q < 0.05$ A^{-1} (larger precipitates) and $0.05 < q < 0.2$ A^{-1} (smaller precipitates).

Due to the size of the magnet used for these experimental results, the largest Q-value that was accessible was 0.2 A^{-1}. However, it seems that the intensity drop-off for the nuclear scattering component occurred at 0.1 A^{-1}. This resulted in experimental A-

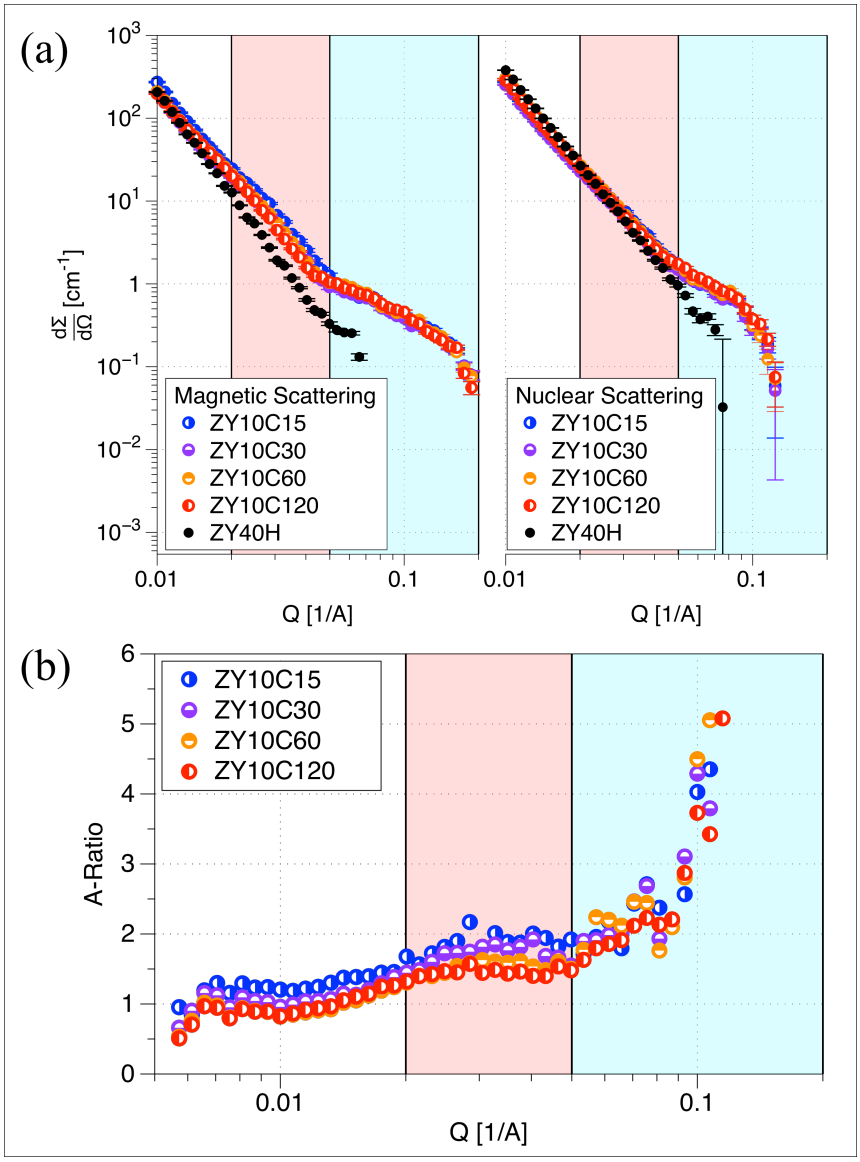


Figure 6.13. (a) The as-measured magnetic and nuclear scattering intensities as a function of increasing scattering vector. From these two intensity curves, the (b) A-ratio as a function of scattering vector is computed.

ratio results that were subject to potential errors in their interpretation. If one interpreted the A-ratio as-recorded, it would seem that the ratio approached 5 at higher Q-values, which would be consistent with the smallest precipitates being of the YAG phase; however, based on the ratio of the as-measured magnetic to nuclear scattering intensities, it appears that this increase is an artifact associated with the premature drop-off in the nuclear SANS intensity at the 0.1 A^{-1} value, driving the A-ratio to infinity at larger Q-values. Consequently, the analyzed A-ratio in the Q-range corresponding to the smallest precipitates was only considered in the region corresponding to $0.05 < q < 0.1$ A^{-1}.

Using the nonlinear least squares fitting (lscurvefit) package available in MATLAB, the precipitate distributions for the precipitates in the larger and smaller Q-ranges of interest were quantified using the local monodispersed approximation previously described in Chapter 4. To implement this procedure, a power-law background fit (Constant x Q^{-4}) was fit to the low-Q portion of the scattering intensity data and was subtracted from the as-measured magnetic scattering data. This highlighted the two precipitate populations, as shown in **Figure 6.14**. Since intensity overlaps existed between the intermediate Q-rage at the intersection of both the larger and smaller precipitate populations but not in the larger Q-range of the smaller precipitates, the precipitate population for the Q-range of $0.05 < q < 0.2$ A^{-1} was then extracted using the MATLAB lscurvefit procedure. Once the smaller precipitate population was quantified, the corresponding intensity was subtracted from the intermediate Q-range and curve fitting was applied to the final larger precipitate population. The summary of precipitate distribution parameters (assuming log-normal precipitate distributions) is tabulated for both precipitate populations (**Table 6.3**).

In all four samples, a high number density of nanoscale (Y-Al-O) precipitates ranging from 2-4 nm in diameter were identified. In addition, a lower number density of slightly larger precipitates (8-20 nm in diameter) were also quantified. However, the number density of these coarser precipitates is three-orders of magnitude lower than for the smallest nanoprecipitates and is not of specific interest in the current analysis since the smallest precipitates are of the most importance in the design of these ODS alloys

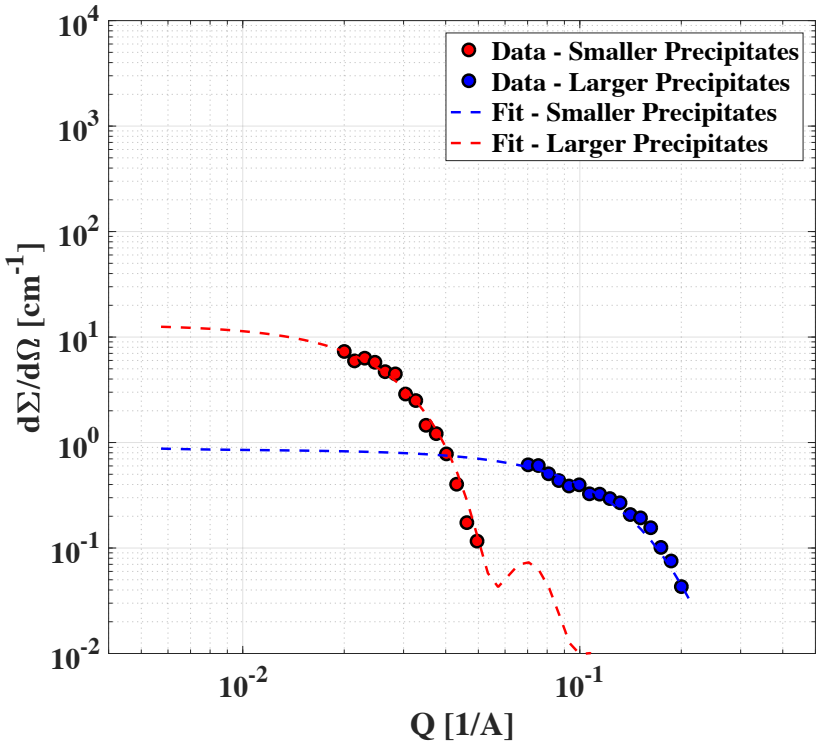


Figure 6.14. Background-subtracted magnetic scattering data for the ZY10C15 sample with respective least-squares fits for both precipitate populations.

Table 6.3. Magnetic SANS fitting results through nonlinear least squares curve fitting for two distributions of precipitates in the two specified Q-ranges of interest. Also reported are the as-measured A-ratios averaged over the Q-range of interest. Reproduced from [203].

Sample	Q range [Å^{-1}]	R [nm]	$\Delta\rho_m$ [Å^{-4}]	N_p [m^{-3}]	f [%]	μ	σ	A-Ratio
ZY10C15	0.05 < q < 0.2	1.47	2.03x10^{-11}	1.24x10^{24}	1.64	2.7	0.2	2.2±0.3
	0.02 < q < 0.05	7.9	1.45x10^{-11}	1.83x10^{21}	0.38	4.3	0.1	1.9±0.2
ZY10C30	0.05 < q < 0.2	1.46	2.15x10^{-11}	1.09x10^{24}	1.41	2.7	0.2	2.2±0.4
	0.02 < q < 0.05	8.3	1.01x10^{-11}	1.06x10^{21}	0.26	4.4	0.1	1.7±0.1
ZY10C60	0.05 < q < 0.2	1.45	2.75x10^{-11}	1.06x10^{24}	1.33	2.6	0.2	2.2±0.3
	0.02 < q < 0.05	8.6	0.45x10^{-11}	2.25x10^{21}	0.60	4.4	0.1	1.5±0.1
ZY10C120	0.05 < q < 0.2	1.54	2.01x10^{-11}	1.00x10^{24}	1.54	2.7	0.2	2.1±0.4
	0.02 < q < 0.05	10.1	0.52x10^{-11}	1.60x10^{21}	0.70	4.6	0.1	1.4±0.1

with high sink strength for nuclear environments. Consistent with the similarity between the as-measured nuclear and magnetic scattering intensities measured between the four samples, all specimens indicated almost identical size distributions for the smallest nanoclusters within the matrix. Since the precipitate distributions were essentially identical for all four samples, only the results for the ZY10C15 and ZY10C60 specimens are highlighted in **Figure 6.15**. Shown in **Figure 6.15(a)** for ZY10C15 and **Figure 6.15(c)** for ZY10C60 are the as-measured ex-situ magnetic SANS intensities, the power-law background fit, the two individual precipitate distribution fits, and the total summation of these intensities for direct comparison. The use of these two precipitate populations show good agreement between the experimentally measured intensities and the fits from the local monodispersed approximation. Also illustrated in this figure are the normalized log-normal size distributions for the smallest nanoprecipitate populations in ZY10C15 (**Figure 6.15(b)**) and ZY10C60 (**Figure 6.15(d)**) in comparison with APT results for the same specimens. Also shown in **Figure 6.15(b)** is the larger distribution of precipitates measured using SANS for the ZY10C15 sample, but this population is essentially negligible in comparison to the large number of nanoscale (Y,Al,O) precipitates within the matrix. The size distributions measured by SANS are narrower than those measured by APT, which could be due to either (a) higher specimen-to-specimen variation in the APT technique or (b) due to the discretization of particle size distributions using the fitting procedure used for SANS analysis. Since the SANS technique provides the macro-scale average distributions of nanoscale precipitates, this result verifies the scaling accuracy of the nanoprecipitate distributions measured via APT.

The number densities measured by the ex-situ magnetic SANS technique are higher than those measured using the APT technique. Though this may be attributed to the two previously identified differences between APT and SANS techniques, it may also be due to the presence of a non-zero oxygen content in the encapsulated quartz vials during the ex-situ furnace anneals. Recalling that the vacuum in the quartz vials was on the order of 10^{-4} Torr, this means that there are still many oxygen atoms within the free volume of the quartz vials. Since the number density of air molecules in the quartz vials

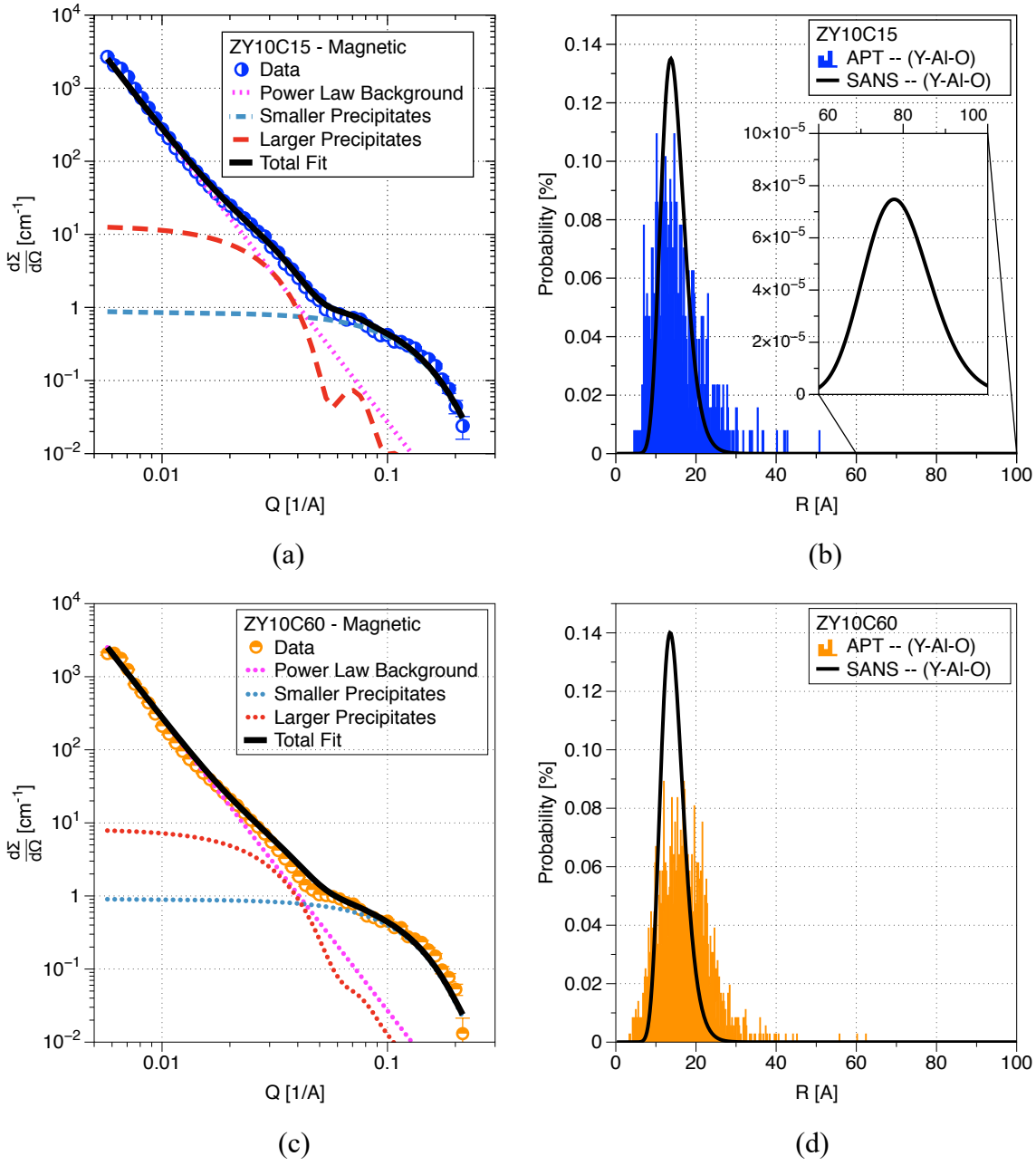


Figure 6.15. Results of SANS nonlinear least squares fits for CrAZY powder annealed for 15 min. (ZY10C15) and 60 min. (ZY10C60) in a 1000°C box furnace. (a) and (c) show the raw SANS data for ZY10C15 and ZY10C60 overlaid with the three functions representing the power-law background and the two populations of nanoprecipitates. For the same specimens, (b) and (d) show the comparison between the nanoprecipitate profiles identified by the APT and SANS technique, respectively. [203]

is proportional to the pressure inside of the quartz tubes through an observation of the ideal gas law (P = nkT), where P is the pressure inside of the tube, n is the number density of molecules, k is the Boltzmann constant, and T is the absolute temperature, the number of air molecules at atmospheric pressure is on the order of $2.4x10^{19}$ cm^{-3} inside of the vial. When the pressure decreases to 10^{-4} Torr, there still remains a number density of air molecules equating to approximately $1.8x10^{9}$ cm^{-3} and 20% of these molecules are diatomic oxygen. Thus, during annealing it is expected that these oxygen atoms will attempt to diffuse into the powder and enhance precipitation kinetics, although most of this oxygen will simply react with the powder surface to create a passive alumina layer on the powder surface preventing the further diffusion of oxygen into the powder. Even with this potential source of error in the SANS data, there exists qualitative agreement between the APT and SANS precipitate distributions presented in **Figure 6.15.**

The SANS technique was utilized not only to quantify the precipitate populations for comparison with the APT results, but to also provide information about the possible structure of the nanoscale precipitates through the comparison of the magnetic nature of these precipitates with stochiometric (Y,Al,O) phases through the comparison of the measured A-ratios with those of these expected phases. The measured A-ratios (~2.2 for the smallest precipitates) deviate significantly with those expected for the YAG (5.24), YAP (9.53), or YAM (3.28) phases. The possible reasons for the significant deviations from these expected phases must be discussed. For the present comparison, only the YAG or YAP phases will be compared since all of the APT results indicate that the Y/Al ratios for all identified (Y,Al,O) precipitates deviate significantly from the 2:1 ratio expected for the YAM phase.

Recalling the definition of the A-ratio, the function is dependent on the magnetic and nuclear scattering contrasts between the matrix and the precipitates, which are themselves dependent on the magnetic and nuclear scattering length densities for the matrix and the precipitates, respectively. Since the magnetic and nuclear scattering length densities of the matrix have been calculated and are constant, the A-ratio becomes only a function of the magnetic and nuclear scattering length densities of the precipitate, which

will change as a function of composition and structure. In-fact, the A-ratio can be re-written as:

$$A(q) = 1 + \frac{\left(\rho_{\mathrm{m}}^{Mat} - \rho_{\mathrm{m}}^{Prec}\right)^2}{\left(\rho_{\mathrm{n}}^{Mat} - \rho_{\mathrm{n}}^{Prec}\right)^2} = 1 + \frac{\left(\rho_{\mathrm{m}}^{Mat} - \rho_{\mathrm{m}}^{Prec}\right)^2}{\left(\rho_{\mathrm{n}}^{Mat} - \frac{b_n^{Prec}}{\Omega_{\mathrm{Prec}}}\right)^2} \quad \ldots\ldots\ldots\ldots\ldots\ldots \quad (6.1)$$

As the composition of the precipitate changes, so does the magnetic (ρ_{m}^{Prec}) and nuclear (ρ_{n}^{Prec}) scattering length density. To quantify these changes and to estimate the resulting effects on the A-ratio, the various parameters comprising these two scattering length density values are varied based on assumptions about the character of the precipitates. First and foremost, these nanoscale precipitates are quite small, with an average diameter of only ~3 nm. The average lattice parameters for cubic YAG and orthorhombic YAP unit cells are 1.195 nm [228] and (0.521-0.743 nm) [229], respectively. This means for the equivalent spherical volume of the average precipitate, it would only comprise ~9 and ~69 unit cells of the YAG and YAP unit cells, respectively. For YAG specifically, the low number of equivalent stable unit cells coupled with the significant strains associated with the observed coherency of these nanoscale (Y,Al,O) precipitates with the surrounding matrix may mean that the local atomic density within these precipitates (Ω_{Prec} in Eq. 6.1) may deviate from the ideal precipitate value (94 atoms/nm^3) to the atomic density within the matrix (83 atoms/nm^3). In-fact, the Fe and Cr matrix atoms may be present within the precipitates to stabilize the structure as it nucleates and grows to stable sizes [230]. In addition, it may be possible that Fe may be occupying tetrahedral or octahedral Al sites in the YAG structure or Y sites in the YAP structure [231]. In the event that the atomic density decreases within the precipitates to approach that of the matrix, this decreases the scattering length density of the precipitate and consequently decreases the A-ratio (Eq. 6.1). Musa et al. calculated the lattice parameter change for $Y_3Al_xFe_{5-x}O_{12}$ for increasing Al concentrations. Based on this lattice parameter and the 160 atoms per unit cell for the YAG phase, the atomic density of the $Y_3Al_xFe_{5-x}O_{12}$ phase is as an increasing function of Al content is plotted in **Figure**

6.16. The structure shows a linear change in atomic density as a function of Fe vs. Al site occupancy in the YAG lattice, but it does also indicate that the un-strained atomic density only approaches that of the FeCrAl matrix as Fe completely displaces all of the Al sites, which is not what has been noted through APT. Assuming that there may be at least some matrix atoms stabilizing the small structure, and assuming that coherent strains may be artificially reducing the local atomic density across the nanoprecipitates, a re-calculation of the A-ratios with the assumption that ($\Omega_{\mathrm{Prec}} = \Omega_{\mathrm{Mat}}$) results in corresponding values of 3.5 for YAG and 3.9 for YAP, which are still well above the measured A-ratios in this work.

The aforementioned discussion has to this point only focused on the change in A-ratio as a function of precipitate atomic density. As potential matrix atoms are included in the precipitate composition, both the magnetic and nuclear scattering lengths will also change as an increasing function of increasing precipitate matrix atom fraction. Thus, the magnetic and nuclear scattering length densities were calculated as a function of

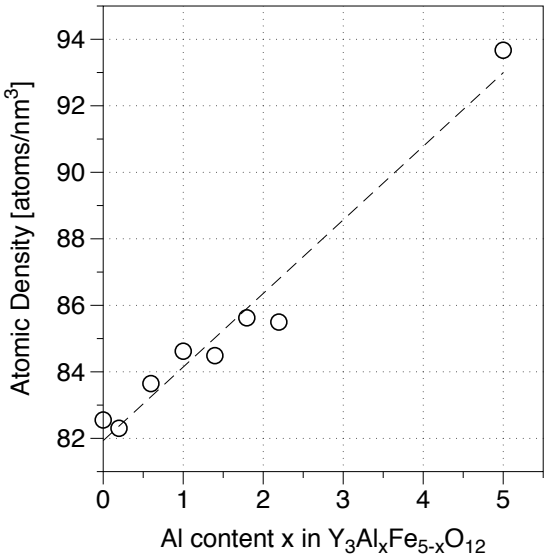


Figure 6.16. The variation of the theoretical atomic density of the cubic garnet $Y_3Al_xFe_{5-x}O_{12}$ phase, where x is the stochiometric composition of Al, data produced using lattice parameter data from Musa et al. [215].

increasing matrix content within the precipitates. For this approximation, the FeCrAl matrix composition was assumed instead of calculating simply increased Fe contributions (since Fe will be the predominant culprit for the magnetic scattering length density variations). This assumption was made because again, no Cr-rich shell surrounded the precipitates in APT, and if only Fe and Al were preferentially separated from the matrix, one would have expected a Cr-rich shell due to a higher enrichment of this element along the precipitate boundary. Even so, since the Fe in the matrix is ~80%, the differences between using the FeCrAl matrix and a pure Fe magnetic scattering contribution will not substantially affect the outcome of the magnetic scattering analysis. Using the assumption that FeCrAl matrix atoms may be constituent atoms within the (Y,Al,O) crystal lattice for crystal structure stabilization, the nuclear and magnetic scattering length densities were calculated for an increasing atomic fraction of matrix measured within the precipitates.

For the magnetic scattering length density estimation, a rule of mixtures approach was utilized so that a linearly increasing fraction of the matrix magnetic scattering length density was added to the initial magnetic scattering length density of the precipitates (assumed zero for non-magnetic "holes" in the FeCrAl matrix). Thus, for 100% FeCrAl matrix, there would be no difference between the precipitates and the matrix and consequently no magnetic contrast to be able to see the precipitates. For the estimation of the nuclear scattering length density as a function of FeCrAl matrix fraction in the precipitates, the NIST Center for Neutron Research scattering contrast calculator was used by adding the desired FeCrAl matrix and either YAG or YAP compositions together in terms of atom percent [218]. This calculator requires an input of the mass density for the calculation, by which the atomic density is calculated. Instead of using the ideal mass densities of the YAG and YAP phases, reduced mass density of 4.09 g/cm^3 and 4.52 g/cm^3 were calculated for each of these respective phases using the molecular weight of each phase and the atomic density of the FeCrAl matrix since the expected atomic density would be expected to decrease with matrix atoms within the microstructure. **Figure 6.17** shows the decrease in both the magnetic contrast between the precipitates and the matrix as well as the decrease in A-ratios for YAG and YAP as an increasing function of FeCrAl

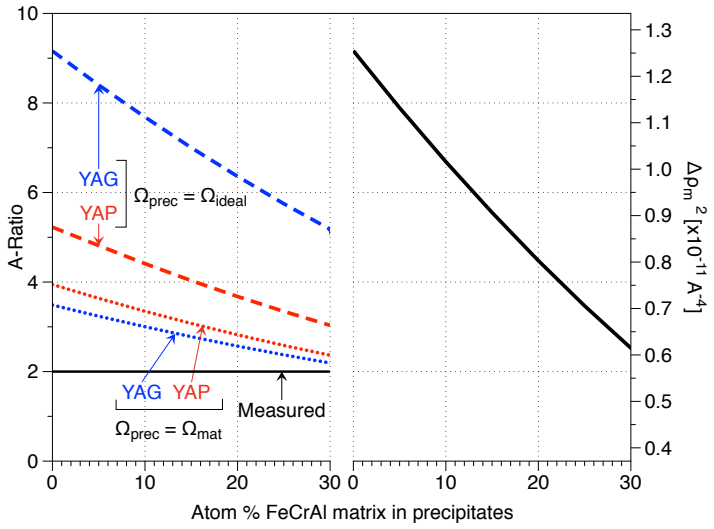


Figure 6.17. The variation of the magnetic scattering contrast (Eq. 3.6) as a function of matrix composition in the precipitates, assuming either ideal or matrix atom densities in the precipitates [203].

in the nanoscale precipitates for both corrected and uncorrected precipitate atomic densities for the YAP and YAG phases, respectively. For an A-ratio around 2.1-2.2 for the smallest nanoscale precipitates, a required matrix (and thus Fe) content within the precipitates must approach ~30%, which would help explain the high Fe and Cr contents measured via APT.

However, this much matrix content in the precipitates is doubtful when comparing the magnetic scattering contrast measured through the SANS fitting procedure to the plot in **Figure 6.17**. Although the shape of the neutron scattering distribution is a function of the form factor and the type of distribution (lognormal in this case), the magnitude of the scattering curve is proportional to the product of the product of the scattering contrast and the number density, which were fit as one parameter during the least squares fitting procedure. The corresponding number densities measured by SANS for ZY10C15 and ZY10C60 in **Table 6.3** are similar but slightly higher than those measured by APT **Table 6.2**. The corresponding magnetic scattering contrast measured by SANS is on the order of $2x10^{-11}$ A^{-4} for the ex-situ annealed samples. Comparing this value with the change in magnetic scattering contrast as a function of matrix composition in the precipitates

(**Figure 6.17**), this would indicate non-magnetic precipitates in the ODS FeCrAl matrix, suggesting that there is no Fe and Cr inside of the precipitates from the matrix. Due to the inverse relationship between the scattering contrast and the precipitate number density in the least-squares fitting procedures, to decrease the contrast by an order of magnitude to match the measured A-ratio would drive the precipitate number density to unrealistic values on the order of 10^{25} m^{-3}, which haven't been measured even for ODS FeCr alloys like the SM10 heat of 14YWT with the highest number densities measured for this type of alloy (**Table 2.3**). It can be concluded then that the nanoprecipitates are most likely non-magnetic and have little to no Fe and Cr within them, and that the lower measured A-ratios are artifacts associated with the limitation in Q-ranges available for probing with the large magnet used for the SANS investigations in this work.

6.4. Comparison with Computational Thermodynamics

The detailed ex-situ APT and SANS investigations presented in this chapter show that the smallest precipitates are enriched only in Y, Al, and O, and that Zr is not competing with Al for the formation of these clusters. This is in direct conflict with previously reported results by Dou et al. whereby Zr additions were shown to shift the measured precipitate compositions from (Y,Al,O)-rich precipitates to the $Zr_3Y_4O_{12}$ phase [105]. A fundamental understanding of the thermodynamic reasons why this is not observed is thus required for the development of ODS FeCrAl alloys with tailored precipitate distributions for high-sink strength applications, since it has previously been shown that the coarsening kinetics of (Y,Al,O) precipitates differs from (Y,Zr,O) precipitates.

In Chapter 2, Ellingham diagrams were presented for various binary oxides, carbides, and nitrides. These diagrams were all produced through reactions of elements with either O_2, N_2, or graphitic C, and represent the Gibbs free energies of reaction using standard reference states for each element. Although many authors have used either these reaction energies or the standard Gibbs free energies of formation for various stochiometric phases in an attempt to argue for what phases will form in ODS FeCrAl

alloys, a discussion limited to these simplified Ellingham diagrams is problematic because it does not take into consideration the compositional variations of these elements in solid solution for the as-milled ODS FeCrAl powders.

A more realistic approach is to use the CALPHAD methodology to model precipitation in these alloys. CALPHAD originally stood for the CALculation of PHAse Diagrams, but has been expanded to include the Computer Coupling of Phase Diagrams and Thermochemistry [232]. The CALPHAD approach is a semi-empirical model that incorporates all of the available thermodynamic data and experimental phase diagrams in literature are used to describe multi-component systems in an attempt to predict stable thermodynamic phases that may exist for a given sample composition. Although this work is not intended to delve into the specifics of the CALPHAD approach, the ThermoCalc program was used to apply the CALPHAD model for the prediction of various phases that may exist within the ODS FeCrAl matrix as a function of temperature. For detailed description about the CALPHAD approach, the reader is referred to more comprehensive reviews elsewhere in the literature [232, 233]. With the help of Dr. Ying Yang at ORNL, the ThermoCalc program was used to predict the molar fractions of various phases and to output the driving energies for formation of these various phases as a function of increasing annealing temperature. The database used for the computational thermodynamic calculations was the TCFE9 database, which is a commercial database that included properties for all elements of interest in this system. The results of these simulations are presented in this section with the aim of explaining the discrepancies between observed nanoprecipitate distributions in the ODS FeCrAl alloys investigated in this work and those fabricated by Dou with Zr addition.

Using the TCFE9 database within the ThermoCalc software and the atomic concentrations of elements within the as-milled CrAZY powder, the mole fractions of various phases expected in the ODS FeCrAl alloy were simulated as a function of increasing processing temperature using a solid-solution model approach for a BCC Fe matrix. The results of the thermodynamic calculations are summarized (courtesy of Dr. Ying Yang at ORNL) in **Figure 6.18**. Three different ODS FeCrAl compositions were

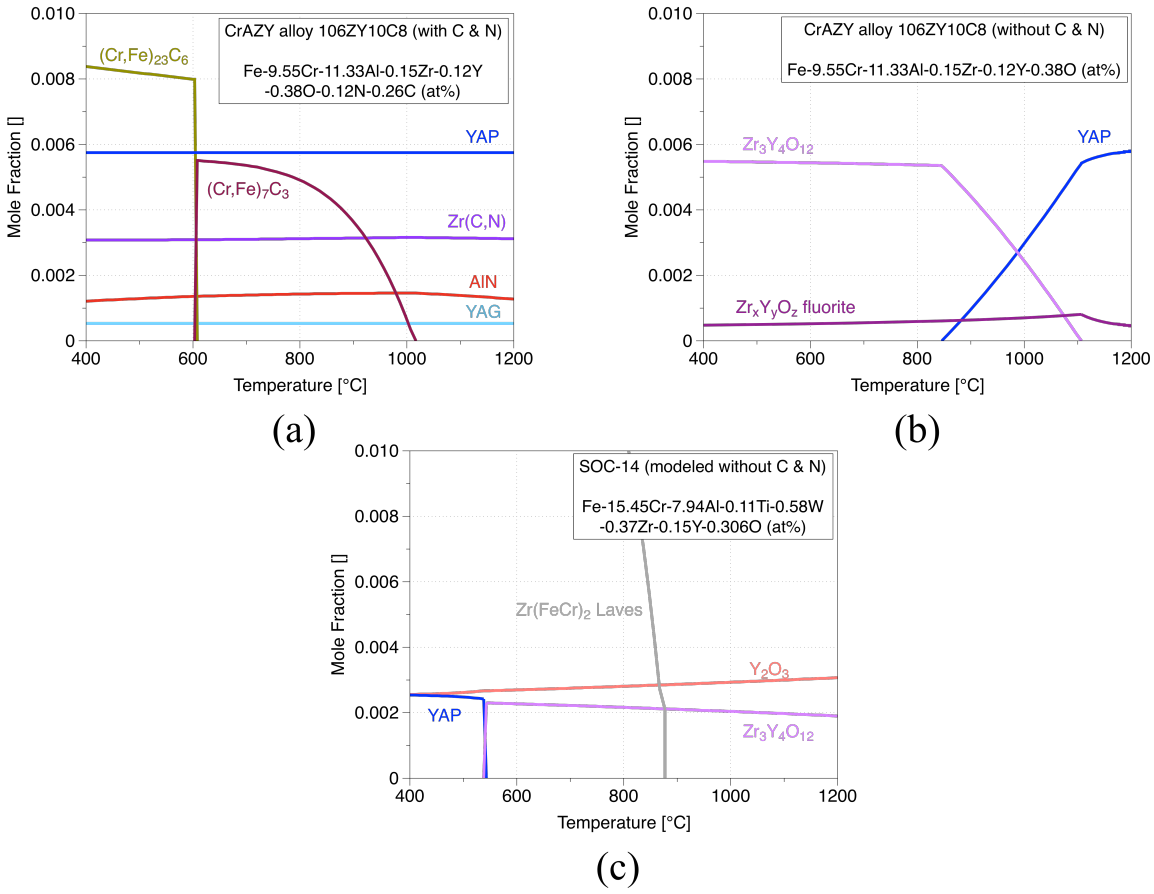


Figure 6.18. Simulated mole fractions of various stochiometric phases in ODS FeCrAl alloys with various inputted compositions using Thermocalc (Courtesy of Dr. Ying Yang at ORNL) [225]. The mole fractions as a function of consolidation temperature are reported for (a) the 106ZY10C8 alloy with C and N impurity elements as reported in **Table 6.1**, (b) the 106ZY10C8 alloy omitting C and N impurities, and (c) the SOC-14 (FeCrAlZrY) ODS FeCrAl alloy developed by Dou et al. [105].

used for these simulations: (1) the as-measured elemental compositions of the 106ZY10C8 alloy with C and N as listed in **Table 6.1**, (2) the 106ZY10C8 composition without C and N within the matrix, and (3) the nominal composition of the SOC-14 ODS FeCrAl alloy with Zr addition (without C and N) by Dou [105]. For the simulation of the 106ZY10C8 extruded CrAZY alloy with C and N addition (**Figure 6.18(a)**), the as-predicted phases show that (Y,Al,O) phases such as YAP and YAG should exist in the matrix, while the Zr preferentially forms Zr(C,N). In addition, Al appears to also interact with N to form AlN at the target temperature of 1000°C. At lower temperatures, it appears that the M_7C_3 and $M_{23}C_6$ type carbides are formed from Fe and Cr in the matrix as well, although at the target temperature there does not appear to be a driving force sufficient for the nucleation of these phases.

If C and N are omitted from the matrix, the carbide and nitride phases are of course omitted from the diagrams, which shifts the types of precipitates noted at the target temperature of 1000°C. In this case, Zr does appear to compete with Al for the Y and O within the lattice. Comparing this simulation (**Figure 6.18(b)**) with that for the SOC-14 ((**Figure 6.18(c)**) shows the importance of Zr in the formation of the expected oxide phases in these alloys. For the SOC-14 alloy, the amount of Zr addition is more than double in comparison to what was added for the CrAZY alloy investigated in this work. This increased Zr addition resulted in the prevention of the (Y,Al,O)-rich phases from forming and instead both Y_2O_3 and $Zr_3Y_4O_{12}$ are preferentially formed.

To better understand the reasons for the differences in nucleation between these alloys, the driving forces for nucleation, specifically the Gibbs free energies of mixing for each stochiometric phase, were also outputted from the ThemoCalc software. A major challenge in the interpretation of this data is the establishment of a “reference state” so that each stochiometric phase can be compared side-by-side. For the current ODS FeCrAl system, the driving forces for nucleation for each phase “X” is presented in reference to the BCC-Fe matrix phase, where $\Delta G_m = \Delta G_m^X - \Delta G_m^{bcc-Fe}$, which is based upon the method outlined by Hillert [234] presented graphically in **Figure 6.19**.

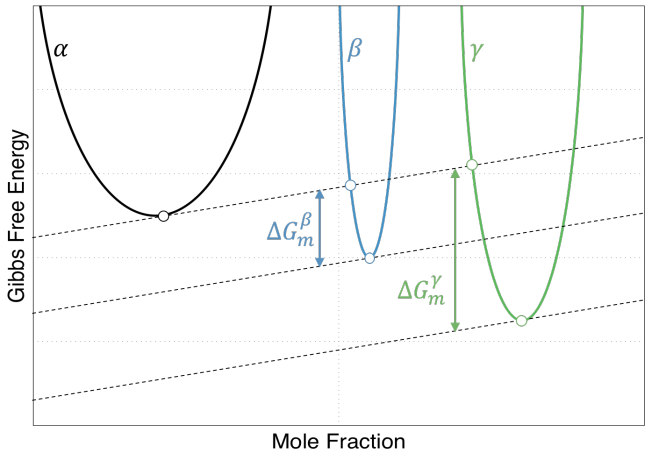


Figure 6.19. Schematic representation of the calculation of the driving force for nucleation for various phases β and γ with respect to a reference phase α, from [234]

The driving forces for nucleation for various expected phases for the 106ZY10C8 composition are plotted as a function of increasing temperature in **Figure 6.20**. Positive values indicate higher affinities for each of the respective phases to nucleate, while negative values indicate that the phase is unstable at the respective temperature. Important conclusions can be drawn from this respective plot based on the driving energies for nucleation for each phase. What is readily apparent from the plot is that the (Y,Al,O) and (Zr,Y,O) oxide phases are the most stable and have the highest driving forces for nucleation.

Surprisingly, the driving force for nucleation for the YAM ($Y_4Al_2O_9$) phase is actually higher than those for YAP or YAG, although this phase was not observed in the outputted molar fraction phase diagrams in **Figure 6.18**. It is important to note that these driving forces do not consider the local atomic concentrations of atoms in the matrix. In previous studies on the Al_2O_3-Y_2O_3 system, it has been asserted that YAM phase forms at lower temperatures (900-1100°C), the YAP phase forms in the range of 1100-1250°C, and the YAG phase forms at higher temperatures (>1250°C) [235]. However, this data was first generated using Al_2O_3-Y_2O_3 diffusion couples and the growth of these oxide layers was limited by the rate of Al diffusion into the yttria phase [236]. In-fact, previous authors investigating (Y,Al,O) nanoprecipitates in ODS FeCrAl alloys have used this

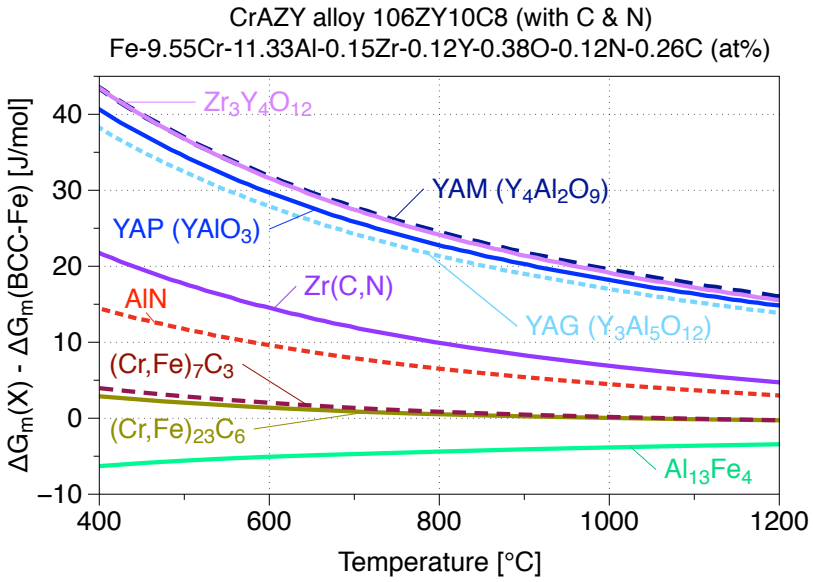


Figure 6.20. A comparison of simulated driving forces for nucleation for various noted stochiometric phases in the ODS FeCrAlZrY alloy system using Thermocalc (Courtesy of Dr. Ying Yang at ORNL). [225]

data as support for their assertions that the YAM phase is the primary type of cluster formed in these alloys [111]. However, this is an erroneous argument because in the diffusion-couple experiment, the reason why these phases formed in this order is primarily due to the fact that due to the lower atomic radius of Al in comparison to Y, the rate limiting step for the formation of these phases was the rate at which Al diffused into Y_2O_3. This would mean that the type of phase being formed was a result of the local atomic ratio between Y/Al at any point in time. Initially as Al diffused into yttria, the ratio of Y/Al would be high, and thus it is not surprising that the phase with the highest Y/Al ratio (YAM) would preferentially form first, followed by YAP and then YAG as more Al was allowed to diffuse through the diffusion couple. It has been shown that for ball milled Al_2O_3-Y_2O_3 powder mixtures, increasing the ratio of Al_2O_3 to Y_2O_3 in the powder mixture above Y:Al (3:5) resulted in the preferential precipitation of the YAG phase in comparison to the YAP phase after annealing [237]. Since the ODS FeCrAl matrix is a solid-solution of the solute elements within the matrix and is not representative of the diffusion-couple previously discussed, this result suggests that the

local atomic concentration of Al and Y, and not the processing temperature, is the primary indicator for the type of (Y,Al,O) phase nucleated in this alloy system. Since the Al concentration is so high in these ODS FeCrAl alloys, the local concentration of Al:Y in the matrix at any position will be much higher than the ratio of Al:Y in the YAG phase, which explains why the current APT and SANS results indicate that YAG is preferentially formed in these alloys.

Since Zr has a higher affinity for oxide formation in comparison to Al, with the higher local concentration of Zr in the matrix for the SOC-14 alloy, it is not surprising that (Zr,Y,O) oxides are preferentially formed in this alloy in comparison to the CrAZY alloys investigated in this work. Even though the Al content greatly exceeds the Zr content, Zr will want to react with whatever impurity element exists in the matrix. So, if no C and N are present in the microstructure, Zr will preferentially react with O and form the $Zr_3Y_4O_{12}$ phase. However, with the large amount of Al in the CrAZY matrix and assuming that C and N exist within the microstructure, two factors must be considered. First, although Zr has a higher affinity for O, C and N have a much higher affinity for Zr than either Al or Cr. Thus, C and N will preferentially interact with any Zr in the matrix first prior to interaction with Al or Cr (and therefore relatively low levels of free Zr would be available for interaction with Al or Cr). Then, the O in the matrix will then react with whatever element has not already interacted with the C and N in the matrix, which is in this case Al since all of the Zr would have already interacted with C and N to form carbonitrides. This combination of computational thermodynamics with the observed experimental results fully explains the discrepancy between differences in nucleation in the current alloy system in comparison with the results obtained by Dou with both Zr and Hf additions in ODS FeCrAl alloys [105, 112].

CHAPTER 7: Nanoprecipitate Nucleation, Growth, and Coarsening Kinetics

Until this point, the focus of this work has been to evaluate the types of precipitates that have nucleated within the matrix, with a specific focus on the evaluation of the compositions and structures of the various identified precipitates to optimize the nanoprecipitate populations within the microstructure. As presented in Chapter 5, although the nanoprecipitates had nucleated and grown to stable sizes at annealing times as low as 15 min. in ex-situ annealed samples, the size of the precipitates had also increased as a function of annealing temperature while the number density had decreased for temperatures exceeding 1000°C. This chapter aims to quantify the nucleation, growth, and coarsening kinetics for these precipitates so that processing parameters maximizing the distribution of the smallest (Y,Al,O) nanoprecipitates can be optimized to ensure the maximum sink strength possible for application in advanced fission or fusion reactors. In-situ SANS results have captured the initial nucleation and growth of these precipitates at low temperatures, while long-term ageing experiments have quantified the coarsening kinetics of these alloys.

7.1. In-situ Observation of Precipitate Nucleation and Growth

The ex-situ APT and SANS results provide strong evidence that the nanoprecipitate nucleation kinetics are quite fast, and that nanoprecipitates nucleate at temperatures much lower than the normal target temperatures used for the consolidation of ODS FeCr and FeCrAl alloys. In an attempt to capture the nucleation and growth of these precipitates and to identify pre-consolidation temperatures that will maximize the nanoprecipitate distributions in these alloys, in-situ SANS measurements were performed on as-milled CrAZY powders. In this experiment, as-milled powders encapsulated in molybdenum foil packets were heated in a vacuum furnace to 1000°C at a heating rate of 20°C/min, with scattering curves recorded in 1 min. intervals. Unfortunately, the size of the vacuum furnace did not permit the application of an applied magnetic field for the

deconvolution of the magnetic and nuclear scattering curves during the course of the experiment. Since the magnetic scattering has been shown to decrease as a function of temperature up to the Curie temperature of the ferromagnetic matrix [193], this means that the corresponding SANS intensity curves were unable to be accurately fit using post-processing nonlinear least squares procedures. Instead, the qualitative shapes of the scattering curves will be used to facilitate a discussion on the nucleation and growth kinetics of the precipitates as a function of increasing time/temperature.

Changes in the as-measured SANS intensities as a function of increasing temperature are presented in **Figure 7.1**. In the plot on the left, the individual SANS intensity curves are presented, while the corresponding temperatures associated with these curves are presented as points on the time-temperature profile. In the low-Q portion of the scattering curve, the background power-law decrease in SANS intensity as a function of Q^{-4} is observed, while the higher-Q portion of the scattering curve shows an increase in scattering intensity with increasing temperature and time. Five different snapshots are provided in the figure to show the qualitative increase in scattering intensity in the same Q-range previously identified in the ex-situ results that correlate to the size range corresponding with the smallest nanoprecipitate population. The secondary larger precipitate distribution was not able to be visually captured due to variations in the lower-Q portion of the curve associated with changes in the magnetic scattering component as a function of temperature.

A significant result from **Figure 7.1** is that the nanoprecipitates appear to nucleate and grow to stable temperatures at temperatures between 500 and 600°C. Although the absolute intensity of the 900°C scattering curve appears to be slightly less than the 600°C curve, this is only because at temperatures exceeding ~700°C the magnetic component of the magnetic scattering was completely lost after exceeding the Curie temperature of the FeCrAl alloy, which can be seen through the corresponding loss in low-Q scattering intensity as well for the 900°C specimen. So, for all comparative purposes, the intensity curve for the 600°C distribution of precipitates is qualitatively identical to the distribution of precipitates at 900°C. The scattering curves for temperatures exceeding 900°C (up to

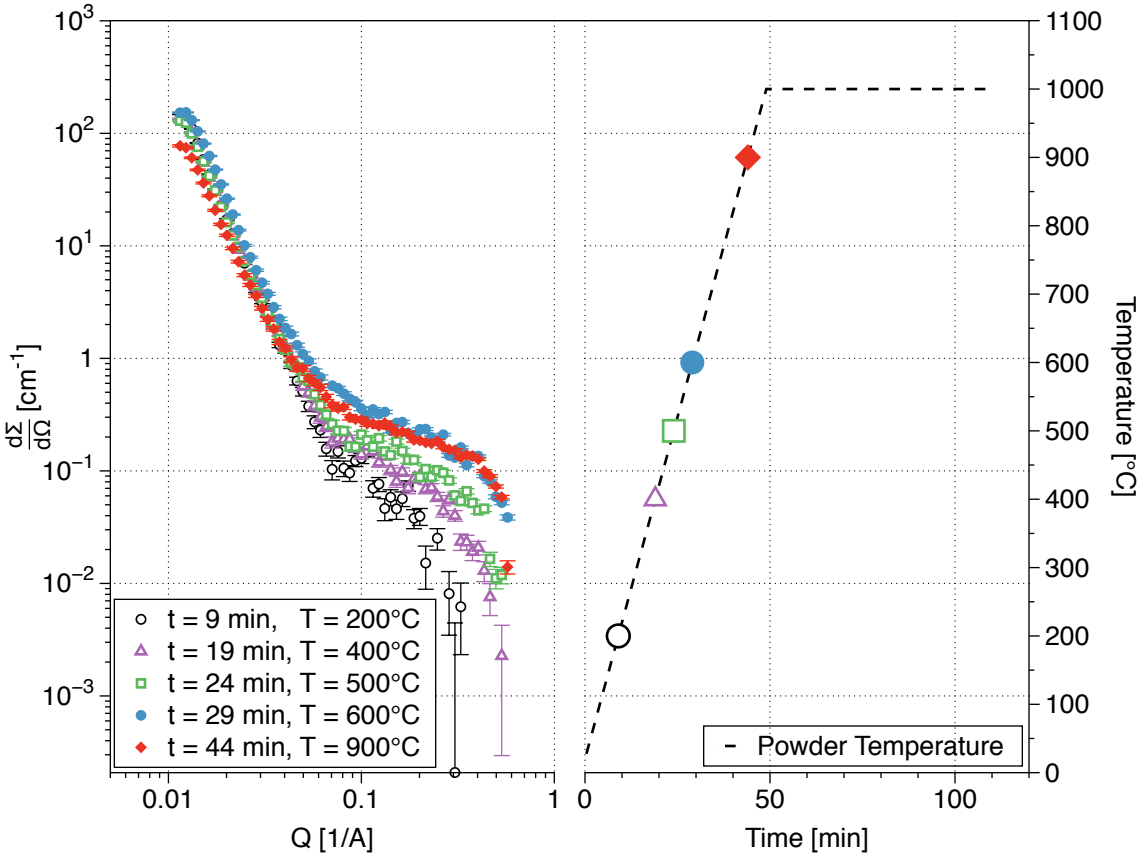


Figure 7.1. Temperature dependent SANS intensities as a function of annealing time and temperature for ZY40H powder investigated through in-situ SANS using a heating rate of 20°C/min. [203]

1000°C through the holding period at the same temperature) are not shown since no change in scattering intensity was observed at these temperatures in comparison to the 900°C value.

One aspect that makes the interpretation of **Figure 7.1** difficult is the inability to deconvolute the contributions from nucleating and growing Zr-rich carbonitrides and other second phase particles in comparison to the smallest (Y,Al,O)-rich precipitates of interest. From the APT results presented on powders and alloys annealed for 60 min. at various temperatures exceeding 1000°C, the Zr-rich precipitates are shown to have sizes ranging from 50-100 nm, which shows that these precipitates nucleate and grow much faster than the more stable Y- and Al-rich oxides. This means that at in some portion of this low-temperature nucleation and growth regime, there may be contributions to the scattering intensity from both the Zr-rich and (Y,Al)-rich precipitates when the particles overlap in size. As the temperature increases and the Zr-rich precipitates continue to coarsen at a faster rate, these larger inclusions eventually become lost in the low-Q region of the scattering curve, so at higher temperatures it can be readily assumed that the entirety of the scattering intensity is attributed only to the smaller population of (Y,Al,O)-rich precipitates. Since the scattering intensity profiles at and above 600°C show no significant changes, the results suggest that at temperatures exceeding 600°C only the (Y,Al,O)-rich precipitates are contributing to the in-situ scattering curve. To deconvolute the onset of nucleation and growth between the two precipitate distributions in the 200-600°C temperature range, advanced magnetic temperature dependent SANS measurements are recommended for future studies.

From this in-situ SANS experiment, the nanoprecipitates are shown to nucleate and grow to stable sizes at temperatures less than 600°C. Since the nanoprecipitate distributions do not significantly change at temperatures exceeding this temperature, it can be readily assumed that the nanoprecipitate distribution for ex-situ annealed sample ZY10C15 (equivalent sample temperature of 715°C) is representative for this in-situ nanoprecipitate population. The number density for ZY10C15 ranged from 0.5-1.2x10^{24} m^{-3} when comparing APT and SANS results. Assuming an equivalent number density of

$1x10^{24}$ m^{-3}, the equivalent distance between a distribution of homogeneously dispersed spheres is ~6 nm. The using the diffusion parameters for Y, Al, and O estimated from literature [238-240], the total integrated diffusion distance for each element was estimated using the SANS time-temperature profile as the input.

From **Figure 7.2**, although O diffuses quickly through the matrix, Y and Al are able to reach the threshold diffusion distance by 600-700°C. It is not surprising then that the nanoprecipitates have finished nucleated and growing by around 600°C in the in-situ SANS results. However, the significant increases in the SANS intensity at temperatures between 200-500°C are inconsistent with these calculations of diffusion distances in BCC-Fe. The in-situ results instead support a defect-assisted heterogeneous nucleation method whereby the initial nucleation and growth of nanoprecipitates is assisted by the significant amount of annihilating and mobile vacancies introduced into the microstructure by the mechanical alloying process. The significant number of dislocations and vacancies can accelerate the diffusion of the larger Al and Y atoms that are forced to diffuse through the lattice since each vacancy is associated with a vacant substitutional lattice site. Accelerated nucleation is also expected if some solute atoms are originally in the lattice with shorter nearest neighbor distances than the average nucleating interparticle spacing. In either case, these results indicate that nanoprecipitates nucleate and grow to stable sizes well below what has previously been conjectured by previous authors [241], which allows for the tuning of alloy annealing temperatures for optimal nanoprecipitate distributions depending on the consolidating methodology.

7.2. Long-term Nanoprecipitate Coarsening Kinetics

As was previously presented in Chapter 6, the nanoprecipitate sizes and compositions showed a slight change in average precipitate composition as a function of increasing extrusion temperature and annealing time. Thus, changes in size and composition are quantified in this chapter in an attempt to predict the distribution of nanoprecipitates with a variety of thermomechanical processing parameters. Although previously shown qualitatively in **Figure 6.12**, the quantitative changes in

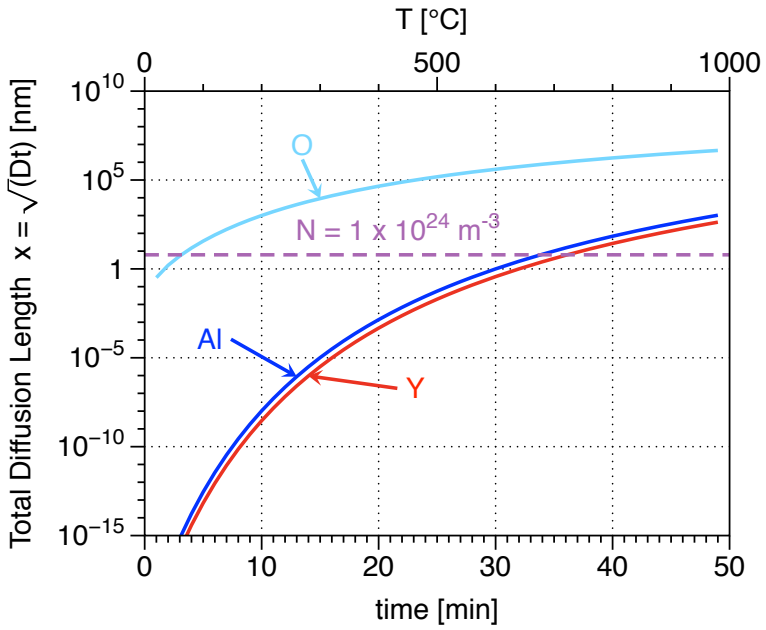


Figure 7.2. Total diffusion distances for Y, Al, and O atoms in BCC-Fe for increasing temperatures from 23-1000°C at a ramp rate of 20°C/min.

nanoprecipitate compositions as a function of increasing temperature and time are shown using the ratio of Y to Al atoms in **Figure 7.3**. For alloys extruded at 1000°C, 1050°C, and 1100°C for 60 min., the average Y/Al ratio for precipitates as a function of precipitate radius appears to tend toward the YAG composition. Though small changes exist, for the average radius (~2 nm) all three samples extruded after 1h anneals at increasing extrusion temperature do not deviate significantly from the YAG composition within the margin of error. For the larger precipitates in the distribution, it appears that as temperature increases any sub-stochiometric compositions deviating from the stochiometric YAG composition are able to shift to match the ratio of 3:5 (Y:Al). More interesting is the trend of larger nanoprecipitate compositions as a function of extended annealing times from 1-500h for samples annealed at 1050°C in **Figure 7.3(b)**. As the annealing time increases, there appears to be a transition for the larger coarsening precipitates to transition from a Y/Al ratio of 0.6 towards a ratio of 1, which signals a compositional shift from YAG to YAP for the larger precipitates. Based on the

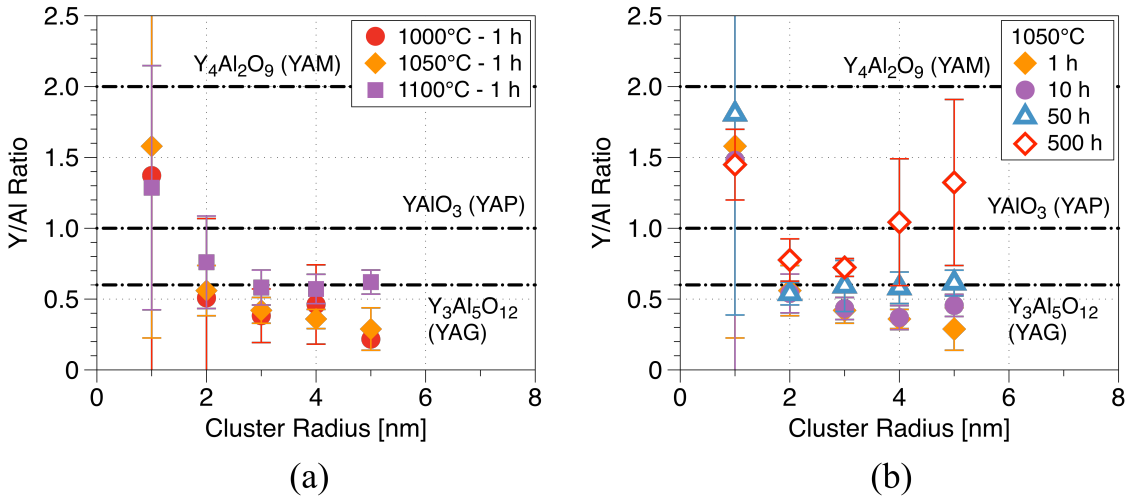


Figure 7.3. (a) the dependence of the Y/Al ratio measured in the precipitates in annealed CrAZY powders/alloys as a function of precipitate radius for 1h heat treatments at 1000°C, 1050°C, and 1100°C. (b) the dependence on the size dependent Y/Al ratio as a function of increasing annealing time for extended heat treatments at 1050°C. Error bars indicate 95% confidence intervals for each sample population. [203]

thermodynamic calculations in Chapter 6, it was predicted that the YAP phase was preferred thermodynamically in comparison to the YAG phase. With the long-term annealing treatment, the high number density of YAG nanoprecipitates may be thermodynamically unstable and prefer to transition to the YAP composition as the precipitates are provided the sufficient time and temperature to coarsen.

To investigate the coarsening kinetics of these nanoscale precipitates, powders were annealed ex-situ at 1050°C up to 500h. APT reconstructions of these CrAZY powders annealed for 10h (ZY15C10h), 50h (ZY15C50h), and 500h (ZY15C500h) are illustrated below in **Figure 7.4**. The nanoscale precipitates within these specimens are highlighted using red 1.5% (Y,YO,AlO) isoconcentration surfaces with matrix Fe atoms in the background. As the annealing time increases, the average size of these nanoprecipitates increases from 4.32 nm in diameter to 8.14 nm while the corresponding nanoprecipitate number density decreases from 1.8 to 0.1×10^{23} m^{-3}. This increase in nanoprecipitate diameter with decreasing number density is consistent with nanoprecipitate coarsening through a conventional Ostwald ripening process that is

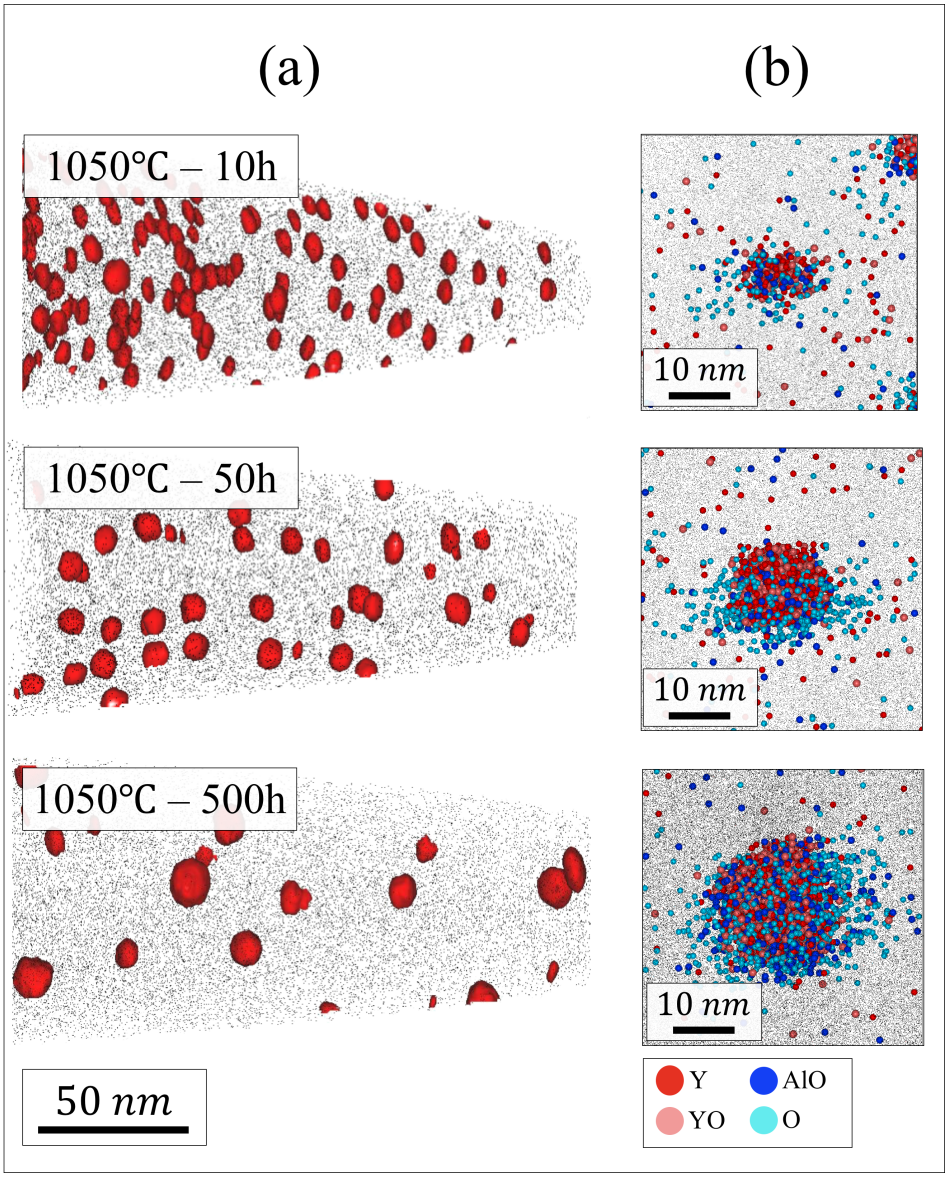


Figure 7.4. (a) APT reconstructions of CrAZY powders annealed at 1050°C for 10-500h. 0.1% of the matrix Fe atoms are shown in black dots while the (Y,Al,O)-rich nanoprecipitates are shown using red 1.5% (Y,YO,AlO) isoconcentration surfaces. Also shown in (b) are atom maps of respective clusters normalized to the same dimensional scale. [203]

characterized by larger precipitates growing at the expense of the dissolution of smaller precipitates, as previously outlined in Chapter 2. In **Figure 7.4(b)**, representative atom maps of Y, YO, AlO, and O show precipitates normalized to the same scale bar, showing more clearly the increasing nanoprecipitate radius as a function of annealing time.

To identify the mechanism by which these precipitates are coarsening, the methodology previously used by Oono for the quantification of coarsening in ODS FeCr and FeCrAl alloys is applied to the current system [78, 79]. Taking the natural logarithm of both sides of the power law relationship in Eq. 2.11 provides the following result:

$$\ln\left(r^n - r_0^n\right) = \ln\left(K_n\right) + \ln\left(t\right) \quad \text{(7.1)}$$

Where $K_n = k * \exp\left(-\frac{Q}{RT}\right)$ is the temperature dependent coarsening constant, t is the annealing time, r is the precipitate radius, and r_0 is the initial precipitate radius. The initial precipitate radius is assumed to be the same as for the ZY10C15 sample (r_0 = 1.56 nm) due to the rapid nucleation and growth kinetics and the assumed stable precipitate size distribution prior to precipitate coarsening at higher temperatures. Since K_n is independent of temperature for isothermal annealing treatments at 1050°C, taking the natural logarithm of K_n results in the following simplified expression:

$$\ln\left(r^n - r_0^n\right) = \ln\left(k\right) - \left(Q/RT\right) + \ln\left(t\right) = C + \ln\left(t\right) \quad \text{(7.2)}$$

For a given power law exponent "n", the dependence on the natural logarithm of the difference in radii raised to the power law exponent should result in a linear relationship with the natural logarithm of time with a slope of m=1. Thus, the power law exponent that describes the coarsening mechanism for this system should theoretically be the value of n that provides a slope that most closely results in a linear fit with a slope of unity for these precipitates. The corresponding linear plots for increasing values of n from 2-6 are plotted in **Figure 7.5(a)**. As the figure indicates, the value that gives the closest value for m=1 is that of n=6, where the corresponding slope is equal to 1.01. This would

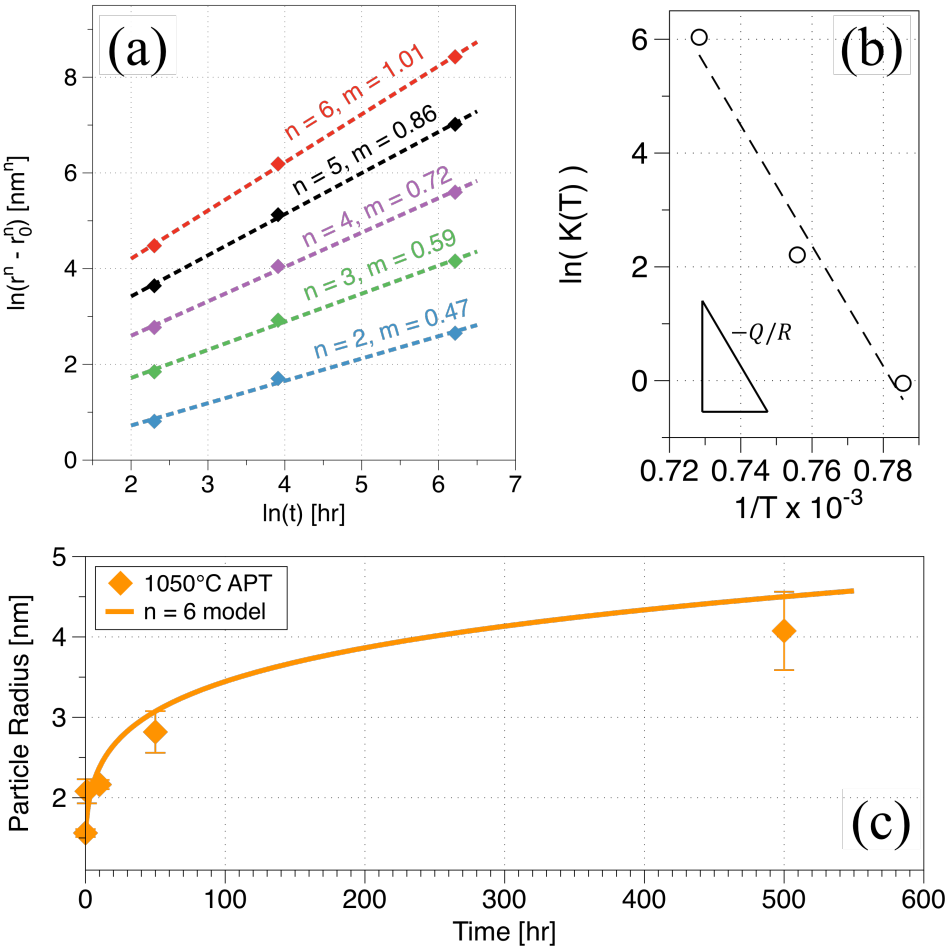


Figure 7.5. (a) the comparison of power law coarsening exponents for CrAZY powders annealed for 10-500h at 1050°C, showing the best linear correlation for an exponent of n=6. The activation energy for coarsening is estimated through the slope calculated in (b) through the linear regression of the natural logarithm of the coarsening curves vs. inverse temperature. In (c) the long term n=6 coarsening model is overlaid with 95% confidence intervals for measured APT precipitate sizes as a function of annealing time at 1050°C. [203]

suggest that the coarsening of these precipitates is dominated by the diffusion of solute atoms along 1D dislocation pipes intersecting the precipitates [76].

Assuming that the coarsening mechanism is the same for temperatures in the range of 1000°C-1100°C, it is possible to estimate the activation energy of this coarsening process. Considering again Eq. 2.11, the slope of $(r^n - r_0^n)$ vs. t provides the temperature dependent constant K_n. Since long-term coarsening data was not able to be recorded for 1000°C and 1100°C, it is assumed in this work that the coarsening of radii from the initial precipitate size (r = 1.56 nm) to the average radii for 1h anneals at 1000°C (r = 1.58 nm) and 1100°C (r = 2.58 nm) also follows the same linear trend matching n=6 coarsening kinetics. For these data points from all three annealing temperatures, the coarsening constants K_6 at each temperature were estimated through linear regressions of $(r^6 - r_0^6)$ vs. t. Considering the temperature dependence of this coarsening exponent (Eq. 7.3), taking the natural logarithm of both sides of the equation results in:

$$\ln(K_6) = \ln(k) + \left(-\frac{Q}{R}\right)\left(\frac{1}{T}\right) \quad \text{(7.3)}$$

The slope of the linear regression between $\ln(K_6)$ vs. $1/T$ results in the ratio between the activation energy for coarsening for the n=6 pipe-diffusion mechanism divided by the universal gas constant (R). The slope of this linear fit in **Figure 7.5(b)** corresponds to an activation energy for coarsening of $Q = 880\ kJ/mol$ with an estimated pre-exponential constant of $k = 9.6 \times 10^{35}\ h^{-1}$. This activation energy is within the range of previously estimated (Y,Al,O) precipitate activation energies for pipe diffusion previously reported by Oono in ODS FeCrAl alloy SOC-9 (480 kJ/mol) and SOC-14 (747 kJ/mol) and is less than the activation energy for pipe-diffusion estimated by the same author for (Y,Ti,O) precipitates in a 9Cr ODS FeCr alloy (891 kJ/mol). A corresponding plot of the coarsening data estimated for the 1050°C anneals and the n=6 coarsening model are overlaid together in **Figure 7.5(c)**.

In the previously presented coarsening kinetics modeling, only powders annealed for 10-500h were used for fitting. This is because all of these were in powder form and more careful control over the time/temperature profile was possible. The sample annealed for 1h at 1050°C is of the form of an extruded bar, and it is unclear the control that was kept for the time/temperature profile for this sample when this alloy was consolidated in the machine shop. Thus, to supplement the previous analysis, **Figure 7.6** shows deviations that exist in the power law coarsening behavior with extruded alloy 106ZY15C added to the linear regression. This figure shows three linear regressions through various points in the plot (1-50h), (1-500h), and (10-500h). When sample 106ZY15C with less control of the time/temperature profile is added to the linear regression analysis, the coarsening exponent deviates significantly to higher values and the linear fit decreases significantly in confidence. Irrespective of the change, higher coarsening exponents would only shift the coarsening behavior to more sluggish kinetics with significant decreases in the fit of the regression due to the outlying nature of this data point. Due to the short annealing time, and the sluggish coarsening kinetics, it is

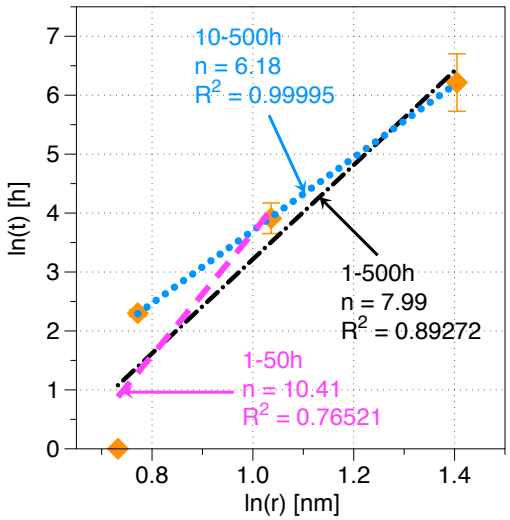


Figure 7.6. Kinetic exponent calculations using linear regressions through various sets of 1-500h annealed samples at 1050°C. The outlying nature of extruded sample 106ZY15C (1h) in comparison to annealed powder samples 10-50h is noted.

unlikely that such a high order coarsening exponent exists for the current system, and it will be shown that the current model fits well with the experimental data for the time/temperature regimes studied in this work.

Although quantifying the long-term coarsening behavior is important for estimating the viability of precipitate distributions to resist coarsening after long term reactor exposures, for this scope of this study it is more important to accurately estimate how the nanoprecipitate coarsening kinetics affect the as-consolidated precipitate distributions. It is therefore of importance to apply the long-term coarsening model to the short-term annealing temperature profiles experienced by the powder prior to consolidation via extrusion with increasing extrusion temperature in an attempt to be able to predict the sink strength of ODS FeCrAl alloys as a function of thermomechanical processing history. To approach this challenge, consider the annealing temperature profile of powder heated to 1000°C measured via thermocouple in a representative 2" extrusion can in **Figure 4.5**. Using this temperature profile, a scaling procedure was implemented in MATLAB to simulate the expected temperature profiles for samples extruded at 1000°C, 1050°C, and 1100°C. Using the simulated temperature profiles as input time-temperature curves, the n=6 coarsening model was applied to estimate the extent to which the nanoprecipitate populations would coarsen during pre-extrusion annealing treatments at each target extrusion temperature. The results of this simulation are presented in **Figure 7.7**. Even for short-term anneals at temperatures greater than 1000°C the nanoprecipitates begin to increase in size. With only a 50°C increase in temperature, the average size of the nanoprecipitates increases by 27%, while a temperature increase of 100°C results in a simulated 78% increase in precipitate size in comparison to the 1000°C extrusion temperature. Considering that the nanoprecipitate number density measured via APT for the ZY10C60 sample is 4.19×10^{23} m^{-3} in comparison to 0.79×10^{23} m^{-3} for CrAZY_H1 extruded at an extrusion temperature 100°C higher, this coarsening during alloy consolidation must be avoided if a high number of nanoprecipitates are desired for increased radiation resistance in reactor environments.

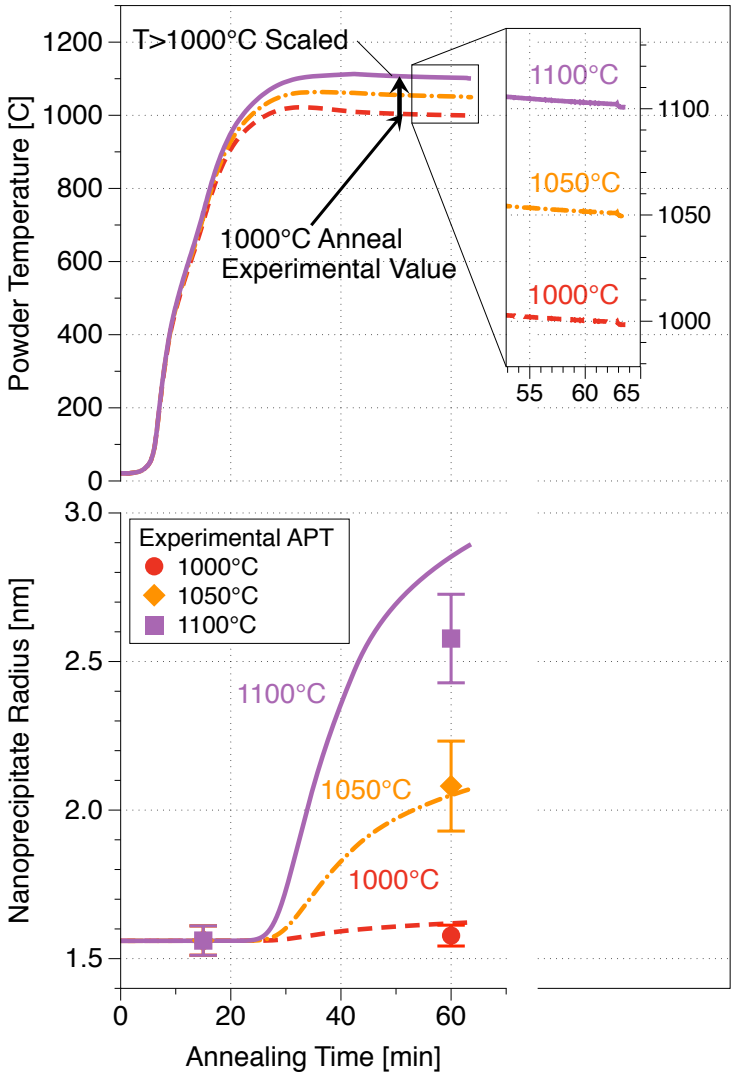


Figure 7.7. The simulation of precipitate size increases during pre-extrusion annealing treatments of using 1000°C, 1050°C, and 1100°C simulated time-temperature profiles scaled from the as-measured 1000°C powder temperature profile measured in **Figure 4.5**. The modeled sizes as a function of time are compared with APT data measured at the three respective temperatures. Errors for APT data are reported as 95% confidence intervals. [203]

Although the coarsening model applied in this study appears to capture the coarsening of the nanoscale (Y,Al,O) nanoprecipitate population as extrusion temperature increases, there are multiple important observations that are associated with the observed coarsening behavior in comparison to the literature data. In comparison with the higher order (n=6) coarsening kinetics observed here, comprehensive evaluations of nanoprecipitate coarsening kinetics in ODS FeCr alloy MA957 performed by Alinger and Cunningham showed either n=5 or n=6 (dislocation pipe-diffusion) coarsening kinetics for the smallest (Y,Ti,O) precipitates [77, 115, 167, 186]. Oono's previous investigations of a 9Cr ODS alloy coarsened at 1200-1350°C also indicated that dislocation pipe diffusion (n=5) kinetics dominated precipitate coarsening [78], and the team's later work on SOC-14 and SOC-9 alloys (ODS FeCrAl with and without Zr, respectively) in the same temperature range indicated coarsening kinetics dominated by either grain boundary (n=4) or dislocation pipe diffusion (n=5) mechanisms [79]. Earlier works on particle coarsening in legacy ODS FeCrAl alloy MA956 showed particle coarsening kinetics varying between n=4 and n=6 [160]. Thus, it would appear that the rate at which the nanoprecipitates coarsen in the current ODS FeCrAl alloy system are highly similar to the results previously presented in the ODS literature.

An unique attribute of the current CrAZY system is that the nanoprecipitate sizes are much smaller in comparison to other ODS FeCrAl alloys. **Figure 7.8** shows the variation of the natural logarithm of precipitate radius with the natural logarithm of annealing time for the ODS FeCr and FeCrAl alloys in literature. As a general trend, the ODS FeCrAl alloys exhibit precipitate sizes that are much larger than those for ODS FeCr alloys. A part of the reason why this is the case is because the alloy MA956 used for precipitate coarsening studies was recrystallized at high temperature (1350°C for 1h) prior to the start of the coarsening study, which resulted in a higher starting precipitate size. However, alloys SOC-9 and SOC-14 were only extruded at 1150°C, which is an identical temperature to the 3h HIP treatment used on 14YWT by Alinger. Even with thermomechanical processing at the same temperature, the precipitate sizes for SOC-14 and SOC-9 were 2-3x the initial precipitate size for the 14YWT alloy. While the

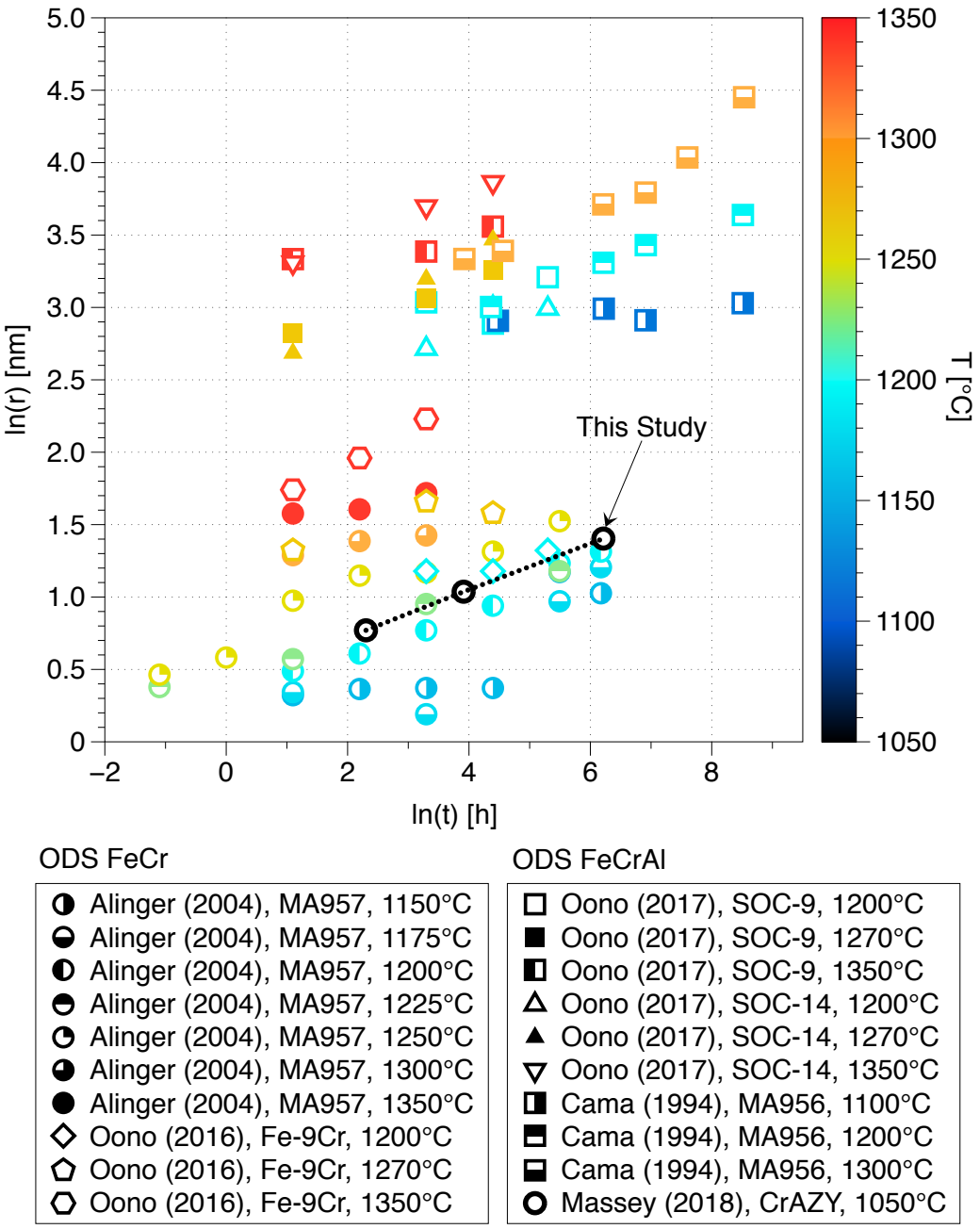


Figure 7.8. A comparison of coarsening data for ODS FeCr and ODS FeCrAl alloys reported in literature [78, 79, 115, 160] with the long term coarsening behavior of the CrAZY powder annealed up to 500h at 1050°C.

coarsening kinetics of ODS FeCrAl alloys and FeCr alloys both follow higher-order power law kinetics, the activation energies for precipitate coarsening in the ODS FeCrAl alloys are therefore lower than those for FeCr variants, which results in less thermal stability for (Y,Al,O) precipitate populations in comparison to (Y,Ti,O) precipitates. The CrAZY alloy system investigated in this study used a lower consolidation temperature than any of the previously studied ODS FeCrAl alloys where coarsening data exists. This lower thermomechanical processing temperature (1000°C) resulted in nanoprecipitate sizes rivaling those for ODS FeCr alloys. This means that it is possible to develop ODS FeCrAl alloys with competitive sink strengths in comparison to best-practice heats of FeCr alloys 14YWT or MA957.

Even though the current model is sufficient for the purposes of optimizing the processing parameters for ODS FeCrAl alloys for short annealing times, future work should be performed on both ODS FeCr and FeCrAl alloys due to the complexities associated with the alloy microstructures. To better illustrate the need for future investigations, consider the annealed CrAZY powder microstructures ZY10C15 and ZY10C60 analyzed by SEM-BSE previously in **Figure 5.2**. These microstructures are almost fully recrystallized, with only a small fraction of the powder retaining nanometer scale fine-grained regions. The powders coarsened at 1050°C for up to 500h all have the same type of recrystallized microstructure. As mentioned in Chapter 2, during the recrystallization process, the recrystallization front sweeps away the high number of dislocations previously accumulated within the microstructure during the mechanical alloying process. Because there was no externally applied force to deform the powder and re-develop the high number of dislocations usually within the ODS alloy, the powders should only have a small number of large grain boundaries and few dislocations within the grains. Thus, for the representative particle in the matrix, there should not be a grain boundary nearby, nor should there be any number of dislocations intersecting the particle by which accelerated paths for solute diffusion would exist. This would suggest that the n=6 coarsening mechanism noted for this CrAZY alloy should not be governing the

coarsening kinetics, and instead a volumetric diffusion (n=3) or interface incorporation (n=2) limiting condition should have been more appropriate.

Taking closer look at the theoretical power law derivations shows that simply comparing the power law exponent may be an erroneous way to estimate the mechanisms by which these precipitates are coarsening, even for the consolidated versions of the ODS alloys. For example, in Speight and Ardell's approach to the derivation of grain boundary precipitate coarsening kinetics (n=4), it is assumed that the precipitates all lie on the grain boundaries, and that the grain boundary diameter is sufficiently large in comparison to the precipitate diameter [71, 75]. Although it is well known in the ODS literature that larger precipitates preferentially exist along grain boundaries, these are only a small fraction of the total number of precipitates. Grain boundaries are already sinks for radiation induced defects, which is why there are defect free zones near grain boundaries after irradiation experiments. Framing the coarsening discussion just for these grain boundary precipitates omits the smaller precipitate distribution homogeneously distributed throughout the grains.

Neglecting the grain boundary coarsening of the smallest precipitates, there does exist a high density of dislocations (10^{13}-10^{15} m^{-2}) in consolidated ODS FeCr and FeCrAl alloys [60]. This high density of dislocations means that there may in fact be some evidence for the pipe-diffusion approximation; however, TEM investigations have shown that the density of dislocations varies widely between grains in as-extruded ODS alloys, with some grains being free of dislocations altogether [59]. Assuming that the dislocation density is high and on the order of 10^{15} m^{-2}, and assuming that this dislocation density is dispersed homogeneously with a corresponding number density of precipitates of 10^{24} m^{-3}, the average distance between the dislocations is ~31 nm while the average distance between precipitates is only ~6 nm. This would imply that only 20% are associated with dislocations at any point in time. In Vengrenovich's model (n=6), it is assumed that as precipitates coarsen, the pinning force decreases as coherency begins to be lost between the precipitate and the surrounding matrix, allowing the dislocation to detach and then

propagate to surrounding precipitates [76]. Consequently, it is not a faulty assumption that in the extruded ODS alloys, n=6 coarsening kinetics may dominate.

It is nevertheless intriguing that in both recrystallized powders (essentially dislocation-free) and in the consolidated alloys the n=6 power law is applicable. There is thus a possibility that the attribution of coarsening in all of these studies may be due to a different higher-order mechanism that has not yet been formulated. The possibility of a different mechanism is reinforced by derivations by Hoyt that has shown that in the event that either grain boundary or dislocation pipe diffusion is supplemented by volumetric diffusion, the coarsening power law exponent simplifies to n=3 irrespective of the higher-order coarsening mechanism [242]. Since solute atoms in the ODS matrix are expected to diffuse in a manner that combines all of these mechanisms, it is surprising that such sluggish (n=6) coarsening behavior exists for precipitate populations in both ODS FeCrAl and FeCr alloys. Although beyond the scope of the current work, the dependence of coarsening kinetics on microstructure should be a topic of continued interest in future studies.

7.3. Applied Kinetics to the Design of ODS FeCrAl with high Sink Strength and Ductility

Using the knowledge obtained about the compositions and coarsening kinetics of the smallest (Y,Al,O) nanoprecipitates in the CrAZY alloy system, an innovative two-step annealing treatment has been used for the development of an extruded alloy with an optimized nanoprecipitate number density while maintaining alloy ductility. Using the conventional processing route for extruded ODS alloys in **Figure 2.7**, CrAZY powder (ZY40H-CM08) was subjected to two different types of pre-extrusion annealing treatments. First, the as-milled powder was heated for 1h at 1050°C prior to extrusion at the same temperature. The nanoprecipitate distribution for this alloy (106ZY15C) has already been evaluated and presented previously in **Table 6.2**. The second annealing treatment involved utilizing a lower-temperature 850°C heat treatment for 1h to allow for nanoprecipitate nucleation and growth without substantial coarsening followed by

extrusion at 1050°C. The alloy was held at 1050°C for only a short time to allow the sample to reach a homogeneous temperature prior to extrusion to minimize subsequent coarsening. This new alloy was given the name designation 105ZYA15C for the following comparison of microstructures, precipitate distributions, and mechanical properties.

The microstructures of alloys 106ZY15C and 106ZYA15C are illustrated in **Figure 7.9** for both the longitudinal and transverse orientations. Similarly to the other extruded ODS alloys presented in this work, the grains in these CrAZY have significant textures in both orientations. In the transverse orientation, the grains indicate a strong orientation in the [110] orientation, which is consistent with the preferred sip plane of (110) for the BCC microstructure. The grain textures in the longitudinal plane show strong (111) and (001) orientations, both perpendicular to the [110] preferred grain alignment along the extrusion axis. The primary difference associated with the use of the two-step pre-extrusion annealing process for 106ZYA15C is readily apparent through the comparison of the grain size distributions of the two alloys. **Figure 7.10** shows that the average grain size for the 106ZYA15C is only 538 nm, while the average grain size for the 106ZY15C alloy measures more than twice this value (1.154 μm). Since identical extrusion cans, extrusion aspect ratios, die sizes, and extrusion temperatures were identical, the same amount of deformation was experienced by both samples, so the only difference that could explain this refinement of grain size is the way by which dislocations propagate through the microstructure and develop the grain and sub-grain network structures within the microstructure. Assuming that the same bi-modal annealed powder microstructure exists for both powders (although the effect of heating rate on the fraction and size of abnormally grown grains has not fully been investigated), the refined grain size of 106ZYA15C can be explained through the increased pinning of dislocations by the higher number density of precipitates within this alloy.

APT measurements conducted on both the 106ZY15C and 106ZYA15C illustrate the differences in precipitation achieved by the two-stage annealing procedure. As illustrated by **Figure 7.11**, the nanoprecipitate distribution in the 106ZYA15C specimen

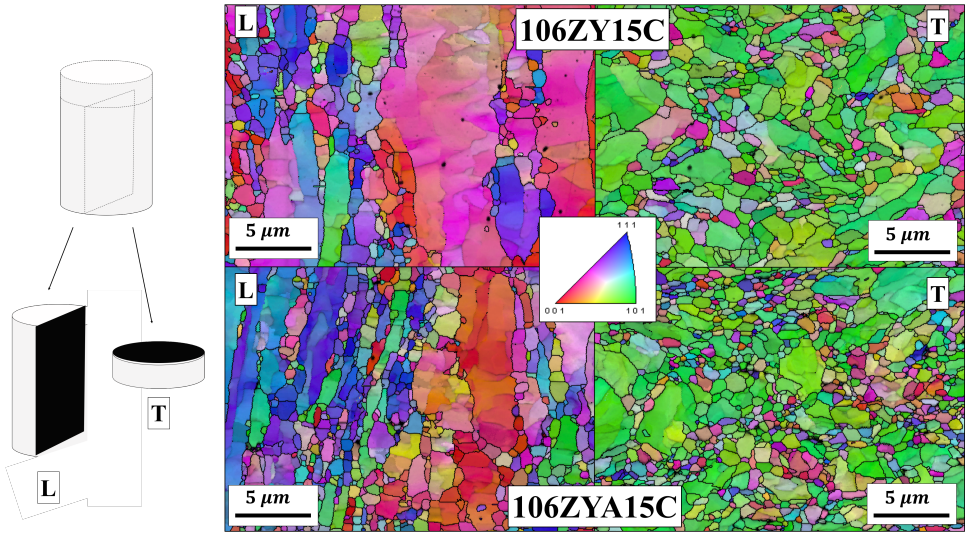


Figure 7.9. EBSD orientation maps for a CrAZY ODS FeCrAl alloy annealed at 850°C for 1h followed by extrusion at 1050°C (106ZYA15C) in comparison to alloy annealed for 1h at 1050°C followed by extrusion at the same temperature (106ZY15C)

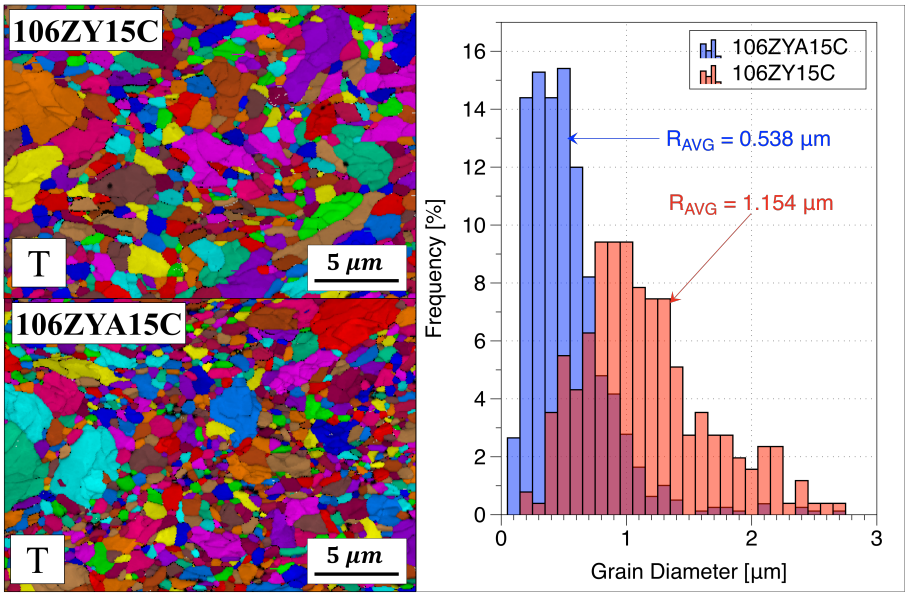


Figure 7.10. EBSD grain maps representing each grain as a unique color for a CrAZY ODS FeCrAl alloy annealed at 850°C for 1h followed by extrusion at 1050°C (106ZYA15C) in comparison to alloy annealed for 1h at 1050°C followed by extrusion at the same temperature (106ZY15C). Also shown are the respective grain size distributions measured by EBSD for both alloys.

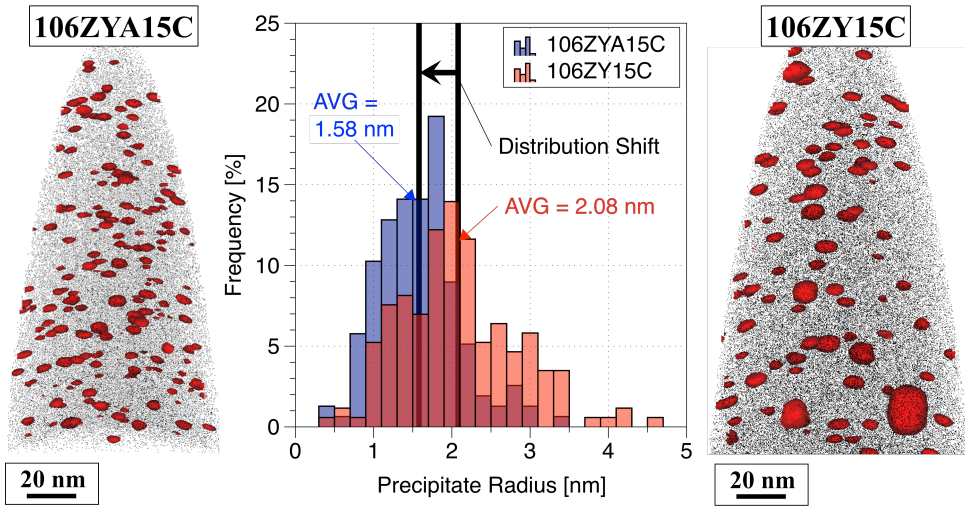


Figure 7.11. APT reconstructed control volumes for 106ZYA15C (annealed 1h at 850°C) vs. 106ZY15C (annealed 1h at 1050°C) showing red (Y,Al,O) nanoprecipitates in red with black Fe matrix atoms in the background. Also illustrated is the shift in nanoprecipitate size distributions due to the difference in pre-extrusion annealing temperatures.

is finer than for the 106ZY15C sample. In the figure, identical 1.5% (Y,YO,AlO) isoconcentration surfaces are illustrated atop a matrix of Fe atoms. The average nanoprecipitate size and number density increase from 1.58 nm and 4.3×10^{23} m^{-3} to 2.08 nm and 1.1×10^{23} m^{-3} for samples 106ZYA15C and 106ZY15C, respectively. Although not shown, the compositions of the precipitates in the 106ZYA15C match those measured and presented previously for the ZY10C15 and ZY10C60 specimens.

This shift in nanoprecipitate compositions and grain size has a significant impact on the predicted irradiation resistance of the CrAZY alloy in radiation environments. The types of irradiation-induced degradation phenomena were previously described in Chapter 1 and are both a strong function of irradiation dose and irradiation temperature, but it has been shown that to mitigate many of these phenomena (irradiation-induced hardening, void swelling, etc.) it is important to quantify the intrinsic resistance of each material to the accumulation of defects within the microstructure. One measure that can be evaluated is the cumulative sink-strength (S) of features within the microstructure that serve to preferentially remove excess defects from the microstructure. The sink strength for ODS materials largely comes from the high number density of nanoscale precipitates

within the microstructure, but grain boundaries and dislocation networks also contribute to this cumulative sink strength term [1]. The sink strength for precipitates with a given radius (r_p) and number density (N_p) is calculated as $S_p = 4\pi r_p N_p$. For grain boundaries, $S_{GB} = 60/d_{GB}^2$, where d_{GB} is the grain boundary diameter, although this term decreases as the total sink strength increases due to overlaps between interaction fields between different sinks [243]. For dislocations, the sink strength is approximately equal to the dislocation density ($S_d = \rho_d Z_d$), where $Z_d \sim 1$ is a capture efficiency for the dislocations. The dislocation densities for both of these alloys were not able to be measured explicitly, but the as-extruded dislocation density is expected to be on the order of 10^{14} m^{-2} for these alloys [60]. Although the total sink-strength will vary slightly due to the aforementioned interrelation of the different sink strengths, as a first approximation the sum of these three components can be compared to access the difference in radiation resistance as a function of processing path.

For alloys 106ZYA15C and 106ZY15C, the values of these sink strengths for the measured grain sizes and precipitate distributions are presented in **Table 7.1**. As can be clearly seen from the sink-strength calculations, the refinement of the precipitate distribution using the two-step annealing approach has tripled the precipitate sink strength for alloy 106ZYA15C in comparison to alloy 106ZY15C. The resulting decrease in grain size due to the refined precipitate population likewise resulted in an order of magnitude greater grain boundary sink-strength term. Although the dislocation densities

Table 7.1. Calculated sink strengths for 106ZYA15C and 106ZY15C

	106ZYA15C	106ZY15C
Average Precipitate Radius (r_p)	1.58	2.08
Precipitate Number Density (N_p)	4.3×10^{23} m^{-3}	1.1×10^{23} m^{-3}
Average Grain Diameter (d_{GB})	538 nm	1154 nm
Representative Dislocation Density ($\boldsymbol{\rho_d}$)	10^{14} m^{-2}	10^{14} m^{-2}
Precipitate Sink Strength (S_p)	8.54×10^{15} m^{-2}	2.88×10^{15} m^{-2}
Grain Boundary Sink Strength (S_{GB})	2.07×10^{14} m^{-2}	4.51×10^{13} m^{-2}
Dislocation Sink Strength (S_{GB})	1.00×10^{14} m^{-2}	1.00×10^{14} m^{-2}
Total Sink Strength	8.84×10^{15} m^{-2}	3.02×10^{15} m^{-2}

were assumed to be on the same order of magnitude, it would actually be expected for there to be a slightly higher dislocation density with a smaller grain size and a higher number of precipitates for the 106ZYA15C sample as well. The result is striking in terms of irradiation resistance. Zinkle previously established that for resistance to irradiation induced hardening or void swelling in the presence of He-stabilized cavities, a total sink strength on the order of 10^{16} m^{-2} is desired [1]. Thus, alloy 106ZY15C annealed and extruded at 1050°C would not be expected to be as resistant to both of these irradiation degradation phenomena in comparison to the higher sink-strength of 106ZYA15C that approaches this threshold value.

Also important for actual application as a structural material is the mechanical response of each alloy as a function of temperature. Although this study has not focused substantially on the effects of various processing parameters on the mechanical properties of as-fabricated ODS FeCrAl alloys, some preliminary results are presented here to illustrate the benefits of the two-step annealing process utilized for the development of 106ZYA15C. Miniature SS-J3 tensile specimens were machined along the longitudinal orientations of both of the alloys in their as-extruded state, and an MTS hydraulic tensile testing machine was used to perform mechanical property evaluations as a function of temperature from 23-800°C in ambient air atmosphere. The temperature of the specimens at each target test temperature were measured using an attached thermocouple to the sample holder, and each sample was held at the desired test temperature for at least 10 min. to ensure a homogeneous sample temperature. Three different plots are presented in **Figure 7.12** for each specimen: (1) the ultimate tensile strength, (2) the yield strength, and (3) the total elongation of each specimen. The ultimate tensile strength (UTS) is the maximum stress the alloy is able to resist prior to the onset of plastic instability, or in other words the maximum work hardening limit of the alloy prior to the onset of necking and subsequent fracture. The yield strength (YS) measures the resistance of the alloy microstructure to the onset of dislocation motion (plastic deformation), which can be modeled based on the different strengthening contributions of the matrix, the precipitates, the grain boundaries, and the dislocation networks established during thermomechanical

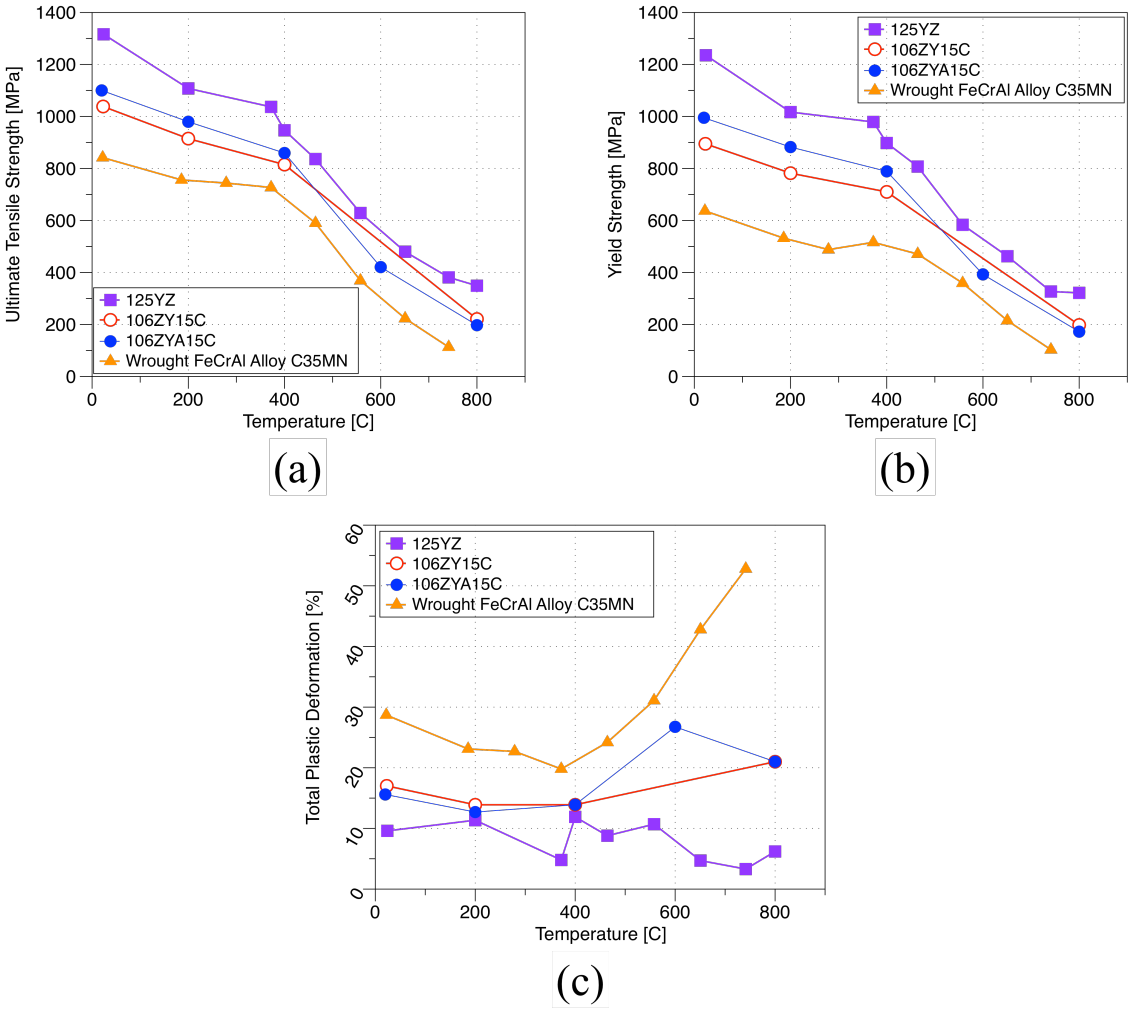


Figure 7.12. The variation of (a) ultimate tensile strength, (b) yield strength, and (c) plastic deformation for alloys 106ZY15C and 106ZYA15C as a function of increasing test temperature. Also shown are an ODS FeCrAl alloy 125YZ [99] and a non-ODS wrought FeCrAl alloy C35MN [8] for comparison.

consolidation and deformation treatments. The total plastic deformation is simply the measure of the total elongation at the point of fracture minus the specimen length at the onset of yielding.

With these definitions in mind, the mechanical properties of these two alloys are compared directly with two model alloys available in the literature. The first, with the name designation 125YZ, is a 1st Generation ODS Fe-12Cr-5.6Al alloy with Zr addition that was milled using identical mechanical alloying parameters. The only difference between this alloy and the CrAZY alloys presented here is the manner by which Zr was added to the matrix (as ZrO_2 powder instead of gas-atomization) and a lower annealing and extrusion temperature of 850°C [99]. Thus, this alloy provides a good reference to the alloy 106ZYA15C that was annealed at the same temperature but extruded at the same 1050°C temperature of 106ZY15C. In addition to this model ODS FeCrAl alloy, a high-strength non-ODS wrought model FeCrAl alloy C35MN with nominal composition (Fe-13Cr-4.5Al-2Mo-1Nb) fabricated through a combination of arc-melting and hot rolling is also included in the comparison [8].

A comparison of the tensile strengths and total deformations of all four alloys illustrates important trends. The alloy 125YZ annealed and extruded at low temperature (850°C) exhibits higher strength than the other variants, but this increase in strength has resulted in a significant deterioration in the alloy's ductility. If the annealing and extrusion temperature is increased to (1050°C), the YS and UTS decrease 300 MPa for room-temperature tensile tests, but the ductility is improved over the entire temperature range. The non-ODS wrought FeCrAl alloy C35MN exhibits the lowest strength, but the ductility is far superior to all of the ODS FeCrAl alloys due to the larger grain size and the lack of obstacles for dislocation motion within the matrix. The use of the two-step annealing process for the 106ZYA15C specimen achieves the same levels of ductility due to the higher extrusion temperature while simultaneously increasing the tensile strengths at lower temperatures ($T < 400°C$) in comparison to the 106ZY15C sample. The higher precipitate number density coupled with a grain size in between that measured for 125YZ (270 nm) and 106ZY15C can be attributed to this optimization of strength and ductility.

Of course, this alloy still exhibits lower ductility in comparison to the non-ODS FeCrAl variant because the high number density of obstacles to dislocation motion and the smaller grain size also inhibits the work-hardening capacity of the ODS alloy in comparison to the wrought FeCrAl alloy.

Through a better understanding of the nanoprecipitate compositions and coarsening kinetics of the smallest (Y,Al,O)-rich nanoprecipitates in these CrAZY ODS FeCrAl alloys, the use of a two-step annealing procedure prior to alloy consolidation has resulted in the development of an ODS FeCrAl alloy that has both a high sink strength for irradiation resistance and an arguably superior mechanical response as a structural material in fission and fusion reactor conditions. These best-practice processing parameters should be extended to the development of both ODS FeCrAl and FeCr alloys for future alloy development efforts.

CHAPTER 8: Conclusions

8.1. Summary of Experimental Findings

In this comprehensive work, it has been found that in the CrAZY alloys developed at ORNL for nuclear applications, fine distributions of (Y,Al,O)-rich precipitates and coarser distributions of precipitates with various compositions comprise the distribution of dispersed second phase particles in these ODS FeCrAl alloys. Through a detailed multiscale approach combining fine-scale APT measurements and macroscale magnetic SANS powder measurements, the smallest nanoprecipitates have been shown to be nonmagnetic and most likely either YAG or YAP depending on precipitate size, processing temperature, and annealing time. It has been shown that impurity C and N contamination within the FeCrAlZr matrix results in the precipitation of Zr(C,N) precipitates with occasional AlN and M_xC_y carbides comprised of Fe and Cr. The impurity sequestration ability of added Zr in the matrix has been quantified through a combination of APT and thermodynamic calculations, which has successfully explained discrepancies in the ODS FeCrAl literature pertaining to the identities of nanoprecipitates as a function of alloy composition.

Coarsening kinetics have been evaluated for the CraZY ODS FeCrAl system, and it has been found that higher-order coarsening kinetics dominate precipitate growth during prolonged annealing treatments at high temperatures. By knowing the thermal processing history of the given ODS FeCrAl alloy, it has been proven that long-term coarsening models can be applied to pre-consolidation annealing treatments to optimize nanoprecipitate distributions in as-fabricated ODS FeCrAl alloys. Through the use of innovative muti-step pre-consolidation annealing treatments, ODS FeCrAl alloys with a high sink strength and optimized mechanical properties can be fabricated that are competitive with ODS FeCr alloys in literature.

8.2. Contributions to the State-of-the-Art

This comprehensive work has provided many insights into the precipitation of various nanoprecipitate populations in ODS FeCrAl alloys, specifically with respect to the roles of alloying elements and impurities on the types of nanoprecipitates that exist within the alloy microstructure. In addition, a detailed analysis of the nanoscale (Y,Al,O)-rich precipitates has highlighted shortcomings in APT compositional correction models widely applied to the nanoscale precipitates in ODS alloys. However, these shortcomings of the APT technique were at least partially offset by magnetic SANS results that highlighted the non-magnetic and defective nature of the nanoprecipitates. The still unknown partitioning of Al between the matrix and precipitates provides significant challenges for the accurate determination of nanoprecipitate compositions.

This work has also highlighted important differences between nanoprecipitate distributions within recrystallized powders and the variety of literature data on recrystallized ODS alloys after cold work and subsequent thermal treatments. The parity between nanoprecipitate distributions in fine and coarse-grained regions in the ball-milled recrystallized powders is in stark contrast to differences in nanoprecipitate distributions in coarse-grained regions in deformed and recrystallized ODS FeCr alloys in the literature. Thus, this study has highlighted the need to better understand possible precipitate dissolution and re-precipitation phenomena as a function of thermomechanical processing history.

Finally, and most importantly, the discussion of ODS FeCrAl alloys has largely been limited to legacy alloys such as PM2000 and MA956 that have distributions of coarser nanoprecipitates and often fully recrystallized microstructures. Thus, in most experimental comparisons between ODS FeCrAl and ODS FeCr alloys in literature, the lack of parity between processing conditions between these alloys has resulted in the discounting of ODS FeCrAl alloys as viable candidates for nuclear applications requiring high sink strength and beneficial low and high temperature strength. However, in the current work it has been shown that although the (Y,Al,O)-rich precipitates exhibit faster coarsening kinetics than the (Y,Ti,O)-rich nanoprecipitates comprising ODS FeCr alloys,

through careful control of the thermomechanical processing history of these CrAZY alloys can result in as-fabricated variants that are competitive with popular ODS FeCr alloys such as 14YWT and MA957. This work has presented a multi-step consolidation procedure whereby nanoprecipitates can first be nucleated without significant coarsening, followed by a short-duration high temperature extrusion step to minimize particle coarsening while simultaneously allowing for improved ductility for these ODS alloys.

8.3. Future Work

There are many aspects to this work that necessitate further investigation. First, the study of (Y,Al,O) precipitates in ODS FeCrAl alloys using SANS techniques has been established as a viable path forward for the analysis of particle compositions and structures. For these fine-scale precipitates in the current CrAZY alloy system, the SANS technique was able to resolve these precipitates, which is in disagreement with previous work by Alinger on the ODS FeCrAl legacy alloy PM2000, which would be expected to have similar precipitate compositions as those seen in this work. Future neutron-scattering work should be performed on these ODS FeCrAl alloys to access the extent to which these precipitates can be resolved and quantified. Furthermore, the scattering vector range that this work was able to cover was limited by the magnet and/or furnace size used to manipulate the sample environment. More advanced studies using in-situ temperature dependent magnetic scattering or the use of polarized neutrons on ex-situ annealed samples may prove more accurate at quantifying the nuclear and magnetic scattering contributions of these nanoscale precipitate populations as they nucleate and grow to stable sizes.

For the APT results presented in this work, it has been routinely shown that there does not exist a sufficient methodology available in the current literature for the accurate estimation of the nanoprecipitate compositions without more knowledge about the local environment at the matrix/precipitate interface. Future work should involve using high-resolution electron microscopy techniques such as electron energy loss spectroscopy (EELS) to investigate whether an Al-deplete and Cr-rich shell exists at the precipitate

boundary. If this is the case, then the compositions of the smallest (Y,Al,O) nanoprecipitates can be corrected using the state-of-the-art chemical composition correction model first presented by Hatzoglou and applied in this work for the ODS FeCrAl system.

The estimation of nanoprecipitate coarsening during thermomechanical consolidation treatments should be carefully considered for future alloy production efforts. In particular, when attempting to compare consolidation methodologies such as extrusion, hot-isostatic pressing, and spark plasma sintering, careful attention should be paid to the temperature profiles for each of these methods instead of the target temperature used for each. Although the grain morphologies, and the corresponding ductility and mechanical response, will be different due to differences in grain size between alloys processed at different temperatures, these differences in microstructure are already expected through these different processing methodologies. For a detailed comparison of alloy properties, instead the user should be targeting processing parameters that create parity between nanoprecipitate dispersion characteristics between alloys developed using different methods. For example, for an ODS FeCrAl alloy extruded at 1100°C, the sample is only at this temperature for approximately 30 min. for the current extrusion procedure investigated in this work. When attempting to compare this extruded alloy with one developed using HIP, the temperature should be lowered because the hold times for HIP treatments at the target temperature are usually multiple hours, which would result in coarser precipitate distributions that are not reasonable to compare.

While this work provided some tensile data for general comparisons between processing conditions, more mechanical property data is needed on these alloys, including comprehensive fracture toughness data. The stringers and wide variety of precipitates in the microstructure may deteriorate alloy mechanical properties and must be compared as a function of temperature and specimen orientation. Finally, ion and neutron irradiations should be performed on these various alloys to access the potential sink-strength benefit for this novel multi-stage processing method.

List of References

[1] S.J. Zinkle, L.L. Snead, Designing Radiation Resistance in Materials for Fusion Energy, Annual Review of Materials Research 44(1) (2014) 241-267.
[2] S.J. Zinkle, J.T. Busby, Structural materials for fission & fusion energy, Materials Today 12(11) (2009) 12-19.
[3] L. Mansur, Theory and experimental background on dimensional changes in irradiated alloys, Journal of Nuclear Materials 216 (1994) 97-123.
[4] K.A. Terrani, S.J. Zinkle, L.L. Snead, Advanced oxidation-resistant iron-based alloys for LWR fuel cladding, Journal of Nuclear Materials 448(1-3) (2014) 420-435.
[5] S.J. Zinkle, K.A. Terrani, J.C. Gehin, L.J. Ott, L.L. Snead, Accident tolerant fuels for LWRs: A perspective, Journal of Nuclear Materials 448(1-3) (2014) 374-379.
[6] B.A. Pint, K.A. Terrani, M.P. Brady, T. Cheng, J.R. Keiser, High temperature oxidation of fuel cladding candidate materials in steam–hydrogen environments, Journal of Nuclear Materials 440(1-3) (2013) 420-427.
[7] J.H. Kim, M.H. Lee, B.K. Choi, Y.H. Jeong, Deformation behavior of Zircaloy-4 cladding under cyclic pressurization, Journal of Nuclear Science and Technology 44(10) (2007) 1275-1280.
[8] Y. Yamamoto, B.A. Pint, K.A. Terrani, K.G. Field, Y. Yang, L.L. Snead, Development and property evaluation of nuclear grade wrought FeCrAl fuel cladding for light water reactors, Journal of Nuclear Materials 467 (2015) 703-716.
[9] C.P. Massey, K.A. Terrani, S.N. Dryepondt, B.A. Pint, Cladding burst behavior of Fe-based alloys under LOCA, Journal of Nuclear Materials 470 (2016) 128-138.
[10] D. Becker, F. Dworschak, H. Wollenberger, Analysis of Point Defect States in Copper V. Temperature Dependence of the Defect Production by Electron Irradiation, physica status solidi (b) 54(2) (1972) 455-462.
[11] W. Schilling, K. Sonnenberg, Recovery of irradiated and quenched metals, Journal of Physics F: Metal Physics 3(2) (1973) 322.
[12] G. Kinchin, R. Pease, The displacement of atoms in solids by radiation, Reports on progress in physics 18(1) (1955) 1.
[13] S. Was Gary, Fundamentals of Radiation Materials Science, Berlin Heidelberg: Springer, 2007.
[14] J.A. Brinkman, Production of atomic displacements by high-energy particles, American Journal of Physics 24(4) (1956) 246-267.
[15] D.J. Bacon, Y.N. Osetsky, R. Stoller, R.E. Voskoboinikov, MD description of damage production in displacement cascades in copper and α-iron, Journal of nuclear materials 323(2-3) (2003) 152-162.
[16] S. Zinkle, L. Seitzman, W. Wolfer, I. Energy calculations for pure metals, Philosophical Magazine A 55(1) (1987) 111-125.
[17] G. Odette, G. Lucas, Recent progress in understanding reactor pressure vessel steel embrittlement, Radiation effects and defects in solids 144(1-4) (1998) 189-231.
[18] S.A. Briggs, P.D. Edmondson, K.C. Littrell, Y. Yamamoto, R.H. Howard, C.R. Daily, K.A. Terrani, K. Sridharan, K.G. Field, A combined APT and SANS investigation of α′ phase precipitation in neutron-irradiated model FeCrAl alloys, Acta Materialia 129 (2017) 217-228.

[19] C. Capdevila, M.K. Miller, J. Chao, Phase separation kinetics in a Fe–Cr–Al alloy, Acta Materialia 60(12) (2012) 4673-4684.
[20] C. Capdevila, M.K. Miller, K.F. Russell, Aluminum partitioning during phase separation in Fe–20%Cr–6%Al ODS alloy, Journal of Materials Science 43(11) (2008) 3889-3893.
[21] C. Capdevila, M.K. Miller, K.F. Russell, J. Chao, J.L. González-Carrasco, Phase separation in PM 2000™ Fe-base ODS alloy: Experimental study at the atomic level, Materials Science and Engineering: A 490(1-2) (2008) 277-288.
[22] C. Capdevila, M.K. Miller, I. Toda, J. Chao, Influence of the α–α′ phase separation on the tensile properties of Fe-base ODS PM 2000 alloy, Materials Science and Engineering: A 527(29-30) (2010) 7931-7938.
[23] P.D. Edmondson, S.A. Briggs, Y.Yamamoto, R.H. Howard, K. Sridharan, K.A. Terrani, K.G. Field, Irradiation-enhanced α ′ precipitation in model FeCrAl alloys, Scripta Materialia 116 (2016) 112-116.
[24] K.G. Field, X. Hu, K.C. Littrell, Y. Yamamoto, L.L. Snead, Radiation tolerance of neutron-irradiated model Fe–Cr–Al alloys, Journal of Nuclear Materials 465 (2015) 746-755.
[25] K.G. Field, K.C. Littrell, S.A. Briggs, Precipitation of α′ in neutron irradiated commercial FeCrAl alloys, Scripta Materialia 142 (2018) 41-45.
[26] M.H. Mathon, Y. de Carlan, G. Geoffroy, X. Averty, A. Alamo, C.H. de Novion, A SANS investigation of the irradiation-enhanced α–α′ phases separation in 7–12 Cr martensitic steels, Journal of Nuclear Materials 312(2-3) (2003) 236-248.
[27] A. Vattré, T. Jourdan, H. Ding, M.-C. Marinica, M. Demkowicz, Non-random walk diffusion enhances the sink strength of semicoherent interfaces, Nature communications 7 (2016) 10424.
[28] C. Jiang, N. Swaminathan, J. Deng, D. Morgan, I. Szlufarska, Effect of grain boundary stresses on sink strength, Materials Research Letters 2(2) (2014) 100-106.
[29] H. Huang, X. Tang, F. Chen, Y. Yang, J. Liu, H. Li, D. Chen, Radiation damage resistance and interface stability of copper–graphene nanolayered composite, Journal of Nuclear Materials 460 (2015) 16-22.
[30] J. Ribis, S. Lozano-Perez, Nano-cluster stability following neutron irradiation in MA957 oxide dispersion strengthened material, Journal of Nuclear Materials 444(1-3) (2014) 314-322.
[31] H. Kishimoto, K. Yutani, R. Kasada, O. Hashitomi, A. Kimura, Heavy-ion irradiation effects on the morphology of complex oxide particles in oxide dispersion strengthened ferritic steels, Journal of Nuclear Materials 367-370 (2007) 179-184.
[32] C.M. Parish, R.M. White, J.M. LeBeau, M.K. Miller, Response of nanostructured ferritic alloys to high-dose heavy ion irradiation, Journal of Nuclear Materials 445(1-3) (2014) 251-260.
[33] A. Certain, S. Kuchibhatla, V. Shutthanandan, D.T. Hoelzer, T.R. Allen, Radiation stability of nanoclusters in nano-structured oxide dispersion strengthened (ODS) steels, Journal of Nuclear Materials 434(1-3) (2013) 311-321.

[34] T. Lazauskas, S.D. Kenny, R. Smith, G. Nagra, M. Dholakia, M. Valsakumar, Simulating radiation damage in a bcc Fe system with embedded yttria nanoparticles, Journal of Nuclear Materials 437(1-3) (2013) 317-325.
[35] T. Chen, J.G. Gigax, L. Price, D. Chen, S. Ukai, E. Aydogan, S. Maloy, F. Garner, L. Shao, Temperature dependent dispersoid stability in ion-irradiated ferritic-martensitic dual-phase oxide-dispersion-strengthened alloy: Coherent interfaces vs. incoherent interfaces, Acta Materialia 116 (2016) 29-42.
[36] C.L. Chen, A. Richter, R. Kögler, The effect of dual Fe+/He+ ion beam irradiation on microstructural changes in FeCrAl ODS alloys, Journal of Alloys and Compounds 586 (2014) S173-S179.
[37] C.L. Chen, A. Richter, R. Kögler, G. Talut, Dual beam irradiation of nanostructured FeCrAl oxide dispersion strengthened steel, Journal of Nuclear Materials 412(3) (2011) 350-358.
[38] R. Schäublin, A. Ramar, N. Baluc, V. de Castro, M.A. Monge, T. Leguey, N. Schmid, C. Bonjour, Microstructural development under irradiation in European ODS ferritic/martensitic steels, Journal of Nuclear Materials 351(1-3) (2006) 247-260.
[39] D.A. McClintock, D.T. Hoelzer, M.A. Sokolov, R.K. Nanstad, Mechanical properties of neutron irradiated nanostructured ferritic alloy 14YWT, Journal of Nuclear Materials 386-388 (2009) 307-311.
[40] D.A. McClintock, M.A. Sokolov, D.T. Hoelzer, R.K. Nanstad, Mechanical properties of irradiated ODS-EUROFER and nanocluster strengthened 14YWT, Journal of Nuclear Materials 392(2) (2009) 353-359.
[41] T. Chen, E. Aydogan, J.G. Gigax, D. Chen, J. Wang, X. Wang, S. Ukai, F.A. Garner, L. Shao, Microstructural changes and void swelling of a 12Cr ODS ferritic-martensitic alloy after high-dpa self-ion irradiation, Journal of Nuclear Materials 467 (2015) 42-49.
[42] D. Gelles, Microstructural examination of commercial ferritic alloys at 200 dpa, Journal of nuclear materials 233 (1996) 293-298.
[43] T. Yamamoto, G.R. Odette, P. Miao, D. Hoelzer, J. Bentley, N. Hashimoto, H. Tanigawa, R.J. Kurtz, The transport and fate of helium in nanostructured ferritic alloys at fusion relevant He/dpa ratios and dpa rates, Journal of Nuclear Materials 367 (2007) 399-410.
[44] K. Yutani, H. Kishimoto, R. Kasada, A. Kimura, Evaluation of Helium effects on swelling behavior of oxide dispersion strengthened ferritic steels under ion irradiation, Journal of Nuclear Materials 367-370 (2007) 423-427.
[45] Q. Li, C.M. Parish, K.A. Powers, M.K. Miller, Helium solubility and bubble formation in a nanostructured ferritic alloy, Journal of Nuclear Materials 445(1-3) (2014) 165-174.
[46] C.M. Parish, K.A. Unocic, L. Tan, S.J. Zinkle, S. Kondo, L.L. Snead, D.T. Hoelzer, Y. Katoh, Helium sequestration at nanoparticle-matrix interfaces in helium + heavy ion irradiated nanostructured ferritic alloys, Journal of Nuclear Materials 483 (2017) 21-34.
[47] W. Coolidge, Ductile tungsten, Proceedings of the American Institute of Electrical Engineers 29(6) (1910) 953-957.

[48] E. Orowan, Discussion on internal stresses, Symposium on internal stresses in metals and alloys, Institute of Metals London, 1948, pp. 451-453.
[49] G.S. Ansell, Oxide dispersion strengthening: proceedings of a symposium, Gordon and Breach, New York, 1968.
[50] A.K. Seeger, in: Proceedings of the second United Nations International Conference on the Peaceful Uses of Atomic Energy, vol.6, United Nations, New York, 1958, p. 250.
[51] J. Friedel, Dislocations Pergamon, New York 274 (1964).
[52] S.J. Zinkle, Y. Matsukawa, Observation and analysis of defect cluster production and interactions with dislocations, Journal of Nuclear Materials 329-333 (2004) 88-96.
[53] U. Kocks, A. Argon, M. Ashby, Thermodynamics and Kinetics of Slip, Volume 19 in Progress in Materials Science, B. Chalmers, JW Christian and TB Massalsk, Eds, Pergamon Press, Oxford, 1975.
[54] U. Kocks, H. Mecking, Strength of Metals and Alloys, Ed.: P. Haasen, V. Gerold, G. Kostorz, Vol. I, Pergamon Press, Oxford, 1979.
[55] A. Foreman, M. Makin, Dislocation movement through random arrays of obstacles, Philosophical magazine 14(131) (1966) 911-924.
[56] J.H. Kim, T.S. Byun, D.T. Hoelzer, C.H. Park, J.T. Yeom, J.K. Hong, Temperature dependence of strengthening mechanisms in the nanostructured ferritic alloy 14YWT: Part II—Mechanistic models and predictions, Materials Science and Engineering: A 559 (2013) 111-118.
[57] Q. Li, Modeling the microstructure–mechanical property relationship for a 12Cr–2W–V–Mo–Ni power plant steel, Materials Science and Engineering A 361(1-2) (2003) 385-391.
[58] C. Lacy, M. Gensamer, The tensile properties of alloyed ferrites, Trans. ASM 32 (1944) 88-110.
[59] J. Bentley, D.T. Hoelzer, TEM Characterization of Tensile-Tested 14YWT Nanostructured Ferritic Alloys, Microscopy and Microanalysis 14(S2) (2008) 1416-1417.
[60] J.-L. Lin, K. Mo, D. Yun, Y. Miao, X. Liu, H. Zhao, D.T. Hoelzer, J.-S. Park, J. Almer, G. Zhang, Z. Zhou, J.F. Stubbins, A.M. Yacout, In situ synchrotron tensile investigations on 14YWT, MA957, and 9-Cr ODS alloys, Journal of Nuclear Materials 471 (2016) 289-298.
[61] J. Shen, Y. Li, F. Li, H. Yang, Z. Zhao, S. Kano, Y. Matsukawa, Y. Satoh, H. Abe, Microstructural characterization and strengthening mechanisms of a 12Cr-ODS steel, Materials Science and Engineering: A 673 (2016) 624-632.
[62] J. Ren, L. Yu, Y. Liu, C. Liu, H. Li, J. Wu, Effects of Zr Addition on Strengthening Mechanisms of Al-Alloyed High-Cr ODS Steels, Materials (Basel) 11(1) (2018).
[63] N. Kamikawa, K. Sato, G. Miyamoto, M. Murayama, N. Sekido, K. Tsuzaki, T. Furuhara, Stress–strain behavior of ferrite and bainite with nano-precipitation in low carbon steels, Acta Materialia 83 (2015) 383-396.
[64] E. Hornbogen, E. Starke Jr, Overview no. 102 Theory assisted design of high strength low alloy aluminum, Acta metallurgica et materialia 41(1) (1993) 1-16.
[65] J.W. Martin, J.W. Martin, R.D. Doherty, B. Cantor, Stability of microstructure in metallic systems, Cambridge University Press1997.

[66] J. Hoffmann, M. Rieth, R. Lindau, M. Klimenkov, A. Möslang, H.R.Z. Sandim, Investigation on different oxides as candidates for nano-sized ODS particles in reduced-activation ferritic (RAF) steels, Journal of Nuclear Materials 442(1-3) (2013) 444-448.
[67] T.B. Reed, Free energy of formation of binary compounds: an atlas of charts for high-temperature chemical calculations, (1971).
[68] X. Gao, H. Ren, H. Wang, S. Chen, Activity coefficient and solubility of yttrium in Fe-Y dilute solid solution, Journal of Rare Earths 34(11) (2016) 1168-1172.
[69] L. Ratke, P. Voorhees, Growth and Coarsening: Ripening in Materials Processing. 2002, Berlin: Springer Verlag.
[70] Z.W. Zhang, L. Yao, X.L. Wang, M.K. Miller, Vacancy-controlled ultrastable nanoclusters in nanostructured ferritic alloys, Sci Rep 5 (2015) 10600.
[71] M. Speight, Growth kinetics of grain-boundary precipitates, Acta Metallurgica 16(1) (1968) 133-135.
[72] H. Freundlich, Kapillarchemie, Akademische Verlagsgesellschaft, 1922.
[73] C. Wagner, Theorie der alterung von niederschlägen durch umlösen (Ostwald-reifung), Zeitschrift für Elektrochemie, Berichte der Bunsengesellschaft für physikalische Chemie 65(7-8) (1961) 581-591.
[74] I.M. Lifshitz, V.V. Slyozov, The kinetics of precipitation from supersaturated solid solutions, Journal of physics and chemistry of solids 19(1-2) (1961) 35-50.
[75] A. Ardell, On the coarsening of grain boundary precipitates, Acta Metallurgica 20(4) (1972) 601-609.
[76] R. Vengrenovich, Y.V. Gudyma, S. Yarema, Ostwald ripening under dislocation diffusion, Scripta Materialia 46(5) (2002) 363-367.
[77] N.J. Cunningham, M.J. Alinger, D. Klingensmith, Y. Wu, G.R. Odette, On nano-oxide coarsening kinetics in the nanostructured ferritic alloy MA957: A mechanism based predictive model, Materials Science and Engineering: A 655 (2016) 355-362.
[78] N. Oono, K. Nakamura, S. Ukai, T. Kaito, T. Torimaru, A. Kimura, S. Hayashi, Oxide particle coarsening at temperature over 1473 K in 9CrODS steel, Nuclear Materials and Energy 9 (2016) 342-345.
[79] N.H. Oono, S. Ukai, S. Hayashi, S. Ohtsuka, T. Kaito, A. Kimura, T. Torimaru, K. Sakamoto, Growth of oxide particles in FeCrAl- oxide dispersion strengthened steels at high temperature, Journal of Nuclear Materials 493 (2017) 180-188.
[80] J. Koehler, M. Cohen, A.I.o. Mining, M. Engineers, Dislocations in Metals, Institute of Metals Division, the American Institute of Mining and Metallurgical Engineers1954.
[81] J.G. Byrne, Recovery, recrystallization, and grain growth, 1965, 179 P. MACMILLAN CO., NEW YORK (1965).
[82] F.J. Humphreys, M. Hatherly, Recrystallization and related annealing phenomena, Elsevier2012.
[83] J. Burke, D. Turnbull, Recrystallization and grain growth, Progress in metal physics 3 (1952) 220-292.
[84] N. Sallez, Recrystallization, abnormal grain growth and ultrafine microstructure of ODS ferritic steels, Materials, Université de Grenoble, PhD Thesis, 2014.

[85] J. Bailey, P.B. Hirsch, The recrystallization process in some polycrystalline metals, Proc. R. Soc. Lond. A 267(1328) (1962) 11-30.
[86] C. Capdevila Montes, H.K.D.H. Bhadeshia, Influence of Deformation on Recrystallization of an Yttrium Oxide Dispersion-Strengthened Iron Alloy (PM2000), Advanced Engineering Materials 5(4) (2003) 232-237.
[87] T. Chou, Recrystallisation behaviour and grain structure in mechanically alloyed oxide dispersion strengthened MA956 steel, Materials Science and Engineering: A 223(1-2) (1997) 78-90.
[88] G. Pimentel, J. Chao, C. Capdevila, Recrystallization Process in Fe-Cr-Al Oxide Dispersion-Strengthened Alloy: Microstructural Evolution and Recrystallization Mechanism, Jom 66(5) (2014) 780-792.
[89] P.R. Rios, F. Siciliano Jr, H.R.Z. Sandim, R.L. Plaut, A.F. Padilha, Nucleation and growth during recrystallization, Materials Research 8(3) (2005) 225-238.
[90] X. Boulnat, N. Sallez, M. Dadé, A. Borbély, J.-L. Béchade, Y. De Carlan, J. Malaplate, Y. Bréchet, F. De Geuser, A. Deschamps, Influence of oxide volume fraction on abnormal growth of nanostructured ferritic steels during non-isothermal treatments: An in situ study, Acta Materialia 97 (2015) 124-130.
[91] X. Boulnat, M. Perez, D. Fabregue, T. Douillard, M.-H. Mathon, Y. De Carlan, Microstructure evolution in nano-reinforced ferritic steel processed by mechanical alloying and spark plasma sintering, Metallurgical and Materials Transactions A 45(3) (2014) 1485-1497.
[92] E. Aydogan, S.A. Maloy, O. Anderoglu, C. Sun, J.G. Gigax, L. Shao, F.A. Garner, I.E. Anderson, J.J. Lewandowski, Effect of tube processing methods on microstructure, mechanical properties and irradiation response of 14YWT nanostructured ferritic alloys, Acta Materialia 134 (2017) 116-127.
[93] C. Zener, Grains, phases and interfaces: an interpretation of microstructure, Trans. AIME 175 (1948) 15-51.
[94] T.B. Massalski, H. Okamoto, P. Subramanian, L. Kacprzak, W.W. Scott, Binary alloy phase diagrams, American society for metals Metals Park, OH1986.
[95] D. Peckner, I.M. Bernstein, Handbook of stainless steels, McGraw-Hill Book Co., New York, 1977.
[96] A.L. Schaeffler, Constitution diagram for stainless steel weld metal, Metal progress 56(11) (1949) 680.
[97] S. Kobayashi, T. Takasugi, Mapping of 475°C embrittlement in ferritic Fe–Cr–Al alloys, Scripta Materialia 63(11) (2010) 1104-1107.
[98] S. Dryepondt, K.A. Unocic, D.T. Hoelzer, C.P. Massey, B.A. Pint, Development of low-Cr ODS FeCrAl alloys for accident-tolerant fuel cladding, Journal of Nuclear Materials 501 (2018) 59-71.
[99] B.A. Pint, S. Dryepondt, K.A. Unocic, D.T. Hoelzer, Development of ODS FeCrAl for Compatibility in Fusion and Fission Energy Applications, JOM 66(12) (2014) 2458-2466.
[100] C.P. Massey, P.D. Edmondson, K.G. Field, D.T. Hoelzer, S.N. Dryepondt, K.A. Terrani, S.J. Zinkle, Post Irradiation Examination of Nanoprecipitate Stability and α'

Precipitation in an Oxide Dispersion Strengthened Fe-12Cr-5Al Alloy, Scripta Materialia in-review (2018).
[101] J.J. Fisher, US Patent 4,075,010, issued 21 February 1978.
[102] R. Yin, Metallurgical process engineering, Springer Science & Business Media, 2011.
[103] S.R. Shatynski, The thermochemistry of transition metal carbides, Oxidation of Metals 13(2) (1979) 105-118.
[104] P. Ettmayer, W. Lengauer, Nitrides, Ullmann's Encyclopedia of Industrial Chemistry, 2000.
[105] P. Dou, A. Kimura, R. Kasada, T. Okuda, M. Inoue, S. Ukai, S. Ohnuki, T. Fujisawa, F. Abe, TEM and HRTEM study of oxide particles in an Al-alloyed high-Cr oxide dispersion strengthened steel with Zr addition, Journal of Nuclear Materials 444(1-3) (2014) 441-453.
[106] K.A. Unocic, B.A. Pint, D.T. Hoelzer, Advanced TEM characterization of oxide nanoparticles in ODS Fe–12Cr–5Al alloys, Journal of materials science 51(20) (2016) 9190-9206.
[107] S. Ukai, M. Fujiwara, Perspective of ODS alloys application in nuclear environments, Journal of Nuclear Materials 307 (2002) 749-757.
[108] A.J. London, S. Santra, S. Amirthapandian, B.K. Panigrahi, R.M. Sarguna, S. Balaji, R. Vijay, C.S. Sundar, S. Lozano-Perez, C.R.M. Grovenor, Effect of Ti and Cr on dispersion, structure and composition of oxide nano-particles in model ODS alloys, Acta Materialia 97 (2015) 223-233.
[109] E.A. Marquis, Core/shell structures of oxygen-rich nanofeatures in oxide-dispersion strengthened Fe–Cr alloys, Applied Physics Letters 93(18) (2008).
[110] L.L. Hsiung, M.J. Fluss, A. Kimura, Structure of oxide nanoparticles in Fe–16Cr MA/ODS ferritic steel, Materials Letters 64(16) (2010) 1782-1785.
[111] L.L. Hsiung, M.J. Fluss, S.J. Tumey, B.W. Choi, Y. Serruys, F. Willaime, A. Kimura, Formation mechanism and the role of nanoparticles in Fe-Cr ODS steels developed for radiation tolerance, Physical Review B 82(18) (2010) 184103.
[112] P. Dou, A. Kimura, R. Kasada, T. Okuda, M. Inoue, S. Ukai, S. Ohnuki, T. Fujisawa, F. Abe, S. Jiang, Z. Yang, TEM and HRTEM study of oxide particles in an Al-alloyed high-Cr oxide dispersion strengthened ferritic steel with Hf addition, Journal of Nuclear Materials 485 (2017) 189-201.
[113] C.P. Massey, S.L. Dryepondt, P.D. Edmondson, K.A. Terrani, S.J. Zinkle, Influence of Mechanical Alloying and Extrusion Conditions on the Microstructure and Tensile Properties of Low-Cr ODS FeCrAl Alloys, Journal of Nuclear Materials 512 (2018) 227-238.
[114] J.-C. Sublet, G. Butterworth, The neutronic basis for elemental substitution in martensitic steels, Journal of nuclear materials 212 (1994) 695-700.
[115] M.J. Alinger, On the formation and stability of nanometer scale precipitates in ferritic alloys during processing and high temperature service, Materials, University of California, Santa Barbara, 2004.

[116] C. Suryanarayana, Mechanical alloying and milling, Progress in materials science 46(1-2) (2001) 1-184.
[117] J.S. Benjamin, Dispersion strengthened superalloys by mechanical alloying, Metallurgical transactions 1(10) (1970) 2943-2951.
[118] C. Suryanarayana, N. Al-Aqeeli, Mechanically alloyed nanocomposites, Progress in Materials Science 58(4) (2013) 383-502.
[119] N.Y. Iwata, T. Liu, P. Dou, R. Kasada, A. Kimura, T. Okuda, M. Inoue, F. Abe, S. Ukai, S. Ohnuki, T. Fujisawa, Effects of MA environment on the mechanical and microstructural properties of ODS ferritic steels, Journal of Nuclear Materials 417(1-3) (2011) 162-165.
[120] Z. Oksiuta, N. Baluc, Effect of mechanical alloying atmosphere on the microstructure and Charpy impact properties of an ODS ferritic steel, Journal of Nuclear Materials 386-388 (2009) 426-429.
[121] Z. Oksiuta, Microstructural changes of Ods ferritic steel powders during mechanical alloying, Acta Mechanica et Automatica 5 (2011) 74-78.
[122] S. Noh, B.-K. Choi, S.H. Kang, T.K. Kim, Influence of mechanical alloying atmospheres on the microstructures and mechanical properties of 15Cr ODS steels, Nuclear Engineering and Technology 46(6) (2014) 857-862.
[123] J.H. Kim, T.S. Byun, E. Shin, J.-B. Seol, S. Young, N.S. Reddy, Small angle neutron scattering analyses and high temperature mechanical properties of nano-structured oxide dispersion-strengthened steels produced via cryomilling, Journal of Alloys and Compounds 651 (2015) 363-374.
[124] N.Y. Iwata, A. Kimura, M. Fujiwara, N. Kawashima, Effect of milling on morphological and microstructural properties of powder particles for High-Cr Oxide dispersion strengthened ferritic steels, Journal of Nuclear Materials 367-370 (2007) 191-195.
[125] B. Dousti, R. Mojaver, H.R. Shahverdi, R.S. Mamoory, Microstructural evolution and chemical redistribution in Fe–Cr–W–Ti–Y2O3 nanostructured powders prepared by ball milling, Journal of Alloys and Compounds 577 (2013) 409-416.
[126] R. Rahmanifard, H. Farhangi, A.J. Novinrooz, Optimization of mechanical alloying parameters in 12YWT ferritic steel nanocomposite, Materials Science and Engineering: A 527(26) (2010) 6853-6857.
[127] I. Hilger, M. Tegel, M.J. Gorley, P.S. Grant, T. Weißgärber, B. Kieback, The structural changes of Y2O3 in ferritic ODS alloys during milling, Journal of Nuclear Materials 447(1-3) (2014) 242-247.
[128] P. Susila, D. Sturm, M. Heilmaier, B.S. Murty, V. Subramanya Sarma, Effect of yttria particle size on the microstructure and compression creep properties of nanostructured oxide dispersion strengthened ferritic (Fe–12Cr–2W–0.5Y2O3) alloy, Materials Science and Engineering: A 528(13-14) (2011) 4579-4584.
[129] T. Chou, H. Bhadeshia, Crystallographic texture in mechanically alloyed oxide dispersion-strengthened MA956 and MA957 steels, Metallurgical Transactions A 24(4) (1993) 773-779.

[130] G.R. Odette, Recent Progress in Developing and Qualifying Nanostructured Ferritic Alloys for Advanced Fission and Fusion Applications, Jom 66(12) (2014) 2427-2441.
[131] G.R. Odette, On the status and prospects for nanostructured ferritic alloys for nuclear fission and fusion application with emphasis on the underlying science, Scripta Materialia 143 (2018) 142-148.
[132] T.S. Byun, J.H. Yoon, D.T. Hoelzer, Y.B. Lee, S.H. Kang, S.A. Maloy, Process development for 9Cr nanostructured ferritic alloy (NFA) with high fracture toughness, Journal of Nuclear Materials 449(1-3) (2014) 290-299.
[133] M.E. Alam, S. Pal, K. Fields, S.A. Maloy, D.T. Hoelzer, G.R. Odette, Tensile deformation and fracture properties of a 14YWT nanostructured ferritic alloy, Materials Science and Engineering: A 675 (2016) 437-448.
[134] M.J. Alinger, G.R. Odette, G.E. Lucas, Tensile and fracture toughness properties of MA957: implications to the development of nanocomposited ferritic alloys, Journal of Nuclear Materials 307-311 (2002) 484-489.
[135] J. Chao, C. Capdevila, Anisotropy in Mechanical Properties and Fracture Behavior of an Oxide Dispersion Fe20Cr5Al Alloy, Metallurgical and Materials Transactions A 45(9) (2014) 3767-3780.
[136] J. Chao, C. Capdevila, M. Serrano, A. Garcia-Junceda, J.A. Jimenez, G. Pimentel, E. Urones-Garrote, Notch Impact Behavior of Oxide-Dispersion-Strengthened (ODS) Fe20Cr5Al Alloy, Metallurgical and Materials Transactions A 44(10) (2013) 4581-4594.
[137] I. Hilger, X. Boulnat, J. Hoffmann, C. Testani, F. Bergner, Y. De Carlan, F. Ferraro, A. Ulbricht, Fabrication and characterization of oxide dispersion strengthened (ODS) 14Cr steels consolidated by means of hot isostatic pressing, hot extrusion and spark plasma sintering, Journal of Nuclear Materials 472 (2016) 206-214.
[138] D. Hoelzer, M. A Sokolov, T.S. Byun, G.R. Odette, D. Klingensmith, D. Gragg, E. Stergar, K. Fields, FCRD Milestone Report: M21AF050901, 2011.
[139] Z. Oksiuta, P. Mueller, P. Spätig, N. Baluc, Effect of thermo-mechanical treatments on the microstructure and mechanical properties of an ODS ferritic steel, Journal of Nuclear Materials 412(2) (2011) 221-226.
[140] Z. Oksiuta, M. Lewandowska, K.J. Kurzydlowski, N. Baluc, Influence of hot rolling and high speed hydrostatic extrusion on the microstructure and mechanical properties of an ODS RAF steel, Journal of Nuclear Materials 409(2) (2011) 86-93.
[141] E. Aydogan, O. El-Atwani, S. Takajo, S.C. Vogel, S.A. Maloy, High temperature microstructural stability and recrystallization mechanisms in 14YWT alloys, Acta Materialia 148 (2018) 467-481.
[142] A. Hirata, T. Fujita, C.T. Liu, M.W. Chen, Characterization of oxide nanoprecipitates in an oxide dispersion strengthened 14YWT steel using aberration-corrected STEM, Acta Materialia 60(16) (2012) 5686-5696.
[143] A. Hirata, T. Fujita, Y.R. Wen, J.H. Schneibel, C.T. Liu, M.W. Chen, Atomic structure of nanoclusters in oxide-dispersion-strengthened steels, Nat Mater 10(12) (2011) 922-6.

[144] I.-S. Kim, J. Hunn, N. Hashimoto, D. Larson, P. Maziasz, K. Miyahara, E. Lee, Defect and void evolution in oxide dispersion strengthened ferritic steels under 3.2 MeV Fe+ ion irradiation with simultaneous helium injection, Journal of Nuclear Materials 280(3) (2000) 264-274.
[145] Y. Wu, E.M. Haney, N.J. Cunningham, G.R. Odette, Transmission electron microscopy characterization of the nanofeatures in nanostructured ferritic alloy MA957, Acta Materialia 60(8) (2012) 3456-3468.
[146] S. Yamashita, S. Ohtsuka, N. Akasaka, S. Ukai, S. Ohnuki, Formation of nanoscale complex oxide particles in mechanically alloyed ferritic steel, Philosophical Magazine Letters 84(8) (2004) 525-529.
[147] H. Sakasegawa, L. Chaffron, F. Legendre, L. Boulanger, T. Cozzika, M. Brocq, Y. de Carlan, Correlation between chemical composition and size of very small oxide particles in the MA957 ODS ferritic alloy, Journal of Nuclear Materials 384(2) (2009) 115-118.
[148] H. Sakasegawa, F. Legendre, L. Boulanger, M. Brocq, L. Chaffron, T. Cozzika, J. Malaplate, J. Henry, Y. de Carlan, Stability of non-stoichiometric clusters in the MA957 ODS ferrtic alloy, Journal of Nuclear Materials 417(1-3) (2011) 229-232.
[149] M.C. Brandes, L. Kovarik, M.K. Miller, M.J. Mills, Morphology, structure, and chemistry of nanoclusters in a mechanically alloyed nanostructured ferritic steel, Journal of Materials Science 47(8) (2012) 3913-3923.
[150] A. Claisse, P. Olsson, First-principles calculations of (Y, Ti, O) cluster formation in body centred cubic iron-chromium, Nuclear Instruments and Methods in Physics Research Section B: Beam Interactions with Materials and Atoms 303 (2013) 18-22.
[151] C.L. Fu, M. Krcmar, G.S. Painter, X.Q. Chen, Vacancy mechanism of high oxygen solubility and nucleation of stable oxygen-enriched clusters in Fe, Phys Rev Lett 99(22) (2007) 225502.
[152] N.J. Cunningham, Y. Wu, A. Etienne, E.M. Haney, G.R. Odette, E. Stergar, D.T. Hoelzer, Y.D. Kim, B.D. Wirth, S.A. Maloy, Effect of bulk oxygen on 14YWT nanostructured ferritic alloys, Journal of Nuclear Materials 444(1-3) (2014) 35-38.
[153] Y.Z. Shen, T.T. Zou, S. Zhang, L.Z. Sheng, Identification of Oxide Phases in Oxide Dispersion Strengthened PM2000 Steel, ISIJ International 53(2) (2013) 304-310.
[154] M. Klimiankou, R. Lindau, A. Möslang, J. Schröder, TEM study of PM 2000 steel, Powder Metallurgy 48(3) (2013) 277-287.
[155] K. Dawson, S.J. Haigh, G.J. Tatlock, A.R. Jones, Nano-particle precipitation in mechanically alloyed and annealed precursor powders of legacy PM2000 ODS alloy, Journal of Nuclear Materials 464 (2015) 200-209.
[156] C.H. Zhang, A. Kimura, R. Kasada, J. Jang, H. Kishimoto, Y.T. Yang, Characterization of the oxide particles in Al-added high-Cr ODS ferritic steels, Journal of Nuclear Materials 417(1-3) (2011) 221-224.
[157] L.L. Hsiung, HRTEM study of oxide nanoparticles in Fe-16Cr ODS ferritic steel developed for fusion energy, Lawrence Livermore National Laboratory (LLNL), Livermore, CA, 2010.

[158] P. Dou, A. Kimura, T. Okuda, M. Inoue, S. Ukai, S. Ohnuki, T. Fujisawa, F. Abe, Polymorphic and coherency transition of Y–Al complex oxide particles with extrusion temperature in an Al-alloyed high-Cr oxide dispersion strengthened ferritic steel, Acta Materialia 59(3) (2011) 992-1002.
[159] B. Dubiel, W. Osuch, M. Wróbel, P. Ennis, A. Czyrska-Filemonowicz, Correlation of the microstructure and the tensile deformation of incology MA956, Journal of materials processing technology 53(1-2) (1995) 121-130.
[160] H. Cama, T. Hughes, Stability of dispersoids in commercially available mechanically alloyed oxide dispersion strengthened alloys after high temperature exposures, Materials for Advanced Power Engineering, Part II, (1994) 1497-1506.
[161] C. Chen, P. Wang, G. Tatlock, Phase transformations in yttrium–aluminium oxides in friction stir welded and recrystallised PM2000 alloys, Materials at High Temperatures 26(3) (2009) 299-303.
[162] P. Dou, A. Kimura, T. Okuda, M. Inoue, S. Ukai, S. Ohnuki, T. Fujisawa, F. Abe, Effects of extrusion temperature on the nano-mesoscopic structure and mechanical properties of an Al-alloyed high-Cr ODS ferritic steel, Journal of Nuclear Materials 417(1-3) (2011) 166-170.
[163] R. Rahmanifard, H. Farhangi, A.J. Novinrooz, S. Moniri, Development of a High-Strength Ultrafine-Grained Ferritic Steel Nanocomposite, Metallurgical and Materials Transactions A 44(2) (2012) 990-998.
[164] N. Cunningham, Y. Wu, G. Odette, D. Hoelzer, S. Maloy, Characterization of a larger best practice heat of 14YWT in annealed powder, HIP consolidated and extruded forms, Fusion Materials Semiannual Progress Report for Period Ending June 30 (2013) 15-26.
[165] D.T. Hoelzer, K.A. Unocic, M.A. Sokolov, T.S. Byun, Influence of processing on the microstructure and mechanical properties of 14YWT, Journal of Nuclear Materials 471 (2016) 251-265.
[166] M.K. West, Processing and Characterization of Oxide Dispersion Strengthened 14YWT Ferritic Alloys, University of Tennessee, 2006.
[167] N. Cunningham, Y. Wu, D. Klingensmith, G.R. Odette, On the remarkable thermal stability of nanostructured ferritic alloys, Materials Science and Engineering: A 613 (2014) 296-305.
[168] M.K. Miller, C.M. Parish, Role of alloying elements in nanostructured ferritic steels, Materials Science and Technology 27(4) (2011) 729-734.
[169] J. Chen, P. Jung, M.A. Pouchon, T. Rebac, W. Hoffelner, Irradiation creep and precipitation in a ferritic ODS steel under helium implantation, Journal of Nuclear Materials 373(1-3) (2008) 22-27.
[170] C.C. Eiselt, H. Schendzielorz, A. Seubert, B. Hary, Y. de Carlan, P. Diano, B. Perrin, D. Cedat, ODS-materials for high temperature applications in advanced nuclear systems, Nuclear Materials and Energy 9 (2016) 22-28.
[171] H. Dong, L. Yu, Y. Liu, C. Liu, H. Li, J. Wu, Enhancement of tensile properties due to microstructure optimization in ODS steels by zirconium addition, Fusion Engineering and Design 125 (2017) 402-406.

[172] B. Gault, M.P. Moody, J.M. Cairney, S.P. Ringer, Atom probe microscopy, Springer, 2012.
[173] R. Gomer, Field emissions and field ionization, American Inst. of Physics1992.
[174] V.J. Araullo-Peters, B. Gault, S.L. Shrestha, L. Yao, M.P. Moody, S.P. Ringer, J.M. Cairney, Atom probe crystallography: Atomic-scale 3-D orientation mapping, Scripta Materialia 66(11) (2012) 907-910.
[175] D. Blavette, F. Vurpillot, P. Pareige, A. Menand, A model accounting for spatial overlaps in 3D atom-probe microscopy, Ultramicroscopy 89(1-3) (2001) 145-153.
[176] C. Hatzoglou, B. Radiguet, P. Pareige, Experimental artefacts occurring during atom probe tomography analysis of oxide nanoparticles in metallic matrix: Quantification and correction, Journal of Nuclear Materials 492 (2017) 279-291.
[177] C. Hatzoglou, B. Radiguet, F. Vurpillot, P. Pareige, A chemical composition correction model for nanoclusters observed by APT - Application to ODS steel nanoparticles, Journal of Nuclear Materials 505 (2018) 240-248.
[178] C.A. Williams, E.A. Marquis, A. Cerezo, G.D.W. Smith, Nanoscale characterisation of ODS–Eurofer 97 steel: An atom-probe tomography study, Journal of Nuclear Materials 400(1) (2010) 37-45.
[179] A.J. London, S. Lozano-Perez, M.P. Moody, S. Amirthapandian, B.K. Panigrahi, C.S. Sundar, C.R. Grovenor, Quantification of oxide particle composition in model oxide dispersion strengthened steel alloys, Ultramicroscopy 159 Pt 2 (2015) 360-7.
[180] M.K. Miller, D.T. Hoelzer, E.A. Kenik, K.F. Russell, Nanometer scale precipitation in ferritic MA/ODS alloy MA957, Journal of Nuclear Materials 329-333 (2004) 338-341.
[181] M.K. Miller, E.A. Kenik, K.F. Russell, L. Heatherly, D.T. Hoelzer, P.J. Maziasz, Atom probe tomography of nanoscale particles in ODS ferritic alloys, Materials Science and Engineering: A 353(1-2) (2003) 140-145.
[182] B.T.M. Willis, C.J. Carlile, Experimental Neutron Scattering, OUP Oxford2017.
[183] A.J. Jackson, Introduction to small-angle neutron scattering and neutron reflectometry, NIST Center for Neutron Research (2008) 1-24.
[184] G. Kostorz, Small-angle scattering and its applications to materials science, Treatise on Materials Science & Technology 1979, pp. 227-289.
[185] V.K. Peterson, G.J. Kearley, Neutron Applications in Materials for Energy: An Overview, Neutron Applications in Materials for Energy2015, pp. 1-9.
[186] M.J. Alinger, G.R. Odette, D.T. Hoelzer, The development and stability of Y–Ti–O nanoclusters in mechanically alloyed Fe–Cr based ferritic alloys, Journal of Nuclear Materials 329-333 (2004) 382-386.
[187] Y.-S. Han, X. Mao, J. Jang, Small Angle Neutron Scattering Study of Nano Sized Microstructure in Fe–Cr ODS Steels for Gen IV In-Core Applications, Journal of Nanoscience and Nanotechnology 13(11) (2013) 7524-7528.
[188] M.H. Mathon, M. Perrut, S.Y. Zhong, Y. de Carlan, Small angle neutron scattering study of martensitic/ferritic ODS alloys, Journal of Nuclear Materials 428(1-3) (2012) 147-153.

[189] J.S. Pedersen, Determination of size distribution from small-angle scattering data for systems with effective hard-sphere interactions, Journal of applied crystallography 27(4) (1994) 595-608.
[190] J.S. Pedersen, Small-angle scattering from precipitates: analysis by use of a polydisperse hard-sphere model, Physical Review B 47(2) (1993) 657.
[191] J.M. Hyde, M.G. Burke, G.D.W. Smith, P. Styman, H. Swan, K. Wilford, Uncertainties and assumptions associated with APT and SANS characterisation of irradiation damage in RPV steels, Journal of Nuclear Materials 449(1-3) (2014) 308-314.
[192] R. Coppola, M. Klimenkov, R. Lindau, A. Möslang, M. Valli, A. Wiedenmann, Recent applications of small-angle neutron scattering in the characterization of irradiated steels for nuclear technologies, Journal of Nuclear Materials 409(2) (2011) 100-105.
[193] S. Shu, B.D. Wirth, P.B. Wells, D.D. Morgan, G.R. Odette, Multi-technique characterization of the precipitates in thermally aged and neutron irradiated Fe-Cu and Fe-Cu-Mn model alloys: Atom probe tomography reconstruction implications, Acta Materialia 146 (2018) 237-252.
[194] M. Alinger, G. Odette, D. Hoelzer, On the role of alloy composition and processing parameters in nanocluster formation and dispersion strengthening in nanostuctured ferritic alloys, Acta Materialia 57(2) (2009) 392-406.
[195] S.-Y. Zhong, J. Ribis, N. Lochet, Y. de Carlan, V. Klosek, V. Ji, M.-H. Mathon, The Effect of Y/Ti Ratio on Oxide Precipitate Evolution in ODS Fe-14 Wt Pct Cr Alloys, Metallurgical and Materials Transactions A 46(3) (2014) 1413-1418.
[196] S.Y. Zhong, J. Ribis, V. Klosek, Y. de Carlan, N. Lochet, V. Ji, M.H. Mathon, Study of the thermal stability of nanoparticle distributions in an oxide dispersion strengthened (ODS) ferritic alloys, Journal of Nuclear Materials 428(1-3) (2012) 154-159.
[197] G. Thomas, Transmission electron microscopy of materials, in: M.J. Goringe (Ed.) New York : Wiley, New York, 1979.
[198] J.I. Goldstein, D.E. Newbury, J.R. Michael, N.W. Ritchie, J.H.J. Scott, D.C. Joy, Scanning electron microscopy and X-ray microanalysis, Springer, 2017.
[199] L. Reimer, Scanning electron microscopy: physics of image formation and microanalysis, Springer, 2013.
[200] A.J. Schwartz, M. Kumar, B.L. Adams, Electron backscatter diffraction in materials science, New York : Kluwer Academic, New York, 2000.
[201] V. Randle, Microtexture determination and its applications, in: M. Institute of (Ed.) London : Institute of Metals, London, 1992.
[202] J. Hren, Introduction to analytical electron microscopy, Springer Science & Business Media, 2013.
[203] C.P. Massey, S.N. Dryepondt, P.D. Edmondson, M.G. Frith, K.C. Littrell, A. Kini, B. Gault, K.A. Terrani, S.J. Zinkle, Multiscale Investigations of Nanoprecipitate Nucleation, Growth, and Coarsening in Annealed low-Cr Oxide Dispersion Strengthened FeCrAl Powder, Acta Materialia (under peer review, 2018).

[204] S.L. Dryepondt, C.P. Massey, M.N. Gussev, Milestone Report: M3FT-17OR020202081, Production and Characterization of Large Batch FeCrAl ODS Alloy, 2017.
[205] C.M. Parish, N.K. Kumar, L.L. Snead, P.D. Edmondson, K.G. Field, C. Silva, A.M. Williams, K. Linton, K.J. Leonard, LAMDA: irradiated-materials microscopy at Oak Ridge National Laboratory, Microscopy and Microanalysis 21(S3) (2015) 1003-1004.
[206] M.K. Miller, K.F. Russell, Atom probe specimen preparation with a dual beam SEM/FIB miller, Ultramicroscopy 107(9) (2007) 761-766.
[207] D.J. Larson, T. Prosa, R.M. Ulfig, B.P. Geiser, T.F. Kelly, Local electrode atom probe tomography, New York, US: Springer Science (2013).
[208] D. Vaumousse, A. Cerezo, P. Warren, A procedure for quantification of precipitate microstructures from three-dimensional atom probe data, Ultramicroscopy 95 (2003) 215-221.
[209] A. Cerezo, L. Davin, Aspects of the observation of clusters in the 3-dimensional atom probe, Surface and Interface Analysis 39(2-3) (2007) 184-188.
[210] L.T. Stephenson, M.P. Moody, P.V. Liddicoat, S.P. Ringer, New techniques for the analysis of fine-scaled clustering phenomena within atom probe tomography (APT) data, Microscopy and Microanalysis 13(6) (2007) 448-463.
[211] E.A. Marquis, J.M. Hyde, Applications of atom-probe tomography to the characterisation of solute behaviours, Materials Science and Engineering: R: Reports 69(4-5) (2010) 37-62.
[212] A.J. London, D. Haley, M.P. Moody, Single-Ion Deconvolution of Mass Peak Overlaps for Atom Probe Microscopy, Microscopy and Microanalysis 23(02) (2017) 300-306.
[213] B. Gault, D.W. Saxey, M.W. Ashton, S.B. Sinnott, A.N. Chiaramonti, M.P. Moody, D.K. Schreiber, Behavior of molecules and molecular ions near a field emitter, New Journal of Physics 18(3) (2016) 033031.
[214] V. Badjeck, M.G. Walls, L. Chaffron, J. Malaplate, K. March, New insights into the chemical structure of Y 2 Ti 2 O 7−δ nanoparticles in oxide dispersion-strengthened steels designed for sodium fast reactors by electron energy-loss spectroscopy, Journal of Nuclear Materials 456 (2015) 292-301.
[215] M.A. Musa, R.a.S. Azis, N.H. Osman, J. Hassan, T. Zangina, Structural and magnetic properties of yttrium iron garnet (YIG) and yttrium aluminum iron garnet (YAlG) nanoferrite via sol-gel synthesis, Results in Physics 7 (2017) 1135-1142.
[216] G.D. Wignall, K.C. Littrell, W.T. Heller, Y.B. Melnichenko, K.M. Bailey, G.W. Lynn, D.A. Myles, V.S. Urban, M.V. Buchanan, D.L. Selby, P.D. Butler, The 40 m general purpose small-angle neutron scattering instrument at Oak Ridge National Laboratory, Journal of Applied Crystallography 45(5) (2012) 990-998.
[217] O. Glatter, A new method for the evaluation of small-angle scattering data, Journal of Applied Crystallography 10(5) (1977) 415-421.
[218] D. Brown, P. Kienzle, Neutron activation and scattering calculator, NIST Center for Neutron Research. (accessed 7.2018).

[219] W. Blau, S. Mager, E. Wieser, Determination of Localized Magnetic Moments in Fe-Cr-Al Alloys and the Electron Structure, physica status solidi (b) 81(2) (1977) 535-544.
[220] C.M. Parish, MT3FT-15OR0204122: Report on the acquisition and installation of FEI Talos F200X S/TEM, Oak Ridge National Laboratory (ORNL), Oak Ridge, TN (United States), 2015.
[221] H. Von Harrach, P. Dona, B. Freitag, H. Soltau, A. Niculae, M. Rohde, An integrated silicon drift detector system for FEI Schottky field emission transmission electron microscopes, Microscopy and Microanalysis 15(S2) (2009) 208.
[222] C.M. Parish, Multivariate statistics applications in scanning transmission electron microscopy X-ray spectrum imaging, Advances in Imaging and Electron Physics, Elsevier2011, pp. 249-295.
[223] P.G. Kotula, M.R. Keenan, J.R. Michael, Automated analysis of SEM X-ray spectral images: A powerful new microanalysis tool, Microscopy and Microanalysis 9(1) (2003) 1-17.
[224] R.L. Klueh, J.P. Shingledecker, R.W. Swindeman, D.T. Hoelzer, Oxide dispersion-strengthened steels: A comparison of some commercial and experimental alloys, Journal of Nuclear Materials 341(2-3) (2005) 103-114.
[225] C.P. Massey, S.N. Dryepondt, P.D. Edmondson, A. Kini, B. Gault, K.A. Terrani, S.J. Zinkle, The Effect of Zr on Precipitation in Oxide Dispersion Strengthened FeCrAl Alloys, Journal of Nuclear Materials (in preparation, 2018).
[226] M. Klimiankou, R. Lindau, A. Möslang, Direct correlation between morphology of (Fe, Cr) 23C6 precipitates and impact behavior of ODS steels, Journal of Nuclear Materials 367 (2007) 173-178.
[227] E.A. Marquis, F. Vurpillot, Chromatic Aberrations in the Field Evaporation Behavior of Small Precipitates, Microscopy and Microanalysis 14(6) (2008) 561-570.
[228] S. Kostić, Z. Lazarević, V. Radojević, A. Milutinović, M. Romčević, N. Romčević, A. Valčić, Study of structural and optical properties of YAG and Nd: YAG single crystals, Materials Research Bulletin 63 (2015) 80-87.
[229] A.B. Muñoz-García, E. Anglada, L. Seijo, First-principles study of the structure and the electronic structure of yttrium aluminum garnet Y3Al5O12, International Journal of Quantum Chemistry 109(9) (2009) 1991-1998.
[230] T. Philippe, D. Blavette, Nucleation pathway in coherent precipitation, Philosophical Magazine 91(36) (2011) 4606-4622.
[231] J. Kvapil, J. Kvapil, J. Kubelka, R. Autrata, The role of iron ions in YAG and YAP, Crystal Research and Technology 18(1) (1983) 127-131.
[232] N. Saunders, CALPHAD (calculation of phase diagrams) : a comprehensive guide, Oxford, New York, 1998.
[233] A. Kroupa, Modelling of phase diagrams and thermodynamic properties using Calphad method: Development of thermodynamic databases, Computational Materials Science 66 (2013) 3-13.
[234] M. Hillert, Phase equilibria, phase diagrams and phase transformations: their thermodynamic basis, Cambridge University Press, 2007.

[235] L. Wen, X. Sun, Z. Xiu, S. Chen, C.-T. Tsai, Synthesis of nanocrystalline yttria powder and fabrication of transparent YAG ceramics, Journal of the European Ceramic Society 24(9) (2004) 2681-2688.
[236] V.B. Glushkova, V.A. Krzhizhanovskaya, O.N. Egorova, Interactions of yttrium and aluminum oxides, Inorg. Mater. (Eng, Transl), 19(1) (1983) 80-84.
[237] X. Guo, K. Sakurai, Formation of yttrium aluminum perovskite and yttrium aluminum garnet by mechanical solid-state reaction, Japanese Journal of Applied Physics 39(3R) (2000) 1230.
[238] S.L. Shang, H.Z. Fang, J. Wang, C.P. Guo, Y. Wang, P.D. Jablonski, Y. Du, Z.K. Liu, Vacancy mechanism of oxygen diffusivity in bcc Fe: A first-principles study, Corrosion Science 83 (2014) 94-102.
[239] C. Hin, B.D. Wirth, J.B. Neaton, Formation ofY2O3nanoclusters in nanostructured ferritic alloys during isothermal and anisothermal heat treatment: A kinetic Monte Carlo study, Physical Review B 80(13) (2009).
[240] P. Klugkist, C. Herzig, Tracer diffusion of titanium in α-iron, physica status solidi (a) 148(2) (1995) 413-421.
[241] M. Laurent-Brocq, F. Legendre, M.H. Mathon, A. Mascaro, S. Poissonnet, B. Radiguet, P. Pareige, M. Loyer, O. Leseigneur, Influence of ball-milling and annealing conditions on nanocluster characteristics in oxide dispersion strengthened steels, Acta Materialia 60(20) (2012) 7150-7159.
[242] J. Hoyt, On the coarsening of precipitates located on grain boundaries and dislocations, Acta metallurgica et materialia 39(9) (1991) 2091-2098.
[243] L.K. Mansur, Theory and experimental background on dimensional changes in irradiated alloys, Journal of Nuclear Materials 216(C) (1994) 97-123.
[244] T.L. Bergman, F.P. Incropera, D.P. DeWitt, A.S. Lavine, Fundamentals of heat and mass transfer, John Wiley & Sons2011.

Appendix

Reconstructed Control Volumes

Table A.1. Visualization of Reconstructed Sample Volumes

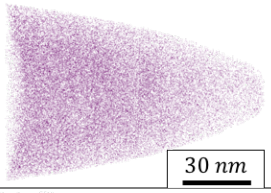
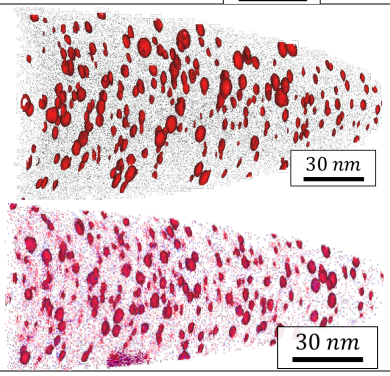
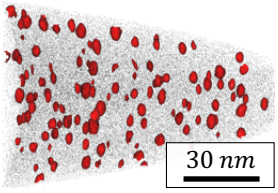
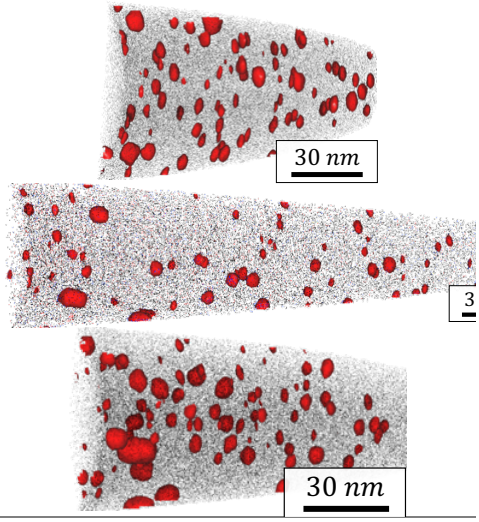
Sample	Processing Condition	Ball Mill	Furnace Temp [°C]	Time [h]	LEAP	Reconstruction(s)
ZY40H	Powder	CM08	n/a	n/a	4000X HR	
ZY10C15	Powder	CM08	1000	0.25	5000 XR	
ZY10C60	Powder (Fine Grained Region)	CM08	1000	1	4000X Si	
ZY10C60	Powder (Fine Grained Region)	CM08	1000	1	4000X HR	

Table A.1 Continued. Visualization of Reconstructed Sample Volumes

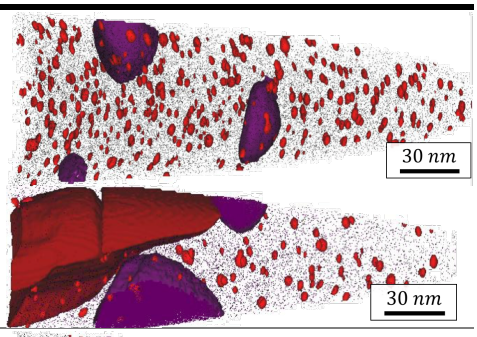
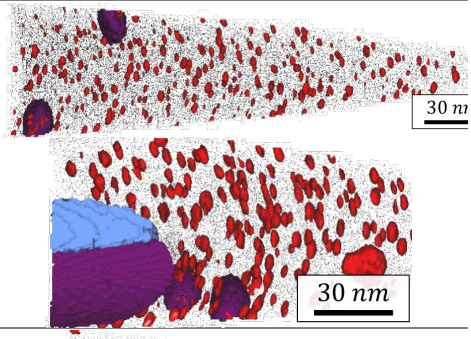
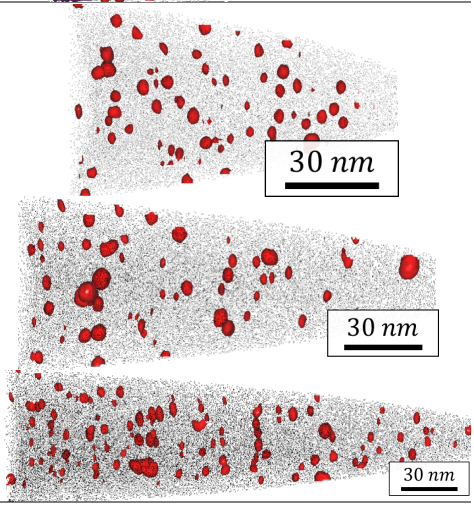
Sample	Processing Condition	Ball Mill	Furnace Temp [°C]	Time [h]	LEAP	Reconstruction(s)
ZY10C60	Powder (Fine Grained Region)	CM08	1000	1	5000 XR	
ZY10C60	Powder (Coarse Grained Region)	CM08	1000	1	5000 XR	
Y10C60	Powder (Fine Grained Region)	CM08	1000	1	4000X Si	

Table A.1 Continued. Visualization of Reconstructed Sample Volumes

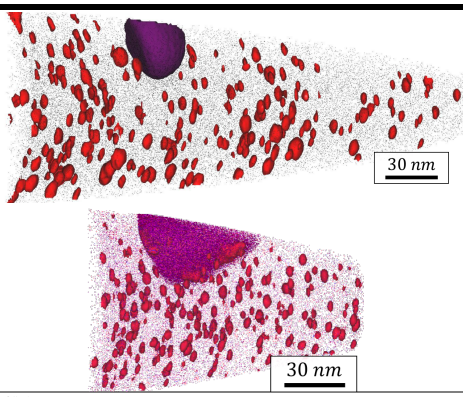
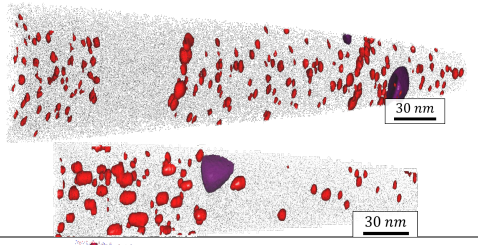
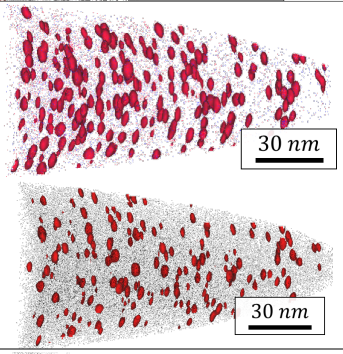
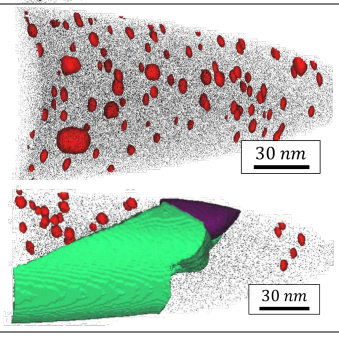
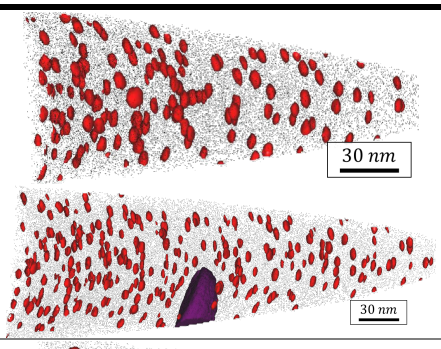
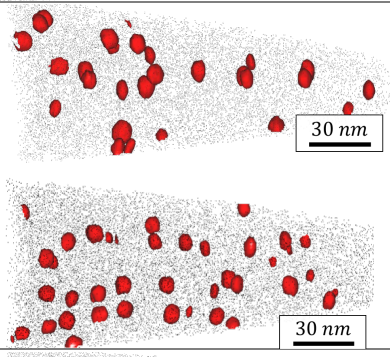
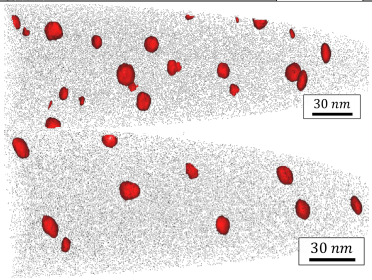
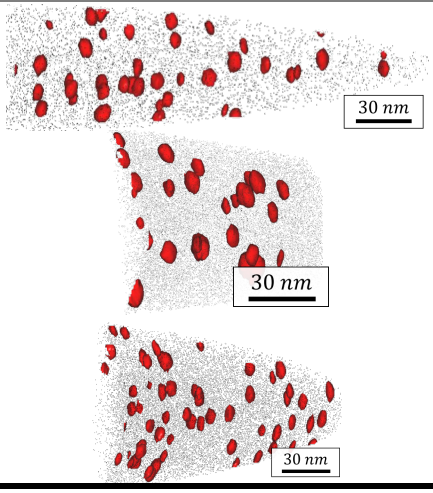
Sample	Processing Condition	Ball Mill	Furnace Temp [°C]	Time [h]	LEAP	Reconstruction(s)
106ZY10C1	Extruded	CM01	1000	1	4000X Si	
106ZY10C8	Extruded	CM08	1000	1	5000 XR	
106ZYA15C	Extruded	CM01	850 1050	1 0.5	5000 XR	
106ZY15C	Extruded	CM01	1050	1	5000 XR	

Table A.1 Continued. Visualization of Reconstructed Sample Volumes

Sample	Processing Condition	Ball Mill	Furnace Temp [°C]	Time [h]	LEAP	Reconstruction(s)
ZY15C10h	Powder	CM08	1050	10	4000X HR	
ZY15C50h	Powder	CM08	1050	50	4000X HR	
ZY15C500h	Powder	CM08	1050	500	4000X HR	
CrAZY-H1	Extruded	CM08	1100	1	4000X HR	

Lumped Capacitance Comparison of Temperature Profiles

One of the major points of comparison in this work was the difference between precipitation in powders annealed for 15 min. and 60 min. in a box furnace within quartz vials. As mentioned in the experimental methods, the sealed and evacuated nature of the quartz vials made accurate estimations of the internal powder temperature impossible; to estimate the powder temperature, and to simultaneously obtain a representative powder temperature profile for later extrusion simulations for particle coarsening, a thermocouple was used to measure the powder temperature in the same extrusion can used for the 106ZY10C1, 106ZY10C8, and 106ZY15C samples with a 200g powder mass. The vials that held the annealed powders for precipitation studies were smaller, with only a few inches in height and a 3cm OD. This section highlights differences in the two heating profiles by fitting the experimentally measured temperature profile using the lumped capacitance method for both conditions.

The lumped capacitance method is a simplified heat transfer model that assumes that the material is being heated so fast by the surrounding environment that there is essentially no temperature gradient being developed across the sample volume. Although

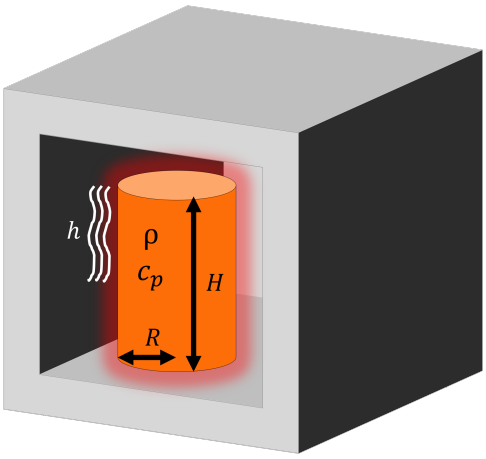


Figure A.1. Visual schematic of the lumped capacitance problem

the scientific implication of this assumption is that the material has an infinite thermal conductivity, practically this model is quite accurate for quenching studies and high heating rates, which is representative of the high temperature furnace heating in this work. The model thus depends only on the convection coefficient (h), the material's density (ρ) and heat capacity (c_p), and the dimensions of the material being heated (R and H for the radius and height of a cylindrical specimen). The lumped capacitance (LC) model takes the following form relating the specimen temperature and time [244]:

$$T(t) = (T_0 - T_\infty) * \exp\left(-\left(\frac{h}{\rho c_p}\right)\left(\frac{A_{cyl}}{V_{cyl}}\right)t\right) + T_\infty \quad \text{(A.1)}$$

where A_{cyl} and V_{cyl} are the surface area and volume of the assumed cylindrical control volume occupied by the powder. A visual representation of the current setup is provided in **Figure A.1**. In this simplified comparison, it is assumed that the density of the powder (including the compaction density), the convection coefficient, and the heat capacity are both constant. Although the heat capacity for quartz (~3.5 W/m/K) is 10x lower than that for steel (~30 W/m/K), due to the small thickness of the vial and extrusion can walls in comparison to the powder control volume it is expected that the current assumptions will provide a conservative estimation of temperature differences. The extrusion can has powder dimensions of 4.83cm OD x 5.4cm while the quartz vial volume occupied by powder is 3cm OD x 3.81cm in height.

Using the experimental temperature profile previously provided in **Figure 4.5**, Eq. (A.1) was used to fit the experimental data using MATLAB's curve fitting toolbox. The value of the initial temperature (T_0=23°C) and target temperature (T_∞=23°C) are known inputs, as well as the surface area and volume of the extrusion can. Thus, the term $\left(\frac{h}{\rho c_p}\right)$ was fit as one constant using the nonlinear least squares procedures available in the curve fitting MATLAB procedure. Once this constant was found, it was plugged back into Eq. (A.1), this time using the area and volume of the vial powder volume. The result are two LC temperature profiles for the can and vial, respectively for direct comparison

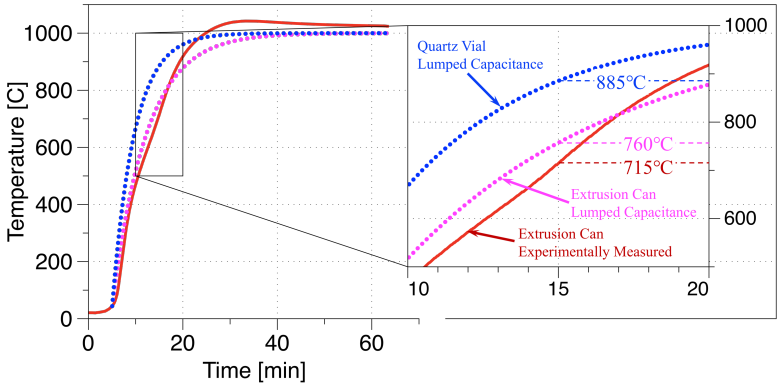


Figure A.2. The comparison of the LC curve fits for the extrusion can and quartz vial with the experimentally measured extrusion can temperature profile.

with the experimental profile. Due to the ~5 min. interval at the initial tail of the curve caused by the loss of furnace heat when the door was opened, the curve fitting was conducted only on the experimental data excluding this tail.

The resulting LC model predictions are illustrated in **Figure A.2**. At times less than 17 min., the LC model for the extrusion can approximated the experimental data fairly well, while above this time the experimental data overshoots the 1000°C target, which provided less agreement until longer annealing times (>40 min.). Due to the smaller sample size, the quartz vial is expected to have a higher temperature than the experimentally measured extrusion can by ~170°C. However, this result does not affect any of the aforementioned results or conclusions in this work since significant precipitate coarsening was not observed until temperatures >1000°C and for longer periods of time. In addition, the good agreement between the in-situ SANS, ex-situ SANS, and ex-situ APT results still suggests a low temperature (400-600°C) nucleation and growth regime with an intermediate temperature regime (600°C < T < 1000°C) where precipitates are stable Thus, the use of the ZY10C15 specimen, irrespective of whether or not it is 715, 760, or 885°C for comparison with specimens that have later coarsened in this study is not an erroneous methodology based on this LC modelling approach.

Vita

Caleb P. Massey was born in Norfolk, Virginia on December 12, 1991 to Michael and Tammie Massey. He attended Grafton High School in Yorktown, Virginia. After graduating, Caleb attended Virginia Commonwealth University (VCU) in Richmond, VA, where he graduated summa cum laude with university honors in May, 2015 with a Bachelor's degree in Mechanical Engineering. A week after graduation, Caleb married his wife Logan Gravitt Massey. After being awarded a Department of Energy Nuclear Energy University Programs (NEUP) fellowship, Caleb continued his education at VCU through enrollment in the university's Mechanical and Nuclear Engineering graduate program. Under the mentorship of Dr. Gokul Vasudevamurthy, Caleb researched various topics spanning from the development of metal-matrix composites to the conceptualization of advanced thermal hydraulic systems for the extension of safety margins in nuclear accident scenarios. After a year of work with vacuum and high-temperature experiments at VCU's High Temperature Materials Laboratory (HTML), Caleb graduated with his Master's degree in Mechanical and Nuclear Engineering in December, 2015. After an unexpected move to Tennessee in the winter of 2015, Caleb enrolled at the University of Tennessee as a graduate research assistant in the Nuclear Engineering Department under Dr. Steven Zinkle, where he studied advanced structural materials for applications nuclear environments. He will obtain his Doctor of Philosophy in Nuclear Engineering in December 2018.